CR-134068

RCS JET-FLOW FIELD INTERACTION EFFECTS
ON THE AERODYNAMICS OF THE
SPACE SHUTTLE ORBITER

FINAL REPORT

GENERAL DYNAMICS
Convair Aerospace Division

RCS JET-FLOW FIELD INTERACTION EFFECTS ON THE AERODYNAMICS OF THE SPACE SHUTTLE ORBITER

FINAL REPORT

November 1973

J. R. Rausch
A. M. Roberge

FOREWORD

SUMMARY

A study was conducted by General Dynamics Convair Aerospace Division for the NASA Johnson Space Center under NASA Contract NAS9-13012 to determine the external effects caused by operation of the reaction control system (RCS) during entry of the Shuttle Orbiter. The North American Rockwell International Preliminary Requirements Review (PRR) configuration was used in assessing the effects of the proposed RCS installation on control amplification factors and aerodynamic heating.

Applicable analytic and/or empirical methods were identified from a review of available material. These efforts concentrated on jet plume - external flow interaction effects, which as shown later, did not prove to be the significant effect. Analytic methods exist for two-dimensional jets while empirical results must be relied on for three-dimensional jets. An experimental program was established to extend empirical methods to the PRR configuration.

Tests were conducted by Convair in the NASA Ames Research Center at Mach 7.4 and the NASA Langley Research Center at Mach numbers 4.0, 2.95 and 2.5. Force data were obtained at all conditions with heat transfer data also obtained in the high Mach number test. A description of the simulation parameters and test programs as conducted are presented along with a discussion of the final data and analysis of results.

Force data were obtained for the basic airframe characteristics plus induced effects when the RCS is operating; the thrusters themselves being non-metric in the aft position on the OMS pods. Resulting control amplification and/or coupling were derived and their effects on the aerodynamic stability and control of the orbiter and the RCS thrust determined. Control reversal with roll and pitch RCS and strong pitch coupling when using the yaw RCS were the predominant effects, caused primarily by jet plume impingement on ajacent surfaces and not plume-flow field interactions in the classic sense.

A limited assessment of alternate RCS locations pointed to possible alleviation of control problems, with acceptable heating design constraints, by relocation of nose down pitch RCS jets on the bottom of the aft body flap.

Aerodynamic heating analyses limited to the OMS pod based on available methods and experimental data indicate a heating problem, which will require local increase in insulation thickness to maintain acceptable bond line temperatures.

Finally an empirical model of the RCS jet plume impingement/interaction stability and control effects was developed from the data base and used, along with the aerodynamic heating analysis referred to above, to estimate the vehicle aerodynamics and aerodynamic pod heating for the PRR configuration along an entry trajectory.

TABLE OF CONTENTS

TABLE OF CONTENTS (cont'd)

LIST OF FIGURES

LIST OF FIGURES (cont'd)

LIST OF FIGURES (cont'd)

LIST OF FIGURES (cont'd)

LIST OF FIGURES (cont'd)

LIST OF FIGURES (cont'd)

LIST OF TABLES

NOMENCLATURE

Symbol	Definition
A	area (ft^2)
b_{ref}	lateral-directional reference length (ft)
c	specific heat of model material (Btu/lbm-°R)
$\bar{c}$	wing chord reference length (ft)
c_p	specific heat of air at constant pressure (Btu/lbm-°R)
C_ℓ	body axis rolling moment coefficient
C_m	body axis pitching moment coefficient
C_N	body axis normal force coefficient
C_n	body axis yaw moment coefficient
C_p	pressure coefficient
C_t	thrust coefficient
C_y	body axis side force coefficient
d	diameter (ft)
erfc	complementary error function (1-erf)
F_j	jet reaction force (lbf)
F_N	normal force loading produced by jet-stream interaction (lbf)
H	jet penetration height (ft)
h	heat transfer coefficient ($Btu/ft^2 sec$-°R)
KE	kinetic energy parameter (ft^2/sec^2)
K	force or moment amplification factor
k	thermal conductivity (Btu/ft-sec-°R)
1	location of the jet downstream from leading edge (ft)
L	reference length (ft)
$\dot{m}$	mass flow (lbm/sec)
M	molecular weight (lbm/mole) (section 2)

NOMENCLATURE (CONT'D)

Symbol	Definition
M	Mach number
M_{JFE}	full expanded plume Mach number
n	number of jets in cluster
P	pressure (lbf/ft^2)
q	dynamic pressure (lbf/ft^2)
R	gas constant $(ft^2/sec^2 - °R)$
r	radius (ft)
R_e	Reynolds number
S_{ref}	wing reference area (ft^2)
t	time (sec)
T	thrust (lb) (Section 3)
T	temperature (°R)
V	velocity (ft/sec)
X_{max}	distance along jet axis to maximum plume diameter (ft)
X	distance along jet axis
x	streamwise distance
x_r	radial distance (ft)
y	distance normal to wall (ft)
α	angle of attack (deg)
β	angle of yaw (deg); also $\sqrt{M^2 - 1}$
Δ	normal shock standoff distance (ft)
$\Delta \nu$	initial plume turning angle
δ	flow deflection angle
θ_N	nozzle angle (deg.)
θ	angular orientation around jet (deg)
μ	dynamic viscosity $(lbf-sec/ft^2)$

NOMENCLATURE (CON'D)

Symbol	Definition

ρ density (lbm/ft^3)

ζ pressure ratio, P_{sep}/P_∞

γ ratio of specifc heat

Φ momentum parameter (lbf)

Φ correlation factor using blast wave analogy

Subscripts

amb	ambient conditions
AV	average
aw	adiabatic wall conditions
c	rocket chamber condition
i	initial condition
j	jet exit conditions
jc	jet cluster
jt	jet throat
ℓ	local condition or rolling moment
lam	laminar
MAC	mean aerodynamic chord
m	material or pitching moment
n	yawing moment
N	normal force
o	total conditions
r = 1'	scaled to one foot radius sphere

NOMENCLATURE (CONT'D)

Subscripts	Definition
ref	reference
s	stagnation point
sep	separation
t	throat
turb	turbulent
w	wall conditions
y	side force
p	peak
∞	free stream condition
r	radial
pc	phase change
1	conditions upstream of normal shock

1.0 INTRODUCTION

Control of the Space Shuttle Orbiter in orbit is provided by a reaction control system (RCS), by aerodynamic surfaces during the approach and landing, and by the combination of reaction control and aerodynamic controls from entry through transition. During entry the control requirements are shared with the aerodynamic controls being used to trim and maneuver the vehicle while the reaction controls are used to provide the dynamic damping of the vehicles response to maneuvers and atmospheric disturbances. Figure 1-1 presents an entry profile showing the regions of reaction control, combined control, and aerodynamic control for a representative shuttle orbiter entry.

The effect of lateral jet plume inducing significant changes in the total vehicle aerodynamic characteristics is well known as "jet interaction" and has been studied for a number of years as a potential control scheme. Thus, RCS plume induced disturbances cannot be ignored during the Shuttle orbiter entry but must be investigated to determine the magnitudes of any aerodynamic interference forces and moments resulting from RCS operation in order that the control system performance can be verified and its weight minimized.

This report documents the work performed under NASA Contract NAS 9-13012. The basic objectives of this program were to assess the aerodynamic interference effects on a representative Space Shuttle orbiter induced by the reaction control system jets interacting with the external flow over the vehicle and to obtain force and heat transfer data of these interference effects.

The study was conducted in five phases:

a) Literature Survey and Test Parameter Selection
b) Model Design, Fabrication, and Calibration
c) Wind Tunnel Tests
d) Data Analysis
e) Configuration Evaluation

and the results are documented in this report.

Reference 1 presents the test data for the force tests. The primary tests were performed at a nominal Mach number of 4.0 with Mach effects assessed at Mach numbers of 2.5, 2.95 and a very limited set at Mach 7.4. The tests were performed primarily at Reynolds numbers of 1.0×10^6/ft and 3.0×10^6/ft with a limited amount being obtained at 5×10^6/ft to assess Reynolds number effects. The plume simulation was accomplished

using tunnel auxiliary air as a "cold gas" simulation through scaled rocket nozzles. The rocket nozzles were mounted separate from the model so that the forces measured were of the vehicle and interference only.

During the force test, pitch, roll, and yaw RCS nozzles were simulated using nozzles whose geometry was determined by matching full scale exit pressure ratio, momentum ratio, and thrust ratio on a reference entry trajectory. The primary force test variables were Mach, angle of attack, model geometry, and nozzle supply pressure.

The heat transfer tests were performed at a Mach number of 7.4 using temperature sensitive paints as the means of obtaining heating data. The heating data were obtained at a Reynolds number of 3×10^6/ft, angles of attack of 25, 30, and 35 degrees and yaw angles of 0 and 5 degrees. The plumes were simulated using nitrogen as the test gas with helium used for two runs. The yaw nozzle was the primary nozzle simulated and heat transfer data was only taken on the OMS pod containing the RCS package. Primary test variables were angles of attack and yaw.

In addition to the force and heat transfer data, surface flow visualization was obtained at Mach 7.4 using a titanium dioxide oil mixture and at Mach 4 using a fluorescent oil technique.

The configuration chosen to perform this study was the preliminary requirements review (PRR) configuration of the space shuttle orbiter shown in Figure 1-2. The reaction control system used during entry is located in the Orbital Maneuvering System (OMS) pods located on the rear of the body at the base of the fin. Figure 1-3 shows the location of the thrusters on the OMS pod. Each pod contains 12 engines with 4 in the yaw plane and 4 firing up and 4 firing down in the vertical plane. A nominal entry uses only 2 of the 4 engines in each plane, however, pitch control is obtained by using the vertical thrusters in both pods symmetrically and roll control by asymmetric firing of the vertical thrusters.

Figure 1-1. Aft RCS Mission Profile
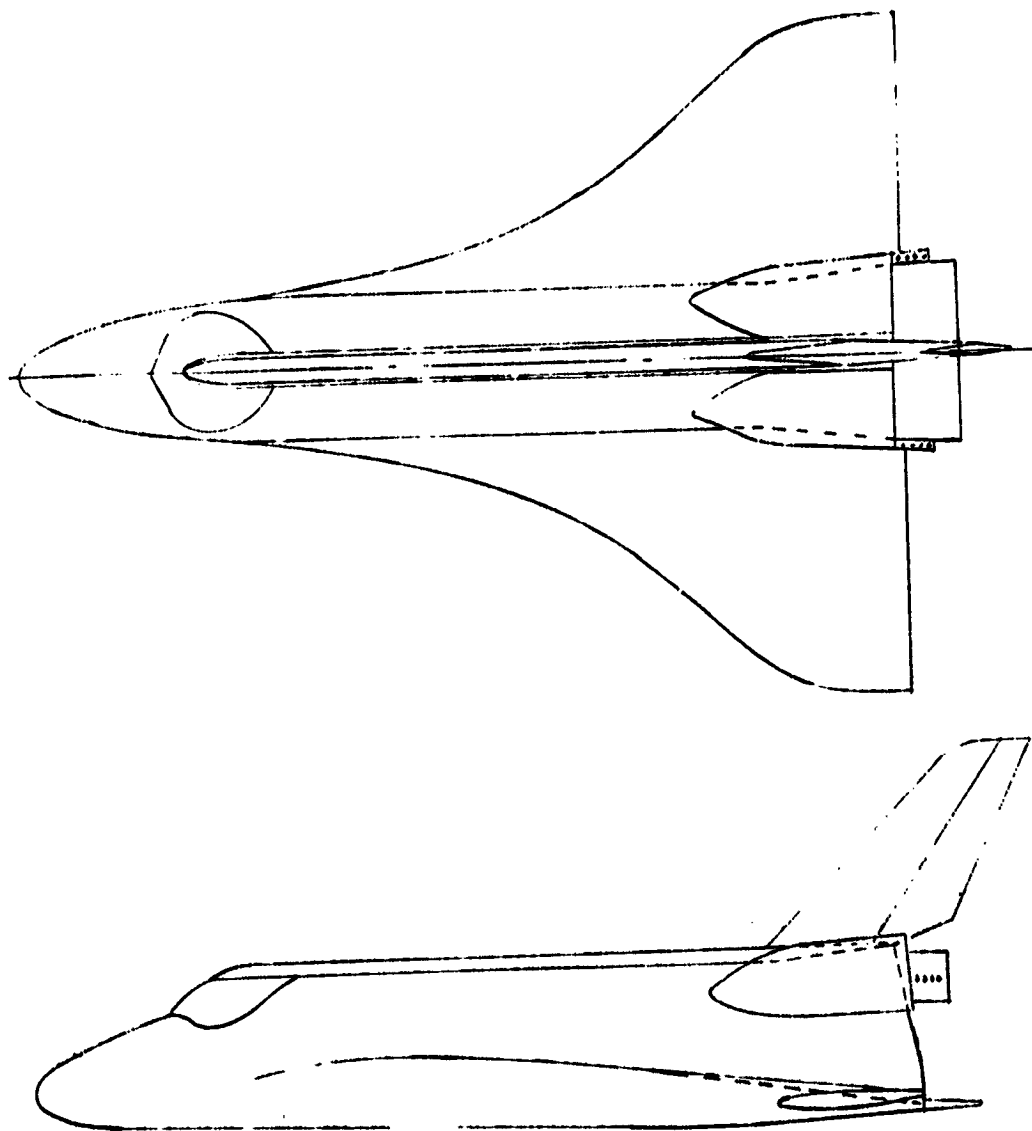
Figure 1-2. PRR Configuration Sketch

OMS POD

4 Pitch/Roll Thrusters

Left Rear Module

4 Yaw Thrusters

4 Pitch/Roll Thrusters
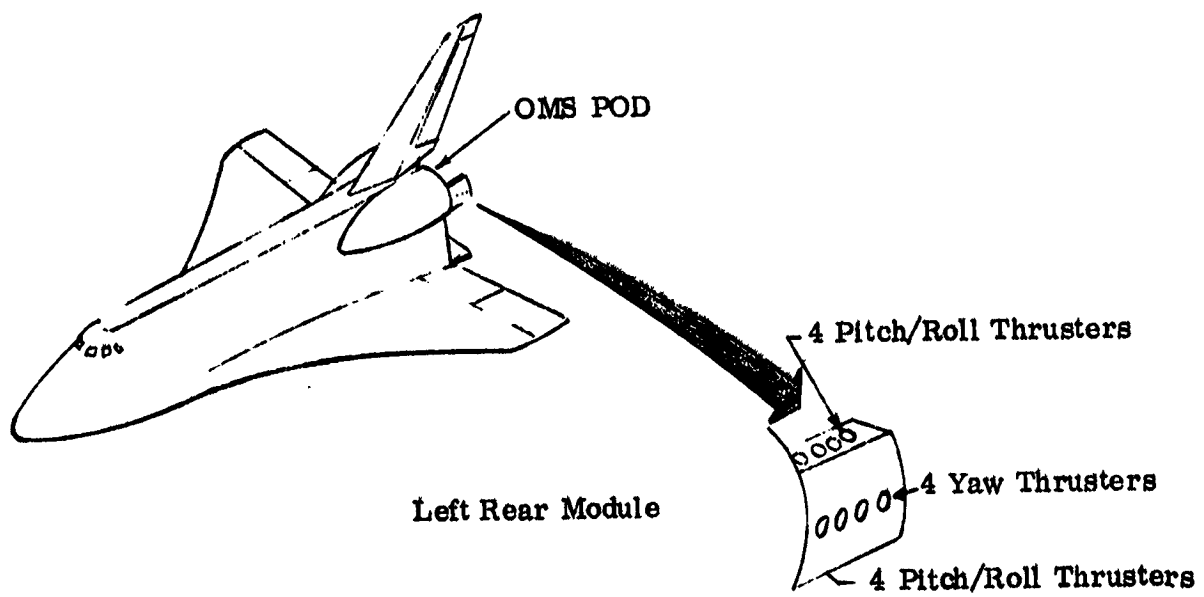
NOTE A SIMILAR MODULE IS MOUNTED ON RIGHT
OMS POD

Figure 1-3. Rear RCS Package Location

2.0 ANALYTIC METHODS

2.1 LITERATURE SURVEY

In the beginning of this study it was assumed that the primary interaction would be classic jet interaction between the flow along the side of the body and the yaw jets. It was envisioned at that time extensive interaction would occur between the yaw jets and the flow over the OMS pods. The RCS jets are far from the wing and vertical fin so that impingement on and interactions with wing and fin flow were expected to be small.

Therefore, the objectives of the literature survey at the start of the program were to review available experimental data, correlation techniques and analytical procedures for separated hypersonic flow due to lateral jet interference applicable to the RCS thrusters for entry vehicles. An extensive literature search was performed both on a NASA linear tape search and a DDC search on jet and cavity effects under company-funded research. More than 1000 report titles were obtained, of which approximately 140 were found of interest to this study. The key objective was to find all experimental and analytical data pertaining to local pressure and heat transfer distribution due to cavity and jet interference and these references are found in Appendix A.

The reports which were found most suitable for cavity effects are those presented by the investigation of reference A-1 through A-24. The literature surveys for documents applicable to the jet-flow field interaction are those of references A-21 through A-144.

Analytical techniques which define the jet-stream interaction problem for two-dimensional jets (slot orifices) are fairly well described by the models utilized for numerous studies such as by Vaughan, Barnes, et al, Thayer and Kaufman, references A-134, -105, -141, and-118, for both supersonic and sonic jets interacting with a high speed stream. The description of the three-dimensional flow field resulting from the disturbance of a transverse circular jet with a stream is more difficult to define and most of the investigations utilized experimental data for their analysis. The free stream and jet gas parameters become important considerations to define the interaction. The majority of the investigations were initiated to obtain the jet-stream interference force augmentation or surface loading. The studies of Strike, Billig, et al and Wilson, reference A-122, A-143, and A-132, resulted in some description of the three-dimensional flow field, however, little or no attention has been given to the heat transfer problem. Only the experimental results presented by Brevig and Strike in references A-22 through A-24 were found to be specifically applicable to this study and to the OMS pod heat transfer analysis.

The test results showed, however, that the plume interactions far from the nozzle interacting with the separated flow over the wing tip (yaw nozzle) or impinging on the

wing trailing edge (pitch/roll nozzle) are more important to the induced moments on the vehicle and the resulting control effectiveness. Thus a limited survey was made of plume impingement and plume interactions which is presented in Appendix B. No suitable documents were found for these problems.

2.2 JET INTERACTION ANALYTIC MODEL

An analytic model of the classic jet interaction effects was developed from available information, and Figure 2-1 presents a sketch of a typical three-dimensional laminar jet-stream interaction flow field constructed with the aid of the experimental data of references 2 and 3 along with the interferogram photograph of Figure 2-2. It can be observed that the jet plume acts as a protuberance that causes the boundary layer to separate around the jet. Within the separation region, counter-rotating vortices are formed and where they meet and turn downward, a stagnation region is experienced. As noted by the pressure distribution, a plateau pressure is established, around the jet in the separated region. Also noted are the pressure rise to several times that of the plateau pressure at the stagnationline of the strong vortex flow region. Exception to this is a small region just behind the jet where the pressure is first reduced by the interaction and then increases at jet reattachment. The stagnation condition will cause strong pressure and a resulting heat transfer spike around the jet. As indicated by the sketch, the jet flow is confined by an intercepting shock at the jet boundary and then passes through a strong shock, the Mach disk. The extent of the separation region may be determined by the size of the jet protuberance or the height of the Mach disk. Around the jet, the airstream will pass through a boundary layer separation shock and then through a jet interaction bow wave. A reattachment shock is usually observed downstream of the jet where it turns to follow the wall. In the interferogram photograph of Figure 2-2, the fringe line spacing corresponds to a variation in the local gas density. In a high density region such as a shock wave, the line density will increase. A top view of the various flow regions over the surface, shown in Figure 2-1, was constructed from experimental data results and photographic observations in laminar flow.

In turbulent flow, the jet-stream interaction will affect only a small portion of the surface, while for transitional flow condition, the region of interaction will have characteristics which combines both laminar and turbulent flow interaction. The experimental pressure data of Figure 2-3 indicate these characteristics, where the different types of flow were obtained by increasing the angle of attack. It should be noted that in some cases the flow will separate from the leading edge of the surface when the jet dynamic pressure is much higher than the stream dynamic pressure in laminar flow.

2.2.1 JET INDUCED PRESSURE - In order to predict the control amplification which results from jet interaction it is necessary to predict the extent of the separated region and the plateau pressure in this region and both of these quantities have

been shown by Vaughan (reference 4) and others to be primarily dependent on the jet penetration height or Mach disc height. Most of the data to date is based on slot injection (2-D) or sonic orifice injection. However, for a supersonic orifice Adamson and Nicholls (reference 5) have proposed the following correlation:

$$\frac{H_D}{d_j} = 0.69 \, M_j \left[\frac{\gamma P_j}{P_{amb}} \right]^{1/2} \tag{2-1}$$

While for a 2-D slot injection Vaughan (reference 4) used the following relation

$$H_D = \frac{2}{3} \, d_t (V_j / C_t) \, \frac{P_{o_j}}{P_D} \, \sin \alpha_{AV} \tag{2-2}$$

where $\sin \alpha_{AV}$ corrects for the flow deflection up to the disk in case of a non-normal injection.

The experimental data of references 2 and 3 presented in Figure 2-4 indicate that the penetration height, H_D, normalized to the jet exit diameter, d_j, can be correlated by momentum ratio by the empirical relation:

$$\frac{H_D}{d_j} = 0.27 \left(\frac{\Phi_j}{\Phi_{ref}} \right)^{0.57} \tag{2-3}$$

where $\quad\quad\quad \Phi$ is the momentum flux

$$\Phi_j = \gamma_j \, P_j \, M_j^2 \, A_j$$

$$\Phi_{ref} = \gamma_\infty \, P_\infty \, M_\infty^2 \, A_j$$

and the jet conditions are taken at the nozzle exit.

The normalized length of the disturbance or the upstream separation distance, x_{sep}, of reference 3 appeared related to momentum ratio also and a laminar flow relationship was obtained by curve fitting the data of Figure 2-5:

$$\left[\frac{x_{sep}}{d_j}\right]_{lam} = 10.2 \left[\frac{\Phi_1}{\Phi_{ref}}\right]^{0.264} \tag{2-4}$$

It should be noted that these equations are based on air as the stream and jet gas medium for a total temperature ratio $T_{o_j}/T_{o,\infty}$ of 0.4. The effect of the ratio of specific heat , molecular weight and total temperature will be considered later.

Reference 3 found that a good approximation of the effective slope of the dividing streamline is defined by the tangent of the jet penetration height, H, divided by the upstream separation distance, x_{sep}

$$\tan \delta = H/x_{sep} \tag{2-5}$$

The pressure in the separation region can then be obtained from the oblique shock relation:

$$\tan \delta = \frac{\zeta - 1}{\gamma_\infty M_\infty^2 - \zeta + 1} \sqrt{\frac{2\gamma_\infty M_\infty^2 - (\gamma_\infty - 1) - (\gamma_\infty + 1)\zeta}{(\gamma_\infty + 1)\zeta + (\gamma_\infty - 1)}} \tag{2-6}$$

where $\zeta = P_{sep}/P_\infty$

These laminar flat plate relationships were found to be inadequate for the turbulent flow case and the method used by Vaughan (reference 4) for turbulent flow prediction would appear to be better. An empirical relation was obtained for the separation region pressure as function of the upstream Mach number in reference 3 and is shown in Figure 2-6

$$\left[\frac{P_{sep}}{P_{ref}}\right]_{turb} = 1 + 0.38\, M_{ref} \tag{2-7}$$

while a turbulent separation distance empirical expression

$$\left[\frac{x_{sep}}{d_j}\right]_{turb} = 0.635 \left[\frac{\Phi_1}{\Phi_{ref}}\right]^{0.96} \tag{2-8}$$

is shown in Figures 2-7.

The peak pressure in the strong vortex region in laminar flow was further correlated with the jet to stream momentum flux ratios and the data presented in Figure 2-8 gives the following empirical equation

$$\left[\frac{P_p}{P_{ref}}\right]_{lam} = 4.82 \left[\frac{\Phi_1}{\Phi_{ref}}\right]^{0.165} \tag{2-9}$$

A correlation of the location of this peak in laminar flow was also obtained from the data of Figure 2-9

$$\left[\frac{x_p}{d_j}\right]_{lam} = 0.795 \left[\frac{\Phi_1}{\Phi_{ref}}\right]^{0.495} \tag{2-10}$$

Typical pressure distributions in laminar and turbulent flows on a flat plate around a conical nozzle produced by the interference of an expanding supersonic air jet plume with an enveloping high speed stream is shown in Figure 2-10. In laminar flow the upstream pressure in the separated region is shown to decrease in magnitude as the flow travels around the jet, due mostly to the increase in local flow velocity. This radial plateau pressure, P_{sep}, decreases to about 50% of the centerline value at $\theta = 90°$, and to approximately 10% at $\theta = 45°$.

The effect of jet gas temperature and molecular weight, and clustering on the center-line pressure distribution were also obtained from the experimental results of references 2 and 3 and the following expression was derived for these effects

$$P/P_{ref}{}_{Corr} = P/P_{ref} \text{ (TP) (MP) (NP)} \tag{2-11}$$

where the correction factors TP, MP, and NP are defined below. The data indicate that the jet gas temperature would affect the pressure only slightly as shown on Figure 2-11. The correlation of the data gives a multiplying correction factor to the plateau and peak pressure for air as a function of T_{oj}/T_{o_∞}, expressed as

$$TP = \left[(T_{oj}/T_{o_\infty})/0.4 \right]^{0.25} \tag{2-12}$$

The effect of molecular weight was obtained by comparing the experimental results using helium and air as the injection gases. The data on Figure 2-12 shows that the peak pressure is primarily affected when both gases are at the same total pressure and temperature. The limited amount of experimental data indicate that using helium gas will increase the peak pressure by a factor of 2 while the distance to the peak was also moved closer to the jet by a factor of two. Until more experimental data becomes available the following peak pressure and peak distance correction factor to account for the gas molecular weight based on the ratios of kinetic energy of the jet gases is recommended.

$$MP = \left[\frac{(KE)_{gas}}{(KE)_{air}} \right]^{0.35} \tag{2-13}$$

where

$$KE = \gamma_j \, M_j^2 \, (RT)_j \, A_j$$

A cluster of four supersonic conical nozzles operating at the same mass flow rate as of the single supersonic nozzle was used to obtain the effect of clustering. The data on Figure 2-13 show that the pressure distribution of both configurations is almost identical for the plateau region while the peak pressure is reduced by approximately a factor of two using a cluster of four nozzles. It should be noted that an effective jet exit diameter was used for the four nozzle configuration which was based on the diameter of a single nozzle having the same exit area or

$$d_{jc} = \sqrt{n \, d_j^2} \qquad\qquad x_r \leftarrow \begin{smallmatrix} O \\ + \\ O \end{smallmatrix} \begin{smallmatrix} O \\ O \end{smallmatrix}$$

where n is the number of nozzles and the distance x_r was measured from the center of the cluster. Again, until more experimental data becomes available, the effect of clustering may be taken into account by correcting the peak pressure by the factor

$$NP = 1/\sqrt{n} \tag{2-14}$$

Thus the data of references 2 and 3 show that the separation pressures are related to momentum ratio as the primary parameter and with temperature and gas effects less important.

2.2.2 <u>HEAT TRANSFER DISTRIBUTION</u> - Typical laminar heat transfer distribution obtained from the experimental results of references 2 and 3 around a three-dimensional jet-stream interaction are shown in Figure 2-14. The reference values of heat transfer, h_{ref} correspond to the heat transfer coefficient without jet-stream interactions. It should be noted that the peak values around the jet are located at the same distance from the jet as were the peak pressure data of Figure 2-10. The effect of jet gas total pressure on heat transfer is presented in Figure 2-15 along the jet centerline . Again, the locations of peak values for heating can also be correlated with the peak pressure distance. The data indicate that there is a strong jet-stream mixing in the separated region induced by the jet. The evidence of this mixing is further shown in the heat transfer data of Figure 2-16 which presents the effect of the jet gas stagnation temperature. The effect of molecular weight is indicated by the data of Figure 2-17 which compares the air and helium used as the jet gas. The heating is shown to increase with decreasing molecular weight which was also found to be true with the peak pressure data.

The effect on the state of the boundary layer is shown along the centerline of the jet on Figure 2-18 for laminar, transitional and turbulent flow. The results were obtained by increasing the angle of attack of the flat plate. Similarly to the pressure data in laminar flow, the jet-stream interaction is shown to affect a relatively large portion of the flat plate in laminar flow, while for a turbulent boundary layer, the effect is limited to a smaller portion of the surface around the jet. Also, the transitional boundary layer jet-stream interaction heat transfer distributions will have characteristics of both laminar and turbulent flows. It is noted that peak heating is most critical for a laminar boundary layer. The phase-change paint qualitative heat transfer contours of Figure 2-19 indicate clearly the high heating regions for a laminar and turbulent jet-stream interaction. The paint in these test melts at a prescribed temperature and the edges of the dark areas in the pictures are lines of constant heat transfer. The dark areas will experience higher heating than the remaining surface. This type of data indicate in particular the high heating in the

strong vortex region in laminar flow which has a horseshoe shape and a complicated flow pattern for a turbulent boundary layer.

An attempt was made to correlate the peak heat transfer to peak pressure for the laminar jet-stream interaction. This type of correlation is shown in Figure 2-20 from which a simple empirical expression was obtained

$$h/h_{ref} = 0.89 \ (P_p/P_{ref})^{1.5} \qquad (2-15)$$

Furthermore, since the heat transfer was found to be very sensitive to the variation of the jet gas stagnation temperature, the correlation of the data presented in Figure 2-20a gives a correction factor to the heat transfer, referenced to the value at $T_{oj}/T_{o \infty} = 0.4$ as

$$Th = \left[(T_{oj}/T_{o \infty})/0.4 \right]^{1.5} \qquad (2-16)$$

The effect of clustering and molecular weight on peak heating can be obtained simply by making first a correction to the peak pressure and then use the equation from Figure 2-20 to obtain the heat transfer value.

2.3 RCS PLUME MODEL

2.3.1 FLOW FIELD NEAR RCS

The jet interaction results described in the previous section were (as in all jet interaction models) given for a surface that is exposed to the external flow and the jet alone induces the separation. The question is whether such a model works for aft mounted RCS packages on the shuttle. Figure 2-21 presents a hypersonic approximation of the wake region at the RCS package. The separation line in this case is the projection of the wing leading edge rising with angle of attack and shielding the wing upper surface and OMS pod. Based on such a wake it is evident that jet interaction as such would be a low angle of attack phenomenon ($\alpha < 15°$) and that at high angles of attack all the jets will be exhausting into a wake region allowing the plume to penetrate the flow at some distance from the nozzle. The hypersonic approximation would assume that the wake region is a region of dead or still air with a separation pressure which can be approximated by a base pressure coefficient

$$C_p = \frac{-2}{\gamma \ M^2} \tag{2-17}$$

This is a convenient assumption to make and is used to analyze the plume and impingement characteristics.

In reality the flow field over the leeward surface of the fuselage of delta wing configuration will be very complex at the angles of attack experienced during entry. Vortices will be formed due to wing and body flow separation with reattachment on the side and on the upper surface of the fuselage as shown in the sketch of Figure 2-22. In particular, the vortex which reattaches in the region of the pod location is caused by the lower pressure region experienced over the delta wing upper surface at angles of attack, from which the boundary layer separates and leaves the surface as a vortex sheet of finite thickness which rolls up into a vortex. If the vortex is close enough to a surface, the down flow will cause reattachment and resulting high heating rates. The severity of this phenomenon is influenced by the Reynolds number, Mach number, angle of attack and body geometry. A quantitative dermination of this heating with existing analytical techniques will be very difficult without the experimental data since it is influenced by numerous interrelated parameters.

2.3.2 <u>PLUME SHAPE</u> - If the plume is exhausting into a wake region where the pressures are approaching a vacuum, then it is possible to use an approximate method for the flow field properties by a rocket exhausting into a vacuum as a model. Reference 6 presents a model which assumes that the nozzle flow of an ideal gas expands isentropically from a nearly parallel nozzle of exit radius, r_j, and Mach number, M_j. The flow in the far field approximation approaches radial flow from a point source where most of the mass and momentum were contained in the central core of the jet with density decreasing both along and normal to the jet centerline. The density distribution or a spherical cap at a distance X from the nozzle exit is given by

$$\frac{\rho}{\rho_j} = \frac{E}{2} \left(\frac{V_j}{V_{max}}\right)\left(\frac{X}{r_j}\right)^{-2} (\cos \theta)^{E-1} \qquad (2-18)$$

where

$$E = \frac{1 + \dfrac{1}{\gamma M_j^2}}{\sqrt{1 + \dfrac{2}{(\gamma-1)M_j^2}} - \left(1 + \dfrac{1}{1 + \dfrac{1}{\gamma M_j^2}}\right)}$$

$$\frac{V_j}{V_{max}} = \left(1 + \frac{2}{(\gamma-1) M_j^2}\right)^{-1/2}$$

θ = azimuth angle from jet centerline.

A similar solution of reference 7 gives the density on the centerline as:

$$\frac{\rho}{\rho_o} = B\left(\frac{X}{d_t}\right)^{-2} \qquad (2-19)$$

where $\quad B = \dfrac{D(\gamma)}{4} \left(\dfrac{A_j}{A_t}\right) \left(\dfrac{\rho_e}{\rho_o}\right) M_j^2$

and $\quad D(\gamma) = 0.24$ for $\gamma = 1.4$

$\qquad\qquad = 0.123$ for $\gamma = 1.22$

The far-field approximation appears valid since the RCS nozzles are small relative to the vehicle. For example the wing is apppproximately 30 nozzle diameters from the pitch nozles.

The Lockheed 5 point solution of reference 8 developed from the method of character-istics solutions offers a method for computing plume contours far from the nozzle and was used in predicting the plume impingement area in this study:

$$(X_{max}/r_j) = 1.076 \ f_1^{-.563} \tag{2-20}$$

$$(r_{max}/r_j) = 0.65 \ f_2^{0.91}$$

$$f_1 = \frac{A_1}{A_t} \ \frac{P_\infty}{P_{0_j}} (1 + \gamma M_\infty^2)^{1/4} (1 - \sin \theta_N)^{-1}$$

$$f_2 = (X_{max}/r_j)((\frac{A_1}{A_t})^{1/4} (1 + \gamma M_\infty^2)^{1/8} (1 - \sin \theta_N))^{-1}$$

$$\text{at } X = \frac{1}{4} X_{max}; (\frac{r}{r_j}) = .686 \ (r_{max}/r_j)^{0.963}$$

$$\text{at } X = \frac{1}{2} X_{max}; (\frac{r}{r_j}) = 0.871 \ (r_{max}/r_j)^{0.992}$$

$$\text{at } X = \frac{3}{4} X_{max}; (\frac{r}{r_j}) = 0.969 \ (r_{max}/r_j)$$

The plume diameter at the wing was computed using the 5 point method and then an assumption similar to the vacuum solutions of isentropic flow from the nozzle was used to determine the plume Mach and pressure at that point.

2.3.3 <u>PLUME IMPINGEMENT</u> - The reaction control systems jets exhausting downward will impinge on the wing and body flap. It is also possible that the upward firing jets may impinge at an oblique angle on the fin.

The downward firing jets at high Mach number (and high altitude) will be exhausting into the separated wake area behind the wing (Figure 2-21) which will be high angle of attack ($\alpha = 30°$) and so it is reasonable that the vacuum impingement schematic (Figure 2-23) may be representative of the flow field at plume impingement. A detached shock wave close to the surface would be formed by the high Mach number flow impinging on the plate. The expansion of the jet is unaffected by the shock wave or the surface that caused it because it is at high supersonic Mach number. A region of subsonic flow

exists between the strong shock and the surface as the flow turns and moves out radially from the stagnation point and eventually passes through a sonic line and becomes supersonic again. Reference 7 derived an approximate formula for the shock stand off distance Δ from a mass flow balance and arrived at the following relationship

$$\frac{\Delta}{X} = \frac{1}{K\left[1 + \sqrt{\frac{2}{K}}\right]} \tag{2-21}$$

where $K = \dfrac{\rho_2}{\rho_1}$

and from normal shock reactions:

$$\frac{\rho_2}{\rho_1} = \frac{(\gamma + 1)\, M_1^2}{(\gamma - 1)\, M_1^2 + 2} \tag{2-22}$$

The standoff distance (Δ) was used as a correlation parameter in Section 4 using the 5 point method described above to define Mach ahead of the jet. The solution for stand off distance needs to be iterated starting with the distance to the plate. It was assumed that the surface pressure could be predicted by a Newtonian approximation

$$P_w = 1.85 \frac{\gamma}{2}\, P_1 M_1^2 \cos^2 \theta + P_1 \tag{2-23}$$

because of the high Mach number of the plume and the large turning angle. It was further assumed in the plume impingement calculations performed that the stagnation pressure ($\theta = 0$) could be applied across the whole region of plume impact because the rapid boundary layer build up on the plate will keep the pressure from decaying as $(\cos^2 \theta)$.

2.4 SIMULATION PARAMETERS

2.4.1 <u>JET FLOW PARAMETERS</u> - Thayer (reference 9) showed from a dimensional analysis that any appropriately non-dimensionalized flow field property (FP) for plume flow interaction depends on the following set of dimensionless groups

$$FP = f\left(R_{e_{L'}},\ M_{\ell},\ \gamma_{\ell},\ M_j,\ \gamma_j,\ \frac{P_{oj}}{P_{\ell}},\ \frac{R_j T_{oj}}{R_{\ell} T_{\ell}},\ \frac{D_j}{L'},\ \frac{P_{\ell}}{P_{\infty}},\frac{T_{\ell}}{T_{\infty}}\right) \quad (2\text{-}24)$$

where

$$R_{e_{L'}} = \text{Reynolds number}$$

$$M_{\ell} = \text{local Mach number}$$

$$\gamma_{\ell} = \text{local ratio of specific heats}$$

$$M_j = \text{Jet Mach}$$

$$\gamma_j = \text{Jet specific heat ratio}$$

$$P_{oj} = \text{Jet supply pressure}$$

$$P_{\ell} = \text{local ambient pressure}$$

$$R_j = \text{exhaust gas constant}$$

$$T_{oj} = \text{exhaust gas stagnation temperature}$$

$$R_{\ell} = \text{external flow gas constant}$$

$$T_{\ell} = \text{local ambient temperature}$$

$$D_j = \text{Jet exit diameter}$$

$$L' = \text{reference length}$$

In a sub-scale test program, several parameters can be matched by using a scaled model tested at the correct free stream Mach number. Excluding conditions where real gas effects become important, matching the free stream Mach for a correctly scaled model results in correct values of local conditions of

$$M_\ell, \ \gamma_\ell, \ T_\ell/T_\infty, \ P_\ell/P_\infty$$

Scaled geometry of the jet exit will also insure matching

$$D_j/L'$$

leaving Reynolds number and jet properties still to be handled. Since ambient pressure and temperature in a wind tunnel seldom match free stream properties a parametric variation of

$$R_{e_L}, \ \frac{P_{o_j}}{P_\ell}, \ \text{and} \ \frac{R_j T_{o_j}}{R_\ell T_\ell}$$

can be made to determine the influence of the mismatch of the values on the flow field property. The need for simulating the energy ratio, $R_j T_{o_j}/R_\ell T_\ell$, depends upon the magnitude of this ratio. Thayer has shown that little effect was observed when this value was below a ratio of 9. Thus, if the full scale ratio is 9 or below, any cold gas simulation should be adequate based upon his criteria. The jet interaction data of equations 2-12 and 2-13, however, did show that gas temperature and molecular weight do exert a secondary effect on plateau pressure. Values of the jet Mach number and specific heat ratio must be handled differently. Since sub scale nozzles typically would not represent a realistic simulation of the full scale RCS unit, it becomes difficult if not impossible to match jet properties. However, as Pindzola showed in reference 10, it is the ratio of jet-to-local gas properties and not the absolute values of gas properties which are significant. It then becomes a problem of establishing which simulation parameter is significant in that the cost of simulation grows enormously as more parameters are simulated.

The simulation parameters established by Pindzola are summarized in Table 2-1 along with the addition of Herron's parameter for correlating plume size.

The first two parameters in Table 2-1, the boundary in a quiescent and a moving stream, represent matching the plume initial turning angle, $\Delta \nu$, as it leaves the nozzle. This would be important primarily in conjunction with Herron's parameter, reference 11, which is a correlating parameter for plume size and is directly dependent upon P_{o_j}/P_∞ in defining the Mach number of a fully expanded plume

Table 2-1. Summary of Scaling Parameters

JET CHARACTERISTIC	GENERAL SIMULATION PARAMETER
Boundary in Quiescent Medium	$\left(1 - \dfrac{p_\infty}{p_j}\right) \dfrac{\beta_j}{\gamma_j M_j^2}$
Boundary in Moving Stream	$\left(\dfrac{p_j - p_2}{p_2 - p_\infty}\right) \dfrac{p_\infty \beta_j \gamma_\infty M_\infty^2}{p_j \beta_\infty \gamma_j M_j^2}$
Transmitted Shock	$\dfrac{p_j \gamma_j M_j^2 \beta_\infty}{p_\infty \gamma_\infty M_\infty^2 \beta_j}$
Mass Flow	$\left(\dfrac{p_j^2 \gamma_j M_j^2 (RT)_\infty A_j^2}{p_\infty^2 \gamma_\infty M_\infty^2 (RT)_j A_\infty^2}\right)^{1/2}$
Kinetic Energy	$\dfrac{\gamma_j M_j^2 (RT)_j}{\gamma_\infty M_\infty^2 (RT)_\infty}$
Internal Energy	$\dfrac{(\gamma_\infty - 1)(RT)_j}{(\gamma_j - 1)(RT)_\infty}$
Enthalpy	$\dfrac{(\gamma_\infty - 1)\gamma_j (RT)_j}{(\gamma_j - 1)\gamma_\infty (RT)_\infty}$
Momentum	$\dfrac{p_j \gamma_j M_j^2 A_j}{p_\infty \gamma_\infty M_\infty^2 A_\infty}$
Thrust	$\dfrac{A_j}{A_\infty \gamma_\infty M_\infty^2}\left[\dfrac{p_j}{p_\infty}(1 + \gamma_j M_j^2) - 1\right]$
Sound Power	$p_\infty A_j \dfrac{\gamma_j^4 M_j^8 (RT)_j^4}{\gamma_\infty^{5/2} (RT)_\infty^{7/2}}$
Herrons parameter	$\dfrac{M_j FE}{\gamma_j}$

(M_{IFE}). It would represent plume impingement in a quiescent medium where equation 2-20 or 2-24 show P_{oj}/P_∞ to be an important parameter. The total pressure ratio parameter P_{oj}/P_∞ can be very difficult to match for a scaled nozzle if flight conditions represent very high attitudes where the quiescent medium condition (c.g. space vacuum) is approached because wind tunnel ambient pressures are much higher than free stream requiring very high chamber pressures or an out of scale nozzle.

Jet interaction in the classic sense is best simulated by momentum ratio matching as can be seen from equations 2-3 through 2-8. This parameter establishes the Mach disc or jet penetration height which in turn defines the separated and re-attaching zone pressure and heat transfer behavior. If exit pressure ratio is matached along with momentum ratio on a model tested at the correct free stream Mach number, then thrust ratio is also matched. At higher exhaust Mach numbers, $\beta_j \approx M_j$ and the boundary criteria (initial turning angle) will be closely simulated allowing matching of three Pindzola parameters simultaneously for a scaled nozzle.

Pindzola's parameters allow for scaling nozzles where the test Mach number does not equal that of the free stream. Such a test would violate Thayer's criteria (equation 2-24) because the local Mach number (M_ℓ) would be incorrect. The resultant error may not be large if the interaction is not dependent upon Mach number, a phenomena observed for other aerodynamic behavior in the hypersonic Mach region.

2.4.2 REACTION CONTROL SYSTEM ENGINE PERFORMANCE - The reaction control system engine which was selected to use in this study by NASA-JSC is a hydrazine (N_2H_4) monopropellant thruster using catalyst beds for propellant decomposition. Hydrazine decomposes into ammonia, hydrogen and nitrogen as a monopropellant. The reaction takes place in two separate steps. The first step is the reaction of hydrazine into ammonia and nitrogen.

$$3N_2H_4 \rightarrow 4NH_3 + N_2$$

The second step is in the decomposition of ammonia into nitrogen and hydrogen

$$2NH_3 \rightarrow N_2 + 3H_2$$
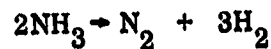
The first reaction is exothermic and the second is endothermic. The combustion temperature of the gas is therefore a function of the amount of the ammonia decomposed, X, which will affect the performance of the engine. Figure 2-24 summarized the performance of the RCS thrusters. The gas chamber temperature, molecular weight and composition were obtained from reference 12. Using a combustion temperature of 2000° F, the following gas composition and molecular weight is obtained with about 40% ammonia dissociation.

$$N_2 = 28\%$$
$$H_2 = 36\%$$
$$NH_3 = 36\%$$
$$\overline{M} = 14.7 \text{ lbm/mole}$$

Using an exit to throat area ratio, A_t/A_t of 20, a jet gas exit temperature of about room temperature will be experienced and a jet exit ratio of specific heat $\gamma_j = 1.22$ was obtained for the mixture of gases.

2.4.3 TRAJECTORY AND NOZZLE FLOW PARAMETERS –

The reference entry trajectory used to establish the flight environmental conditions was the Rockwell nominal guided entry trajectory (trajectory number 2007) provided by NASA-JSC and is shown in Figure 2-25. The Reynolds number for this trajectory is shown in Figure 2-26 based on the vehicle length of 112 feet while, the ambient pressure history is shown on Figure 2-27. Figures 2-28 to 2-34 present various full scale nozzle flow simulation parameters based on the trajectory of Figure 2-25 and the nozzle data from Section 2.4.2. The decline in the momentum ratio curve above Mach 8 in Figure 2-29 occurs only over a limited Mach range and at higher Mach numbers the momentum ratio rises to a value near 1000. Based on the assumption that jet interaction parameters would hold for this problem also, the most important parameters to match are momentum ratio and thrust ratio. However, thrust ratio is matched and plume turning angle is approximated for a scaled nozzle when jet exit pressure ratio and momentum ratio are matched simultaneously at a matched free stream Mach number test condition. These two parameters (exit pressure ratio and momentum ratio) were then chosen to be matched at flight and test Mach numbers of 7.4, 4.0, 2.95, and 2.5 using the computer program of reference 6 to size the scale nozzle. When free stream Mach and tunnel Mach are the same the jet exit Mach (M_j) scales directly

by the ratio of the γ of the rocket exhaust to the test gas to be used.

Reynclds number was to be treated as a test variable and the full scale nozzle total temperature ratio $(R_1 T_{o_1}/R_\infty T_\infty)$ was approximately 8 which places the simulation on the region of Thayers curve where kinetic energy ratio is not an important parameter.
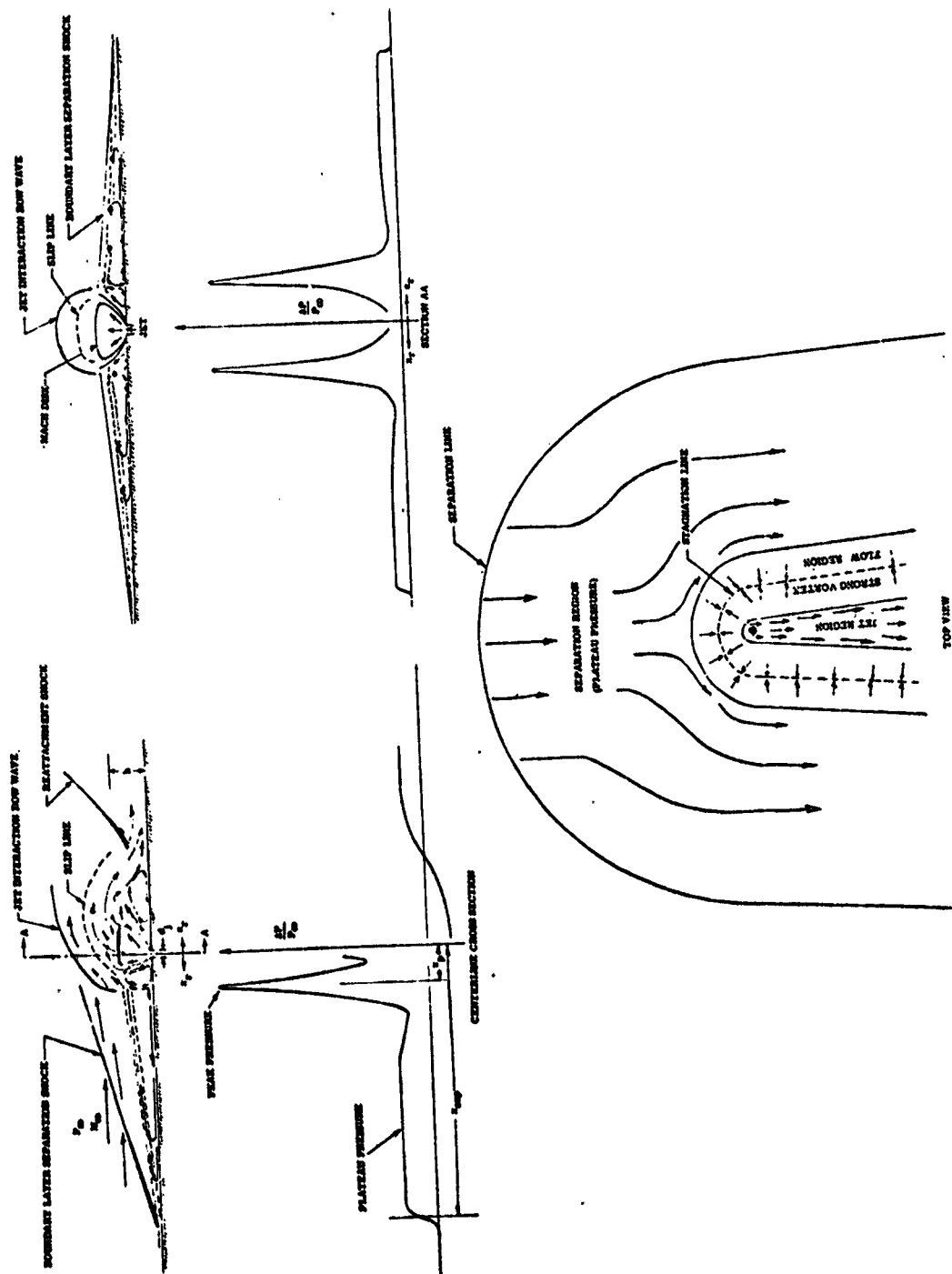
Figure 2-1. Flow Field About a Three-Dimensional Supersonic Lateral Jet in a Laminar High Speed Stream.

$M_\infty = 8$, $\alpha = 0°$, $Re_\infty = 3.7 \times 10^6/FT$

$T_{oj}/T_{o\infty} = 0.4$, $M_j = 2.54$
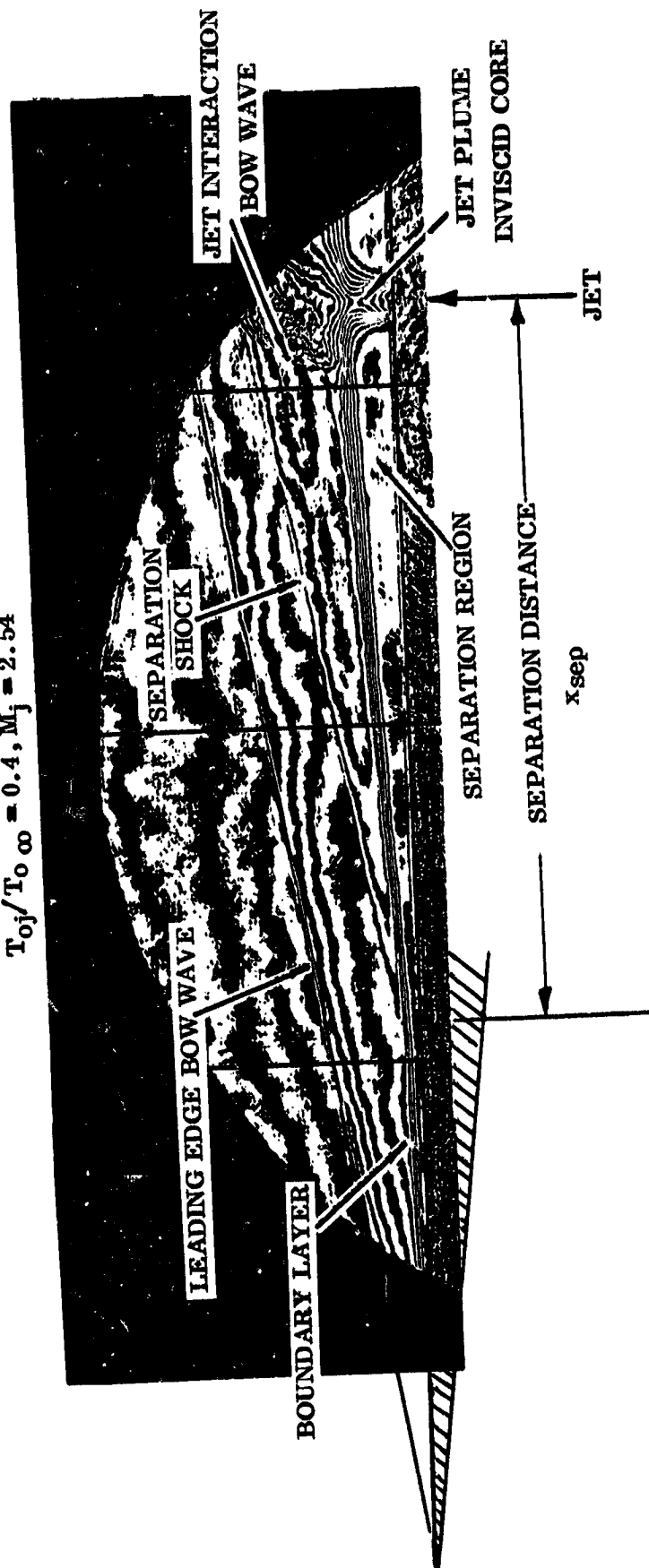
Figure 2-2. Interferogram of a Laminar Jet-Stream Interaction Flow Field Over a Flat Plate
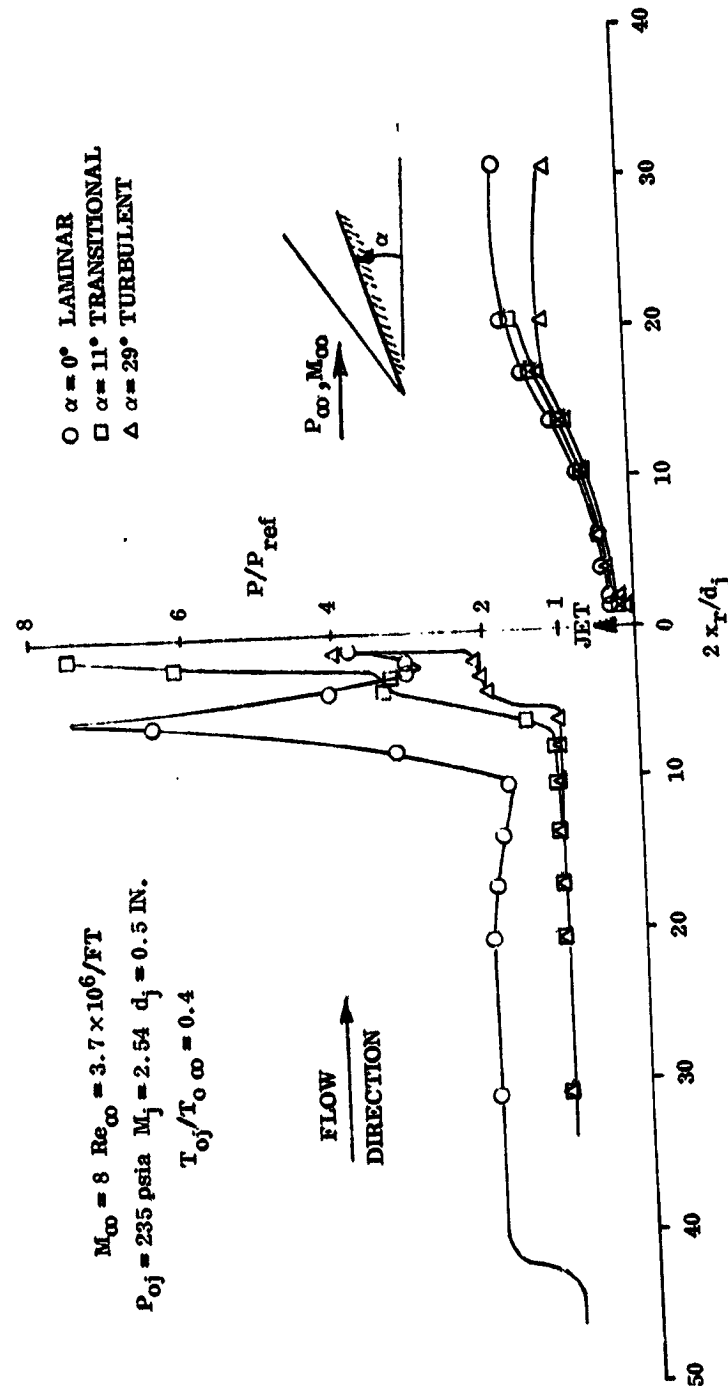
Figure 2-3. Typical Upstream and Downstream Pressure Distributions from Thre -Dimensional Jet-Stream Interaction for Laminar, Transitional and Turbulent Flow over a Flat Plate
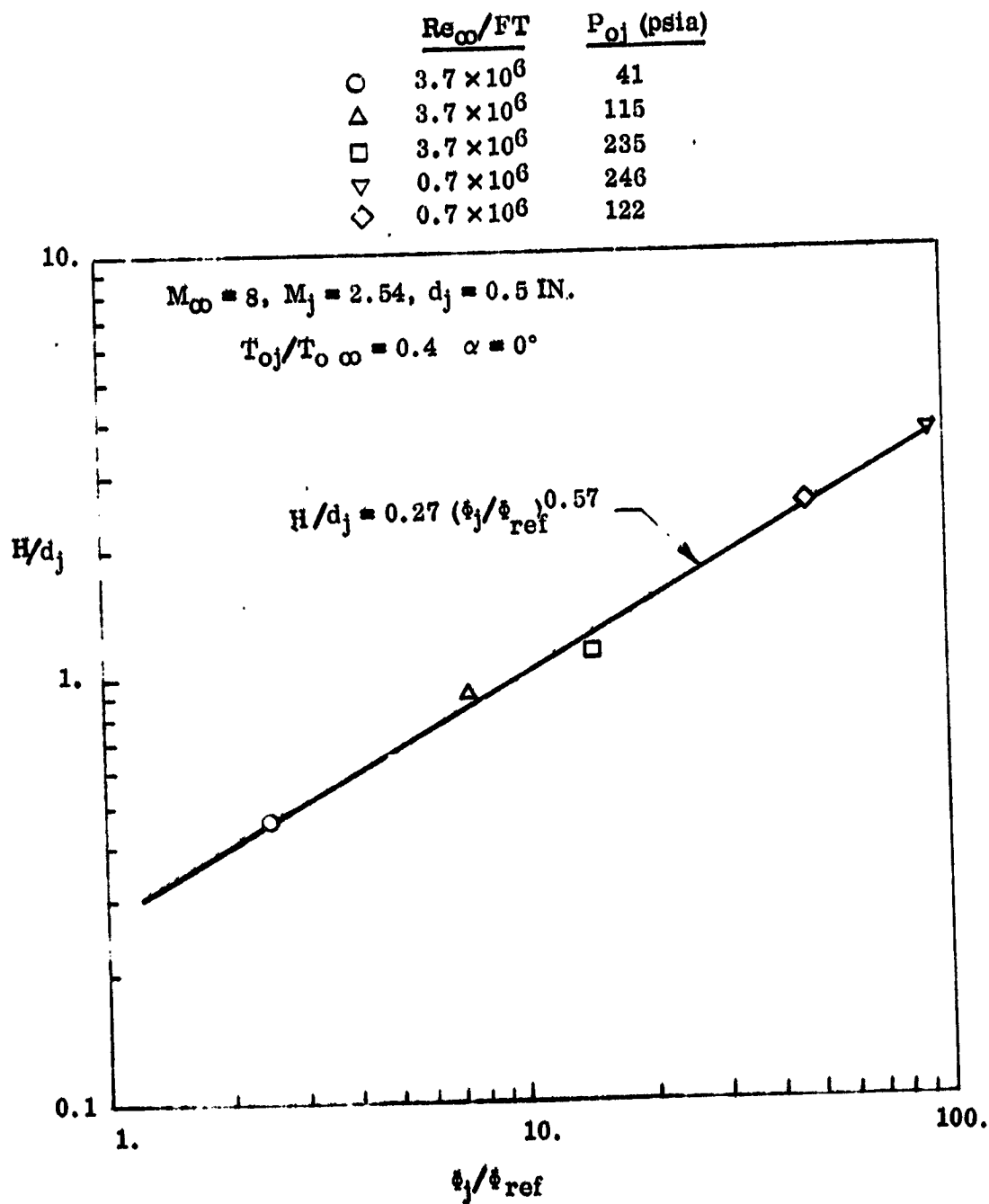
Figure 2-4. Correlation of Supersonic Jet Penetration Height in a High Speed Stream Over a Flat Plate
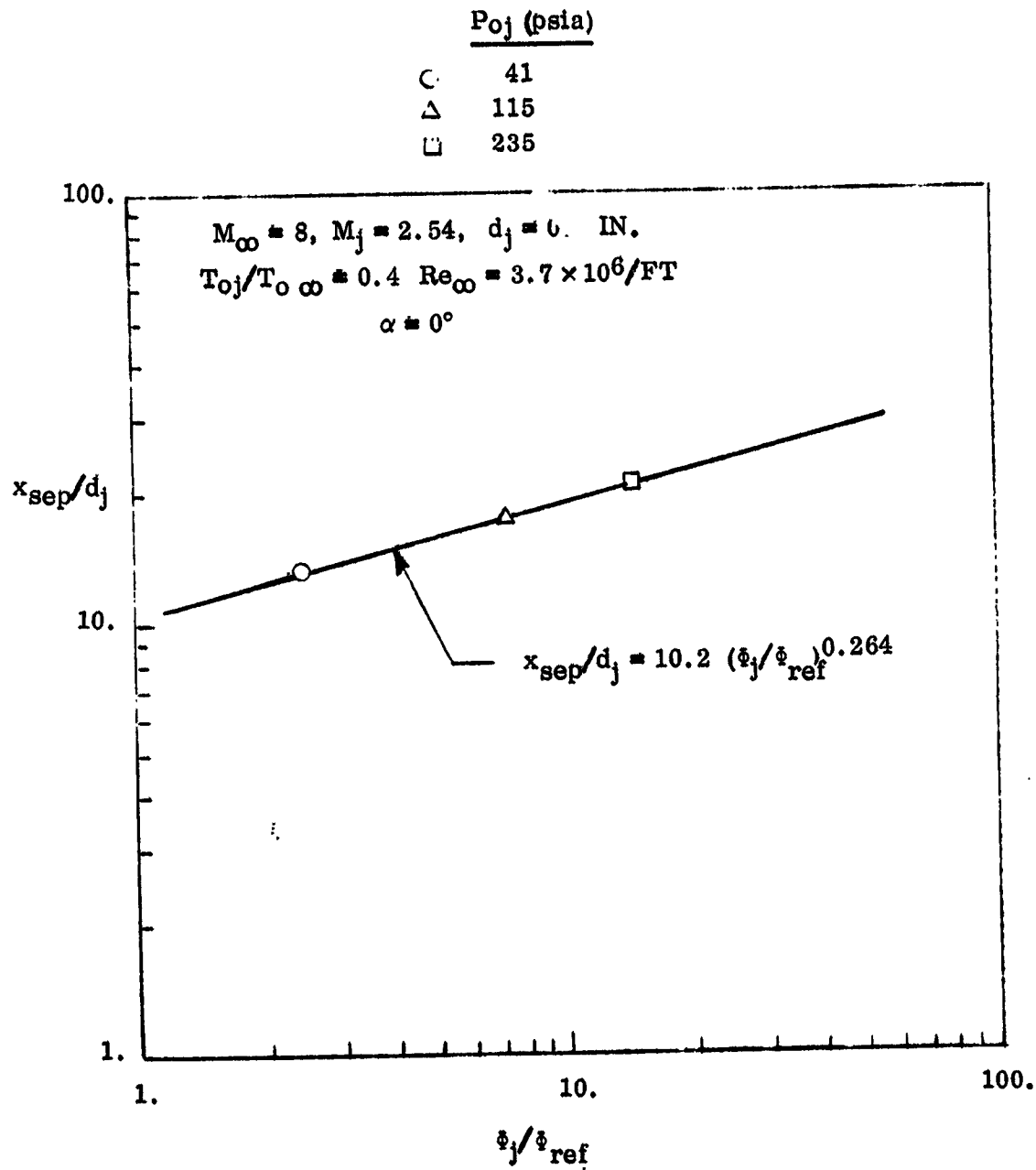
Figure 2-5.Correlation of Supersonic Jet Laminar Upstream Separation Distance in a High Speed Stream Over a Flat Plate
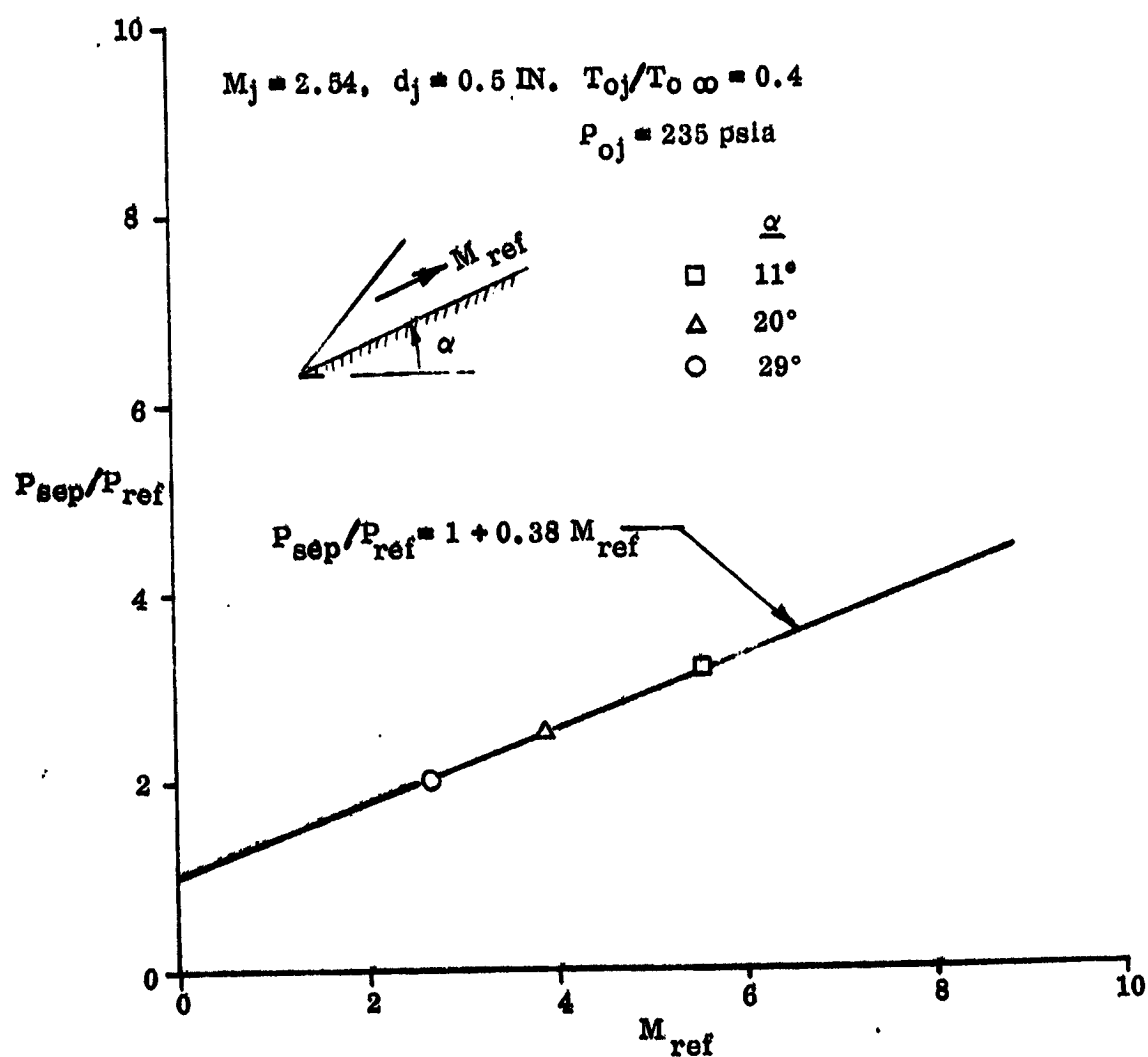
Figure 2-6. Correlation of Supersonic Jet Turbulent Upstream Plateau Pressure in a High Speed Stream Over a Flat Plate at Angles of Attack
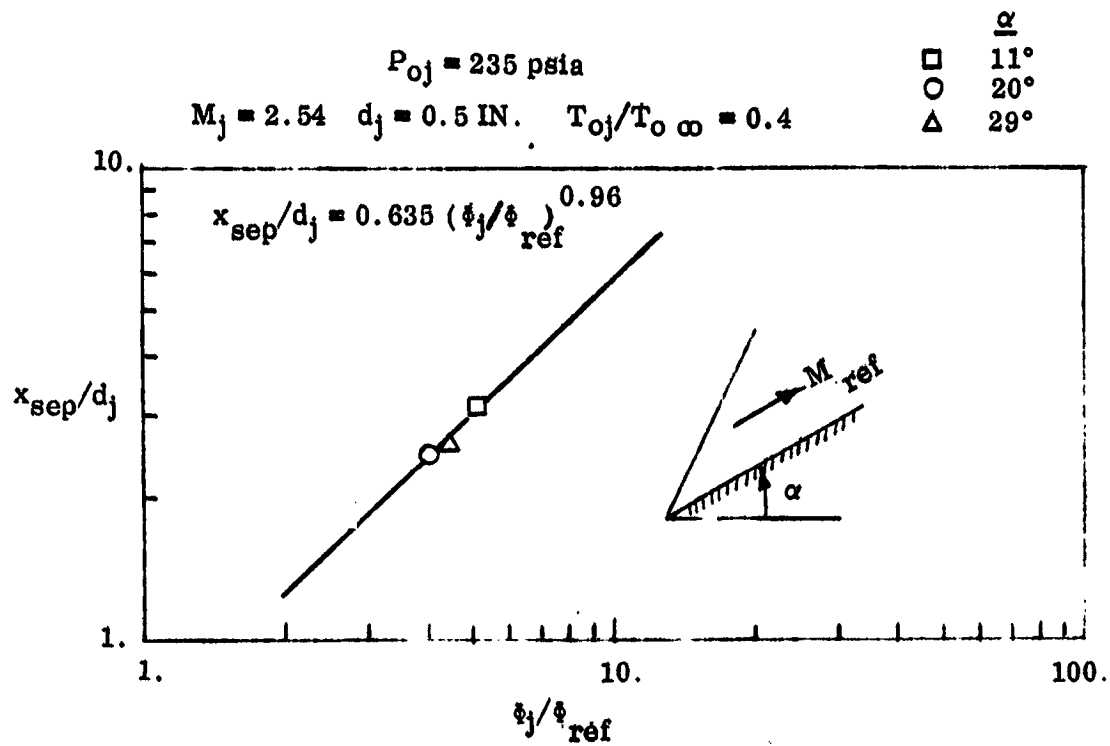
Figure 2-7. Correlation of Supersonic Jet Turbulent Upstream Separation Distance in a High Speed Stream Over a Flat Plate at Angles of Attack

	Re_∞/FT	P_{oj} psia	α	M_{ref}
○	3.7×10^6	40	0°	8.
△	3.7×10^6	118	0°	8.
□	3.7×10^6	233	0°	8.
◊	0.7×10^6	231	0°	8.
▽	0.7×10^6	118	0°	8.
◇	0.7×10^6	45	0°	8.
◁	0.7×10^6	233	10°	5.76
▷	0.7×10^6	235	29°	2.7

$M_j = 2.54 \quad d_j = 0.5 \text{ IN.} \quad T_{oj}/T_{o\infty} = 0.4$

P_p/P_{ref}

$P_p/P_{ref} = 4.82 \; (\Phi_j/\Phi_{ref})^{0.165}$

Φ_j/Φ_{ref}
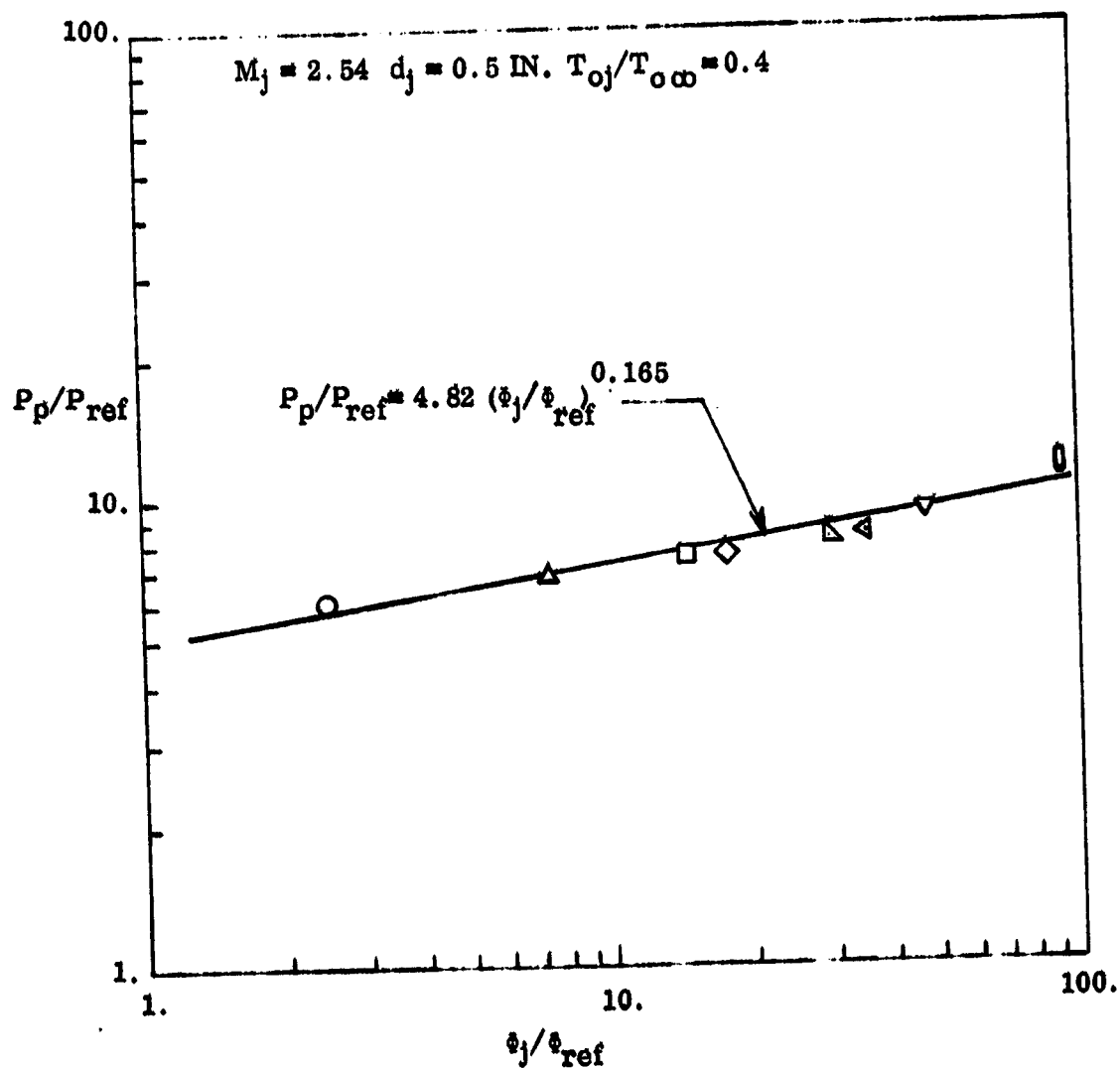
Figure 2-8. Correlation of Supersonic Jet Laminar Peak Upstream Pressure
in a High Speed Stream Over a Flat Plate
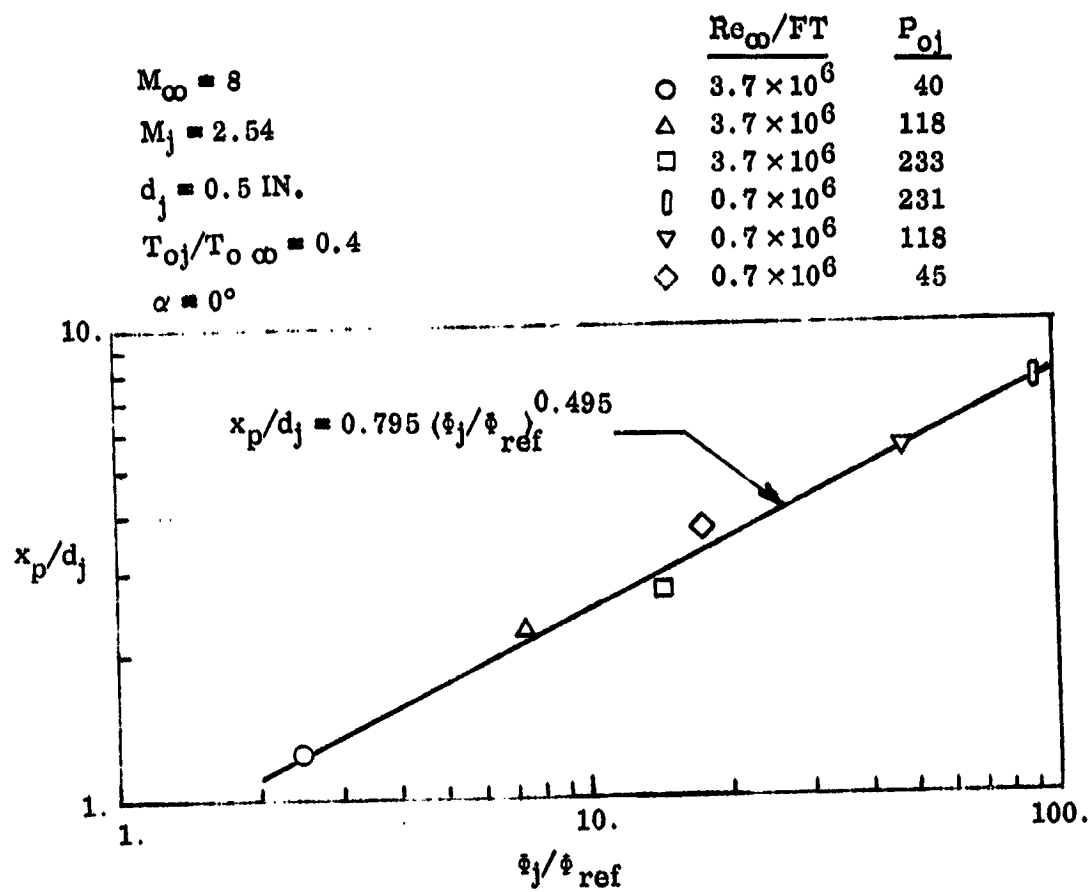
Figure 2-9. Correlation of Supersonic Jet Laminar Peak Upstream Pressure Distance in a High Speed Stream Over a Flat Plate
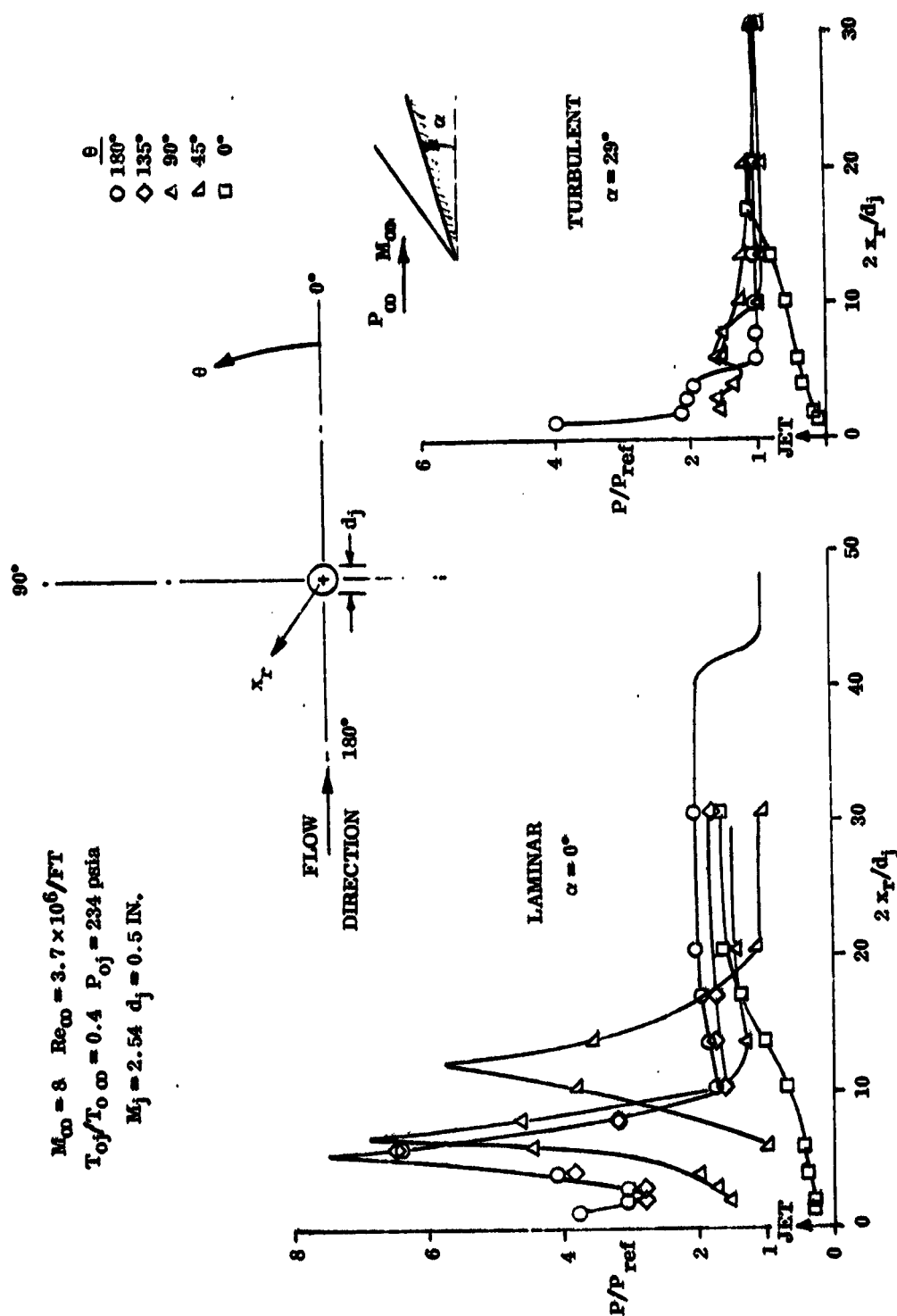
Figure 2-10. Typical Pressure Distributions Around a Three-Dimensional Jet-Stream Interaction in Laminar and Turbulent Flows.
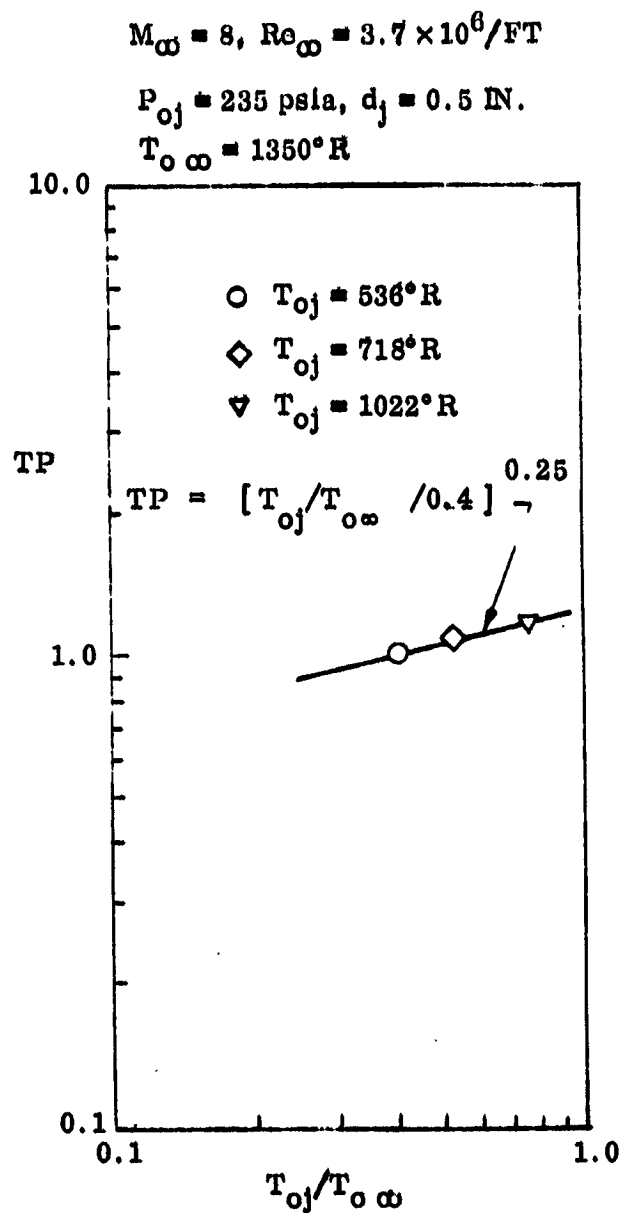
Figure 2-11. Effect of Jet Gas Temperature on Laminar Jet-Stream Interaction Pressure Distribution Over a Flat Plate at $\alpha = 0°$
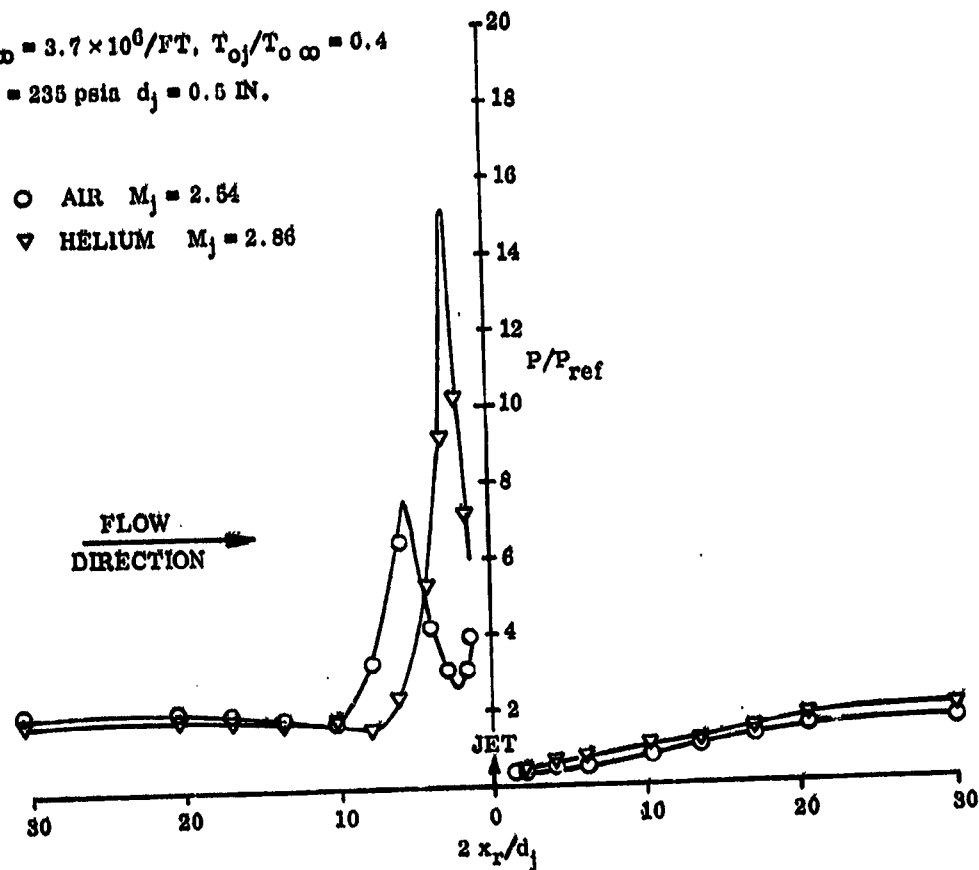
Figure 2-12. Effect of Molecular Weight on Laminar Jet-Stream Interaction Pressure Distribution over a Flat Plate at $\alpha = 0°$
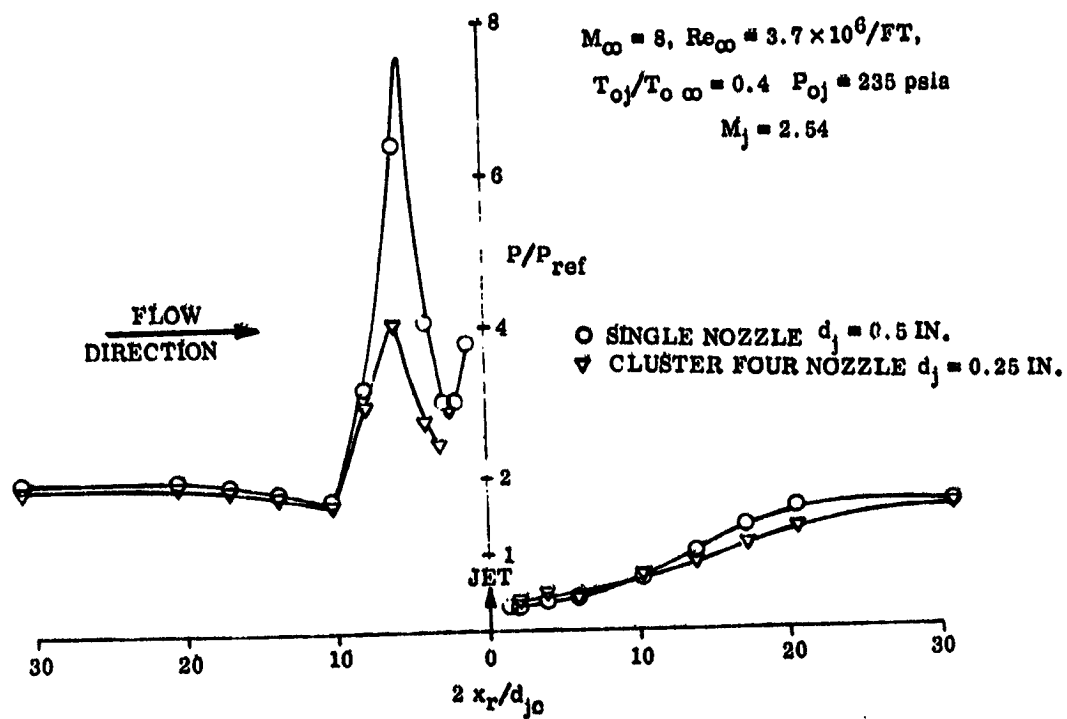
Figure 2-13. Effect of Nozzle Clustering on Laminar Jet-Stream Interaction Pressure Distribution Over a Flat Plate at $\alpha = 0°$
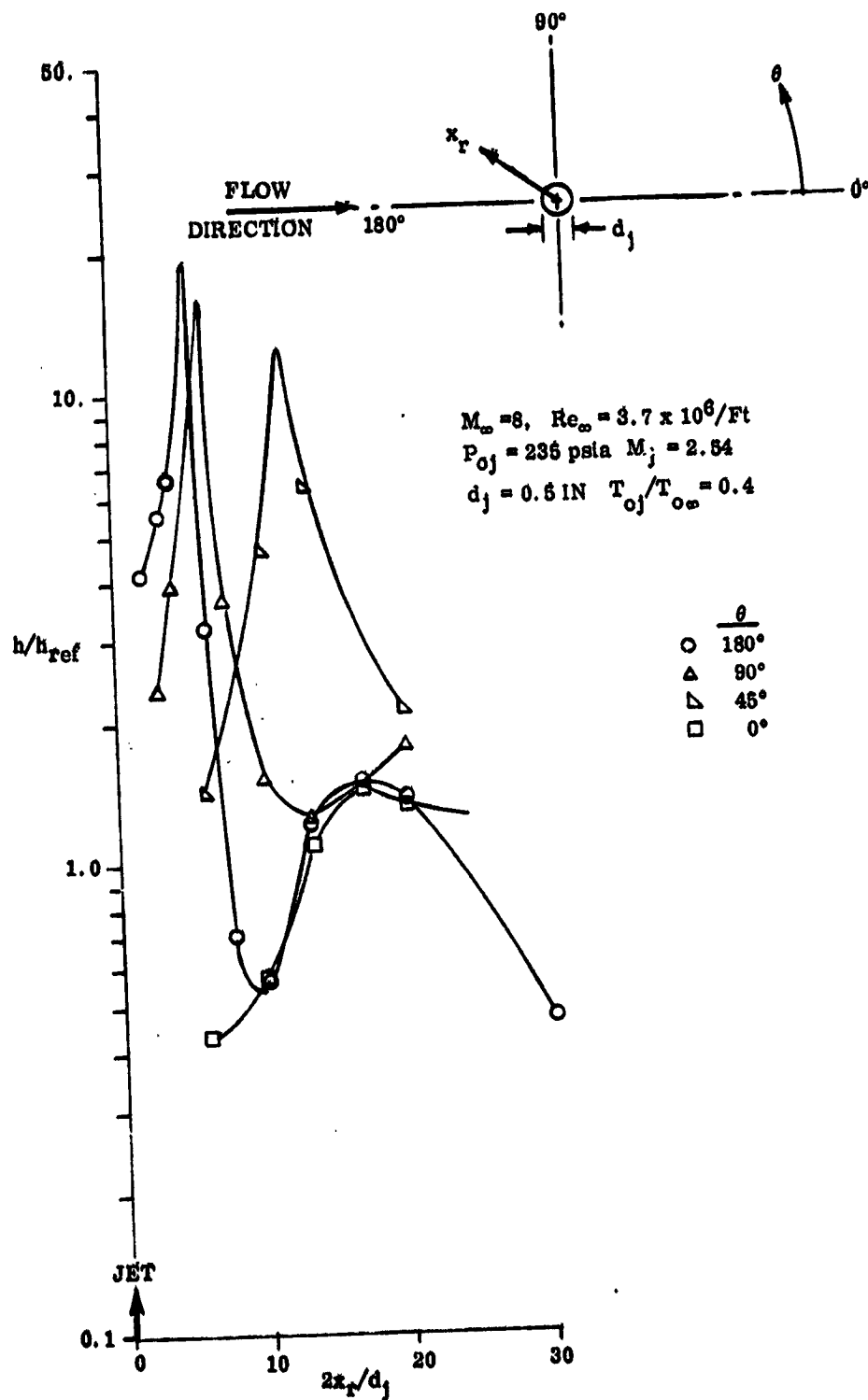
Figure 2-14. Typical Heat Transfer Distributions Around a Three-Dimensional Jet-Stream Interaction, Laminar Flow over a Flat Plate at $\alpha = 0°$
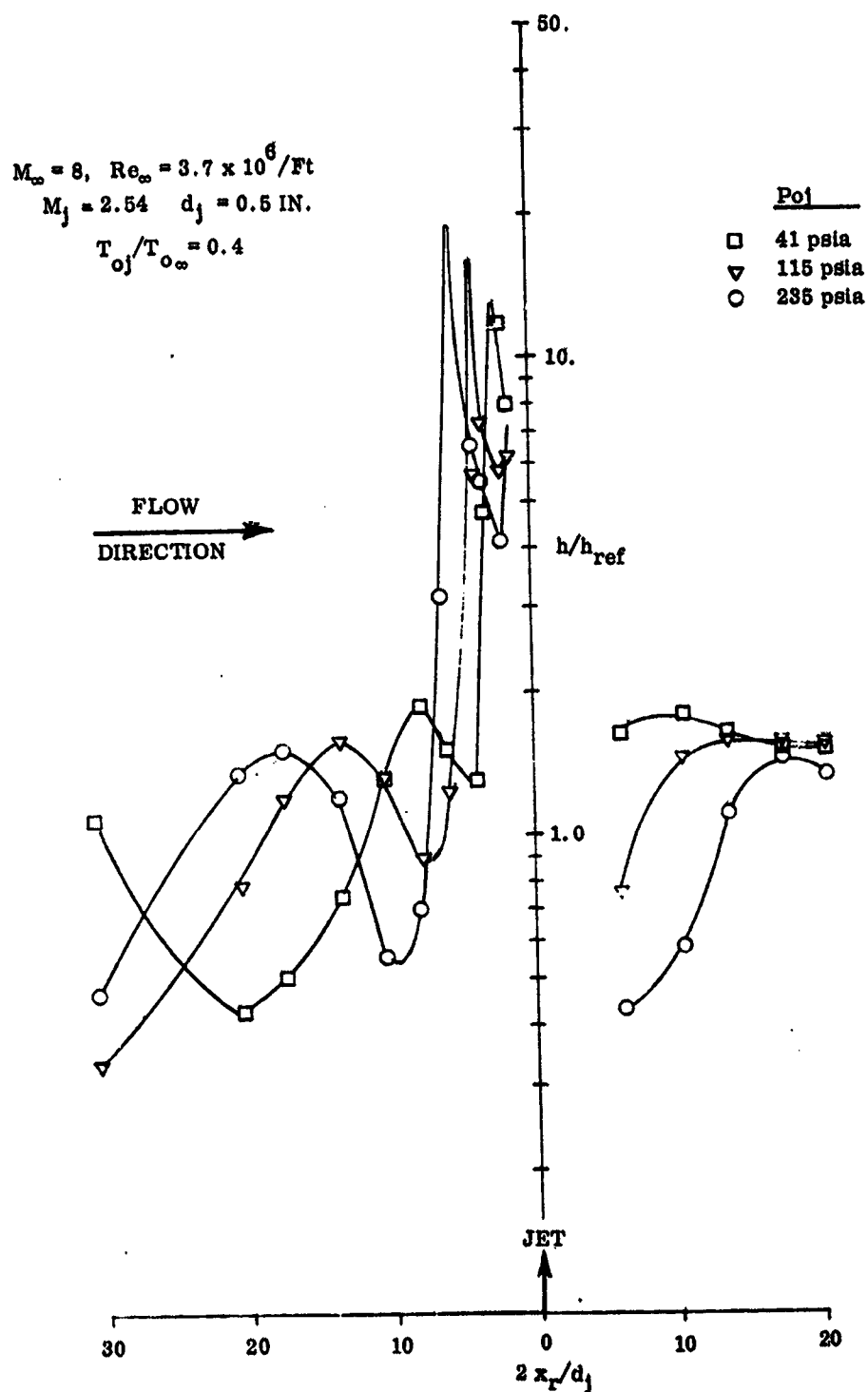
Figure 2-15. Effect of Jet Gas Pressure on Laminar Jet-Stream Interaction Heat Transfer Distribution over a Flat Plate at $\alpha = 0°$
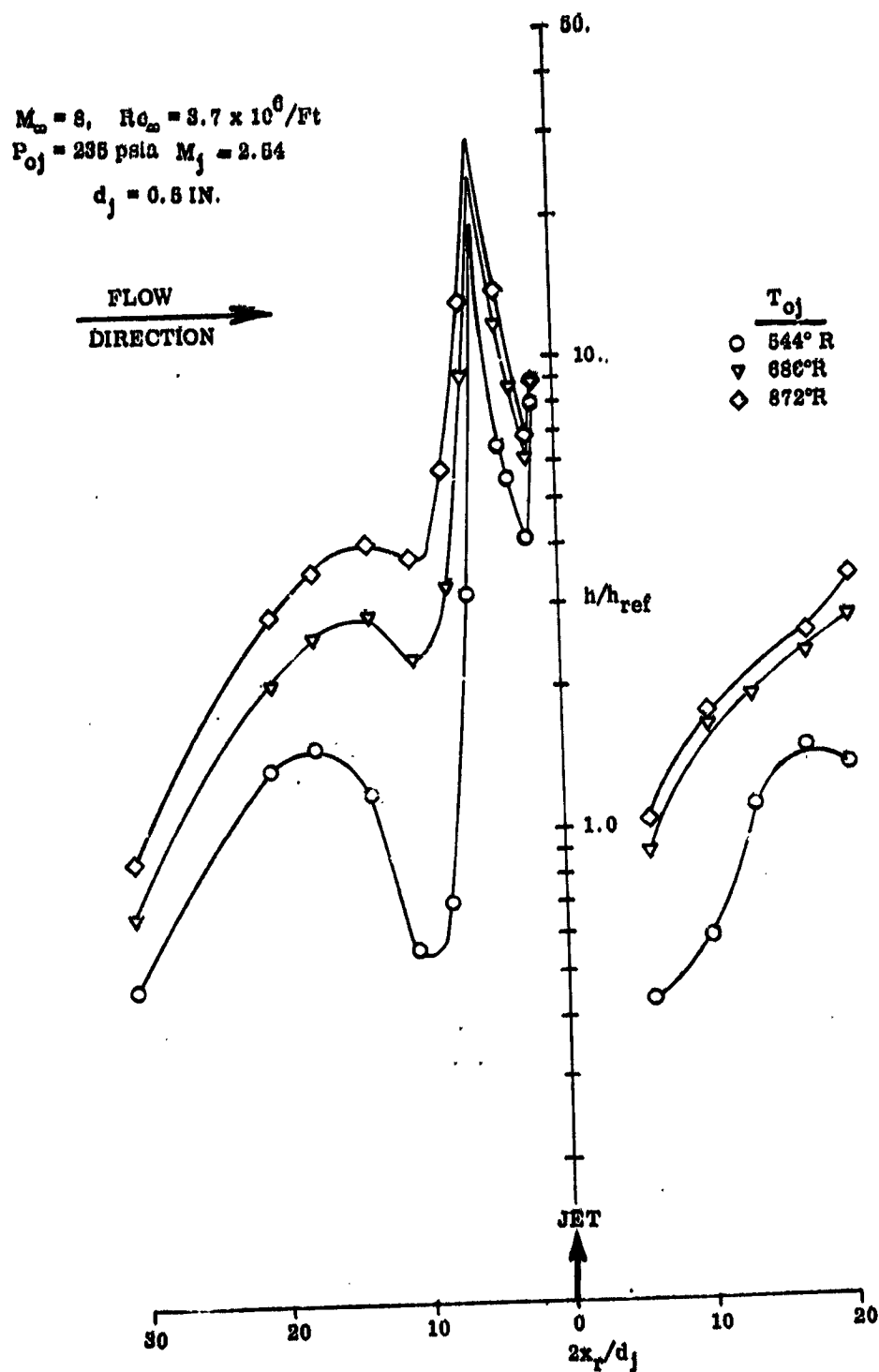
Figure 2-16. Effect of Jet Gas Temperature on Laminar Jet-Stream Interaction Heat Transfer Distribution over a Flat Plate at $\alpha = 0$
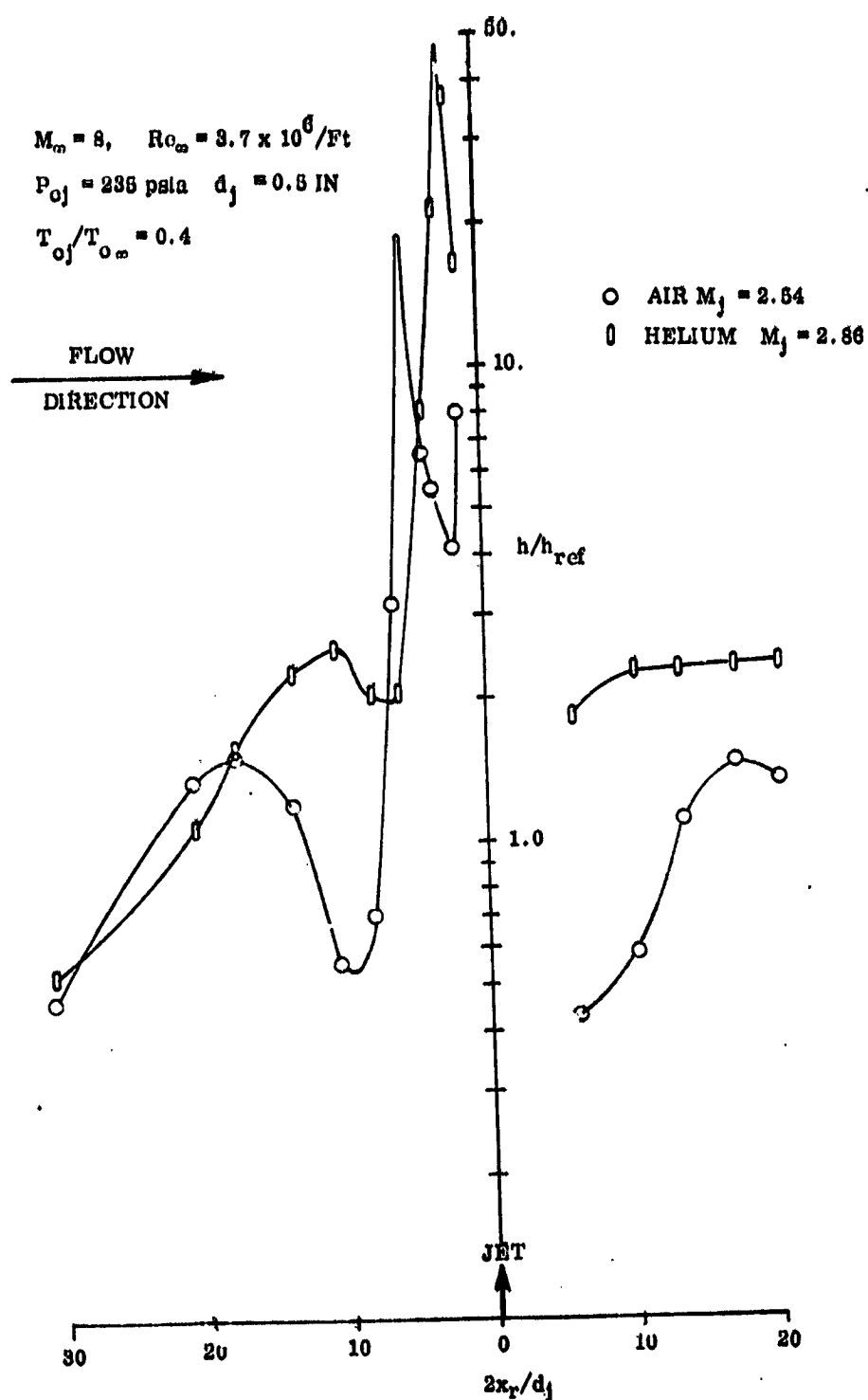
Figure 2-17. Effect of Jet Gas Molecular Weight on Laminar Jet-Stream
Interaction Heat Transfer Distribution over a Flat Plate at
$\alpha = 0°$
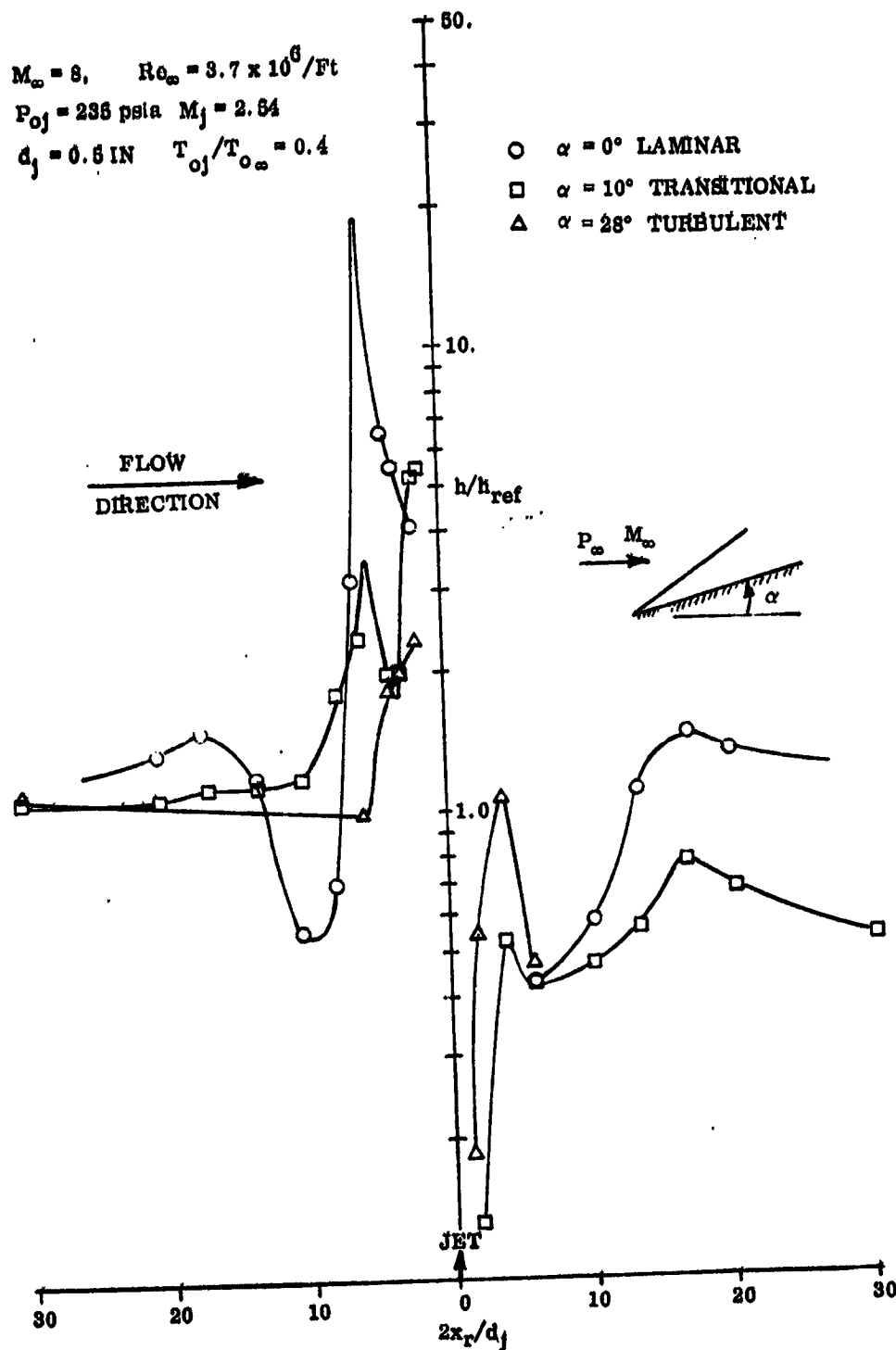
Figure 2-18. Typical Upstream and Downstream Heat Transfer Distributions From Three-Dimensional Jet-Stream Interaction in Laminar, Transitional and Turbulent Flows
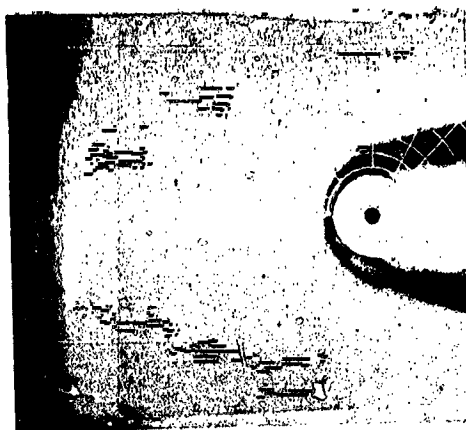
a) Laminar Flow $\alpha = 0°$

$M_\infty = 8,\quad P_{oj} = 235$ psia

$M_j = 2.54\qquad d_j = 0.5$ IN

$R_{e_\infty} = 3.7 \times 10^6/$Ft
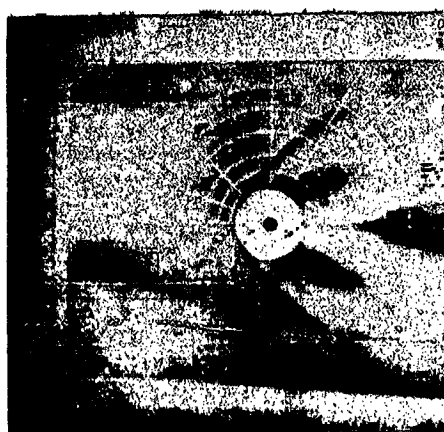
b) Turbulent Flow $\alpha = 30°$

Figure 2-19. Typical Phase Change Paint Data which Indicate High Heating
Regions from Three-Dimensional Jet Stream Interaction
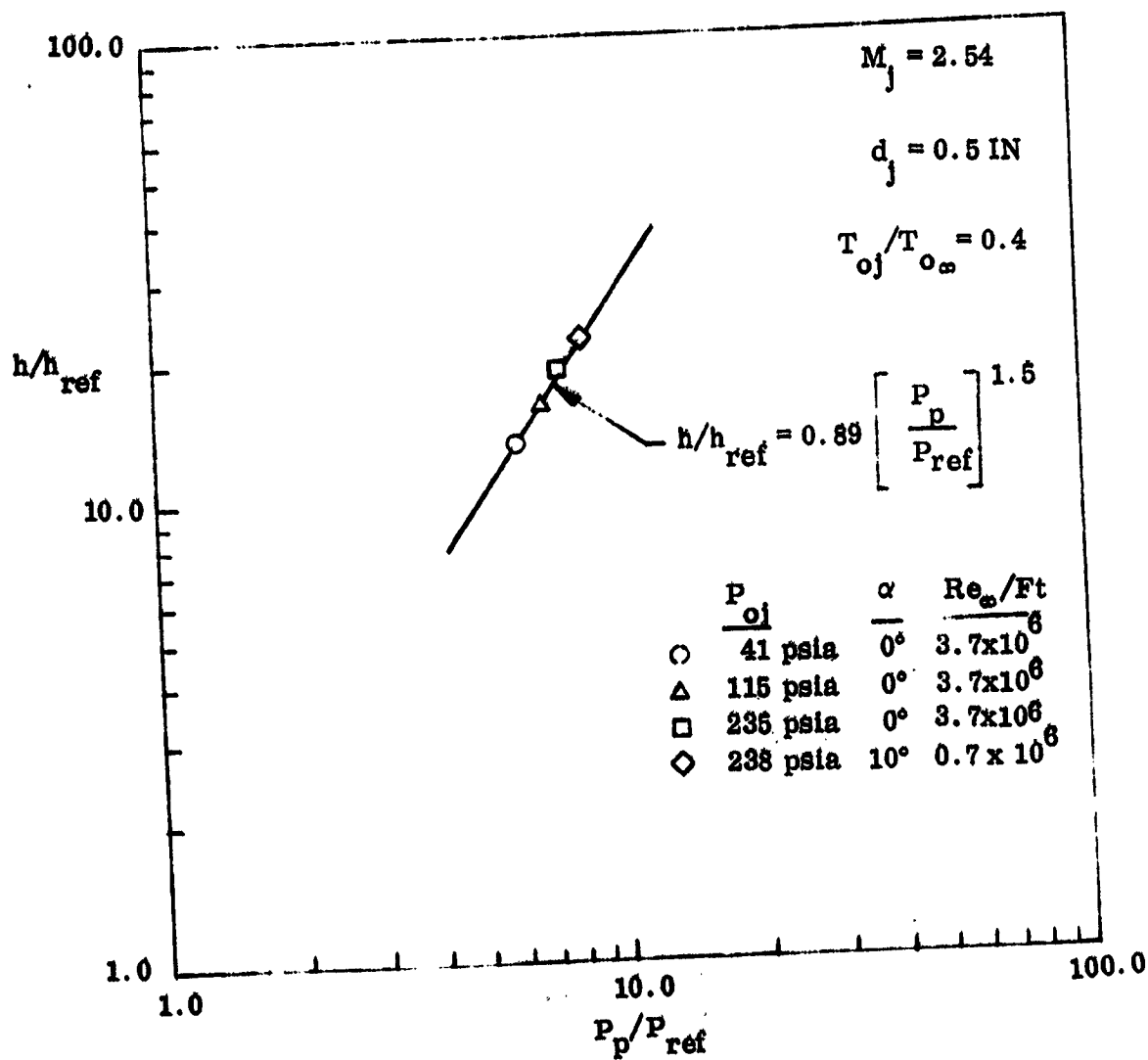
Figure 2-20.   Correlation of Peak Heat Transfer to Peak Pressure for Three-Dimensional Jet-Stream Interactions in Laminar Flow
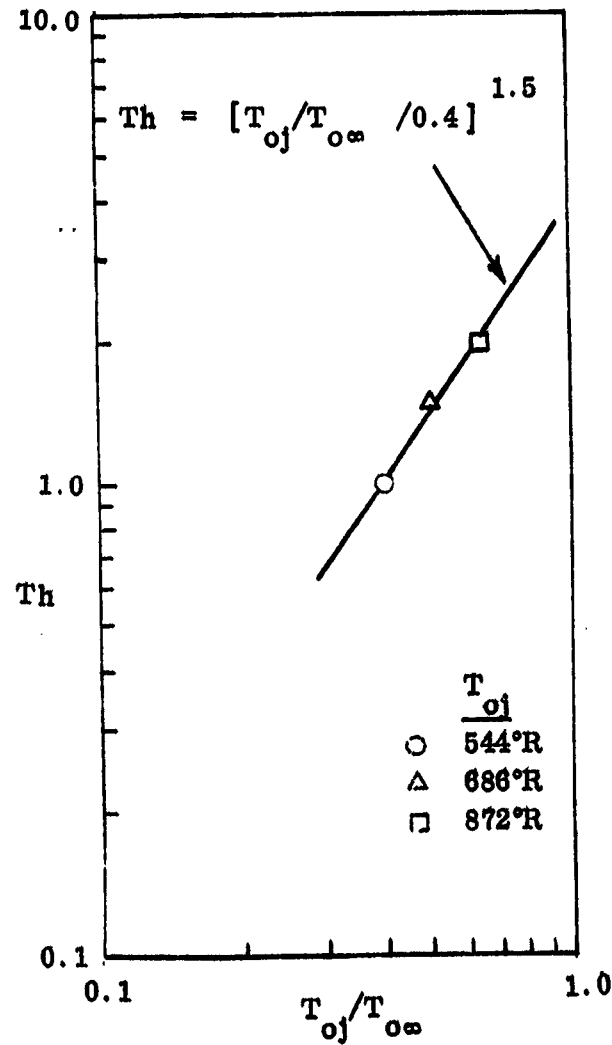
Figure 2-20a. Correlation of Jet Gas Temperature Effect on Peak Heat Transfer for Three-Dimensional Jet Stream Interaction in Laminar Flow
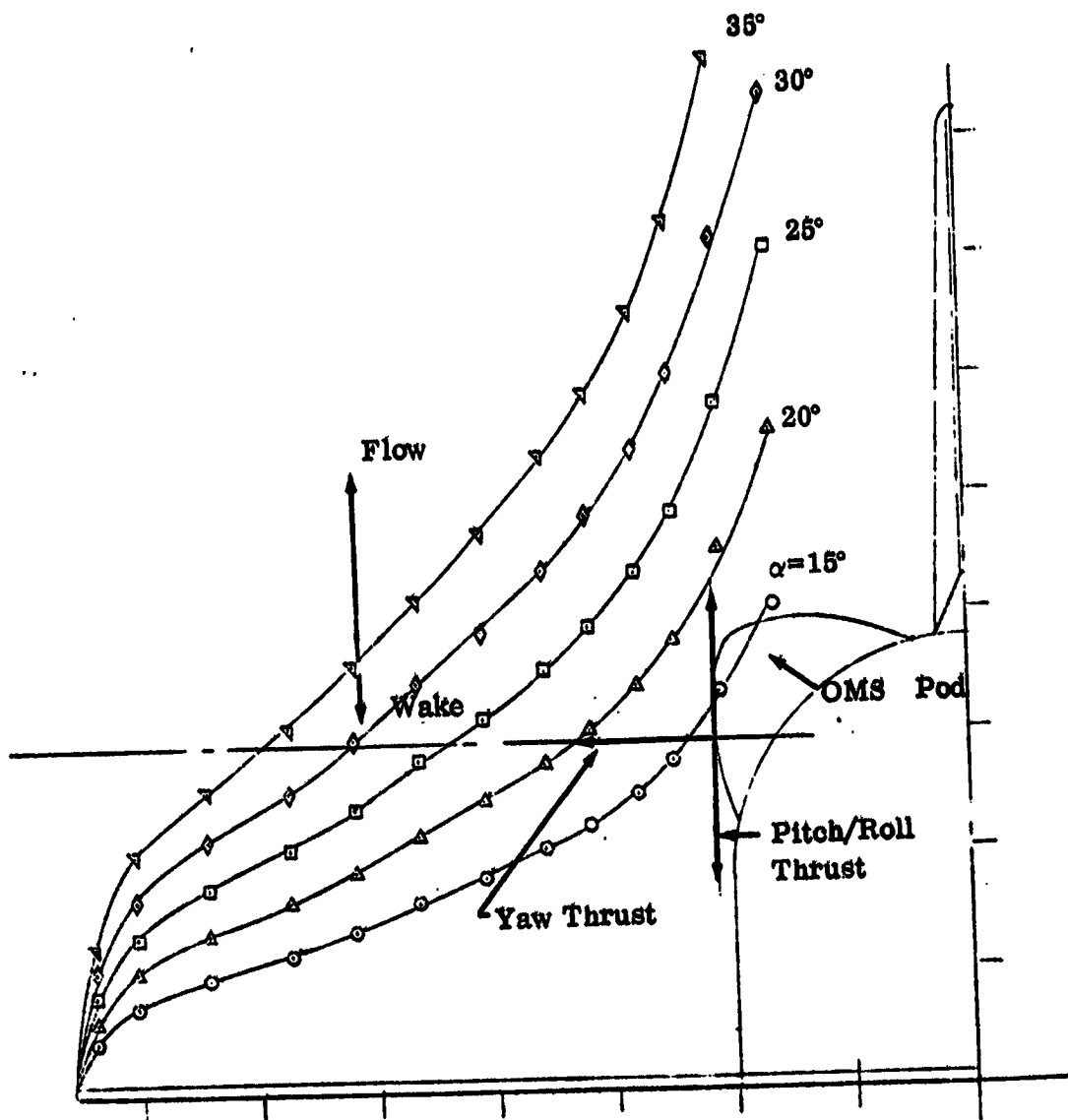
Figure 2-21. Hypersonic Wake at RCS Pod

BODY VORTICES

FLOW SEPARATION

VORTEX

ATTACHED FLOW
ON SURFACE

ATTACHED FLOW

ATTACHED FLOW

BEGINNING OF SEPARATION

REATTACHMENT

VORTEX

SEPARATION

BEGINNING OF
SEPARATION

$M_\infty \sin \alpha$

TYPICAL CROSS SECTION THROUGH WING BODY
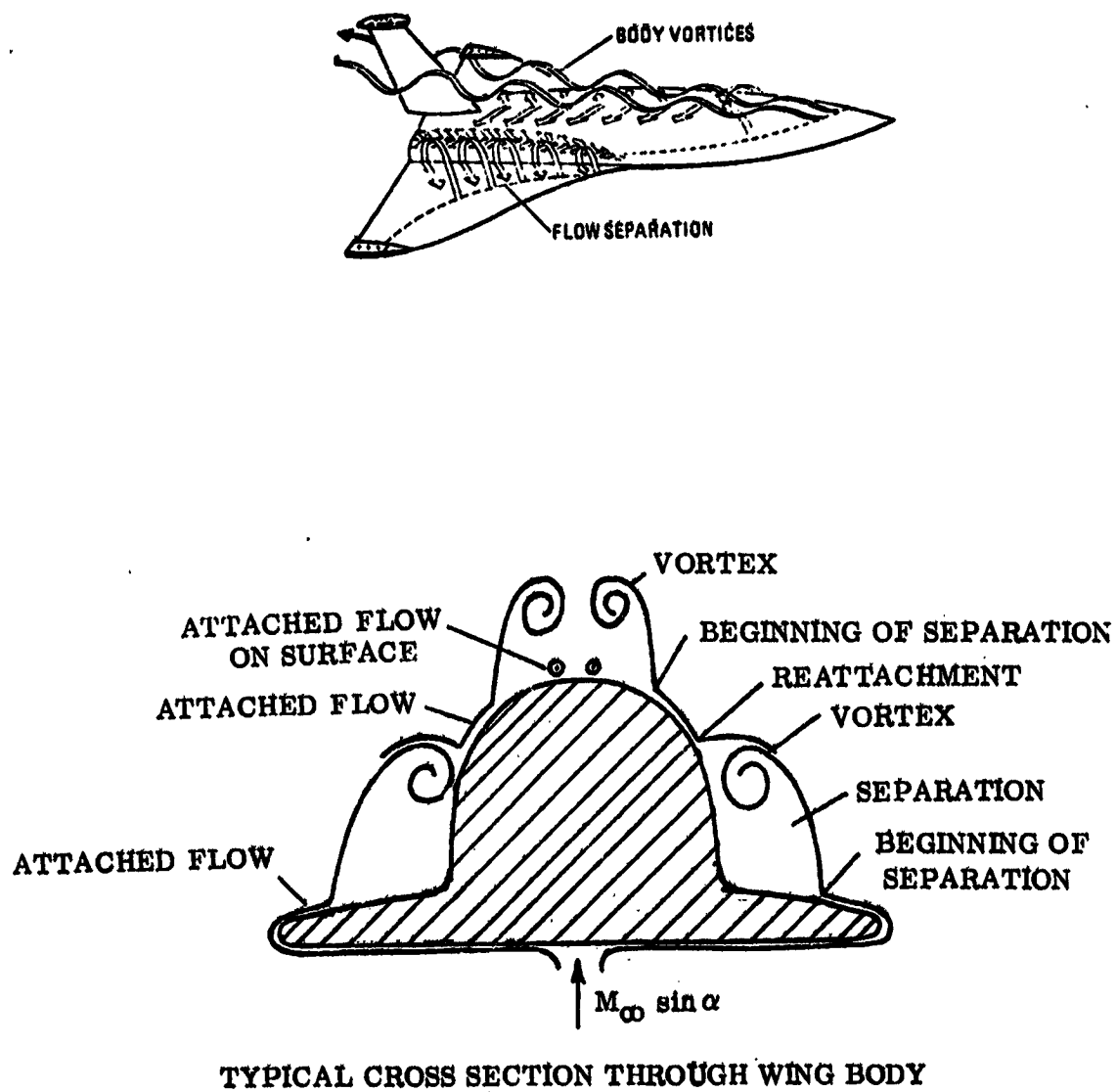
Figure 2-22. Lee-Surface Hypersonic Flow Field on Delta-Wing Orbiter
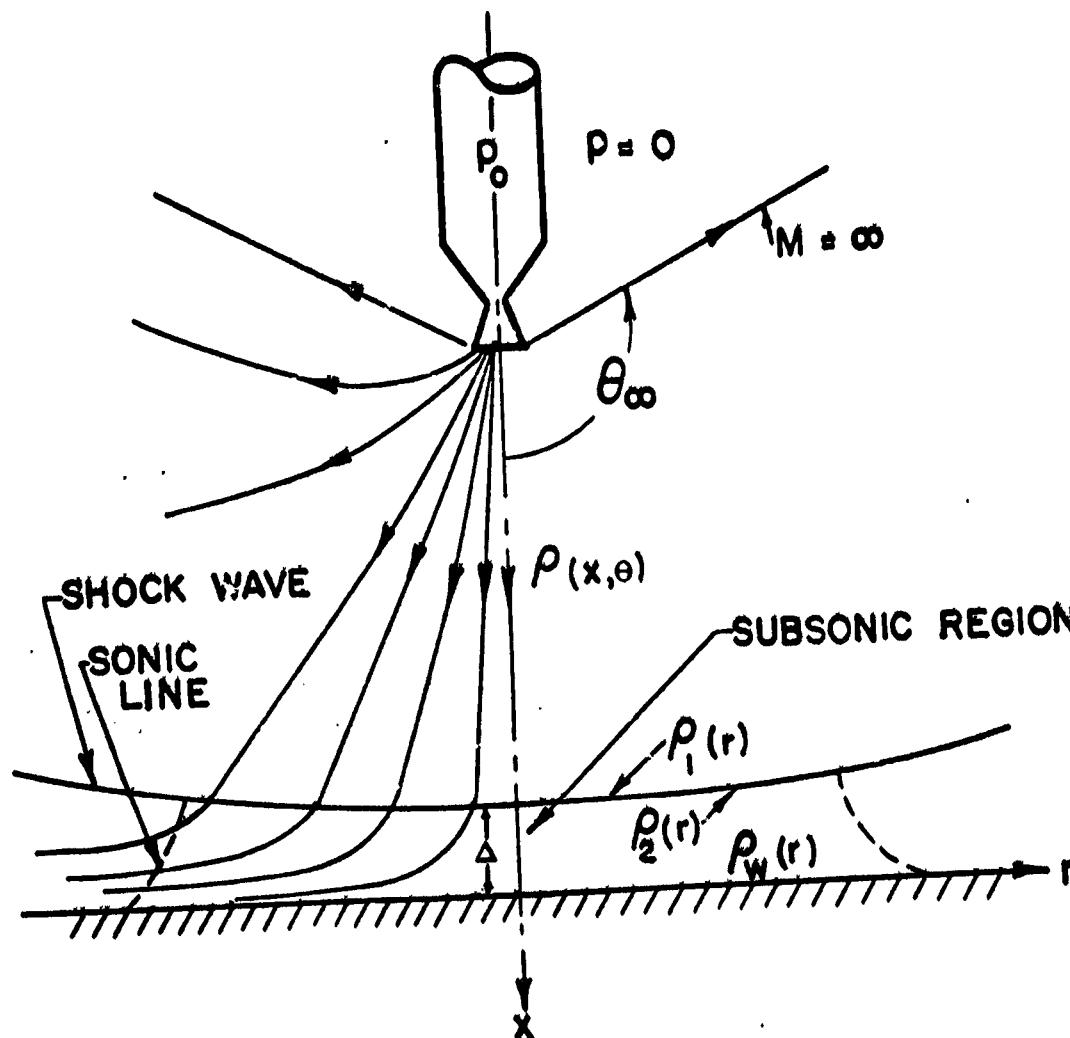
Figure 2-23. Schematic Drawing of a Jet Expanding into a Vacuum and Interacting with a Plane Surface.
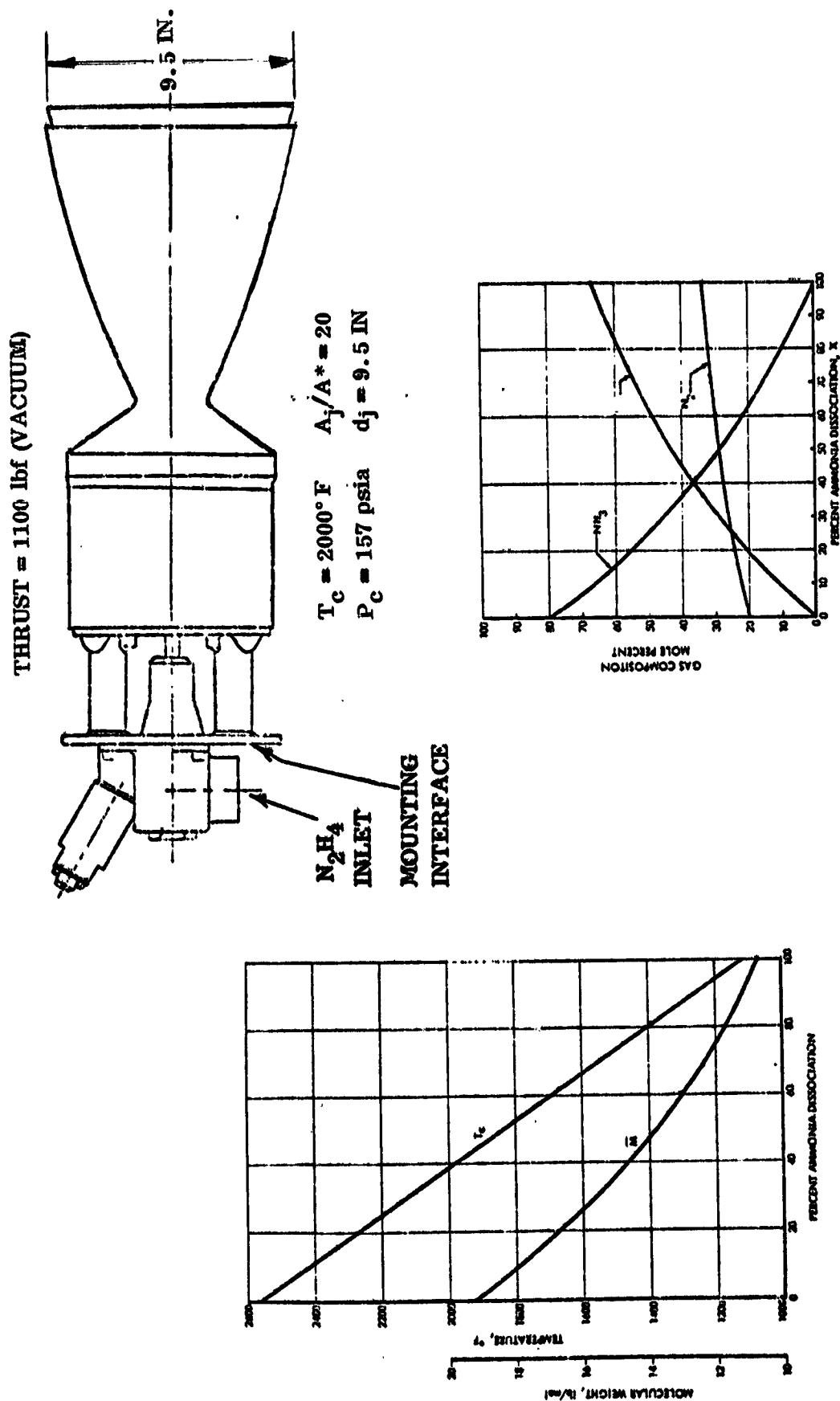
Figure 2-24. Reaction Control System Engine Performance
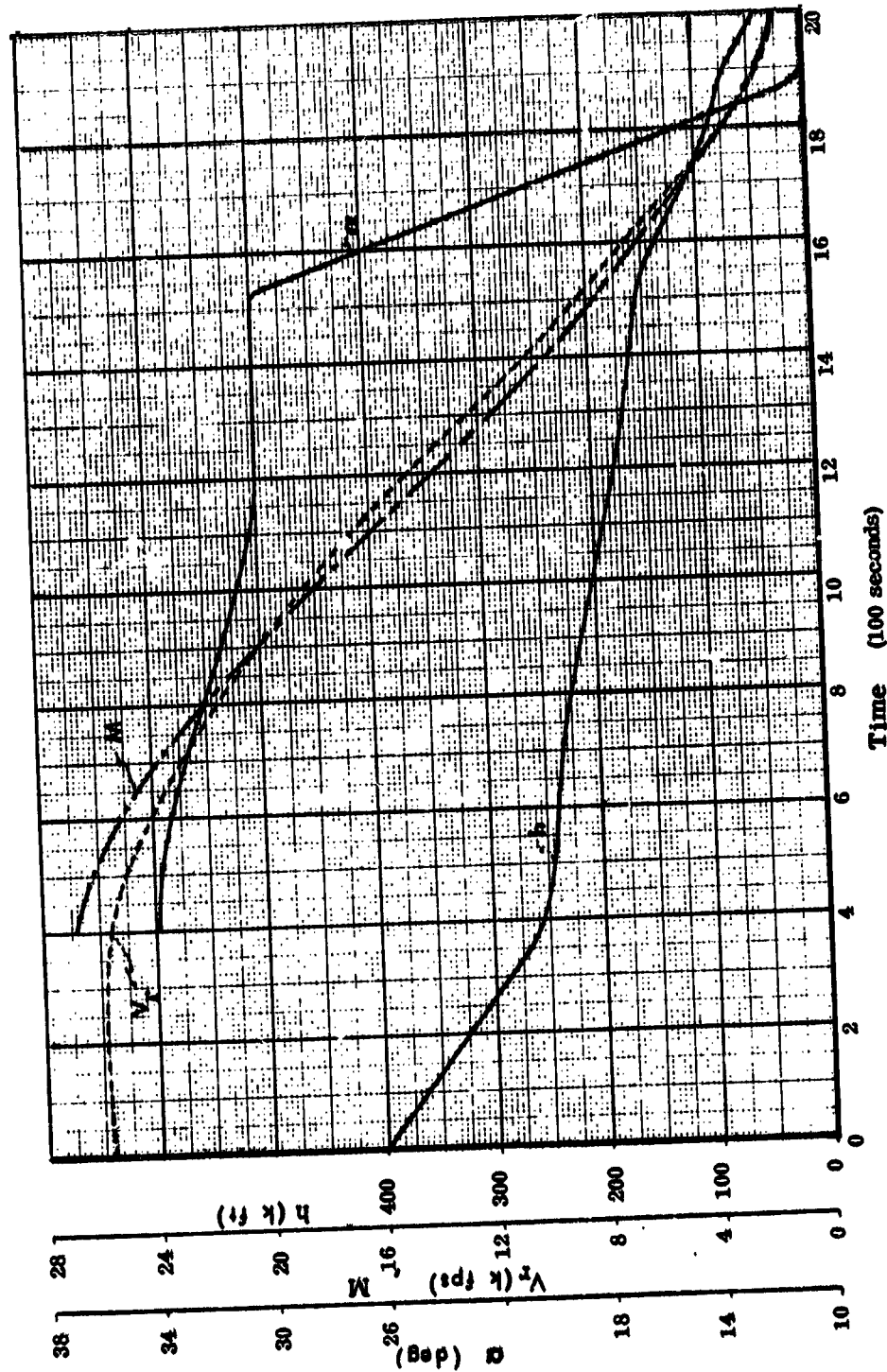
Figure 2-25. Trajectory History
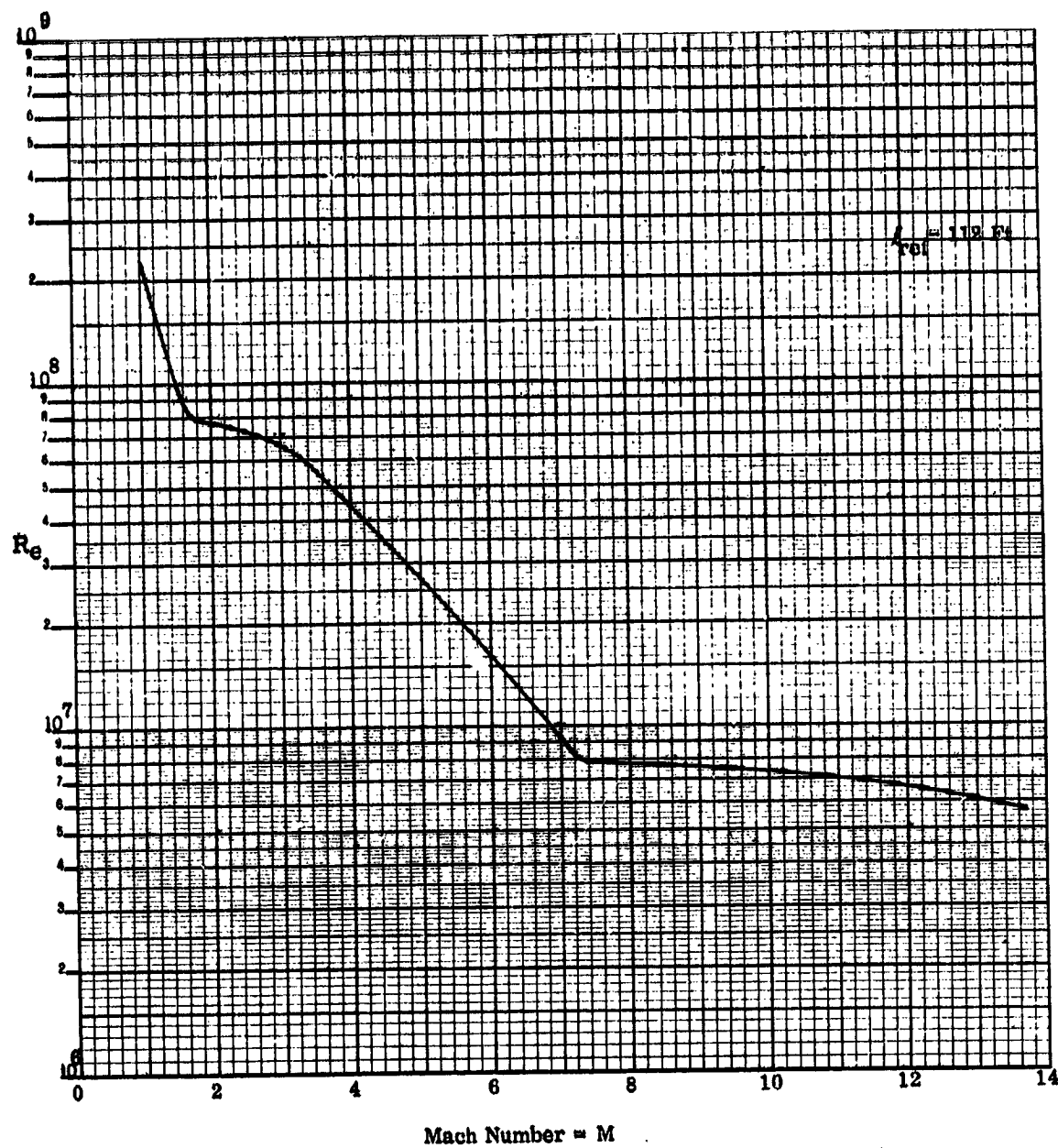
Figure 2-26. Reynolds Number History along Entry Trajectory
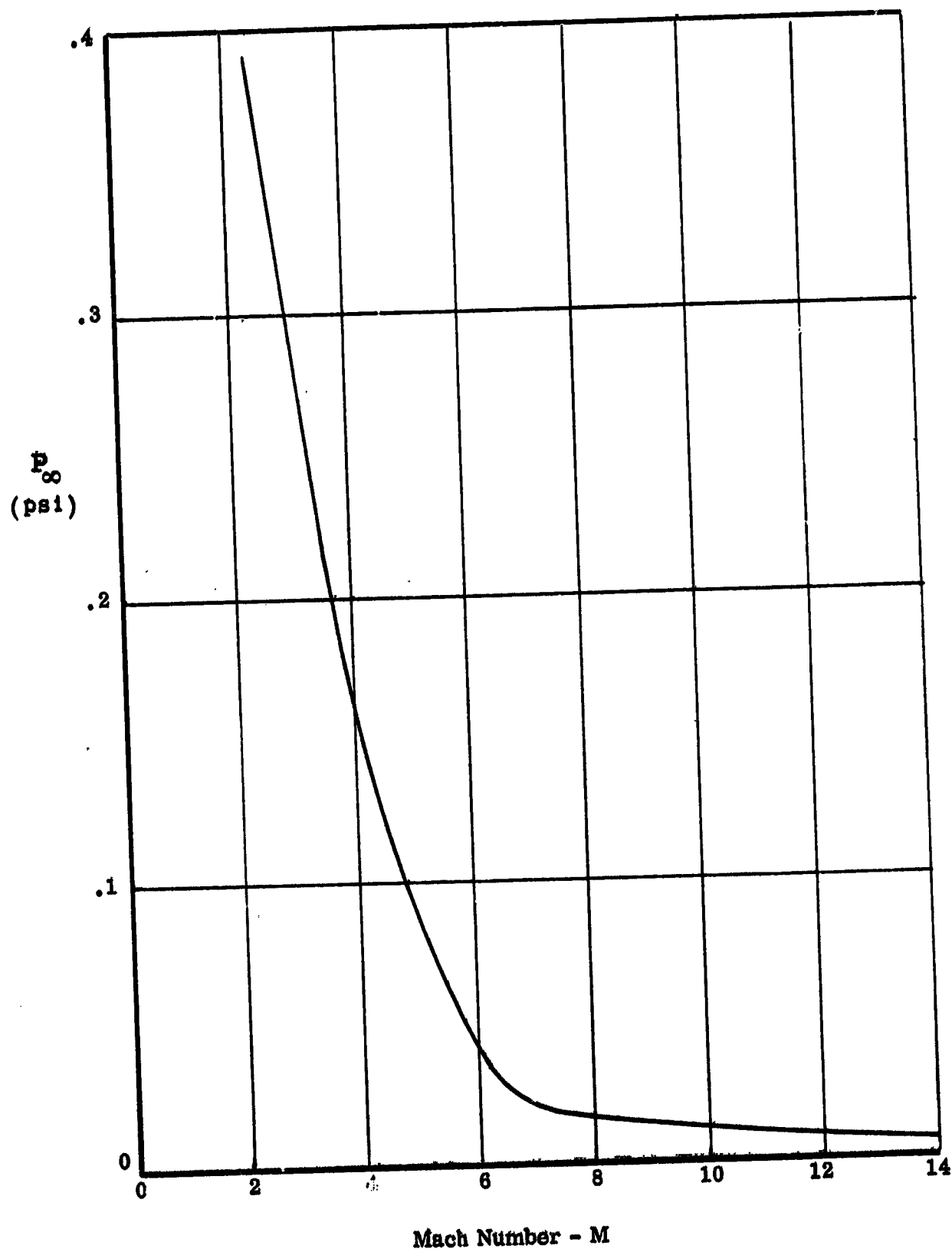
Figure 2-27. AMBIENT PRESSURE ALONG ENTRY TRAJECTORY
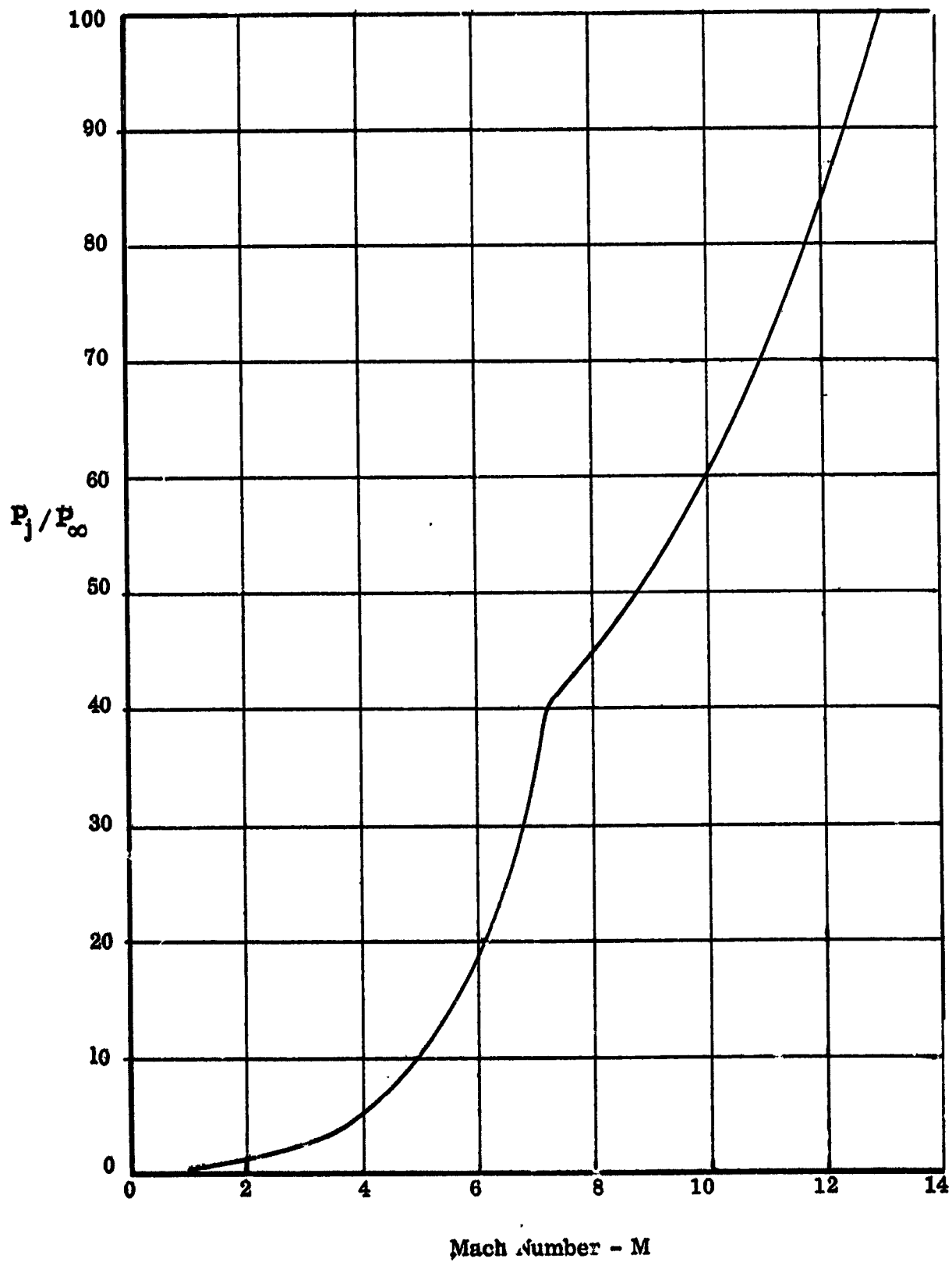
Figure 2-28. Jet Exit Pressure Ratio
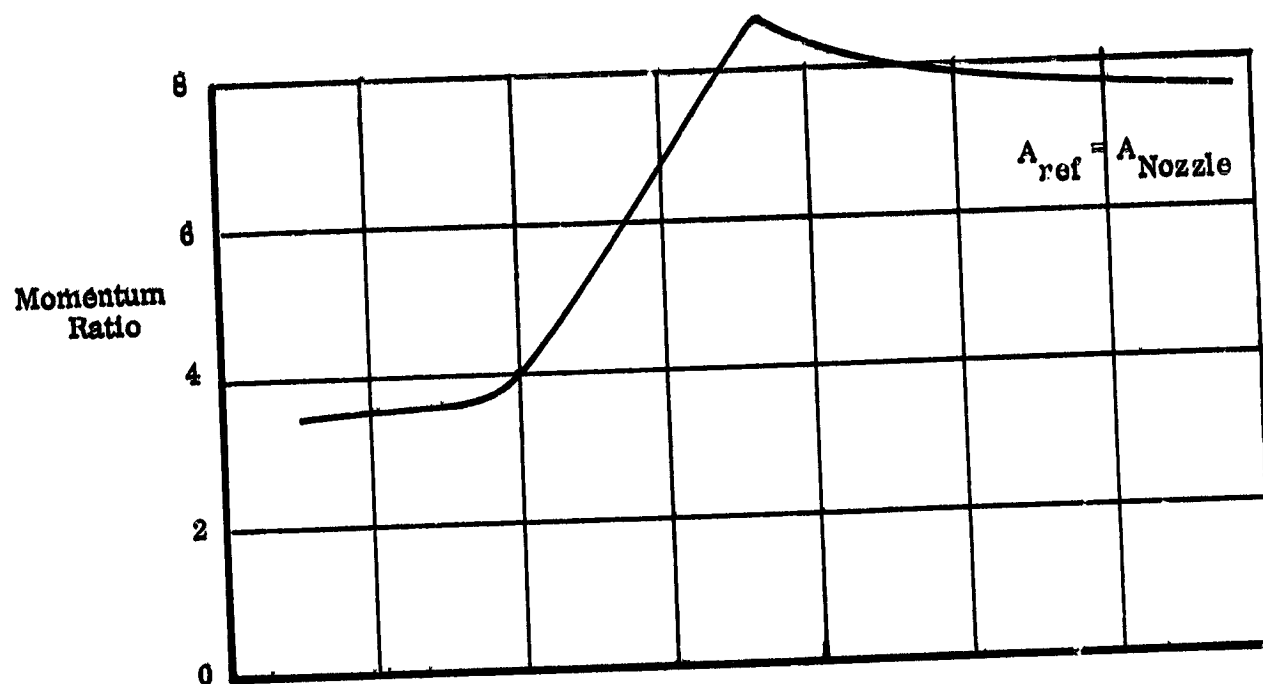
Figure 2-29. MOMENTUM RATIO

Mach Number – M
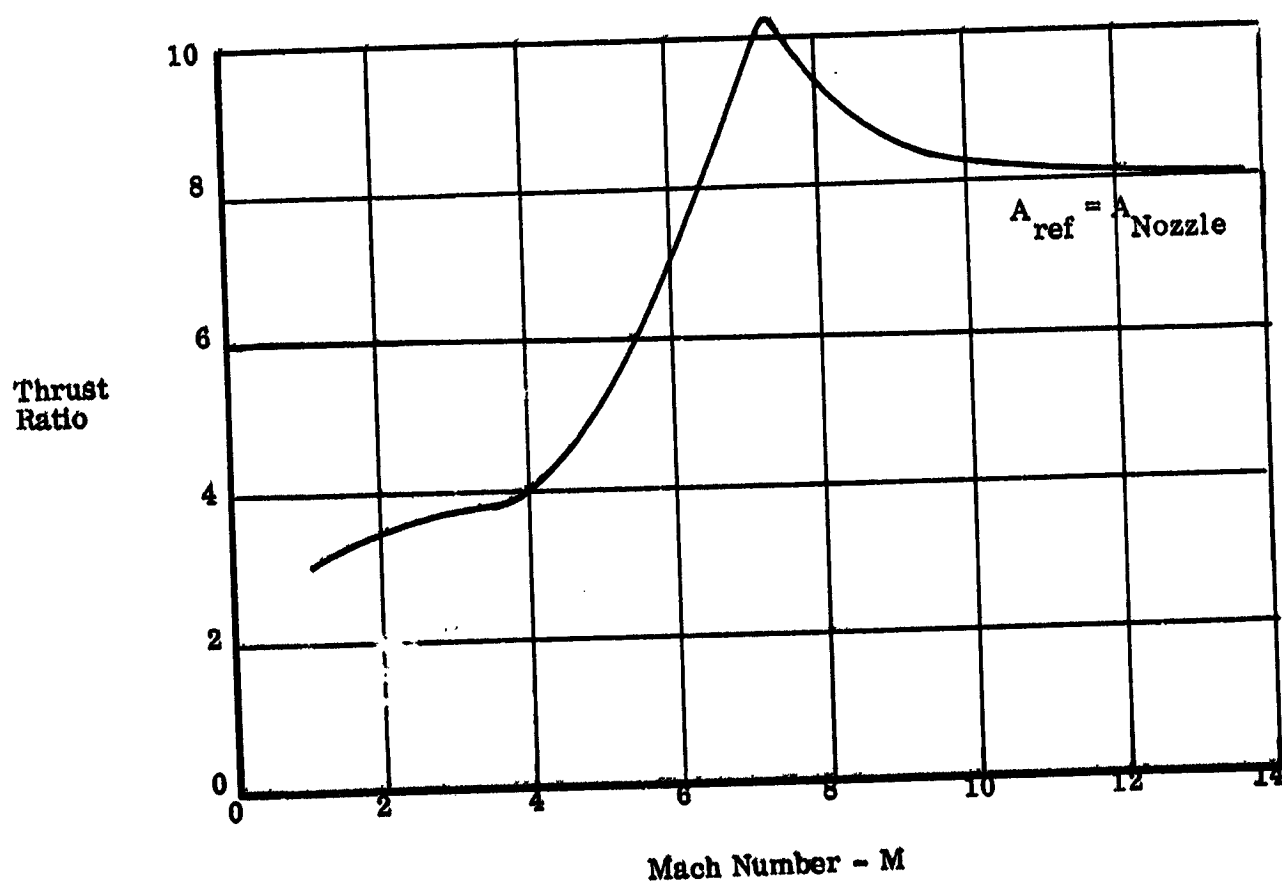
Figure 2-30. THRUST RATIO
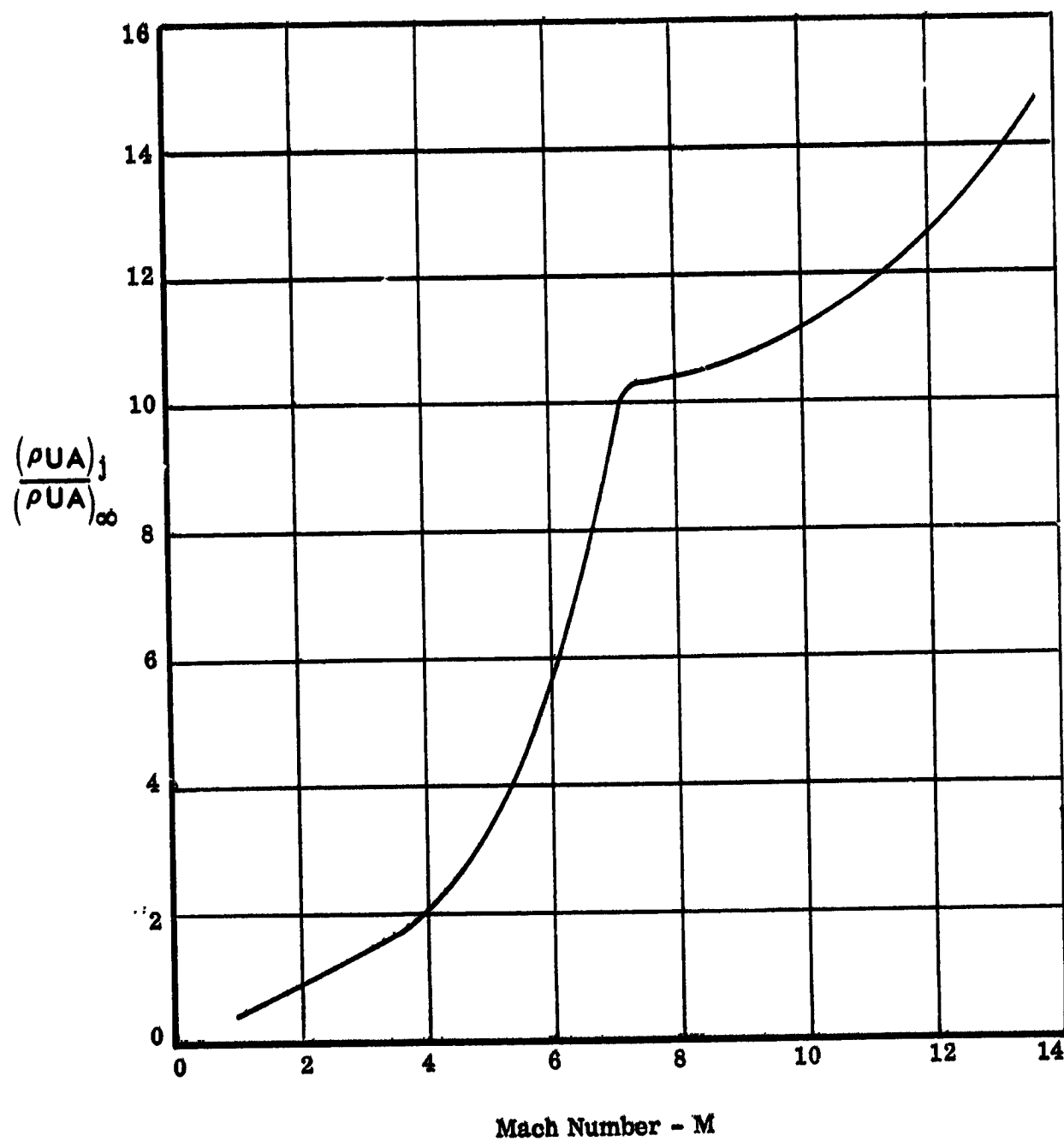
Figure 2-31. MASS FLOW RATIO
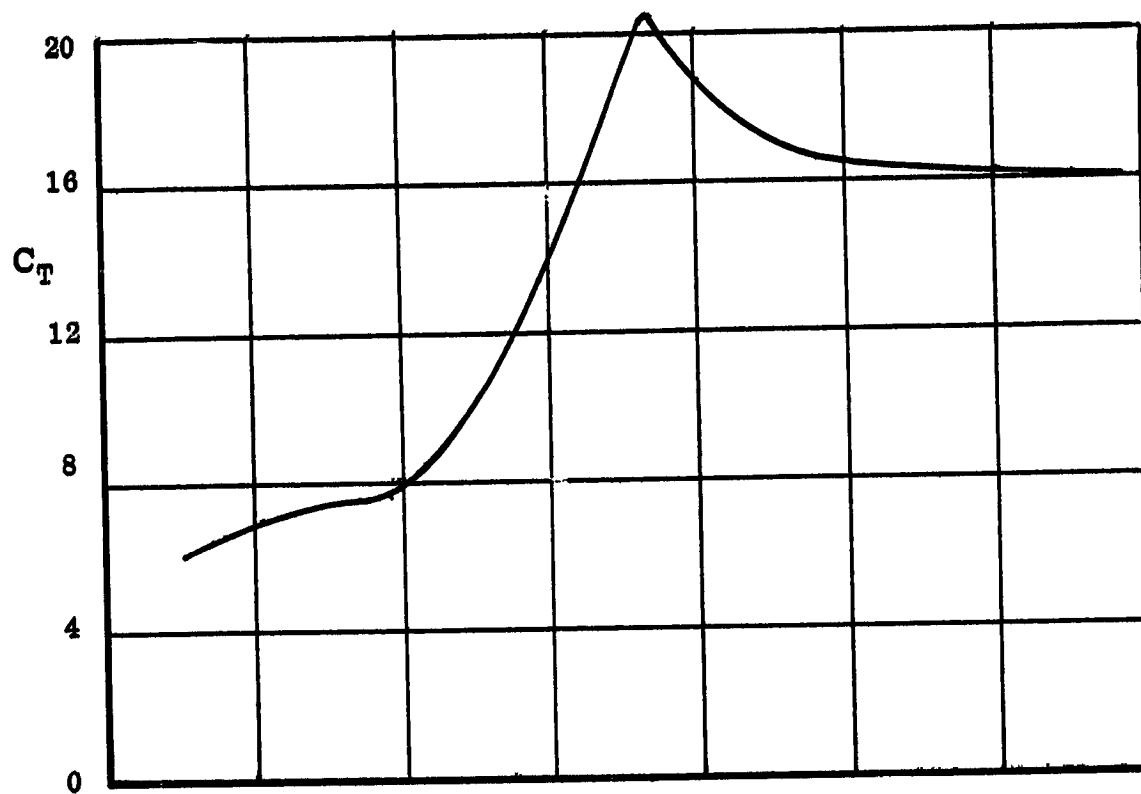
Figure 2-32. THRUST COEFFICIENT

Mach Number - M
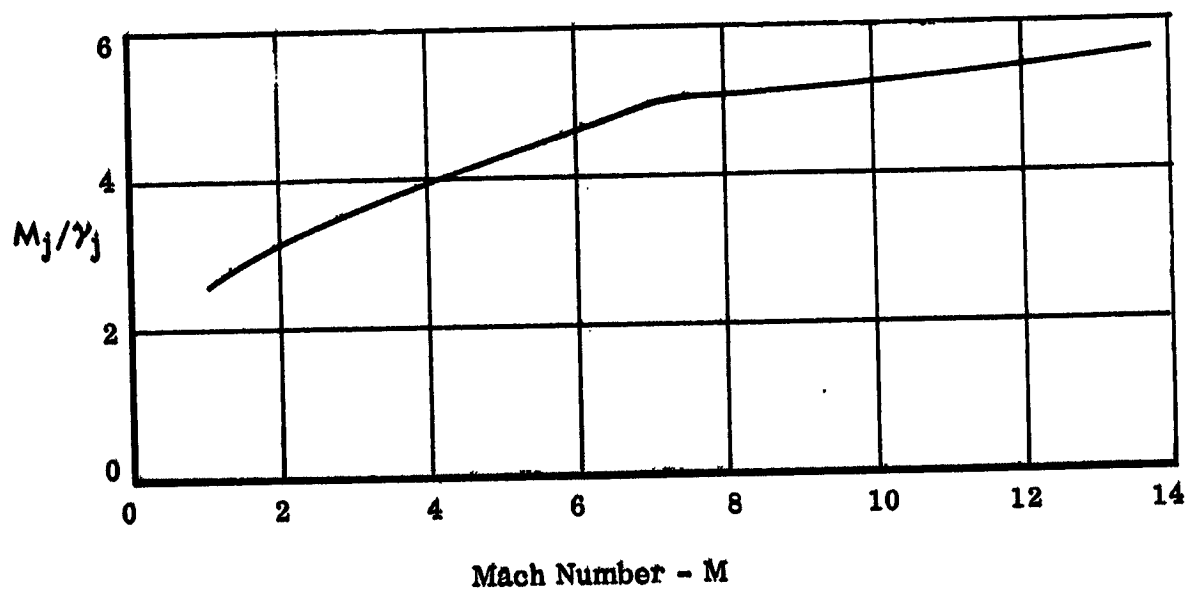
Figure 2-33. HERRON PARAMETER

Mach Number - M
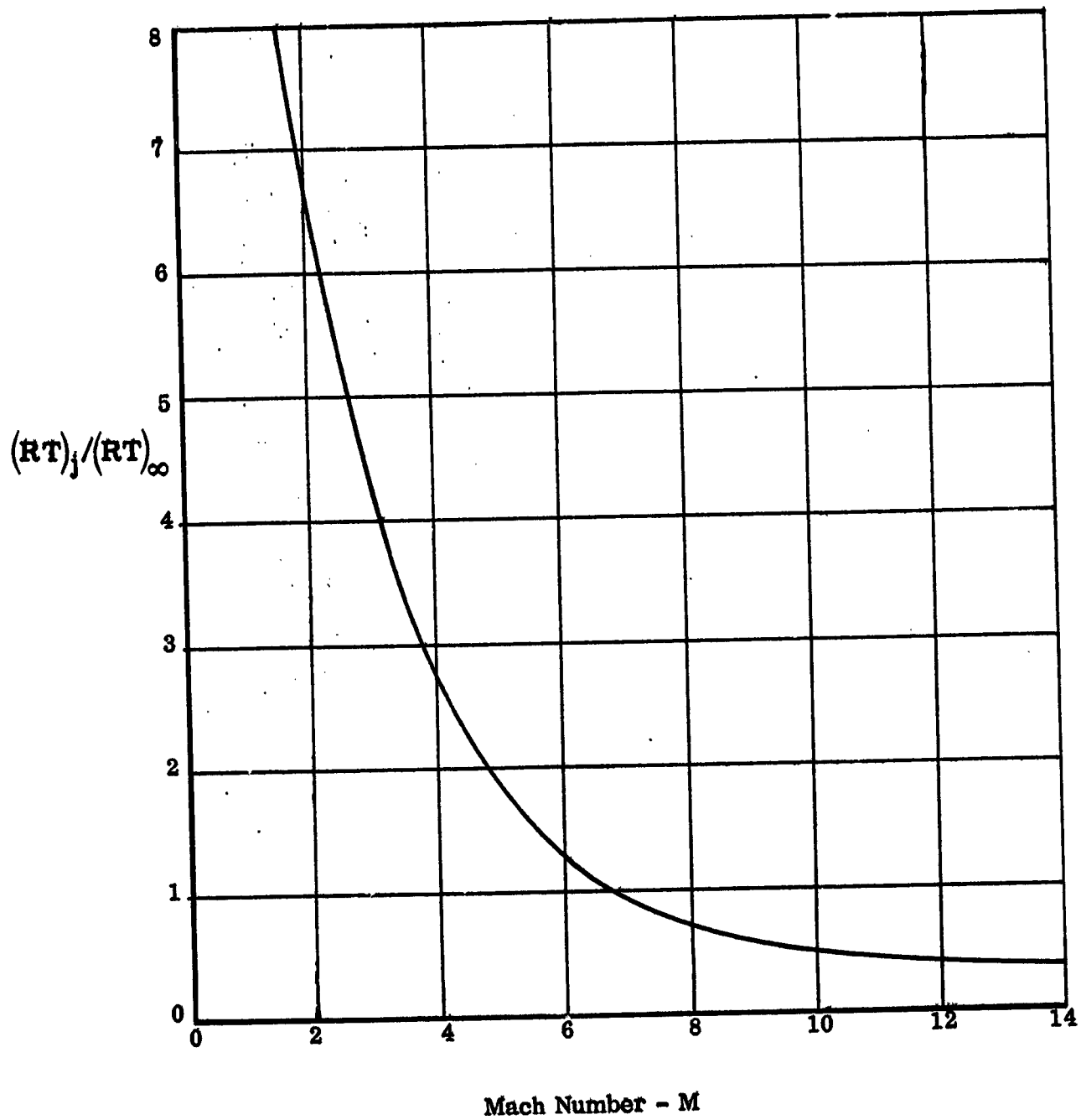
Figure 2-34. KINETIC ENERGY RATIO

3.0 EXPERIMENTAL PROGRAM

3.1 TEST PROGRAM

The NASA-ARC 3-1/2 ft Hypersonic Wind Tunnel (reference 13) was utilized for hypersonic oil flow, heat transfer and limited force tests. This facility is a blowdown tunnel with a steady-state testing time of about 1 to 2 minutes. The pump time between runs is from 1 to 1-1/2 hours and the air is pumped from vacuum spheres to high pressure bottles. During the pump time, a pebble bed heater is heated to the desired tunnel stagnation conditions using gas heaters. The tunnel is run by passing the high pressure air through the pebble bed heater through an axisymmetric nozzle into the test chamber which is connected to the vacuum spheres. The nozzle and test section are cooled by helium which is introduced through an annular slot in the nozzle at the subsonic entrance. The tunnel has a nominal Mach range of 5 to 10 with 3 fixed Mach number nozzles, with a usable test core of about 25 inches; however, the Mach number 7.4 was the only nozzle used during this test program. All tests were made at a nominal Reynolds number of 4×10^6/foot.

The model support system is housed in the test chamber on the right side of the nozzle. This system is hydraulically actuated into and out of the flow and servo-controlled over an angle-of-attack range of ±18°. A sting off-set adapter was used to achieve an angle-of-attack range of +2 to +38° degrees for this test. Two yaw adapters(±5°) were also used during these tests. The model is injected from the side into the nozzle flow after tunnel start and the model is retracted in a similar manner. Injection or retraction transient to or from the tunnel centerline is about 0.5 seconds. Operation of the wind tunnel is automatic with tunnel total pressure programmed into a controller prior to a run. Angles of attack were manually set during a run, yaw angles were set between runs.

Force and pressure data were recorded on magnetic tape and were reduced off line. Heat transfer data was recorded by a 170 frame/second movie camera mounted in the test chamber using temperature sensitive paint as the test medium. Oilflow data was obtained using a titanum/oxide vacuum oil mixture on the model and taking still photographs after the run was completed.

Test section 2 of the Langley Research Center's 4 x 4 ft Unitary Plan Wind Tunnel was used for supersonic force and flow visualization tests. The test section 2 (reference 14) has a nominal operating range from Mach 2.3 through 4.7 and test section dimensions of 48 inches by 52 inches by 84 inches. The Unitary Plan Wind Tunnel (UPWT) is a continuous flow facility in which the Mach number is controlled by an asymmetric sliding nozzle block and in which tunnel stagnation pressure and temperature can be controlled independently of Mach and of each other. The tunnel

conditions used for this test program included:

Mach	Reynolds Number	P_o Tunnel		T_o Tunnel
2.5	$3 \times 10^6/ft$	17.68	PSIA	150° F
2.96	$3 \times 10^6/ft$	22.47	PSIA	150° F
4.0	$1 \times 10^6/ft$	13.67	PSIA	175° F
4.0	$3 \times 10^6/ft$	41.02	PSIA	165° F
4.0	$5 \times 10^6/ft$	68.38	PSIA	175° F

The model was mounted on the adjustable angle coupling on the sting and the angle of attack was set by adjusting the coupling. The angle of attack range of the coupling was from -2° to +40°. The test was limited to 35 degrees for the Mach 4 case with the exception of the high Reynolds number ($5 \times 10^6/ft$) case where sting coupling load limits caused the angle of attack to be restricted to 25 degrees. Yaw angles were set to a maximum of ±5° using the existing support sting mechanism. The model force data was obtained from a NASA provided internal strain gage balance (Langley Balance Number 839) and a limited set of oil flow runs were made using a fluorescent oil technique.

3.1.1 <u>MODEL AND INSTRUMENTATION DESCRIPTION</u> - The wind tunnel model used in this test program was a 0.015 scale model of the PRR orbiter configuration as defined by RI drawings (reference 15) and shown in Figure 3-1 installed in the Langley UPWT. The model consists of the following parts which were cast or machined from 17PH stainless steel.

  a. removable nose
  b. upper fuselage afterbody
  c. lower fuselage afterbody for wing-off
  d. lower-aft fuselage cover (heat shield/cover)
  e. fuselage afterbody fairings
  f. OMS pods
  g. vertical tail
  h. tail-off block
  i. wing
  j. manipulator fairing
  k. wing tip dummy RCS pod
  l. balance adapter for the 6-component balance
  m. non-metric RCS plenum and supply line
  n. seven (7) nozzle configurations
  o. RTV OMS pod

Two left hand OMS pods were made; one from stainless steel for the force tests and the other with an RTV rubber covering for heat transfer tests. The RTV rubber

OMS pod has a white grid on the surface to assist in the heat transfer data reduction. In addition one left nozzle block in a yaw nozzle configuration was also fabricated with an RTV covering for the heat transfer tests. Figure 3-2 presents two views of the complete model showing the RTV rubber OMS pod and nozzle installed on the left side of the model and set of pitch/roll nozzles installed on the right side. Reference 1 presents a complete set of model drawings.

The complete model except for the reaction control system plenum and nozzles was mounted on an internal force balance which was attached to a sting as shown in the sketch of Figure 3-1. Thus the force and moment data obtained during the test did not include the thrust and thrust moments but only the basic configuration and the induced loads from jet interaction. Figure 3-3 shows the location of the jet nozzles relative to the moment reference center of the model.

Section 2 presented the reaction control system engine characteristics and the flight parameters which were to be matched in the wind tunnel tests. Four test Mach numbers were selected at which the flight conditions would be used to design nozzles matching full scale pressure ratio, either momentum ratio or mass flow rate and air or helium as test gases using the computer program of reference 16 to size the nozzles. The three conditions included air as test gas matching momentum ratio and pressure ratio which resulted in a scaled nozzle with an expansion ratio of 7.37, air as the test gas matching mass flow ratio and pressure ratio which resulted in a scaled nozzle with an expansion ratio of 2.58; and helium as test gas matching momentum ratio and pressure ratio which resulted in a scaled nozzle with an expansion ratio of 3.62.

The model nozzles were then designed as 15 degree conical nozzles with a circular throat one diameter in length. Five yaw nozzle blocks were fabricated as shown in Figure 3-4 and include:

a. N_1 – Twin nozzle yaw configuration having an expansion ratio of 7.37

b. N_2 – Twin nozzle yaw configuration having an expansion ratio of 2.58

c. N_3 – Twin nozzle yaw configuration having an expansion ratio of 3.62

d. N_5 – Single nozzle yaw configuration having an equivalent nozzle area as (a) above with an expansion ratio of 7.37

e. N_7 – Twin nozzle yaw configuration in RTV surface having an expansion ratio of 7.37

These yaw nozzles were scarfed by computing the theoretical nozzle exit diameter to a flat surface at the outside of the block contour and contouring the block after

3-3

the nozzles were drilled. The twin nozzle configurations were located so that the centerline of the nozzles were 1.5 exit diameters apart. All yaw nozzles were perpendicular to the longitudinal centerline of the vehicle and parallel to the xy plane.

Two pitch/roll nozzle blocks were fabricated as shown in Figure 3-5 having twin nozzles with an expansion ratio of 7.37. These nozzles are located in the flat upper or lower portion of their blocks and thus are not scarfed. The nozzles are perpendicular to the vehicle centerline and are parallel to the vehicle plane of symmetry. Model strength requirements prevented these nozzles from being mounted as close to the edge of the nozzle block as would be desired for scale location resulting in nozzles located 0.25 inch inboard of the scale location. Figure 3-3 shows the nozzle location relative to the moment reference center.

Vacuum chamber calibrations were performed on each nozzle in order to determine the actual performance of the nozzle set so that the test data could be obtained at the correct thrust levels. Data was obtained at 5 psia and 3 psia backpressure in the chamber using dry nitrogen as the test gas for all nozzles and, in addition, helium for nozzle N_3. The theoretical nozzle characteristics were used to define the supply pressures to be used in the tunnel to match pressure ratio and momentum ratio and these pressures were then corrected to test values using constant thrust and the calibration curves.

The test gases used at NASA-Ames were dry nitrogen and helium which were supplied from high pressure bottles manifolded together to provide a steady flow rate without excessive pressure drop during a data run. The nitrogen bottles were connected to a tank truck of gas which was the primary supply for these tests. Figure 3-6 presents a schematic diagram of the gas control system. The Grove Regulator (R2) was used to adjust the model plenum pressure by monitoring the output of the plenum transducer (TD3) on a digital volt meter. Gas flow into the plenum was turned on and off using the solenoid actuated valve.

The gas used at the Langley unitary tunnel was dry air which was supplied from a high pressure line immediately adjacent to the tunnel. The gas metering system was similar to that shown in Figure 3-6 in a more simplified form. The gas system operator was located next to the tunnel and directly controlled the Grove regulator which monitoring plenum pressure on a digital volt meter. Figure 3-6 without the valves in the test chamber and gages in the control room is a good representation of the flow control system at Langley.

Force data obtained in two test facilities required a different force balance was used at each facility. A Task Mark XIV 1 inch balance was used at the Ames hypersonic tunnel which has an allowable load range of:

a. normal force 800 lb
b. side force 400 lb
c. axial force 100 lb
d. pitching moment 1600 in lb
e. yawing moment 660 in lb
f. rolling moment 250 in lb

The balance used for the tests at the Langley Unitary tunnel was the Langley 839
1.25 inch balance which has an allowable load range of:

a. normal force 800 lb
b. side force 200 lb
c. axial force 60 lb
d. pitching moment 1600 in. lb
e. yawing moment in. lb
f. rolling moment 400 in. lb

The primary test objectives were to obtain force, heat transfer, and oil flow data
from the model with and without RCS simulation in order to determine the interaction
effects between the RCS plumes and the airflow around the vehicle. However, in
order to determine the nozzle thrust for correlation with the other data one pressure
measurement was required in the model nozzle plenum chamber as shown schematic-
ally in Figure 3-6. In addition one copper-constantan thermocouple was mounted in
the nozzle plenum chamber as is shown schematically in Figure 3-6 to provide a
direct measurement of the temperature of the gas supplied to the nozzles. This
gage proved to be fragile during the test programs, however, and little useful
data was obtained from it.

During the heat transfer tests at NASA-Ames additional Iron-Constantan thermocouples
were used to measure the temperature of the RTV surfaces of the OMS pod and the
RTV yaw nozzle block shown in Figure 3-2.

3.1.2 TEST PROGRAM - The hypersonic test program which was performed at
NASA-ARC (HWT test 156) at a Mach number of 7.4 included 17 oil flow runs,
14 heat transfer runs, and 4 force runs as shown in Tables 3-1, 3-2, and 3-3
respectively. Six force data points were obtained on each of the four force runs;
jet on and jet off at three angles of attack. The data was taken in this manner to
minimize the effects of temperature on balance output between the jet on and off
data points. The nozzle chamber pressure given in these tables are nominal values
set for a given run.

RUN	CONFIG.	MACH	TUNNEL P_o PSIA	R_e /ft	α Deg	β Deg	GAS	PLENUM P_o PSIA	COMMENTS
1	BWTN₁	7.4	500	1.85×10^6	0-33	+5	–	–	Blockage run
2			800	3×10^6	30	-5	–	–	Blockage run
3			500		25	-5	–	0	Oil Flow
4					30		N₂	0	
5	BWTN₄		800		30			512	
6	BWTP*		500	1.85×10^6	30	0		531	
7	BWTN₃		800	3×10^6	30			311	
8	BWTN₁				30			330	
9					30		He	–	Wing Tip Pod
10					30		N₂	274	
11					25		N₂	512	
28					25			0	
29					25			512	
30			500	1.85×10^6	30			310	
31	BWTN₄		800	3×10^6	30			310	
32	BWTN₅				30			302	
33					25			506	
34					30			506	
35								511	

* P = Wing Tip Pod Fairing Without RCS Simulation

Table 3-1. Oil Flow Runs at M = 7.4

RUN	CONFIG.	MACH	TUNNEL P_0 PSIA	R_e /FT	α DEG	β	PLENUM P_0 PSIA	GAS	Paint Phase Change °F
12	BWTN7	7.4	800	3×10^6	25	0	0	-	238
13					30	0	0	-	200
14					35	0	0	-	169
15					25	0	525	N_2	238
16	BWTN8				30	0	525	N_2	200
17					35	0	525	N_2	169
18	BWTN42-7				25	0.	272	H_e	238
19					30	0	272	H_e	200
20					25	5	0	-	238
21	BWTN42*				25	5-	525	N_2	200
22					30	5	0	-	200
23					30	5	525	N_2	275
24					30	5	484	N_2	331
25					30	5	484	N_2	238

N_{42} is lefthand roll nozzle blowing up

Table 3-2. Heat Transfer Runs at M = 7.4

RUN	CONFIG.	MACH	TUNNEL P_0 PSIA	R_e /FT	α Deg	β Deg	GAS	PLENUM P_0 PSIA	COMMENTS
36	BWTN$_1$	7.4	800	3×10^6	A	0	N$_2$	599	
37	BWTN$_4$	→	→	→	→	→	N$_2$	593	
38	BWTN$_{40}$						N$_2$	580	
39	BWTN$_f$						N$_2$	595	

Angle of Attack Schedule A

α	Jet
18	On
16	Off
26	Off
26	On
31	On
31	Off

Table 3-3. Force Runs at M = 7.4

Table 3-4 presents the force and oil flow supersonic test program performed at the Langley Unitary Plan Wind Tunnel (UPWT test number 1031) at Mach numbers from 2.5 to 4.0. Eighty two (82) force runs were obtained as were four (4) fluorescent oil flow runs. The primary runs for Mach number effect were made at a unit Reynolds number of 3×10^6/ft while Reynolds variation from 1×10^6 to 5×10^6/ft were obtained at a Mach number of 4.0. The effects of nozzle and vehicle geometry were tested at a Reynolds number of 1×10^6 because the lower tunnel pressure made it possible to test a larger range of nozzle static pressure ratio with the existing air supply. No gas is shown on Table 3-4 because all of the tests were made using dry air as the test gas. In addition to the force data, Schlieren photographs were taken at angles of attack of 20° for Mach 2.5 and 2.96 and at angles of attack of 25°, 30°, and 35° at Mach 4 on most data runs.

The test was made with natural transition. All data were corrected for balance and sting deflections due to aerodynamic loads. Flow angularity corrections were made from existing flow calibrations. No adjustment was made to axial force or drag data for cavity or base pressure.

The reference dimension values used as the constants in the data reduction equations to convert the measured forces and moments into aerodynamic coefficients are:

    a.   reference area $(A_{ref}) = 0.7245$ ft^2

    b.   longitudinal reference length $(c_{MAC}) = 0.6569$ ft

    c.   lateral-directional reference length $(b_{ref}) = 1.2596$ ft

    d.   cavity area $(A_{cavity}) = 0.03883$ ft^2

    e.   reference moment center
        I.   model station 15.951
        II.   model waterline 6.000

RUN	CONF.	M	R_e	α	β	P_{oj}	P_j/P_∞	COMMENTS
	BWTN$_1$	4.0	1 x 10^6/ft	12-35 DEG	0 DEG	0 PSIA	0	
1								
2						33	4.65	
3						188	2.5	
4						310	41.26	
5						310	41.26	
6						310	41.26	
7					+5	0	0	
8					-5	0	0	
9					-5	310	41.26	
10			3 x 10^6		-2.5	600	80	
11					-2.5	0	0	
12					0	100	4.65	
912		2.5	5 x 10^6	12-25		537	25.0	
13			3 x 10^6	0-20		0	0	
14						155	4.65	
15						0	0	
16					-5	187	2.1	
17					-5	187	2.1	
18		2.95			0	0	0	
19						0	0	
20					0	152	2.5	

Table 3-4. Langley UPWT Test Schedule

RUN	CONF.	M	R_e	α	β	P_{oj}	P_j/P_∞	COMMENTS
21	BWTN$_4$	4.0	3×10^6	12-35	0	0	0	
22						103	4.65	
23						559	25.0	
24			5×10^6	12-25		0	0	
25						178	4.65	
26			1×10^6	12-35		0	0	
27						37	4.65	
28						199	2.5	
29						328	41.26	
30						600	80	
631				27.5	−5	0-600	0-80	P_{oj} Sweep
31				12-35		0	0	
32						328	41.26	
33					−2.5	328	41.26	
34						0	0	
35	NO DATA	2.5	3×10^6	0-20	0	99	12.5	
36								
37						0	0	
38		2.95				198	2.10	
39						0	0	
40		2.5				151	2.5	
41	BWTN$_{40}$					0	0	
42						185	2.10	Left side Jet Down

Table 3-4. Langley UPWT Test Schedule (Cont'd)

RUN	CONF.	M	R_e	α	β	P_{oj}	P_j/P_∞	COMMENTS
43	BWTN$_{40}$	2.95	3×10^6	0-20	0	0	0	
44		4.		12-35		151	2.5	
45						0	0	
46			1×10^6			103	4.65	
47						559	25	
48						0	0	
49						37	4.65	
50			3×10^6			199	25	
51						328	41.65	
52						600	80	
53						99	12.5	
54	BWTN$_{41}$					0	0	
55						103	4.65	
56			1×10^6			559	25	
57						0	0	
58						37	4.65	
59						100	12.5	
60						199	25	
61						328	41.65	
62						600	80	
63		2.5	3×10^6	0-20		0	0	

Table 3-4. Langley UPWT Test Schedule (Cont'd)

RUN	CONF.	M	R_e	α	β	P_{oj}	P_j/P_∞	COMMENTS
64	$BWTN_{41}$	2.5 ↓ 2.5	3×10^6	0-20	0	185	2.1	
65						0	0	
66	BWN_{41}	→ 4.0	1×10^6	12-35		151	2.5	
67						0	0	TAIL OFF
68						37	4.65	
69						100	12.5	
70						199	25	
71						328	41.26	
72	BTN_{40}					600	80	
73						0	0	
74						37	4.65	
75						100	12.5	
76						199	25.0	WING OFF
77						328	41.26	
78						600	80	
79	BTN_1					328	41.26	
80						600	80	
81	$BWTN_4$				25	37	4.65	
82					30			
83					30			
84					25			
85						0-600	0-41.26	OIL FLOW

Table 3-4. Langley UPWT Test Schedule (Cont'd)

Figure 3-3 presented a diagram showing the location of the nozzles relative to both the model and balance centers. All data was run at zero control deflection on the control surfaces.

The data presented in this report will be body axis data. This was done to reduce the data manipulations required to obtain the incremental induced affects from the balance measurements.

3.1.3. DATA ACCURACY - Table 3-4 shows that a number of repeat data runs were obtained at the Langley UPWT for the basic configuration with no jet simulation. These repeat runs include the following conditions:

a. 4 runs at M = 4.0, Re = 1 x 10^6/ft
b. 4 runs at M = 4.0, Re = 3 x 10^6/ft
c. 2 runs at M = 4.0, Re = 5 x 10^6/ft
d. 4 runs at M = 2.95, Re = 3 x 10^6/ft
e. 4 runs at M = 2.5, Re = 3 x 10^6/ft
f. 2 runs at M = 4.0, Re = 1 x 10^6/ft, β = 2.5°
g. 2 runs at M = 4.0, Re = 1 x 10^6/ft, β = 5°

and these 22 runs were used to evaluate the data accuracy. A mean value of angle of attack and of all the aerodynamic coefficients was computed for each angle of attack within each of the 7 data sets given in a to g above. The difference between the mean values and the indivudual data points were then computed for the angle of attack and the six component aero data. The aerodynamic coefficient differences were then converted back into force and moment measurements to remove the tunnel dynamic pressure effect by multiplying them by the dynamic pressure for each run and the reference area and appropriate reference length. Assuming that angle of attack, Reynolds number, and Mach number have little effect on balance reading error, we now have a data collection of approximately 130 samples of reading error for each balance force and moment component. Axial force data was not presented because of its low priority in this test program. The root mean square value of each data set was computed and is shown below compared to the quoted balance accuracy of 1/2 percent of full scale and the most propable error is shown in the table on the following page. The most probable error is the value for which the probability of this error is 50%.

	Component	1/2% Full Scale	RMS	MPE = .67 (RMS)
a.	Normal Force	4 lb	1.127 lb	.76 lb
b.	Side Force	1 lb	.206 lb	.139 lb
c.	Pitching Moment	8 in lb	2.3 in lb	1.55 in lb
d.	Yawing Moment	2 in lb	.336 in lb	.266 in lb
e.	Rolling Moment	2 in lb	.566 in lb	.382 in lb

In order to work in coefficient form it is necessary to divide the most probable error by the test condition dynamic pressure and the model reference conditions. Thus in coefficient form the error is worst for the lowest dynamic pressure case which for this test was Mach 4.0, $R_e = 1 \times 10^6$/ft and the incremental errors are:

Component	Error
ΔC_N	.00725
ΔC_Y	.00135
ΔC_m	.025
ΔC_n	.00171
ΔC_ℓ	.00288

When thrust is not included in the balance loads, the errors in amplification take the form

$$\Delta K_M = \frac{2 \Delta C_B}{C_T \pm \Delta C_T} \qquad (3\text{-}1)$$

where

ΔK_M = error in force or moment amplification

ΔC_B = balance force or moment error

ΔC_T = thrust error due to pressure instrumentation

C_T = thrust force or moment coefficient

Figure 3-7 shows the error for the force and moment amplification factors as a function of nozzle supply pressure. These data are plotted against nozzle chamber pressure rather than thrust since it is easier to compare with the run schedule in this manner. The normal force amplification will have a large scatter at all pressures and would not be expected to be very good. In contrast the moment amplification factors should have reasonable scatter.

3.2 HEAT TRANSFER DATA SUMMARY

The space shuttle force model which was modified by fitting the silicone rubber OMS pod and nozzle inserts was tested at a nominal Mach number of 7.4 and a nominal Reynolds number per foot of 3.75×10^6. The angle of attack was varied from 25° to 35° and the yaw angle from 0° to 5°. Jet on and jet off conditions were simulated using both nitrogen and helium as the jet gases. A summary of the run schedule, the test conditions, the model attitude and the jet gas conditions are given in Table 3-5. The exact tunnel test conditions varied only slightly from the nominal values she :vn in that table.

3.2.1 HEAT TRANSFER TEST PROCEDURE

Prior to a run, the silicone rubber surface of the model was cleaned with a solvent and sprayed with a relatively thin coat of a selected (Tempilag®) temperature sensitive paint. The paint displays a phase change from an opaque solid to a colorless liquid at a known temperature. The paints used in this test changed phase from 169° F to 331° F. Uncertainties in the specified phase change temperature are estimated by the manufacturer to be one percent. The OMS pod and nozzle inserts surface phase change progression during each run was continuously photographed by a 35 mm camera mounted in the test chamber. Online monitoring of the progression of the phase change was done through a closed circuit video system. The 35 mm camera was operated at about 10 frames per second and fluorescent light illuminated the model. The camera was started a few seconds before the beginning of the injection cycle and remained on until the model was retracted from the airstream. The model initial temperature was measured using a thermocouple embedded into the rubber part of the model. After a run, the model was removed, residual paint washed off with a solvent and re-painted for another run.

The data reduction of the phase change paint technique assumes that the surface temperature of the rubber model is equivalent to the heating of a semi-infinite slab with a backface temperature that remains constant during the test event. Assuming that the silicone rubber material thermophysical properties are invariant with temperature the heat conduction solution is

$$\frac{\partial T}{\partial t} = \frac{k}{\rho_m} \frac{\partial^2 T}{\partial y^2} \tag{3-2}$$

Using the following boundary conditions

$$T(y, 0) = T_i$$

$$T(\infty, t) = T_i$$

$$\frac{\partial T(0, t)}{\partial y} = \frac{h}{k}\left[T_{aw} - T(0, t) \right]$$

(3-3)

Assuming that the surface is subject to an instantaneous and constant heat transfer coefficient a closed form solution is obtained (reference 17).

$$\frac{T_w - T_i}{T_{aw} - T_i} = 1 - e^{\omega^2} \, \text{erfc} \, \omega$$

(3-4)

where $$\omega = (h\sqrt{t})\sqrt{\tfrac{\rho_m}{k}}$$

At melting, the surface temperature is assumed to be the same as the phase change temperature or $T_w = T_{pc}$. To facilitate data reduction, the tunnel stagnation temperature, T_s, was used instead of the adiabatic wall temperature, T_{aw}. Then the value of the heat transfer coefficient, h, will be independent of the local flow properties. The general solution assumes that there is no error introduced from wall curvature, that the model is isothermal before injection, no radiation from the lights and no temperature distortion from the metallic part of the model. The thermophysical properties of the silicone rubber material used in this test are

$$\rho_m = 92.2 \text{ lbm/ft}^3$$

$$c = 0.304 \text{ Btu/lbm-}°F$$

$$k = 6.25 \times 10^{-5} \text{ Btu/sec-ft-}°F$$

The phase change paint patterns or isotherms, photo-recorded on 35 mm films at discrete time intervals were projected on a table for tracing. Selected isotherms were traced and the heat transfer coefficients computed by the method presented above. These coefficients were then ratioed to the theoretical heat transfer coefficients at the stagnation point on a scaled one-foot radius sphere using the Fay and Riddell equation in the following form (reference 16).

$$h_{r=1'} = \frac{0.94}{\sqrt{r}} \quad c_p (\rho_w \mu_w)^{0.1} (\rho_s \mu_s)^{0.4} \left[2RT_s (1-P_\infty/P_s) \right]^{0.25} \tag{3-5}$$

Since the model scale is 1.5%, r=0.015 ft for this test. The heat transfer coefficients computed for the scaled sphere are also presented in Table 3-5.

3.2.2 HEAT TRANSFER DATA ANALYSIS

Typical heat transfer distributions presented as isotherms over the pod, obtained from the phase change paint test data are shown in Figure 3-8 and for comparison Figure 3-9 shows oil flow pictures of a nearly similar condition. Indicated for the jets off condition are the high heating regions over the pod from wing induced vortex reattachment. With the yaw RCS thrusters operating, the flow over the pod becomes separated over a sizable region ahead of the jet. The average heating over the separated region was reduced due to the wing vortex lift-off caused by interaction. However, the plotted data show that the peak heating value produced by the jet will still remain high when compared to the case without interaction.

Figure 3-10 shows the effect of increasing angle of attack in causing the interaction heating to become more symmetric around the centerline of nozzles while Figure 3-11 shows the effects at 5 degrees windward yaw.

A summary of the heat transfer test results with and without jet-stream interactions using nitrogen as a jet gas is shown in Figure 3-12 and 3-13. The data are plotted at $\alpha=30°$ which is the angle of attack used for the major part of the entry trajectory. Also shown is the angle of yaw effect, where a yaw angle of $\beta=-5°$ will essentially double the heating rate from a nominal $\beta=0°$. Figure 3-12 indicates that around the pod, without jet interaction, the heating level would be about 6 times that of the laminar flat plate value at $\beta=0°$ assuming a boundary layer length originating from the orbiter nose. The data with jet-stream interaction show peak heating values higher than without interaction even though, as noted in the isotherm data, the wing vortex is displaced.

Using the correlation obtained from the experimental data of the RCS jet-interaction test at AEDC Tunnel B presented in Section 2.2.2, peak heat transfer value and the location over the model were computed. Fairly good prediction is shown for the peak location while excellent correlation is obtained for the peak heating value, when local heating without interaction is assumed to be that of the laminar flat plate value. It is noted that the peak heating values were obtained by extrapolation of the paint data and that faired curves are similar in shape to those shown in Section 2.2.2 both for the centerline and off centerline distributions.

Table 3-5. Heat Transfer Test Conditions

3.3 FORCE DATA SUMMARY

Table 3-3 and 3-4 summarized the force data runs which were obtained at NASA-ARC and NASA-LRC respectively and this section will briefly show some representative data which was obtained. Complete force and moment coefficients are shown to illustrate the magnitudes of the changes caused by the RCS jets relative to the total vehicle aerodynamic coefficients. Interference data which is computed as the difference between jet on and off data are also presented. Reference 1 presents the force data in greater detail. The analysis of this data will be presented in Section 4.

The balance measurements with the jet on included the basic vehicle aerodynamics plus the induced load from jet interference. The definition of amplification factor is:

$$K_M = \frac{\Delta C_{M_i}}{C_{M_T}} + 1 \tag{3-6}$$

where
$$K_M = \text{force or moment amplification factor}$$

$$\Delta C_{M_i} = \text{incremental force or moment coefficient induced on vehicle by jet}$$

$$C_{M_T} = \text{jet force or moment coefficient}$$

The incremental induced effects was computed from the difference between the jet-on and off data.

$$\Delta C_{M_i} = C_{M_j} - C_{M_o} \tag{3-7}$$

where
$$C_{M_j} = \text{measured force or moment coefficient with jet on}$$

$$C_{M_o} = \text{measured force or moment coefficient with jet off}$$

Because the incremental values can be very small and thus sensitive to data scatter, the mean values of the jet-off coefficient data were used as the best estimates of the Langley data at its mean value of angle of attack and this corrected for the angle of attack difference from the mean to the jet on case.

$$\Delta C_{M_1} = C_{M_j} - \left[\overline{C}_{M_o} + \frac{d\overline{C}_M}{d\bar{\alpha}} \left(\alpha_j - \bar{\alpha}_o \right) \right] \qquad (3\text{-}8)$$

where

$\overline{C}_{M_o}$ = mean value of jet off force or moment coefficient

$\bar{\alpha}_o$ = mean value of jet off angle of attack

α_j = jet on angle of attack

$\dfrac{d\overline{C}_M}{d\bar{\alpha}}$ = slope of $\overline{C}_{M_o}$ at $\bar{\alpha}_o$

The slope $\left(\dfrac{d\overline{C}_M}{d\bar{\alpha}} \right)$ of coefficient was obtained by curve fitting the mean value data of all six force and moment coefficients versus mean angle of attack with 3 point curve fit equation.

$$\overline{C}_{M_o} = A_1 + A_2 \,\bar{\alpha} + A_3 \,\bar{\alpha}^{\,2} \qquad (3\text{-}9)$$

and computing the slope at the $\bar{\alpha}$ for the mid point

$$\frac{d\overline{C}_{M_o}}{d\bar{\alpha}} = 2\,A_3 \,\bar{\alpha} + A_2 \qquad (3\text{-}10)$$

of the interval. No such corrections were made of the Mach 7.4 data because of the limited data.

The thrust force and moment coefficients were computed at each jet on data point using the thrust equation (3-11).

$$T = A_T P_{oj} \sqrt{\frac{2\gamma^2}{\gamma-1}\left(\frac{2}{\gamma+1}\right)^{\frac{\gamma+1}{\gamma-1}}\left(1-\left(\frac{P_j}{P_{oj}}\right)^{\frac{\gamma-1}{\gamma}}\right)} + A_E\left(P_j - P_\infty\right) \qquad (3-11)$$

where

T = thrust ~ lb

A_T = nozzle throat area ~ in^2

A_E = nozzle exit area ~ in^2

γ = exhaust gas ratio of specific heats

P_∞ = ambient pressure ~ psia

P_j = nozzle exit pressure ~ psia

P_{oj} = nozzle chamber pressure ~ psia

The nozzle throat area was computed from the nozzle calibration data, the exit area was computed from calibration data throat area and design expansion ratio, the nozzle exit pressure (P_j) was computed from chamber pressure (P_{oj}) and design expansion angle, P_∞ was assumed to be tunnel ambient pressure and was recorded for each data point, and P_{oj} nozzle chamber pressure which was recorded for each data point. Thus point to point variation in thrust due to supply pressure and tunnel operation should be accounted for in the thrust force and moment coefficients and in amplification factor presented in this section.

3.3.1 BASIC CONFIGURATION DATA - Figure 3-14 presents the effect of Mach number on the vehicle aerodynamics without RCS operation as a function of angle of attack. The normal force data Figure 3-14a and the axial force data Figure 3-14c show typical decreases in force data with increasing Mach number at constant angle of attack while the pitching moment Figure 3-14b shows an increasingly nose up moment illustrating the increasing importance of nose and leading edge bluntness effects and decreasing leeward surface negative pressures at higher Mach numbers.

3.3.2 YAW JET DATA - The yaw thrusters are fired on one side at a time for yaw control. As shown in Figure 1-3 the yaw engines fire over the trailing edge of the wing in a spanwise direction. The left side yaw engines were the only engines simulated in these tests, thus, the engine thrust will cause a positive side force and a negative yawing moment. Figure 3-15 presents a representative sample of the force data obtained with yaw jet on data obtained at Mach 4.0 with a range of supply pressures from 35 psia to 600 psia. This data shows that the yaw jet induced no significant change in normal force and axial force. There is, however a definite increase in nose up pitching moment with increasing chamber pressure. The lateral directional data Figure 3-15d shows that the left yaw jet acts principally to induce a left wing down roll particularly at angles of attack above 20°. There appears to be no yawing moment induced and a slight increase in side force noticed at the highest chamber pressure.

Figures 3-16 and 3-17 present the incremental force and moment data as well as the side force and yawing moment amplification factors at the scaled flight conditions where freestream nozzle momentum ratio and exit pressure ratio were matched. The incremental yawing moment data of Figure 3-17 shows very little scatter around zero and the amplification factor lies between .9 and 1.0 indicating very little adverse interference. The incremental side force data of Figure 3-16 in contrast shows more scatter as predicted in the error analysis, with Mach 4.0 data consistently higher. This is interpreted as the result of the reading errors since the nozzle pressure at Mach 4.0 was only 100 psia for matching and a probable error ΔK_y, of .4 was estimated (Figure 3-7). Figure 3-18 shows the close agreement between the Mach 4.0 and Mach 7.4 data when compared on a pressure ratio match only. Figure 3-19 shows that there may be a slight pressure ratio effect on yaw amplification but no discernable Reynolds number effect over the range from 1×10^6/ft to 5×10^6/ft at Mach 4.0. The effect of yaw angle from +5° to 15° is shown on Figure 2-20 where positive yaw shows a slight gain in yaw amplification. Figure 3-21 shows that jet supply pressure effects are negligible on yaw amplification. Figure 3-22 shows more clearly the pitch up and roll induced on the vehicle. Figure 3-23 shows that the yaw jet plumes are apparently bent over to impinge on the wing.

3.3.3 ROLL JET DATA - Roll control simulations were performed for positive roll (right wing down) with the nozzles on the left side exhausting down toward the wing while the right side nozzles exhausted up past the vertical fin. In this way a roll couple was to be generated without any other forces or moments. Figure 3-24 presents a sample of the data obtained with roll jets off and a comparison of the effects of nozzle chamber pressure on vehicle aerodynamic characteristics at Mach 4.0. The normal force shows a slight reduction as the chamber pressure is increased while the pitching moment shows a large nose up pitching moment is

generated sufficient in size to counteract the basic configuration moment and trim the vehicle at 15° angle of attack for the highest chamber pressure tested. The axial force which includes base pressure decreases with increasing nozzle chamber pressure to about 50% at the highest pressure tested. The lateral-directional data does appear to show a strong angle of attack influence on the changes induced by chamber pressure with the induced effects being strongest at the lowest angle of attack. Positive roll jets operation induces a negative rolling moment on the vehicle which opposes the control, a nose right yawing moment, and a side force to the left.

The incremental rolling moment data at scaled flight conditions (Figure 3-25) shows that the right wing down roll jets induce a left wing down rolling moment on the vehicle. The net result is a decreasing amplification factor with increasing angle of attack with complete cancellation (K_ℓ=0) at about 20 degrees angle of attack and roll reversal at angles above this. Figure 3-26 shows good agreement between Mach 4 and Mach 7.4 amplification factor data at the same nominal pressure ratio indicating small Mach number affects except at the highest angle of attack. Figure 3-27 shows a strong effect of supply pressure (and thus momentum ratio) at lower angles of attack with an abrupt reduction the incremental rolling moment at angles above 25°.

The effect of operating the two sides of the roll control separately is shown in Figures 3-28 and 3-29. The plume interference with vertical fin flow is strongly dependent on angle of attack (Figure 3-29) decreasing as the body shields the fin from the flow. In contrast the data of Figure 3-28 shows that the induced roll from the plume interaction with the wing flow is essentially independent of angle of attack and is of sufficient magnitude to completely cancel or reverse the control input. Figure 3-30 shows oil flow visualizations of the interaction of the plumes with the wing and vertical fin. Note the difference in flow in the wing in views a and b in particular.

The induced effects shown in Figure 3-24 are shown in incremental form in Figure 3-31. The roll jets induce a small reduction in normal force, a sizeable nose up pitching moment, and a large reduction in axial force which must all be due to the plume/wing flow interaction. At the same time the plume/fin interaction produces a large favorable yaw at moderate angles of attack. The induced side force, and yawing moment appear to be sensitive to angle of attack while, axial force and pitching moment are most sensitive to nozzle pressure and largely independent of angle of attack.

In summary, the test results show that the roll control thrusters induced large counteracting loads on the vehicle at all Mach numbers which result in very low control effectiveness and even reversal. The problem was shown to be largely due to the plume interaction with the wing flow.

3.3.4 <u>NOSE DOWN PITCH DATA</u> - The pitch jet effect data were obtained using the pitch jet on one side only on the assumption that the cross feed effect are small. More recent Rockwell data has indicated that the effects are small but significant in terms of reducing amplification on the nose-down pitch jets as the plumes impinge on the body flap and feed across the base of the vehicle. The single side data does indicate the trends and cross feed is a secondary effect.

Figures 3-32 to 3-35 present a summary of the nose down pitch data obtained in these tests with Figure 3-33 showing that a pitch reversal was experienced at all Mach numbers tested in this program at scaled flight conditions. Figure 3-34 shows a large variation in the incremental pitching moment as a function of supply pressure but a zero amplification at all pressures. This curve clearly indicates that momentum ratio is the primary parameter controlling pitch control interaction. Assuming symmetric firing of pitch nozzles, the only other induced force should be an axial force which is shown in Figure 3-35. This figure shows the same sensitivity of axial force to supply pressure seen in Figure 3-31 indicating again it is the plume down onto wing and body flap which is the primary problem of the roll control.

3.3.5 <u>NOSE UP PITCH DATA</u> - Figures 3-36 and 3-37 present data for the nose up pitch jets firing past the fin, again tested with one side firing only. The data show some scatter at higher angles of attack on Figure 3-37 but increasing supply pressure brings the data closer to an amplification of 1. The accuracy of the data improves at higher supply pressure and the interpretation of the data is that no appreciable pitch interference is experienced for these jets.

Figure 3-1.   Langley UPWT Installation

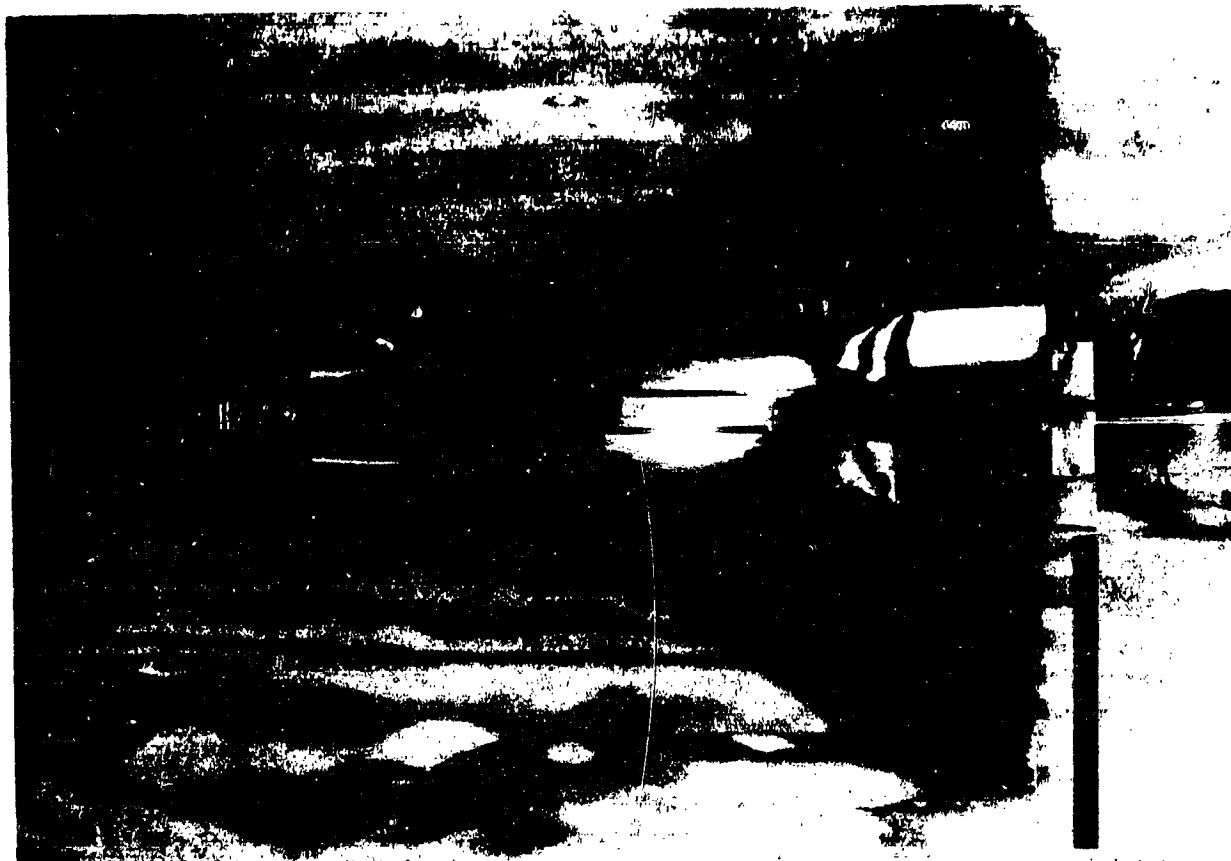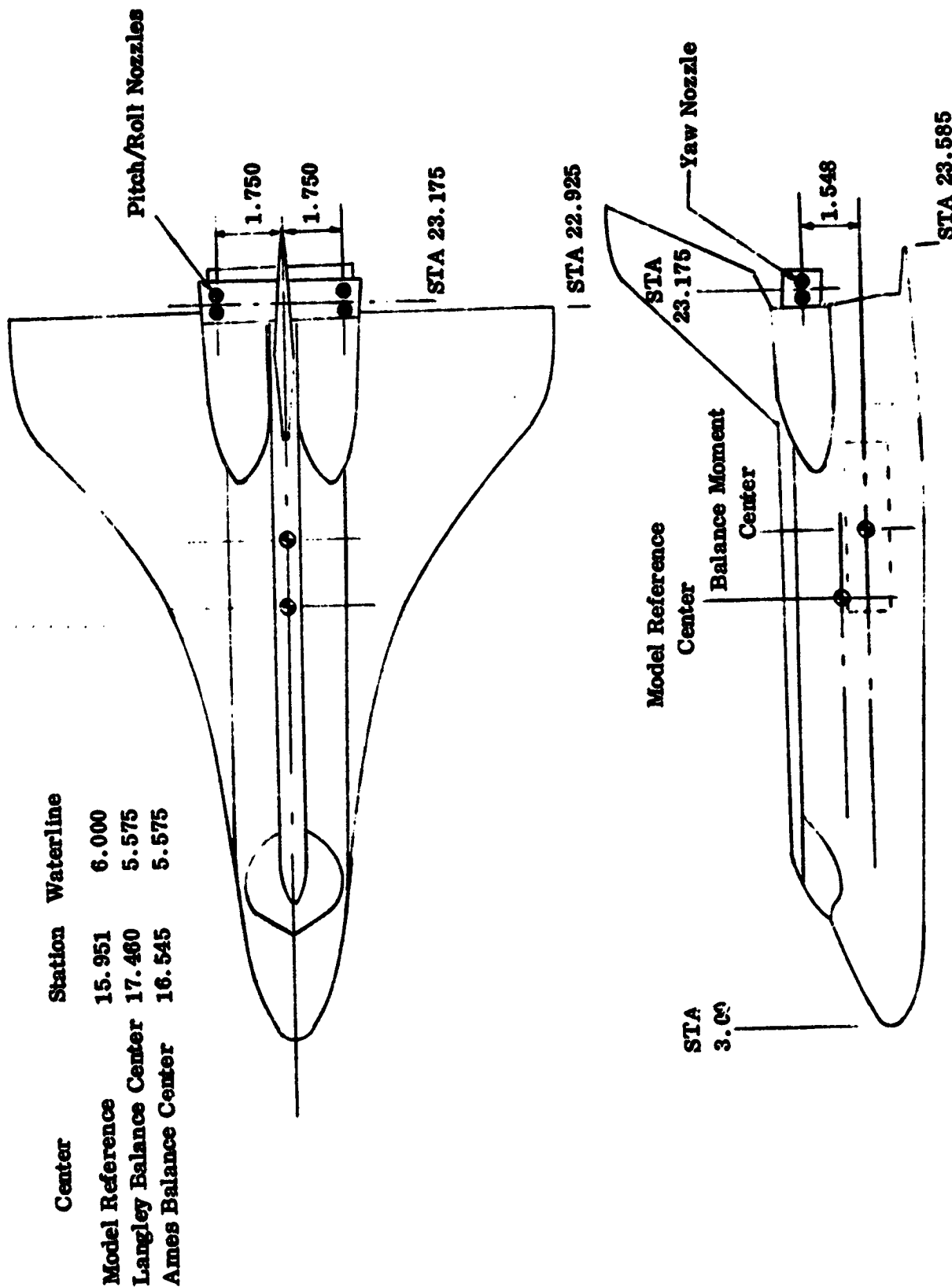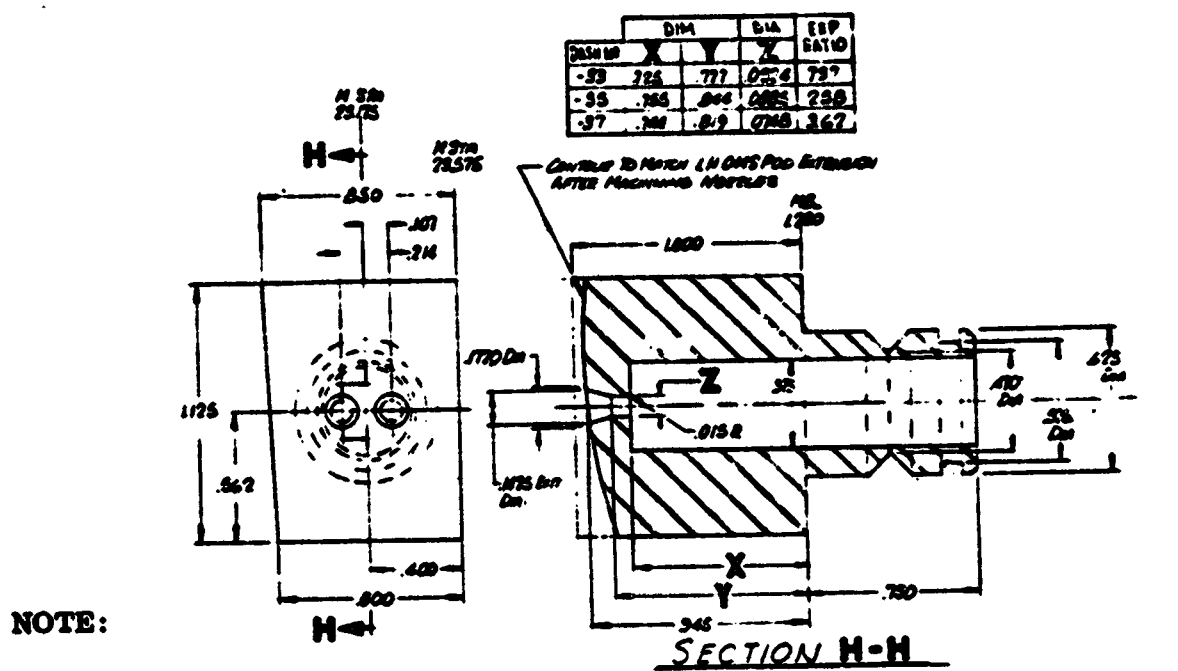Figure 3-2. MODEL WITH RTV OMS POD

Center	Station	Waterline
Model Reference	15.951	6.000
Langley Balance Center	17.460	5.575
Ames Balance Center	16.545	5.575

Figure 3-3. Nozzle Location and Moment Transfer Diagram

DASH NO	DIM X	Y	DIA Z	EXP RATIO
-33	.226	.717	.0354	737
-35	.186	.846	.0585	238
-37	.141	.819	.0748	367

SECTION H·H

NOTE:

1. Code Number N_1 = S.N. -33
2. Code Number N_2 = S.N. -35
3. Code Number N_3 = S.N. -37
4. Code Number N_5 = S.N. -39

-39

SECTION J·J

Figure 3-4. Yaw Nozzles

NOTE:

N_4 = Both nozzles in roll

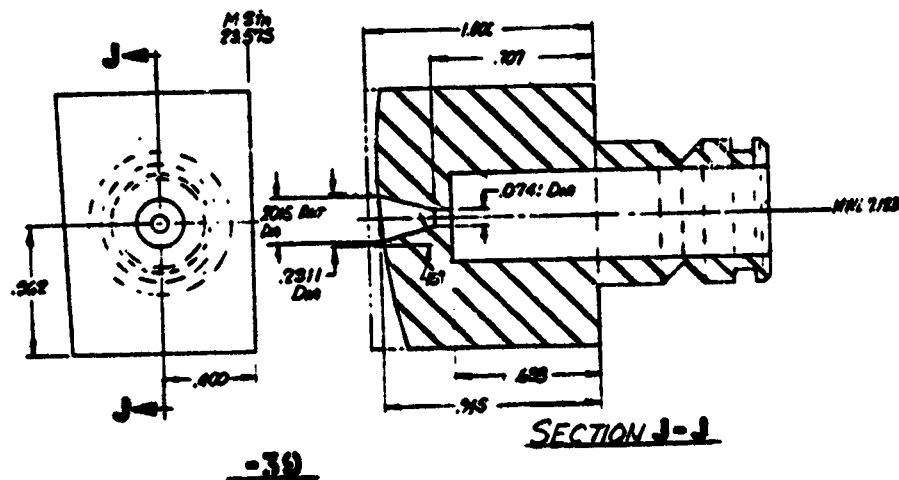N_{40} = -29 Nozzle only

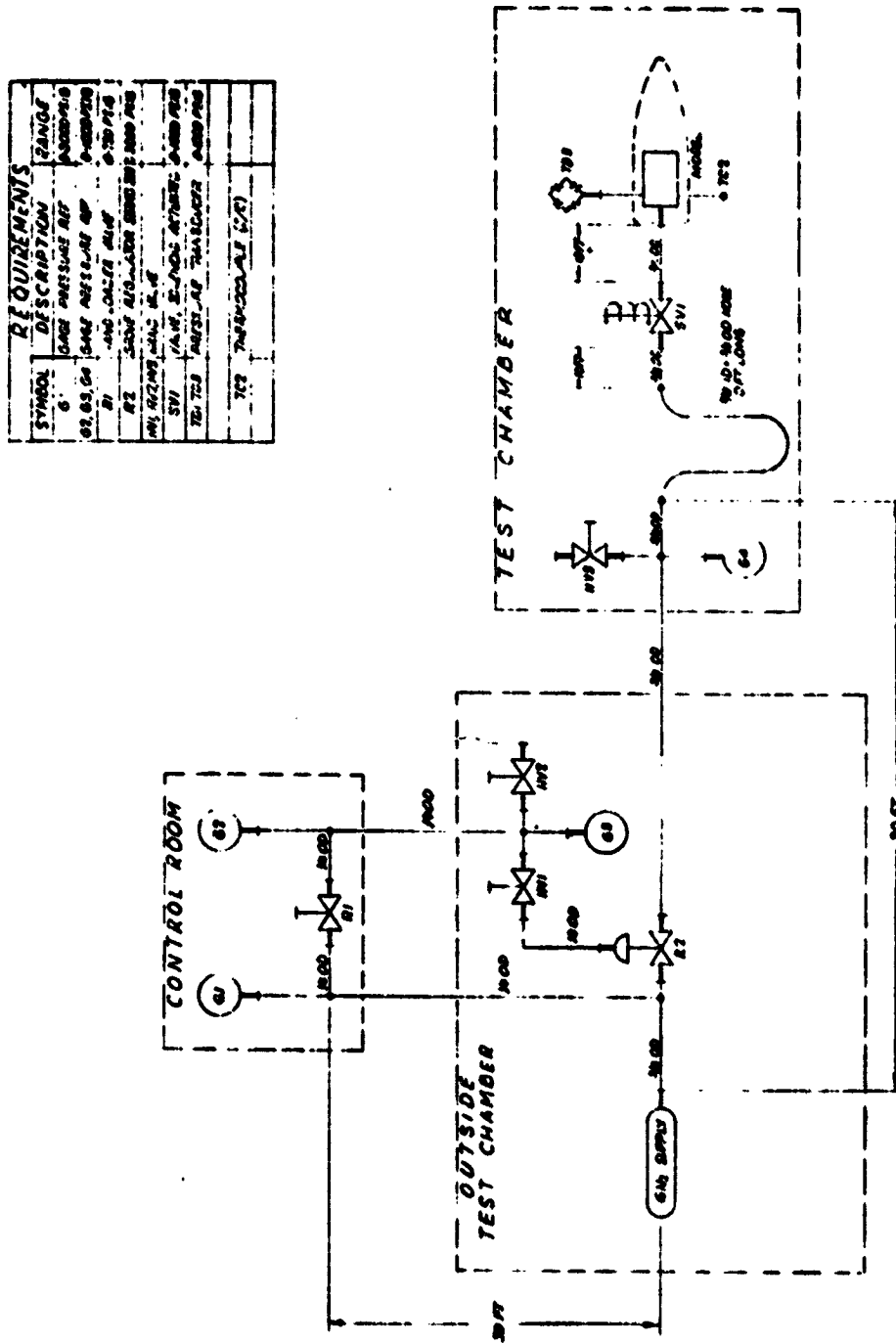N_{41} = -31 nozzle only

Figure 3-5. Pitch and Roll Nozzles
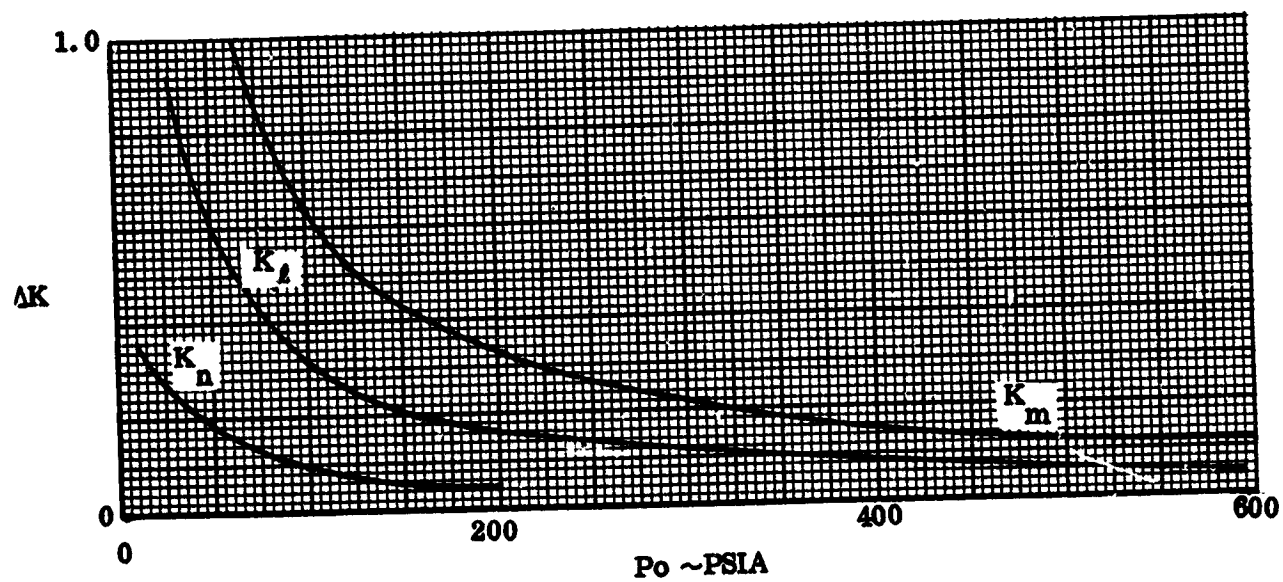
Figure 3-6. Schematic Diagram of High Pressure Gas Supply and Control
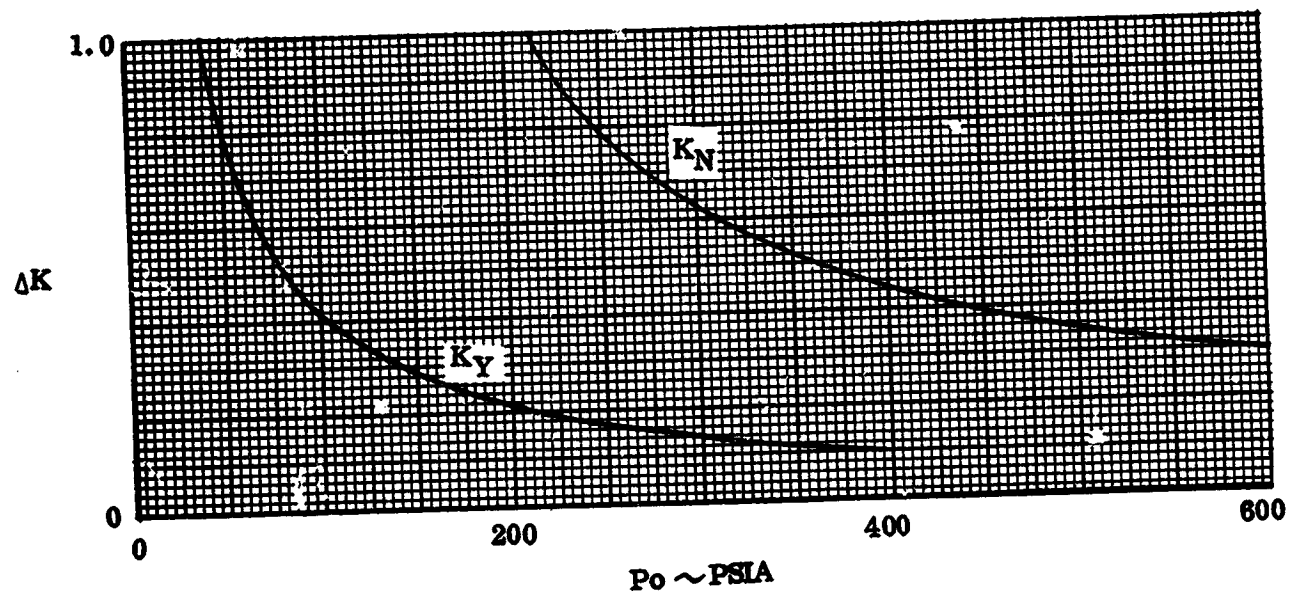
Figure 3-7. Most Probable Error in Amplification Factor
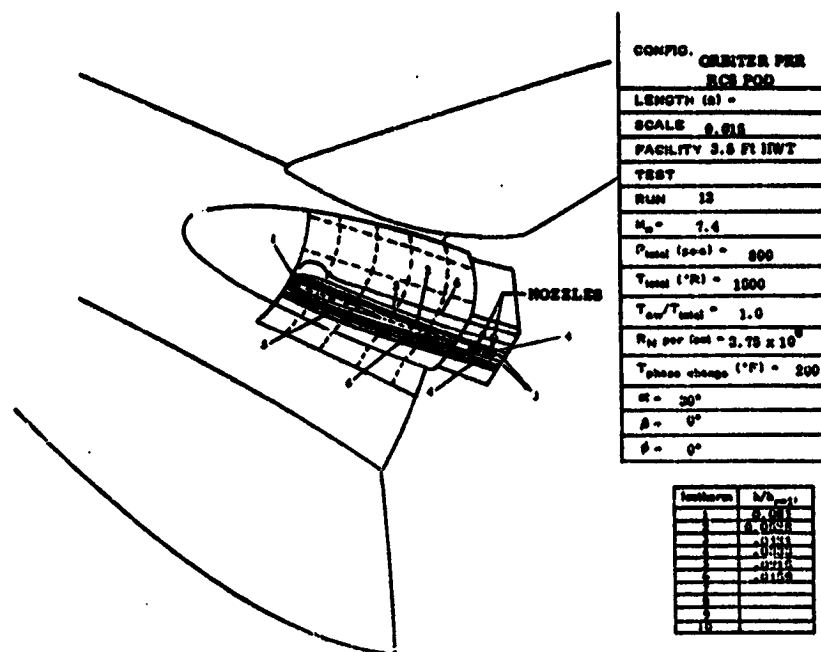
a) Jets Off.
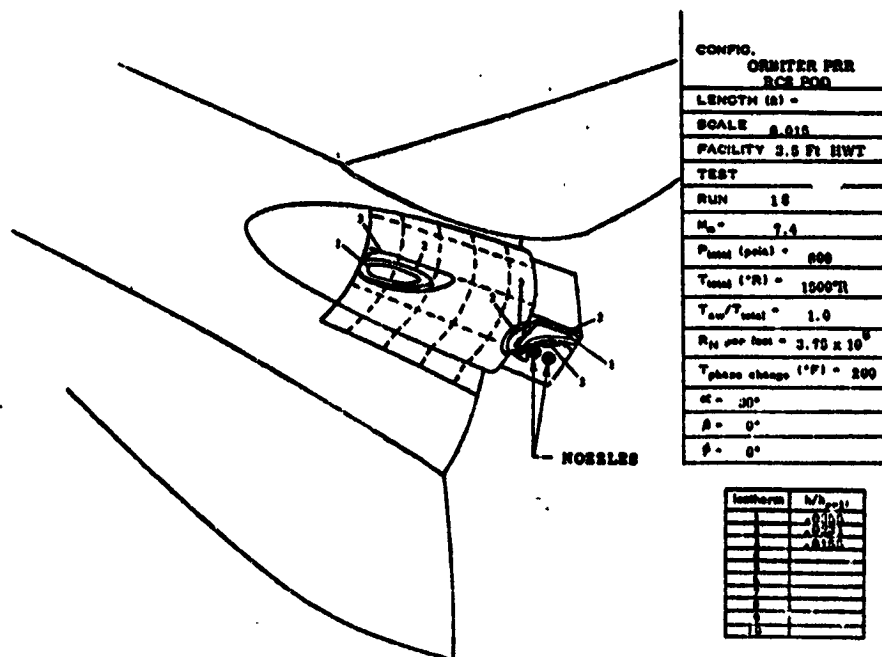
b) Jets on

Figure 3-8. Typical Phase-Change Paint Heat Transfer Data
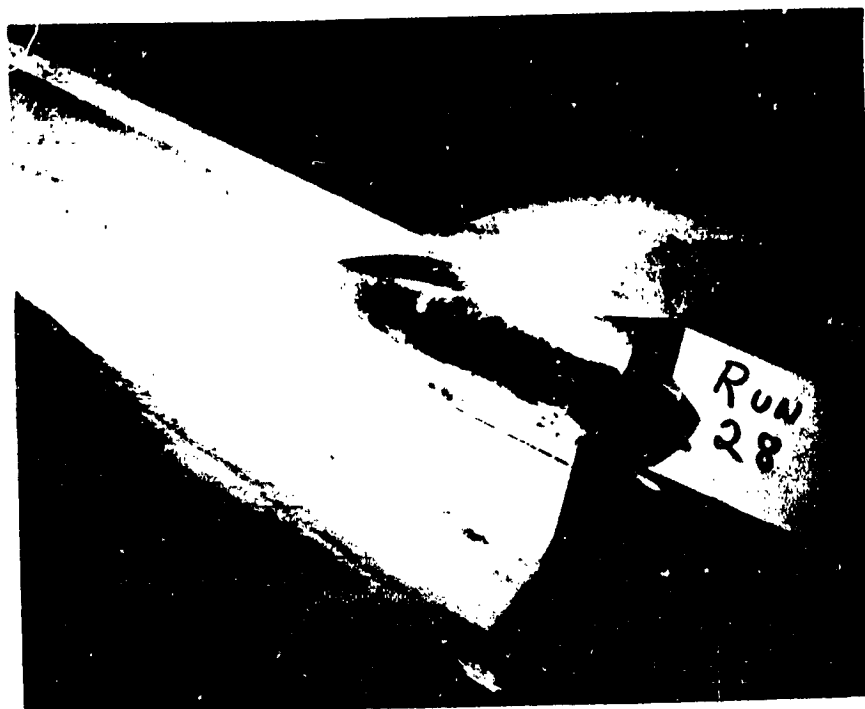
a)   Jet Off

b)   Jet On

Figure 3-9. Oil Flow Visualization; Effect of Yaw Jet Operation; $\alpha=25°$, $P_{oj} = 512$
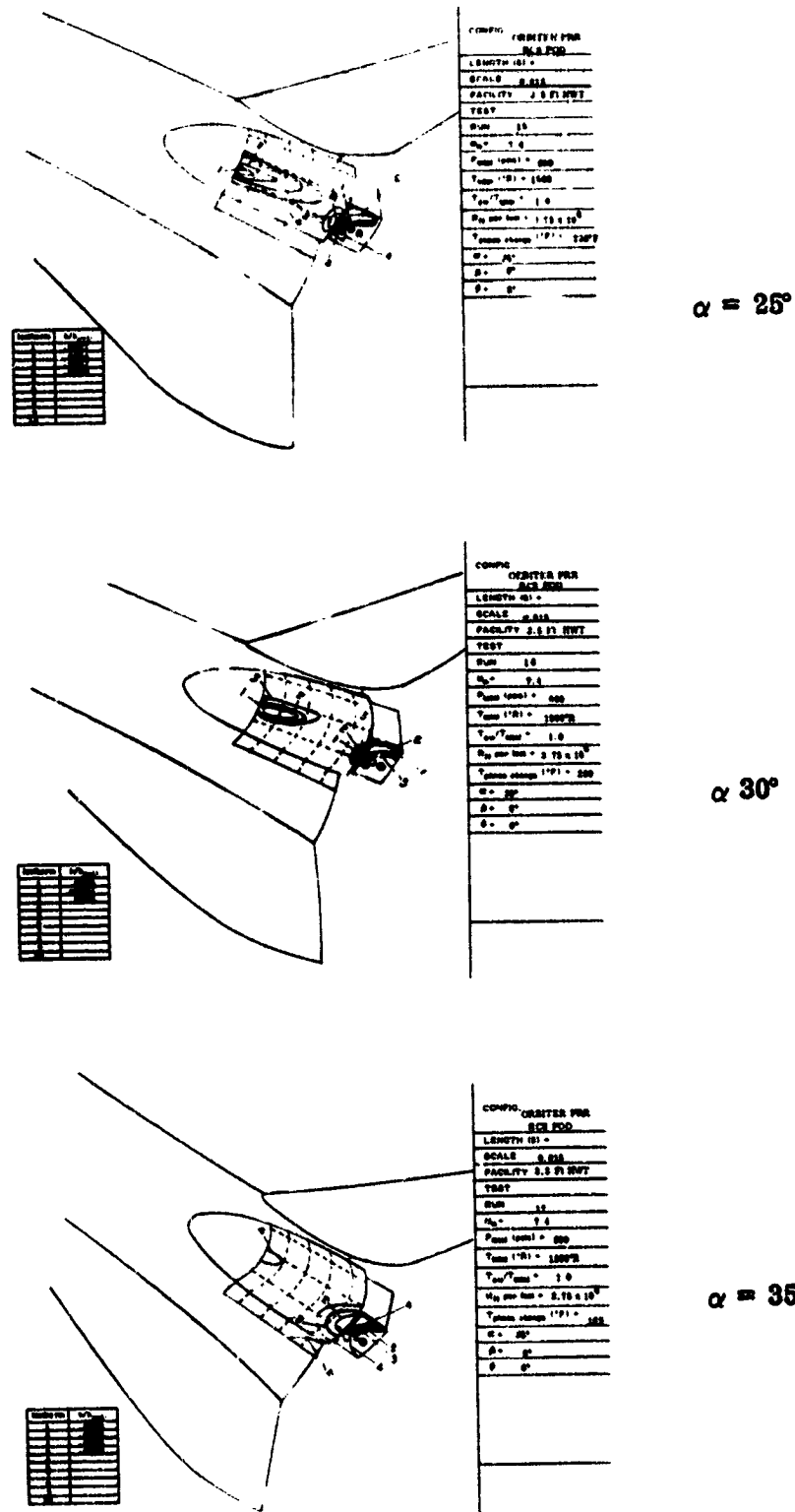
Figure 3-10. Effect of Angle of Attack on Pod Heating
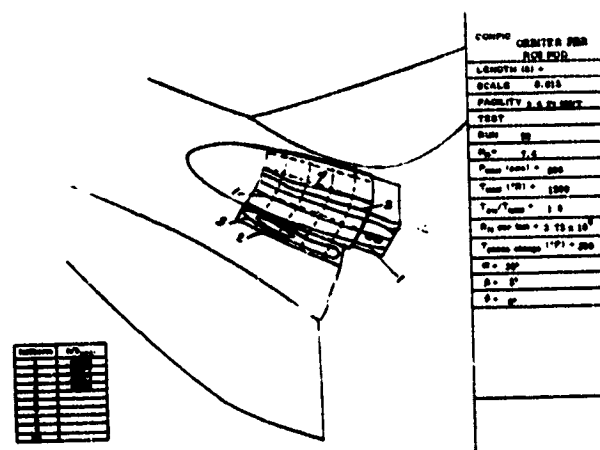
JET OFF
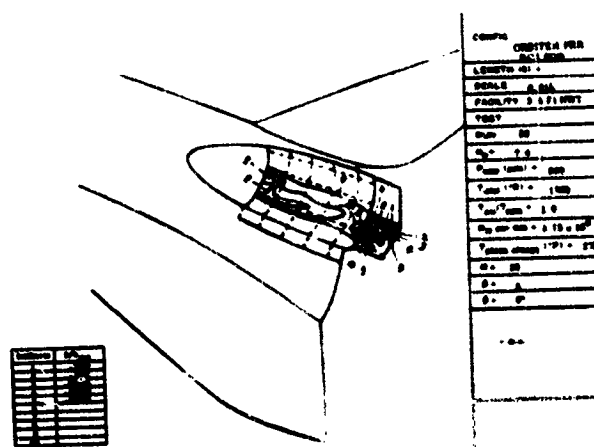
JET ON

$\alpha = 30°$

$\beta = -5°$

Figure 3-11. Effect of Jet on 1° Windward Yaw Pod Heating
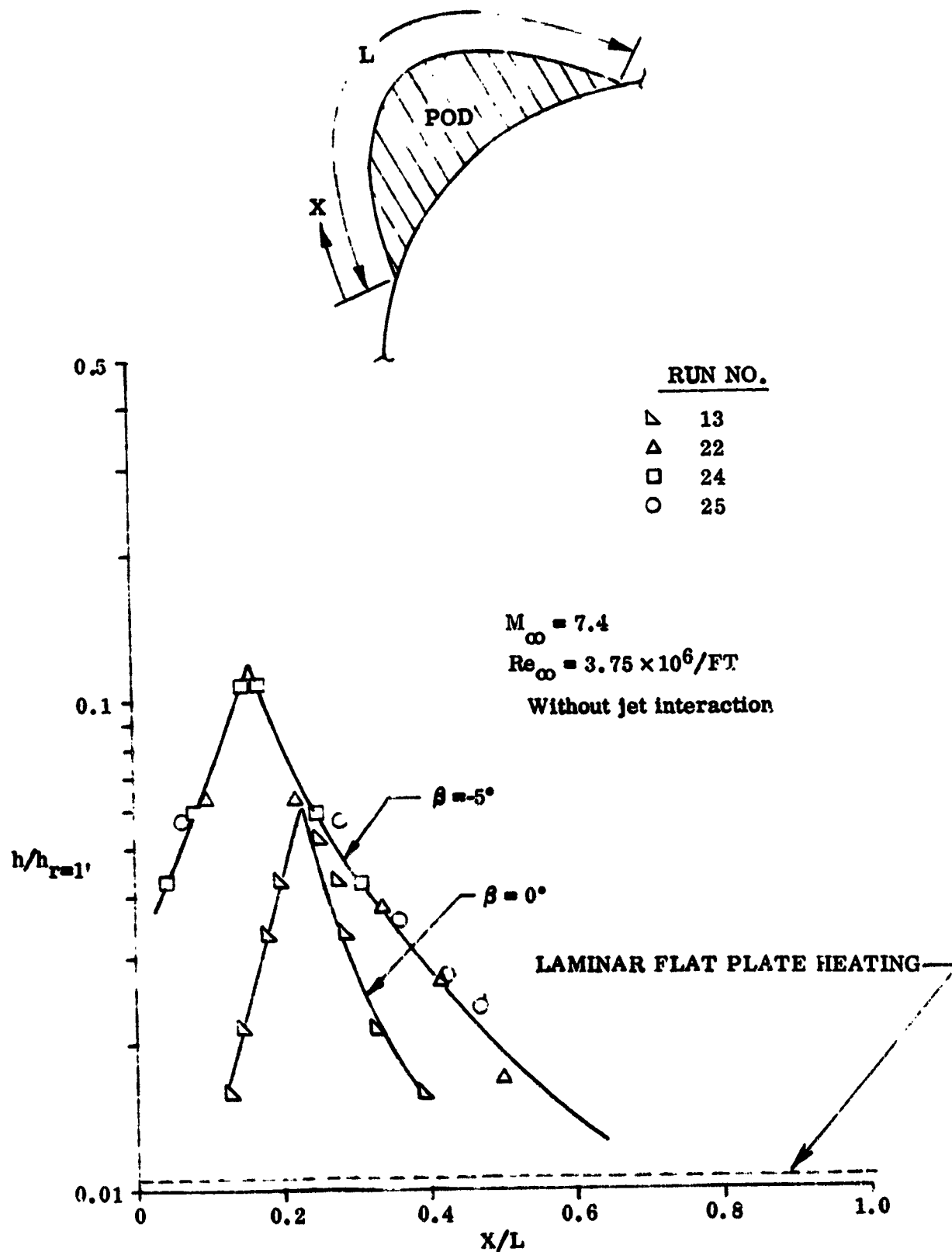
Figure 3-12. Heat Transfer Distribution Around Pod Just Ahead of Yaw RCS Jets at $\alpha = 30°$
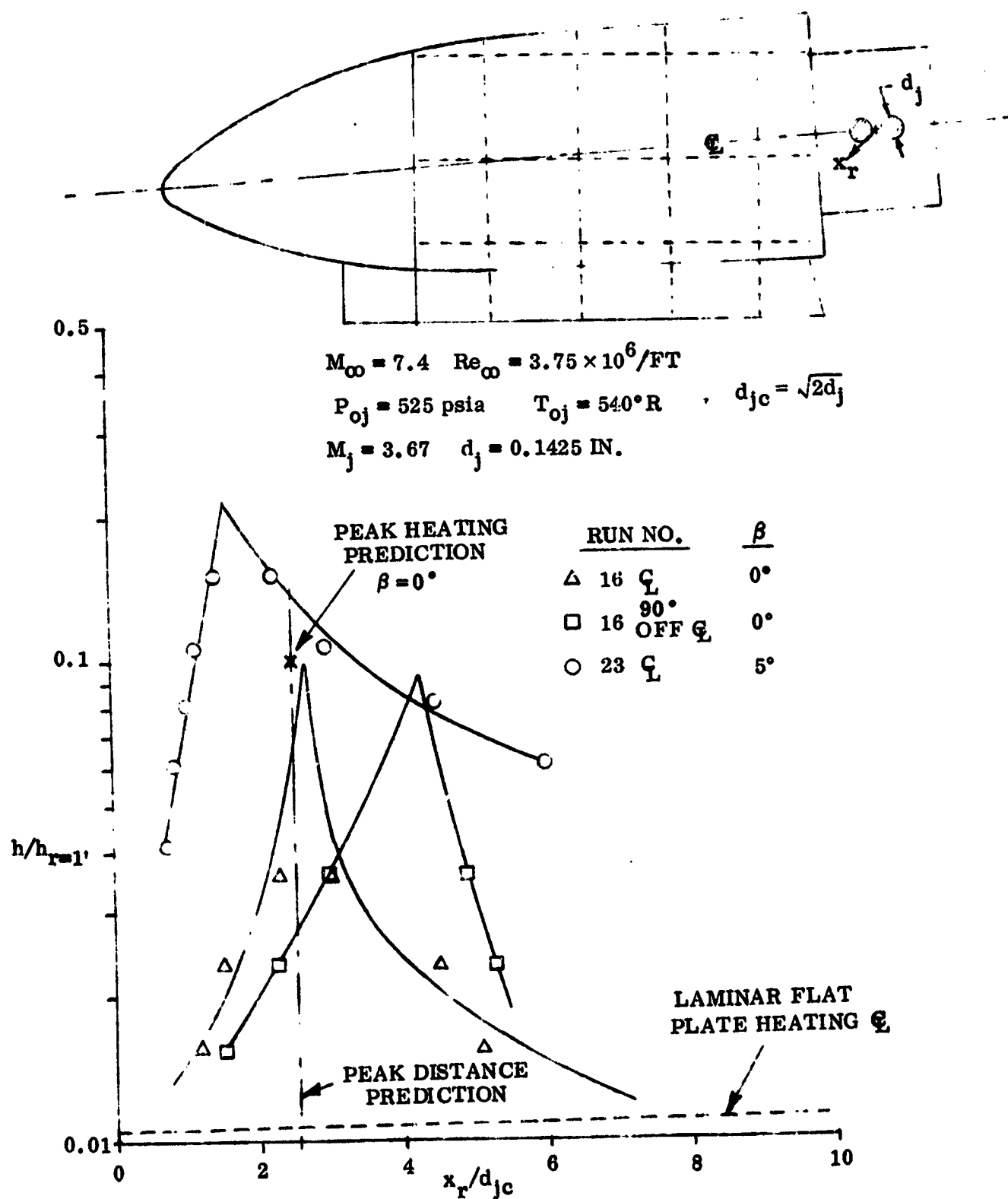
Figure 3-13. Heat Transfer Distribution Along the Yaw RCS Jets at $\alpha = 30°$

a) Normal Force

Figure 3-14.   .   Effect of Mach Number - Jet Off

Angle of Attack ∽ Deg
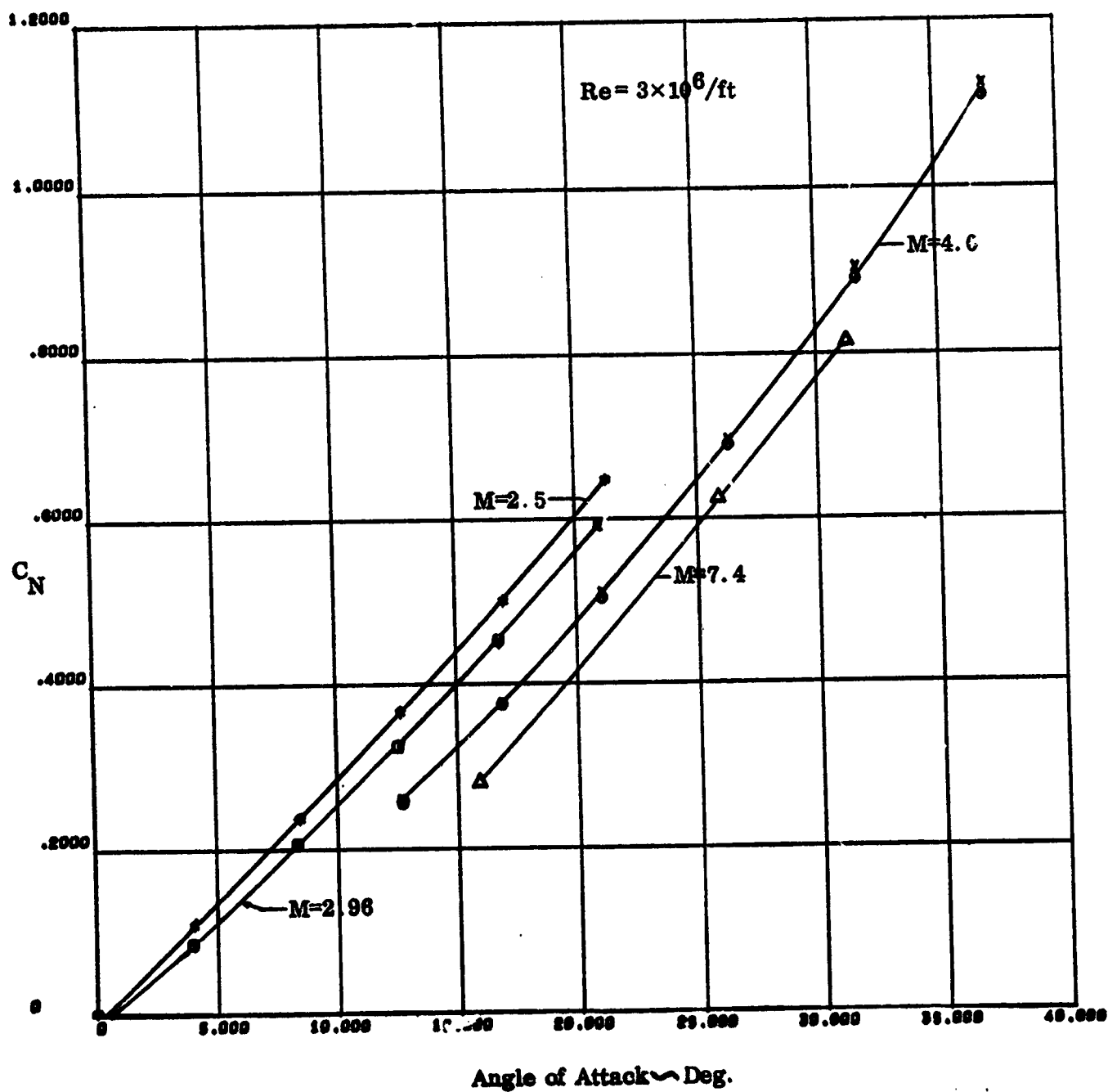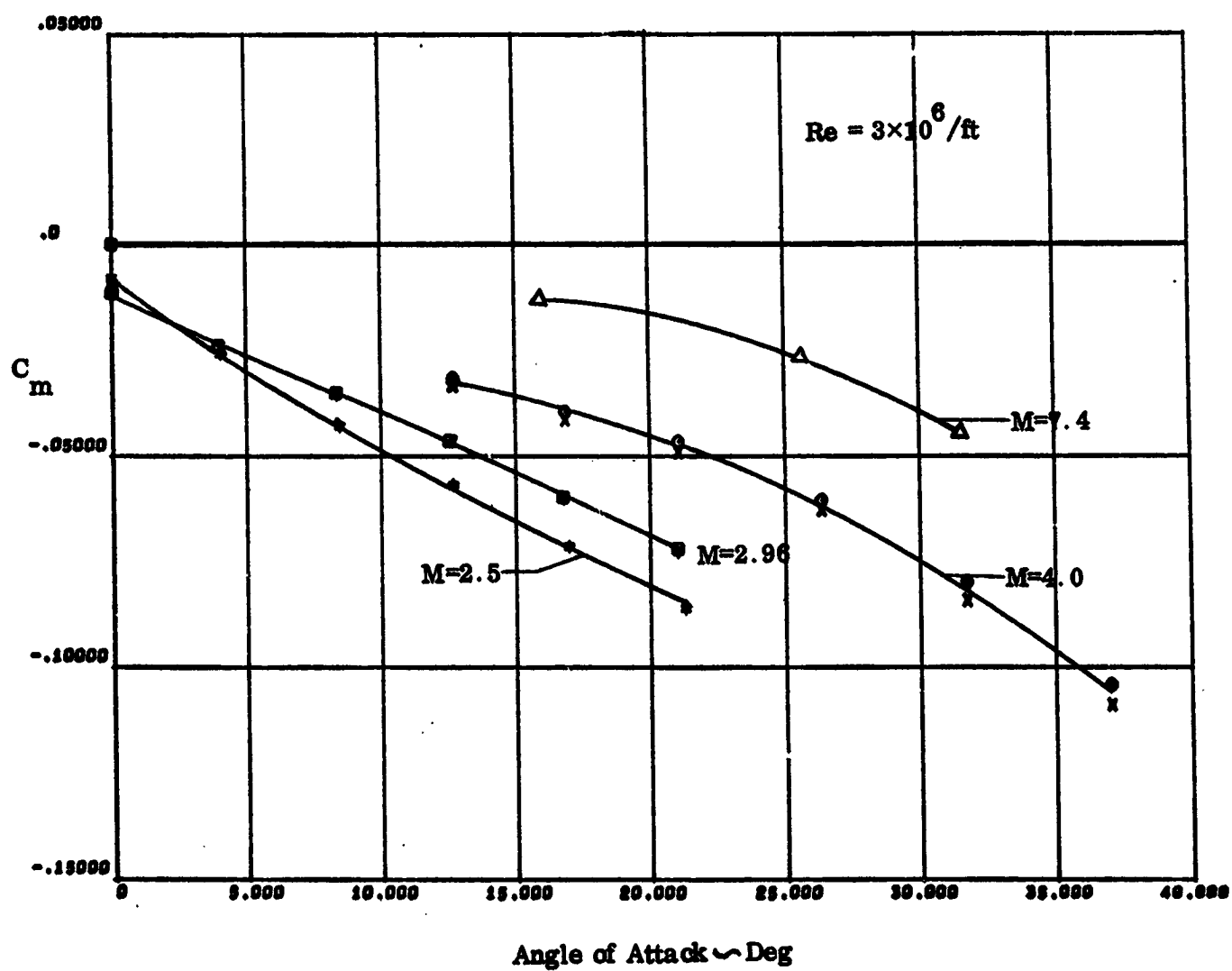
b) Pitching Moment

Figure 3-14. Effect of Mach Number - Jet Off

Angle of Attack—Deg

c) Axial Force

Figure 3-14.   Effect of Mach Number - Jet Off

Angle of Attack∾Deg
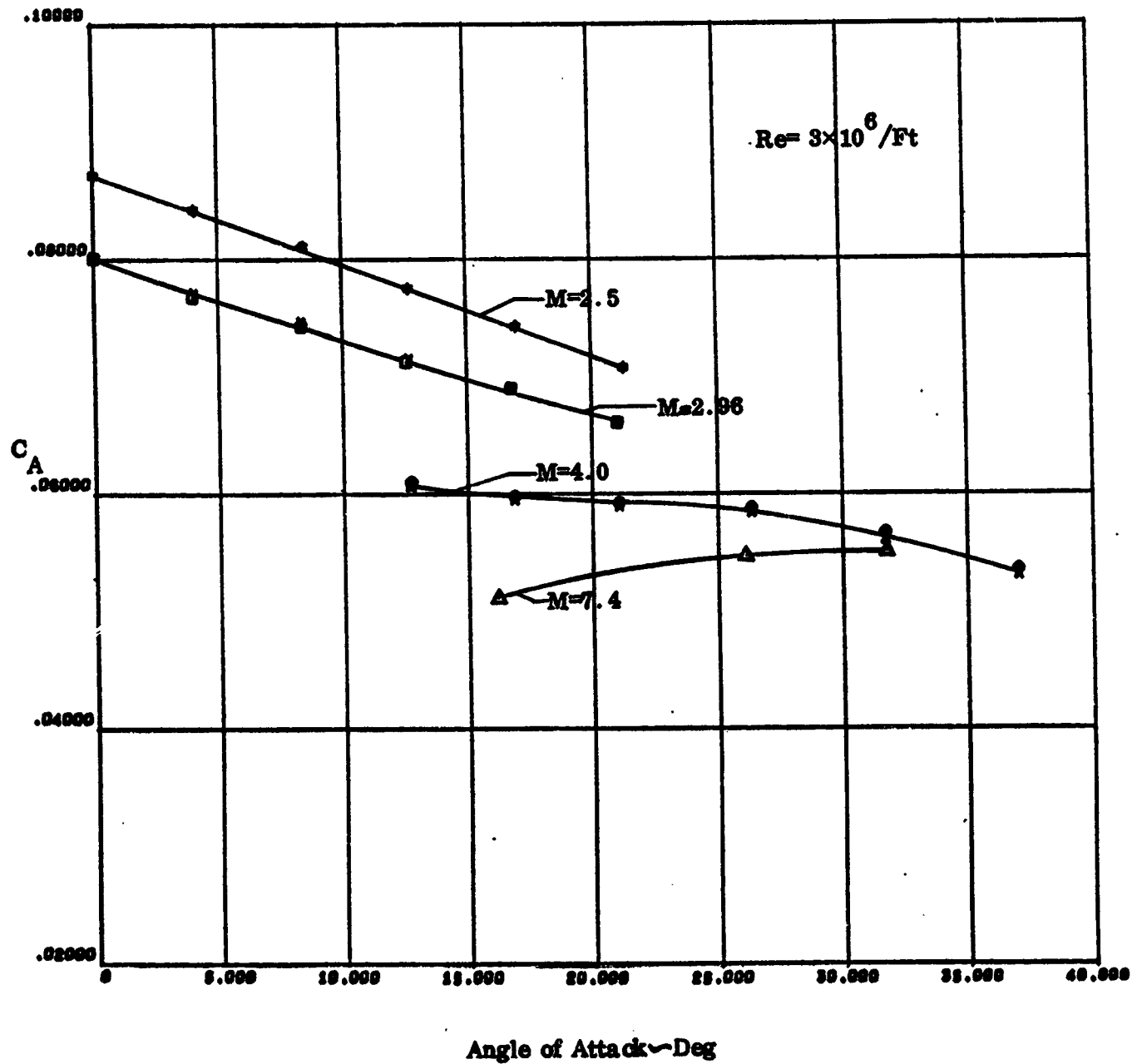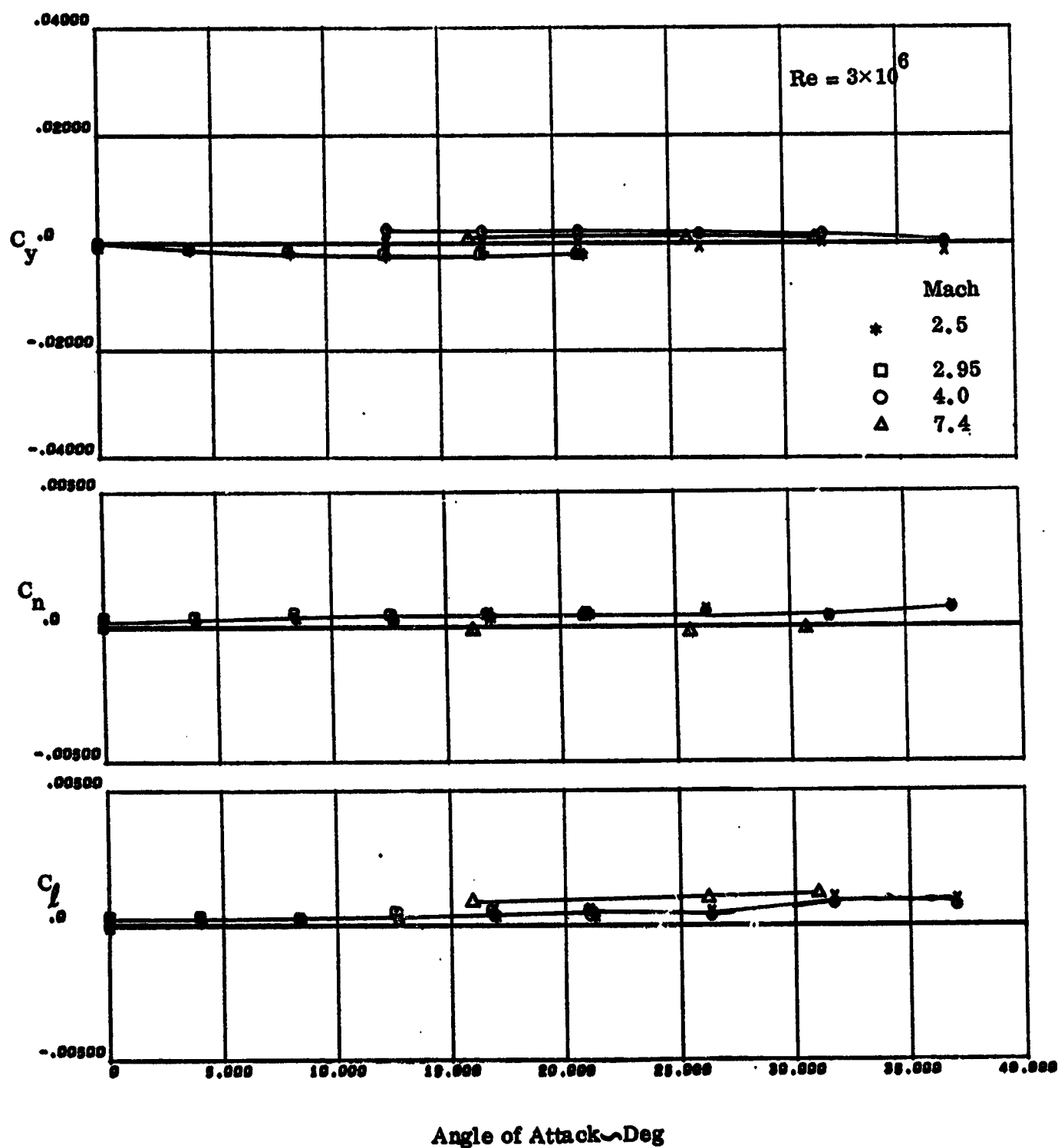
d) Lateral - directional

Figure 3-14. Effect of Mach Number - Jet Off

Angle of Attack∼ Deg

a) Normal Force
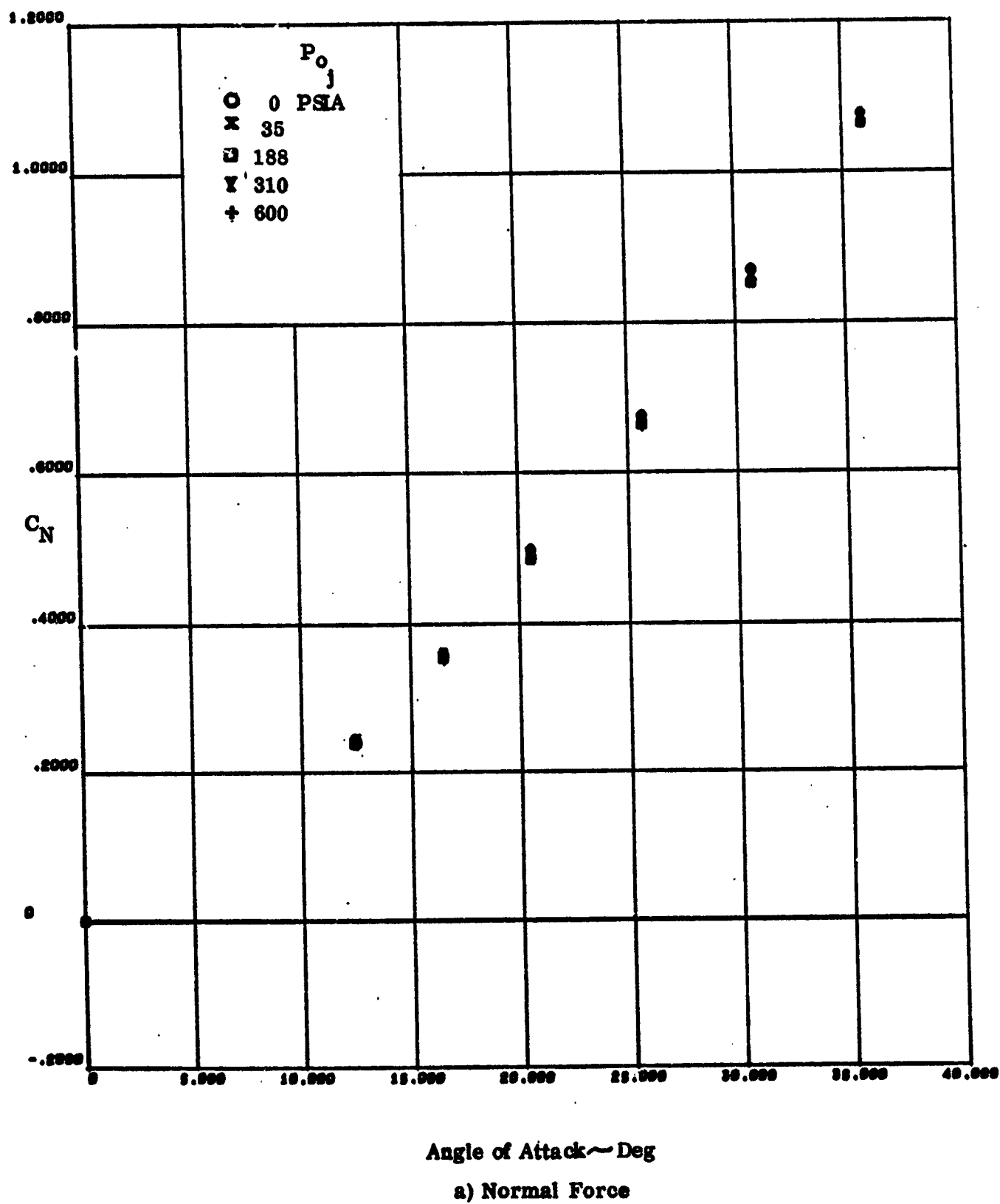
Figure 3-15. Effect of Pressure With Yaw Jet On Left Side at Mach 4.0, Re=1×10^{6}/Ft
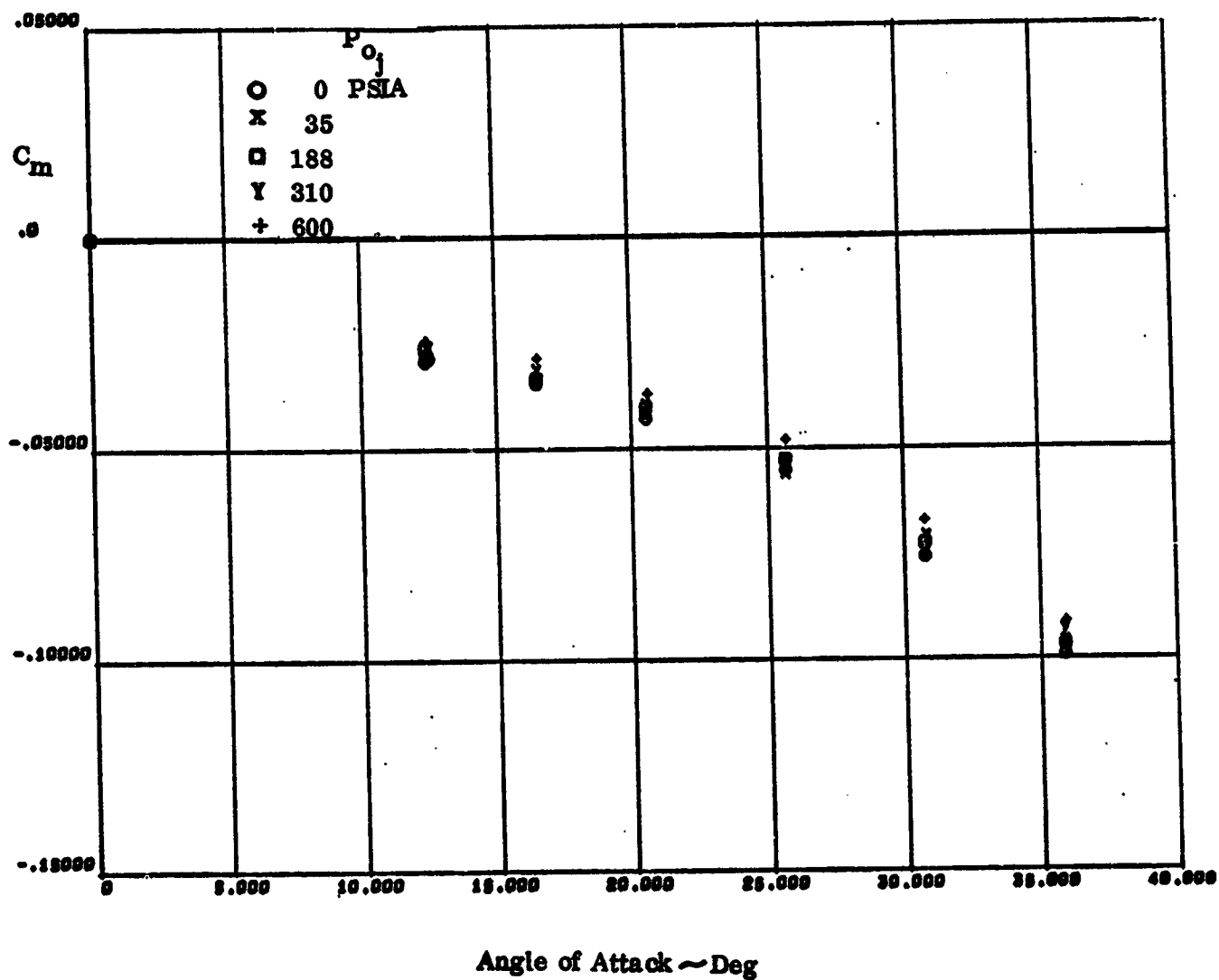
b) Pitching Moment

Figure 3-15. Effect of Pressure with Left Side Yaw Jet On at Mach 4.0, $Re = 1 \times 10^6/Ft$
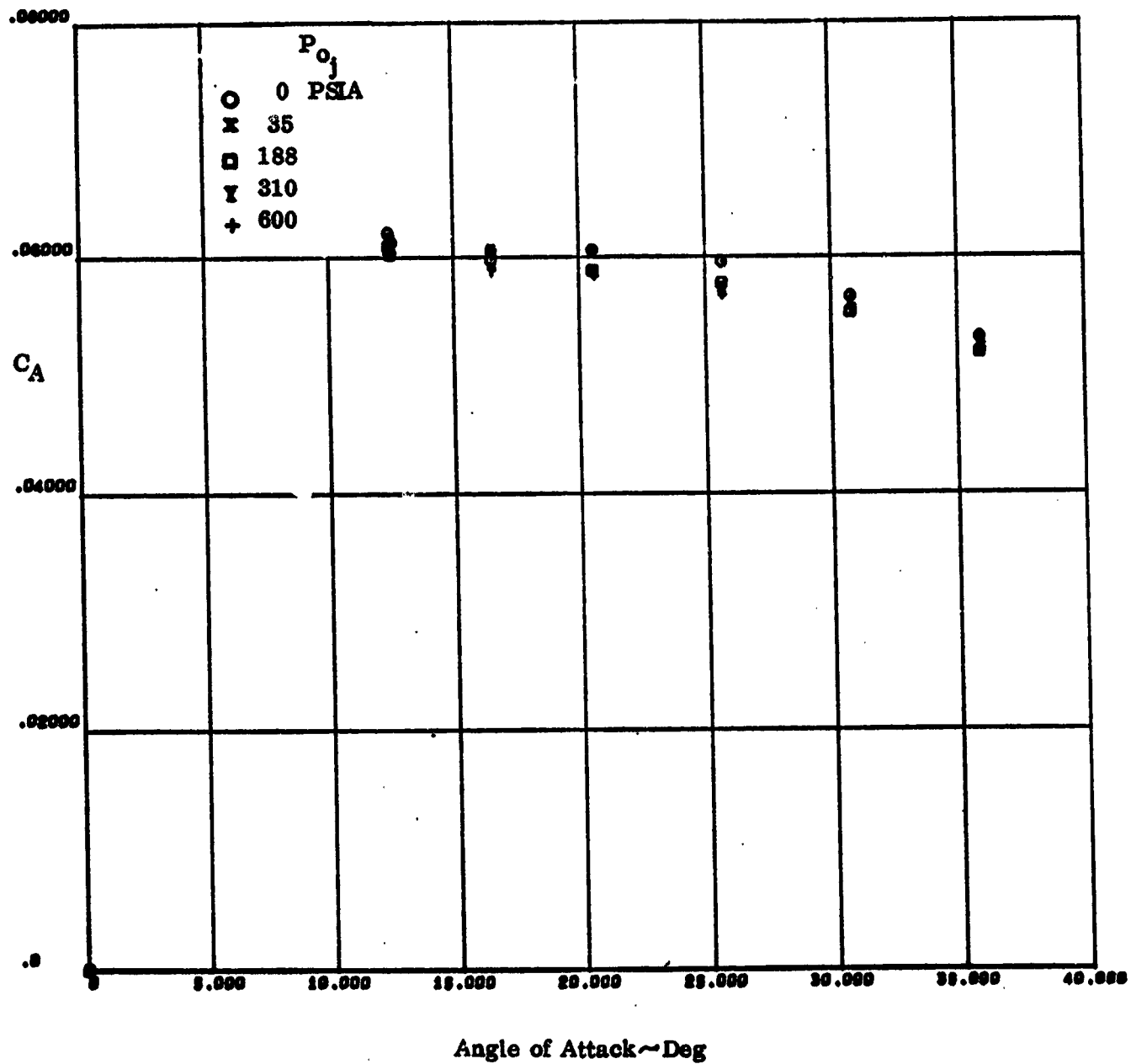
Angle of Attack ~ Deg

c) Axial Force

Figure 3-15.   Effect of Pressure With Left Side Yaw Jet on at Mach
4.0, Re = 1×10^6/Ft

3-45

d) Lateral-Directional

Figure 3-15. Effect of Pressure With Left Side Yaw Jet On at Mach
4.0, Re=1×10⁶/Ft
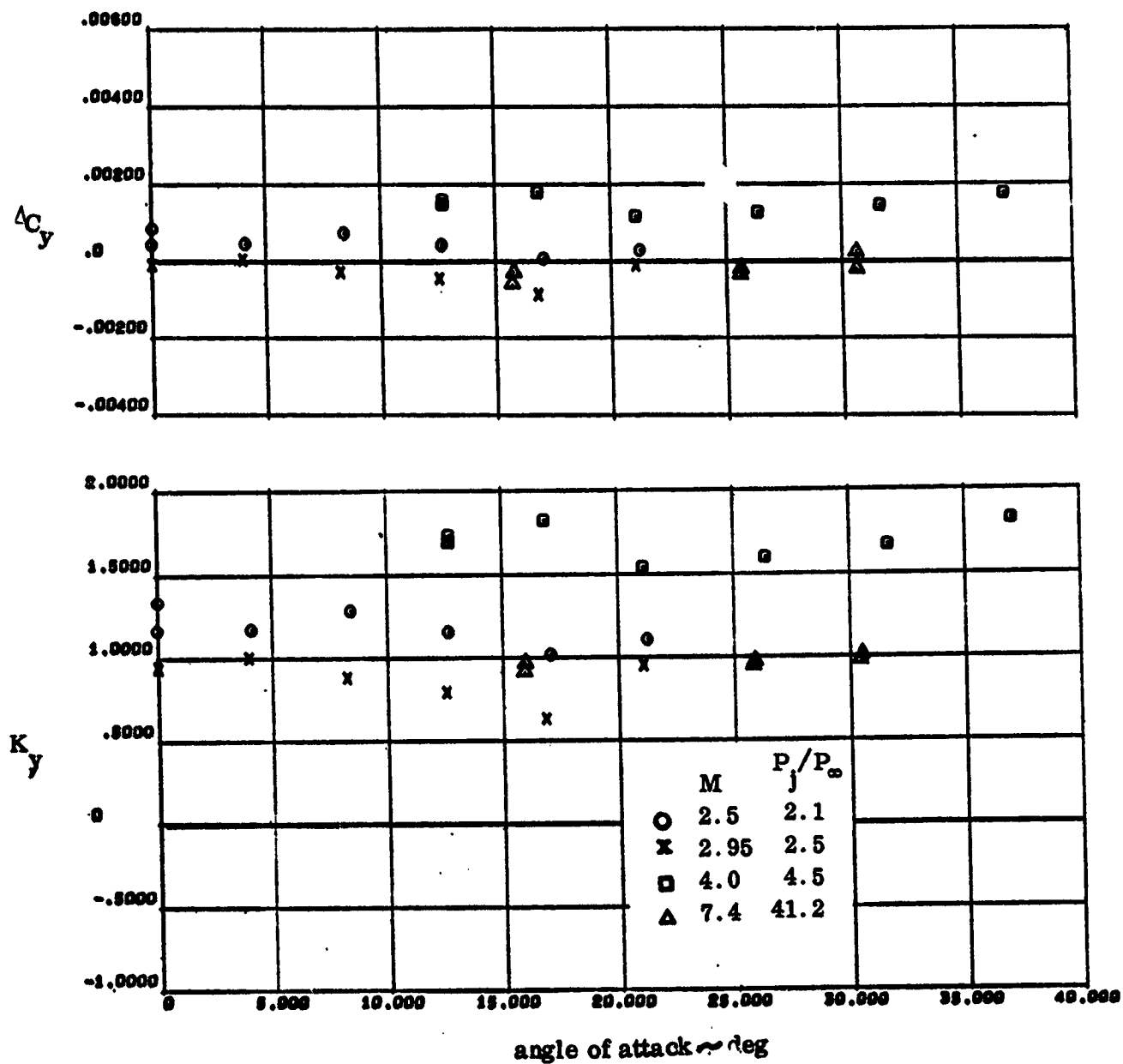
Figure 3-16. Effect of Mach Number on RCS Side Force Amplification
at Scaled Flight Conditions
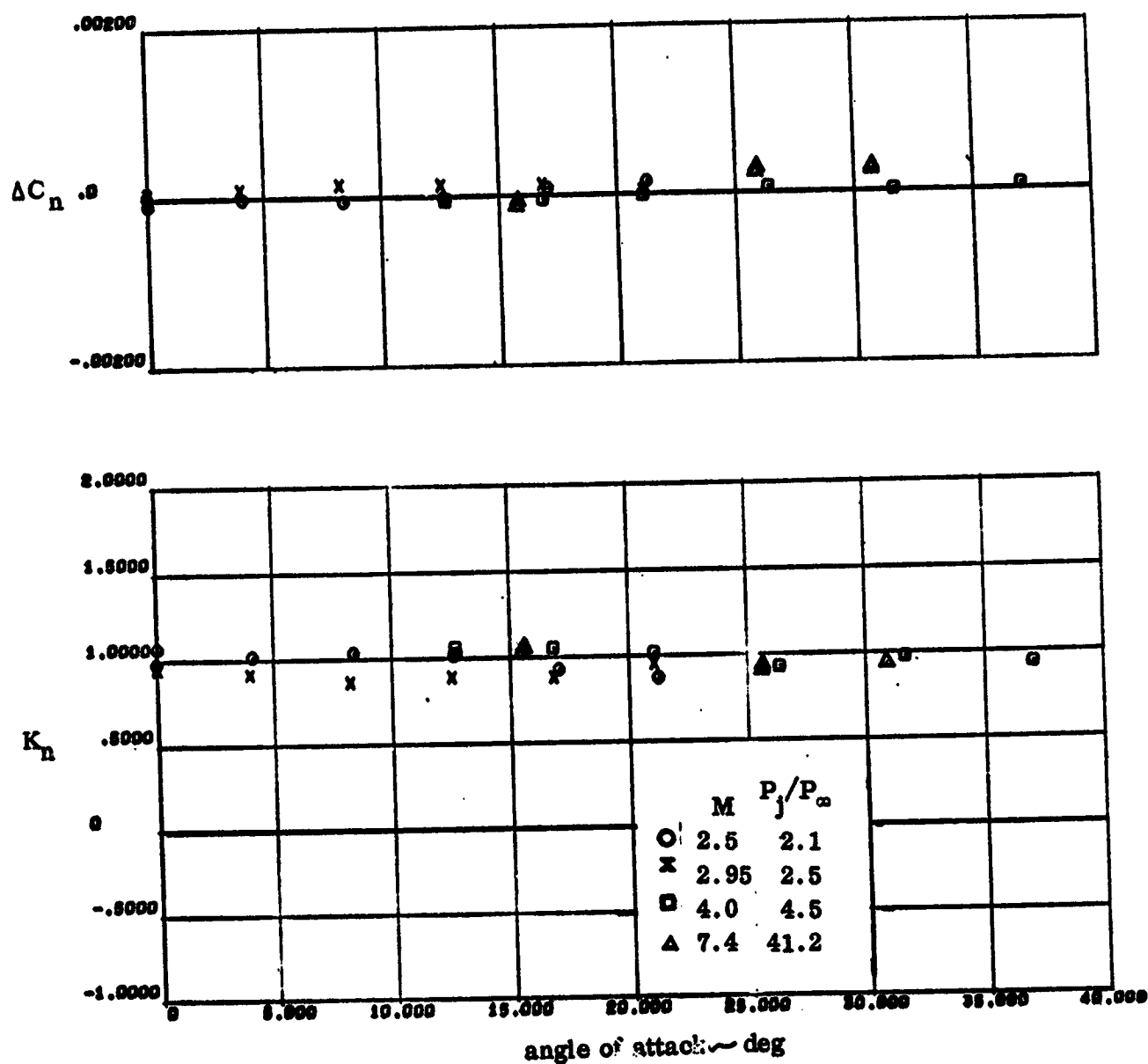
Figure 3-17. Effect of Mach Number on RCS Yawing Moment Amplification
at Scaled Flight Conditions
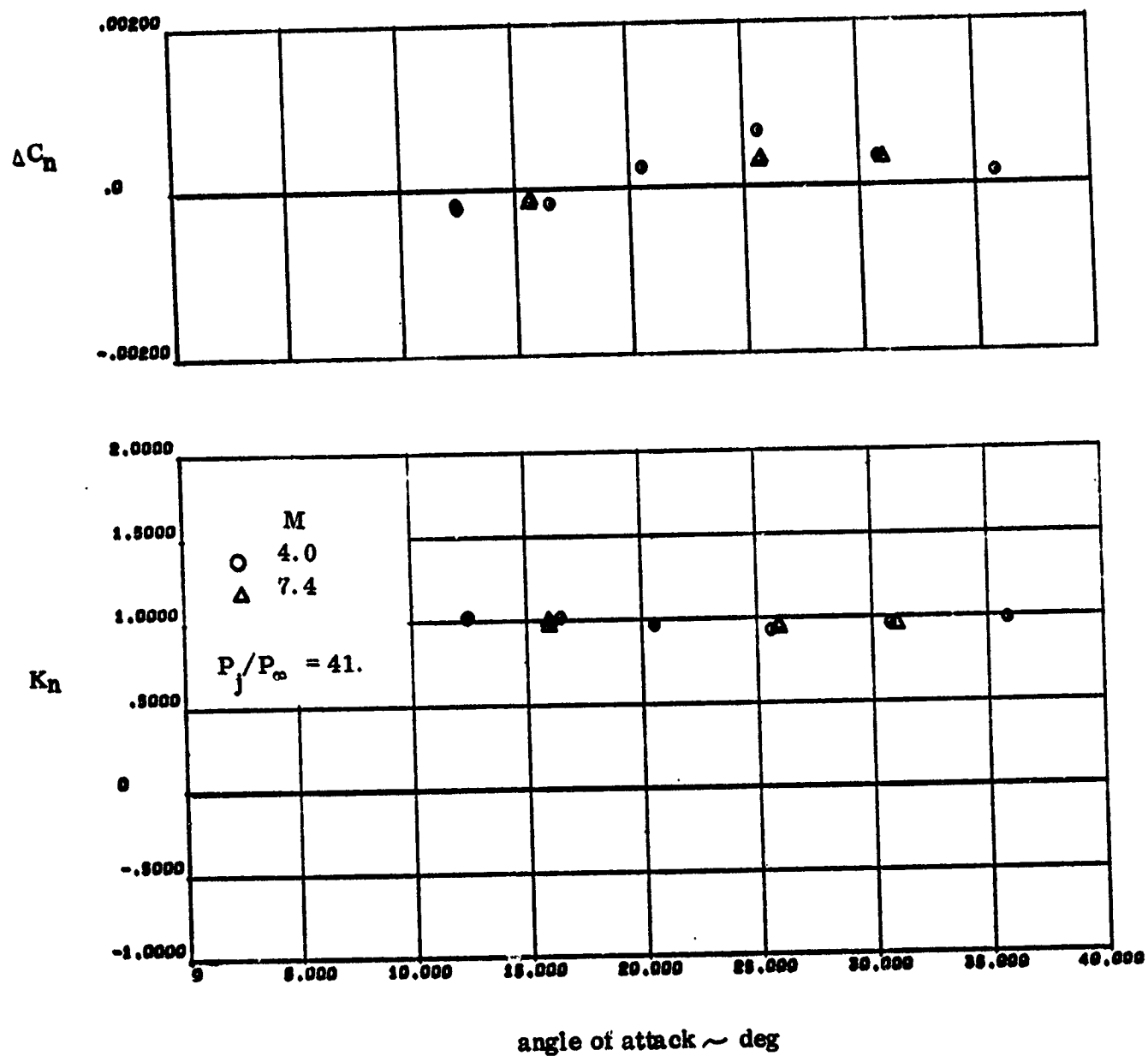
Figure 3-18. Effect of Mach Number on RCS Yaw Amplification
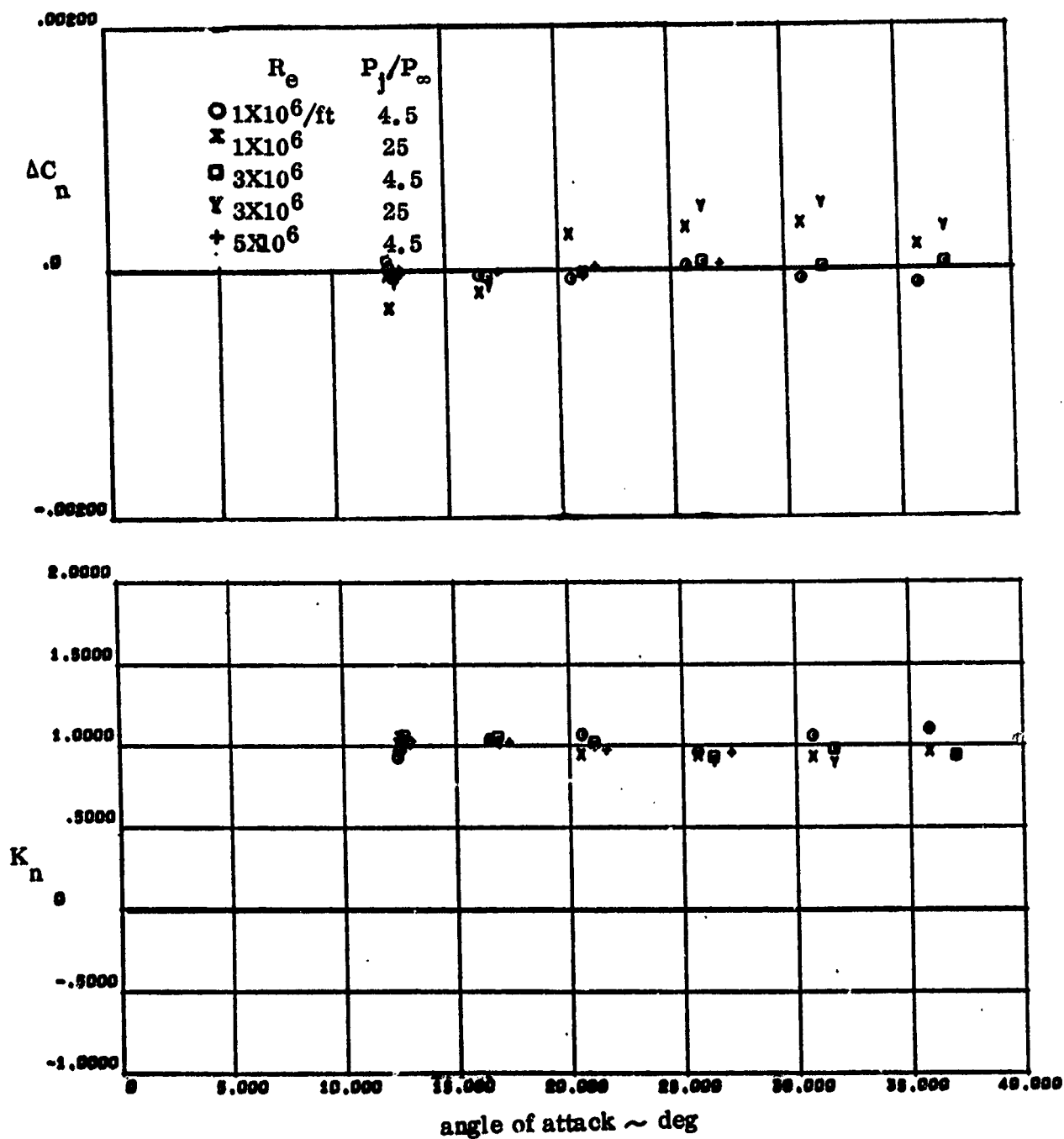
Figure 3-19. Effect of Reynolds Number on Yaw Amplification
at Mach 4.0
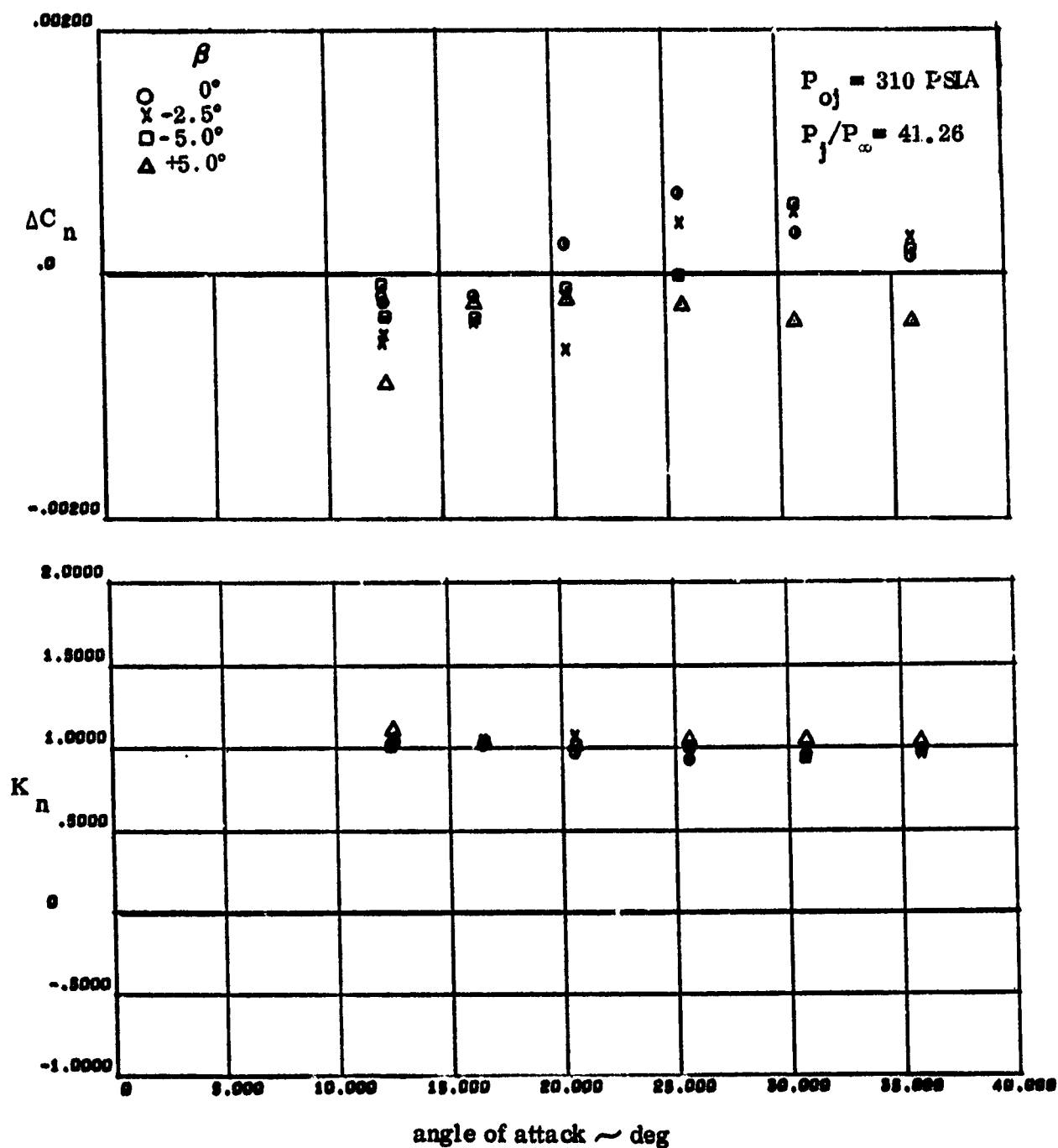
Figure 3-20. Effect of Yaw Angle on Yaw Amplification at Mach 4.0, $Re = 1 \times 10^6$/ft
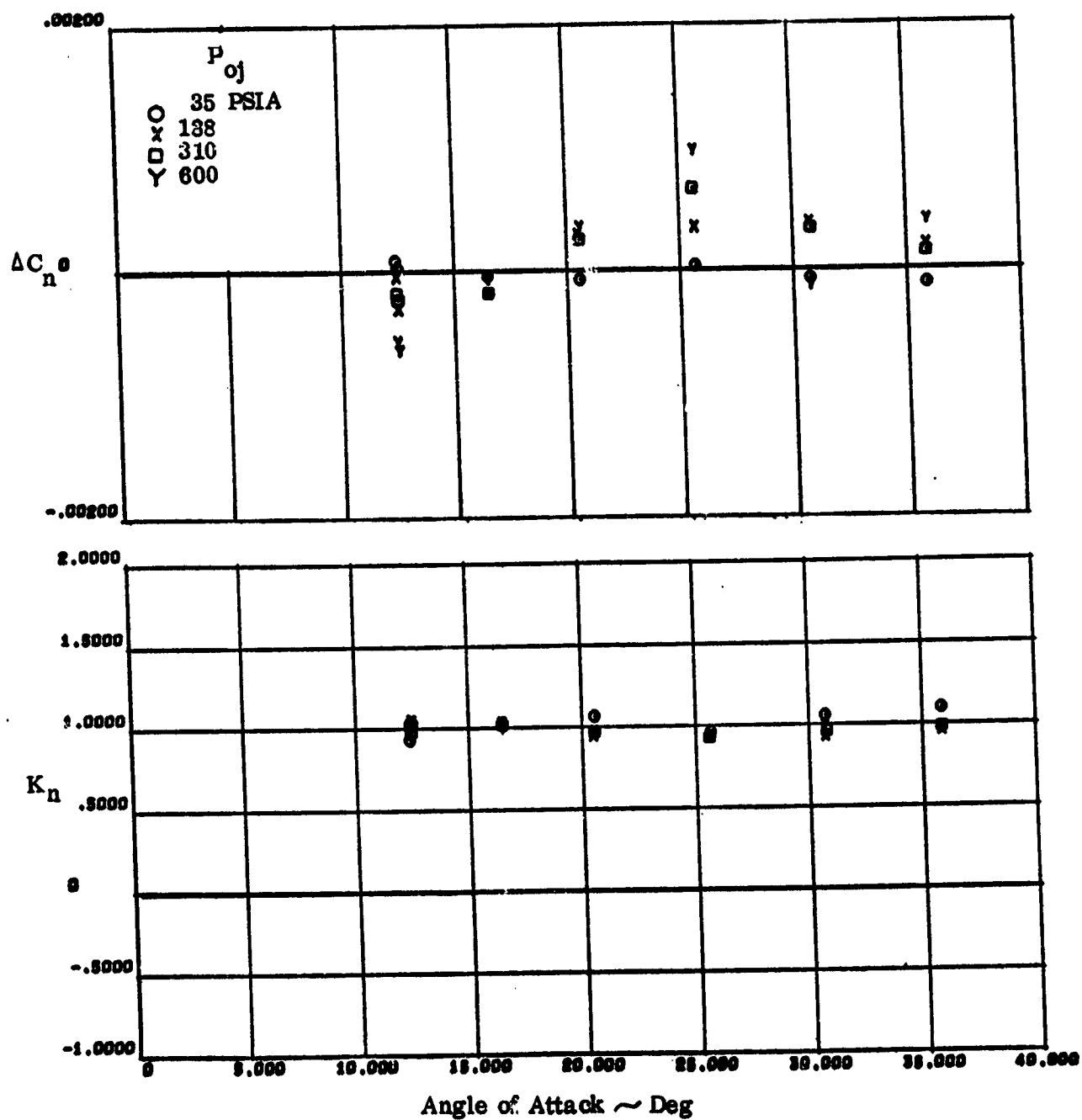
Figure 3-21. Effect of Jet Pressure on Yaw Amplification at Mach 4.0,
Re = 1×10^6/ft
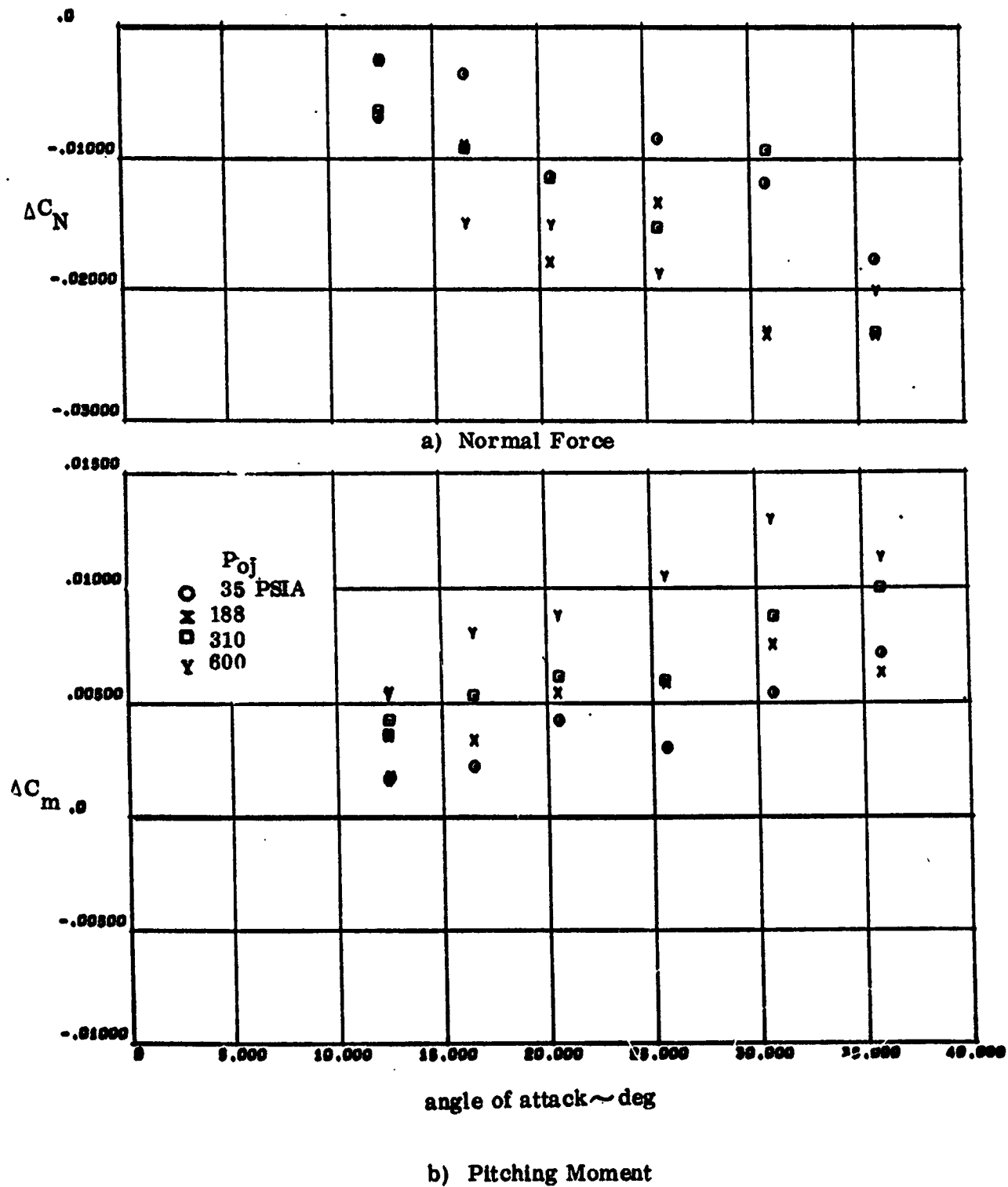
a) Normal Force

b) Pitching Moment

Figure 3-22. Yaw Jet Induced Effects - Effect of Supply Pressure at
Mach 4.0, Re = 1×10^6/ft

c) Axial Force
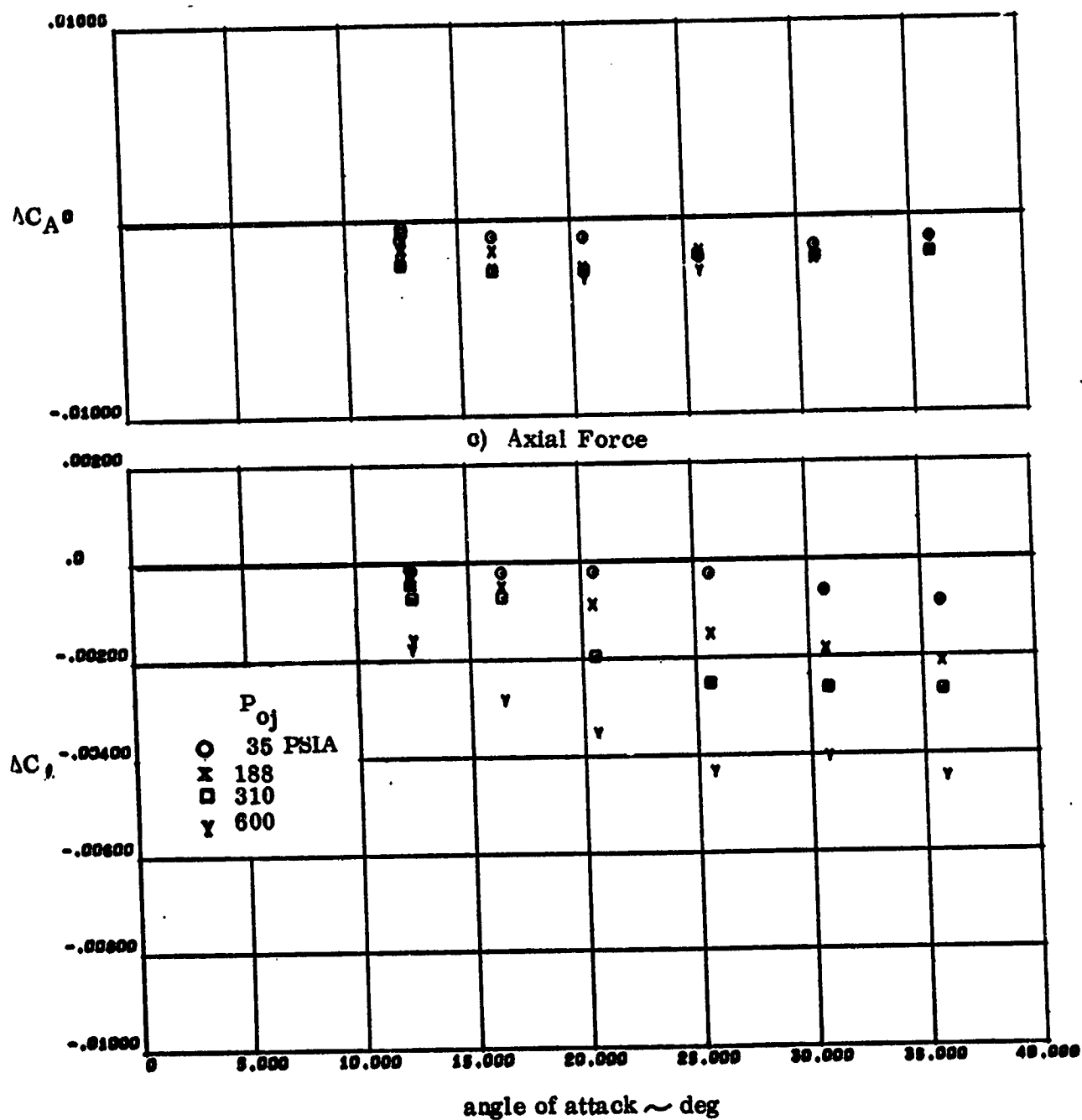
d) Rolling Moment

Figure 3-22. Yaw Jet Induced Effects - Effect of Supply Pressure at Mach 4.0, Re = 1×10^6/ft

$\alpha = 25°$
$P_{oj} = 512$ Psia

$\alpha = 30°$
$P_{oj} = 310$ psia

Figure 3-23.   Oil Flow Visualization; Effect of Yaw Jet Operation on Wing;
M=7.4.

Angle of Attack ~ Deg

a) Normal Force

Figure 3-24.   Effect of Chamber Pressure with Positive Roll
Jets on at Mach 4.0, Re = 1×10^6

Angle of Attack~Deg

b) Pitching Moment

Figure 3-24. Effect of Chamber Pressure With Positive Roll Jets On at Mach 4.0, Re = 1×10^6/Ft

Angle of Attack ～ deg
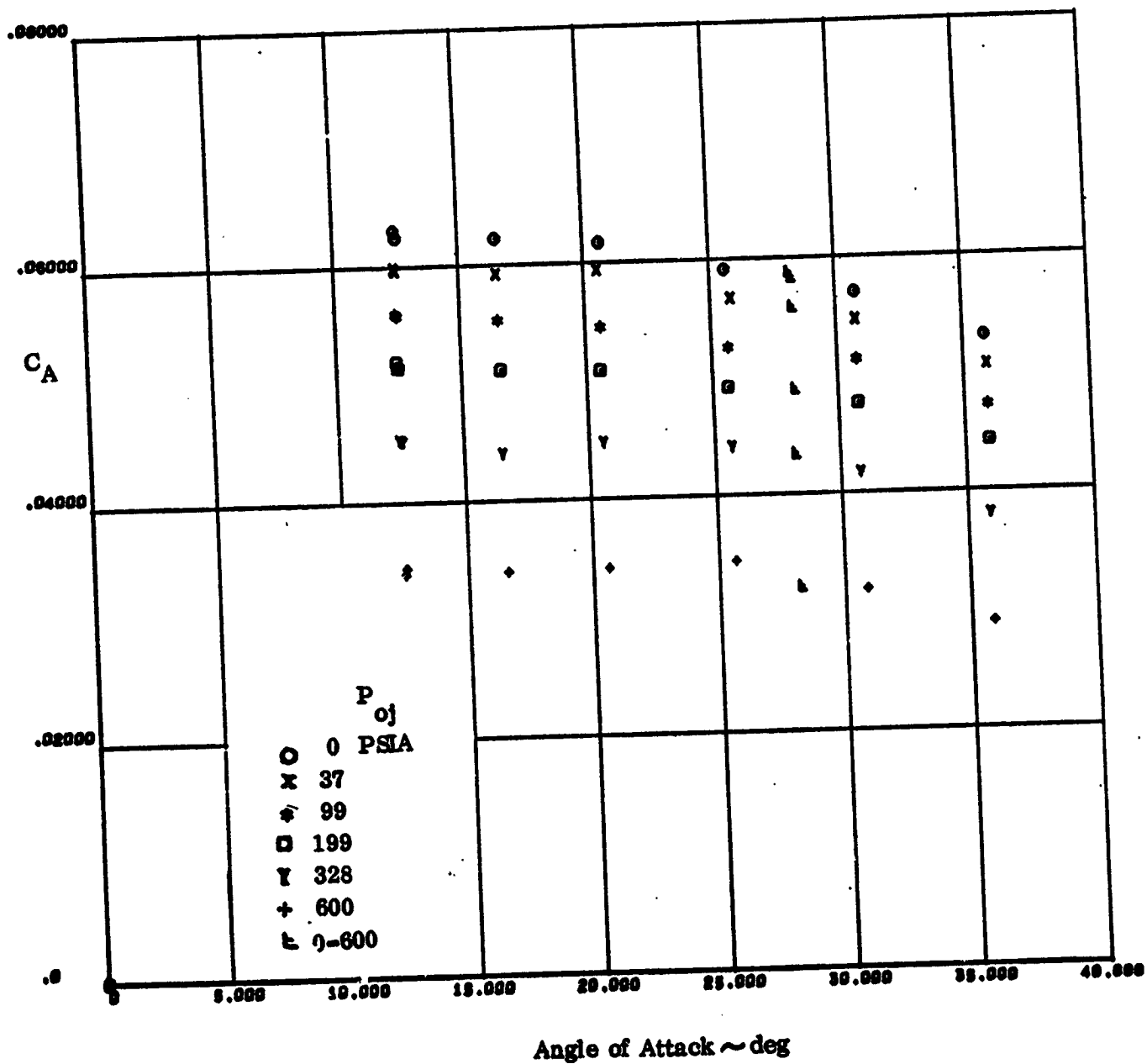
c) Axial Force

Figure 3-24. Effect of Chamber Pressure With Positive Roll Jets On
At Mach 4.0, Re = 1×10^6/Ft

Angle of Attack ∼ Deg

d) Lateral-Directional

Figure 3-24. Effect of Chamber Pressure With Positive Roll Jets On
At Mach 4.0, Re = 1×10^6/Ft
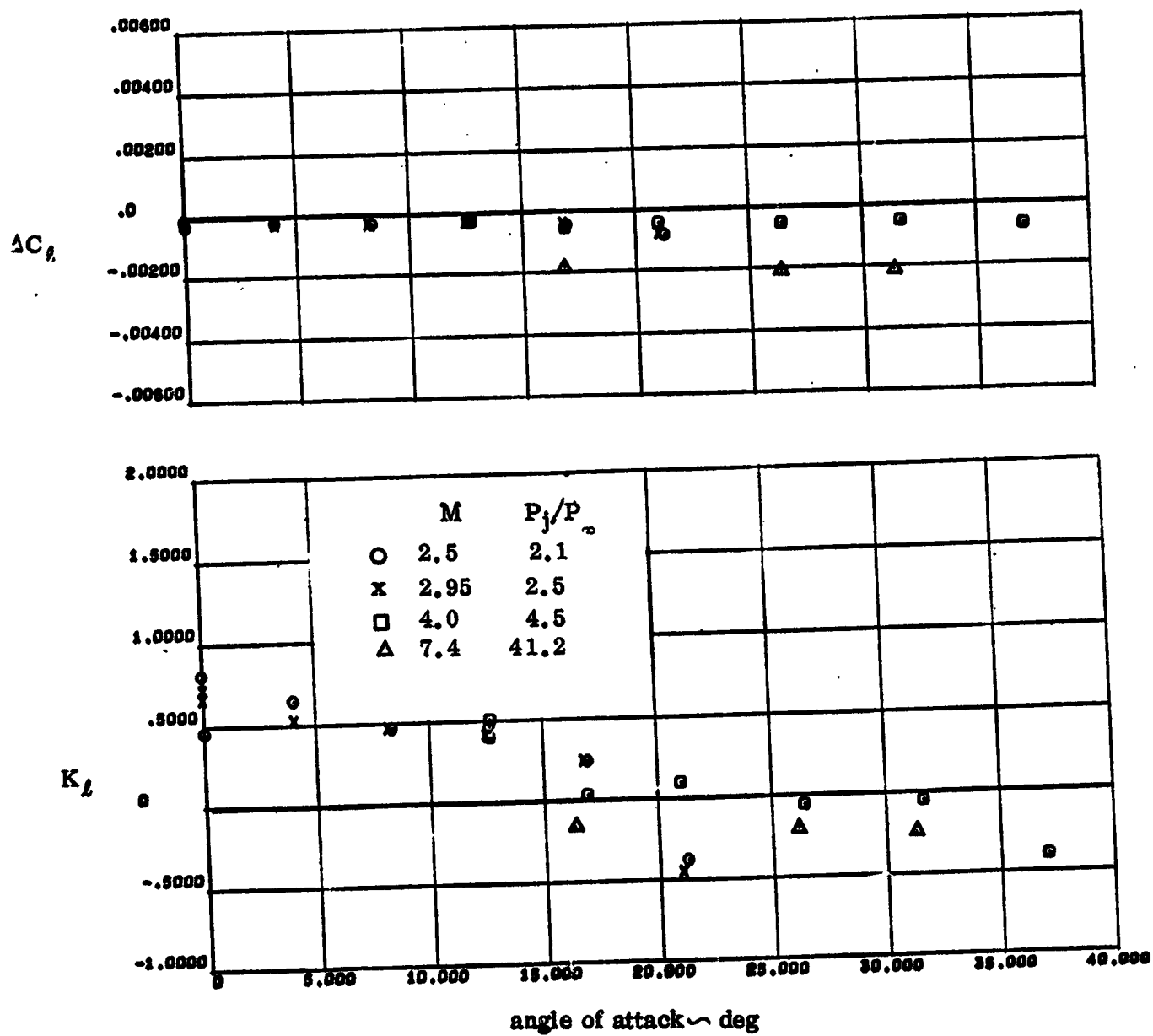
Figure 3-25. Effect of Mach Number on RCS Rolling Moment Amplification at Scaled Flight Conditions
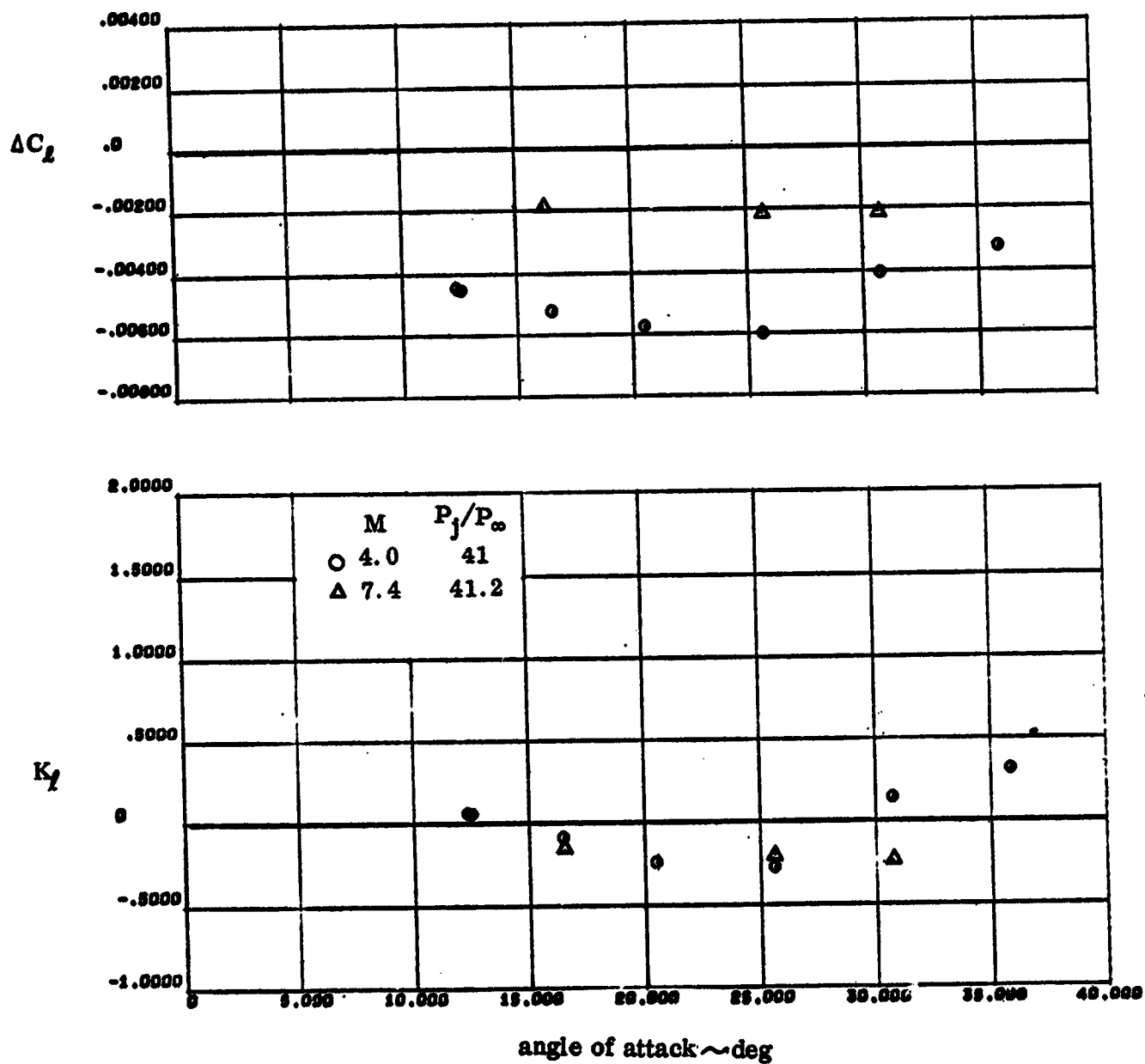
Figure 3-26. Effect of Mach Number on RCS Rolling Moment Amplification
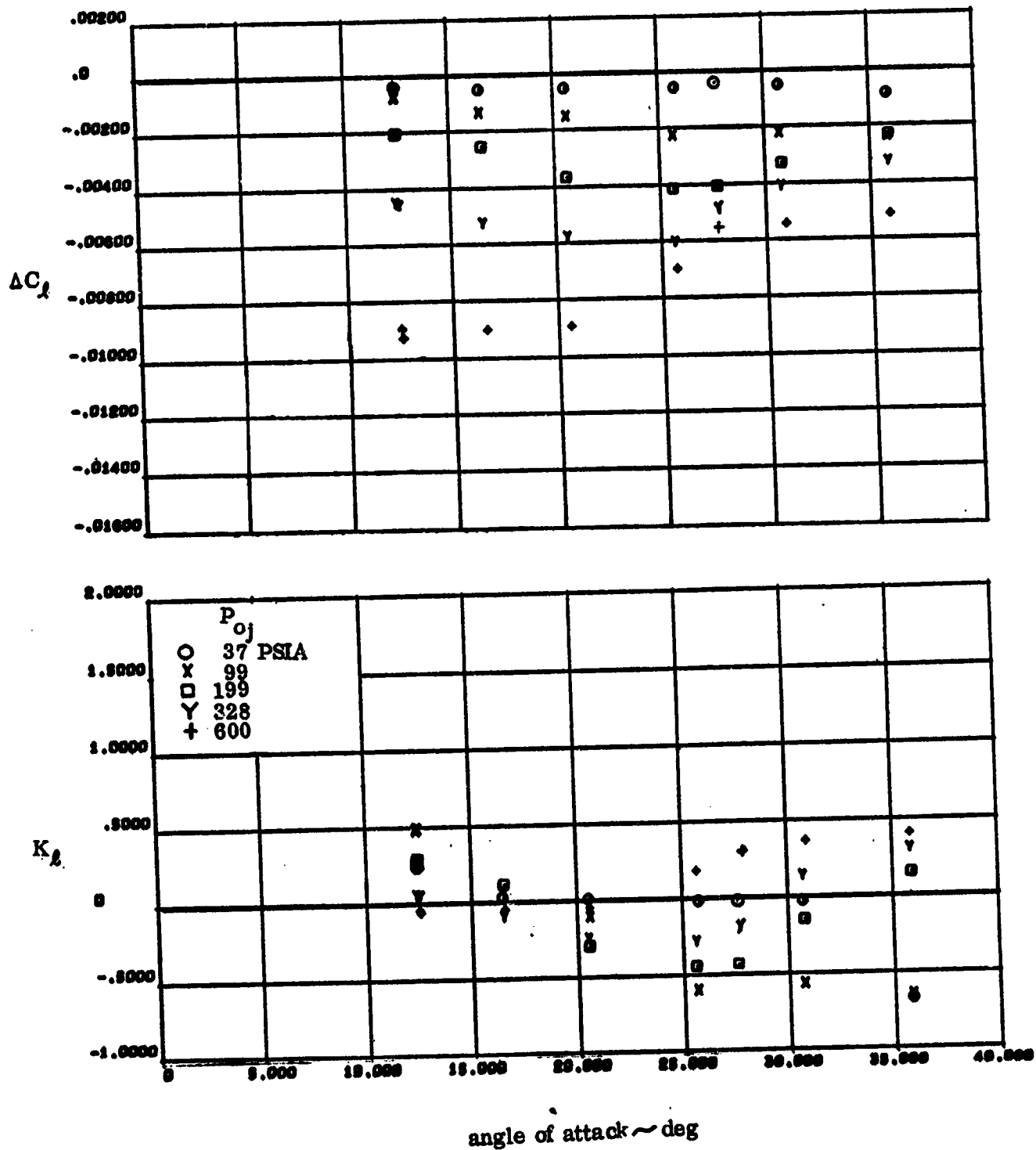
Figure 3-27. Effect of Supply Pressure on Roll Jet Amplification
at Mach 4.0, Re = 1×10^6/ft
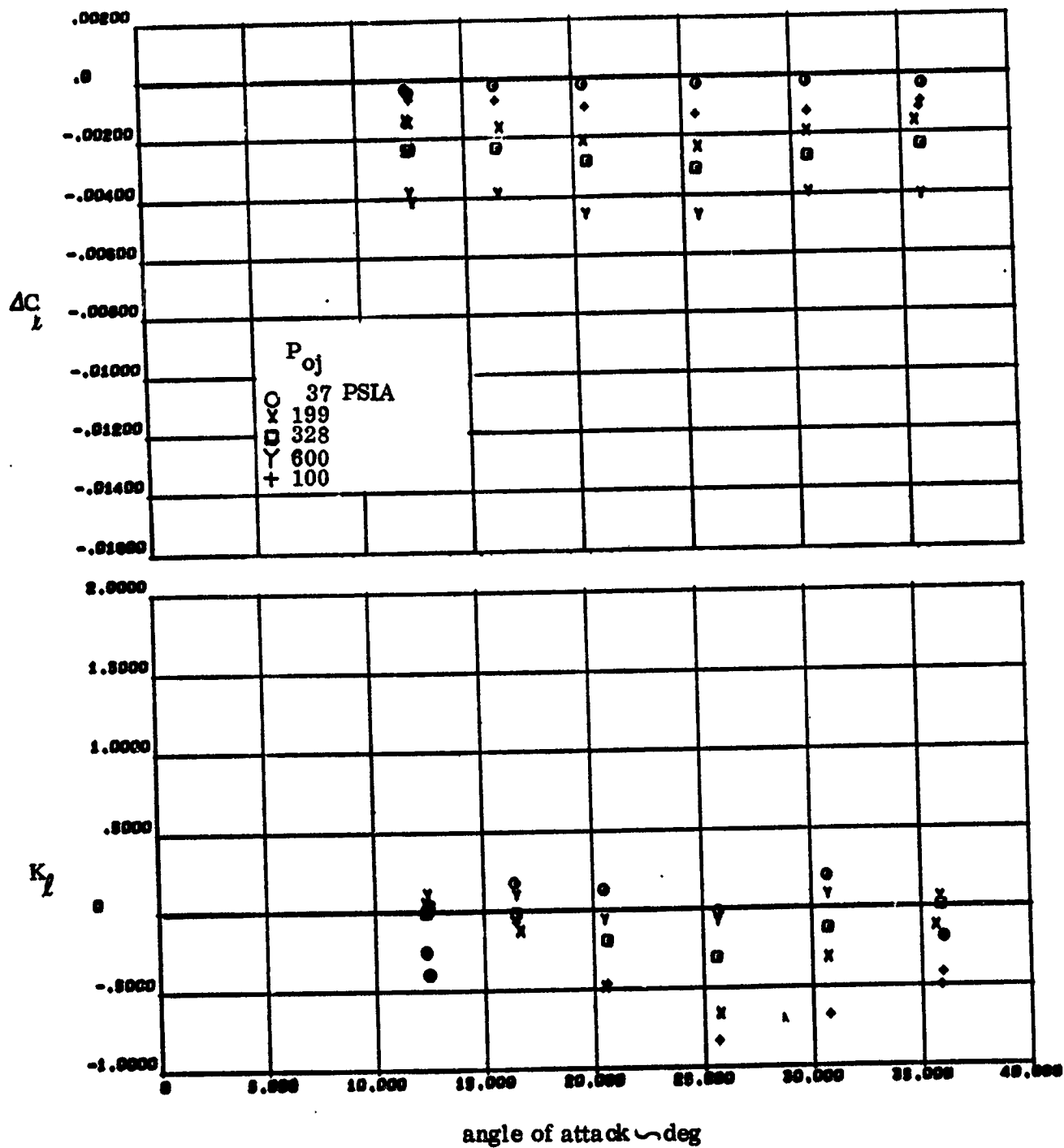
Figure 3-28. Roll Amplification caused by Jet Exhausting Toward Wing
at Mach 4.0, $Re = 1 \times 10^6/ft$
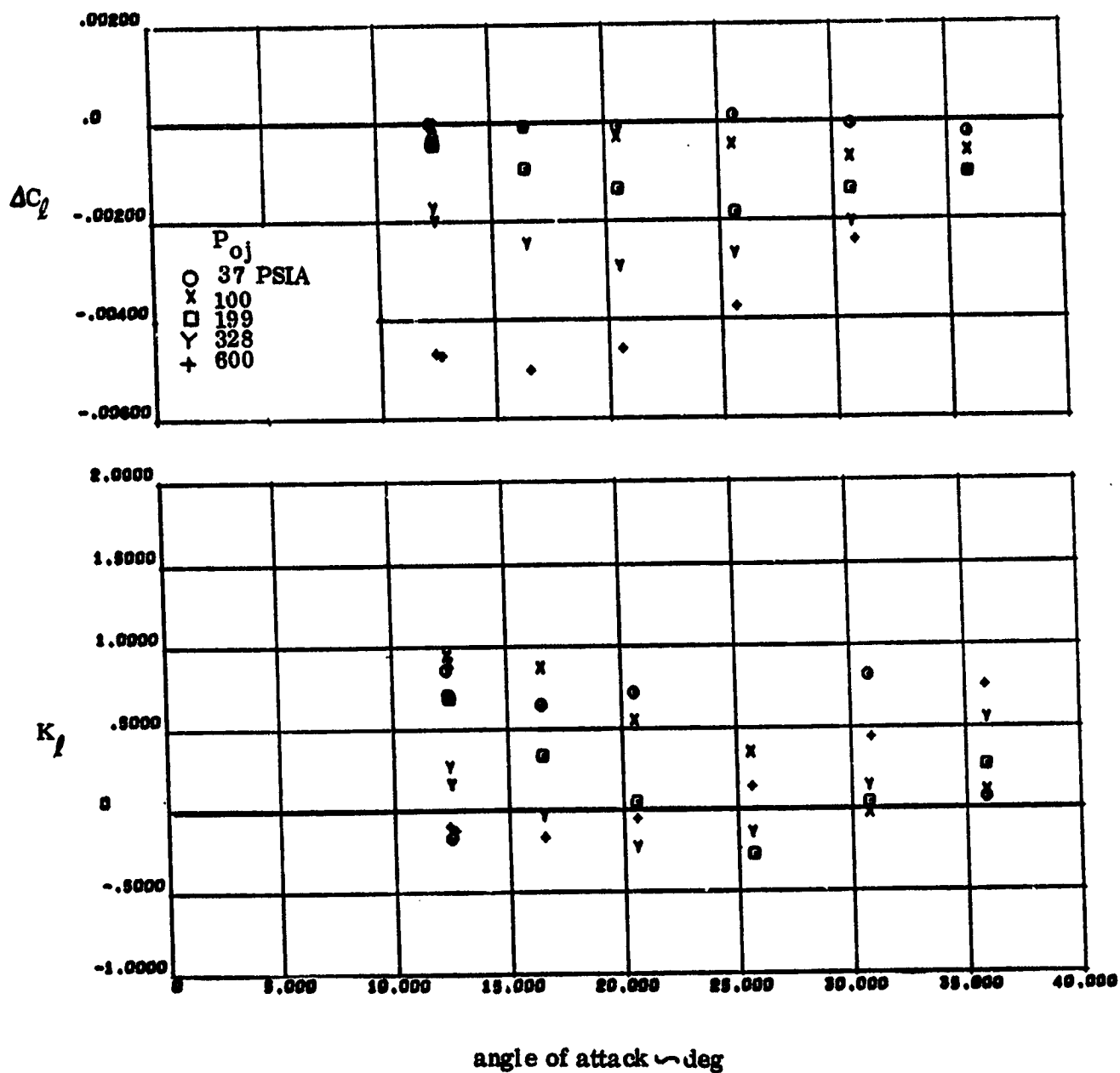
Figure 3-29. Roll Amplification Caused by Jet Exhausting Past Vertical Fin at Mach 4.0, $Re = 1 \times 10^6/ft$
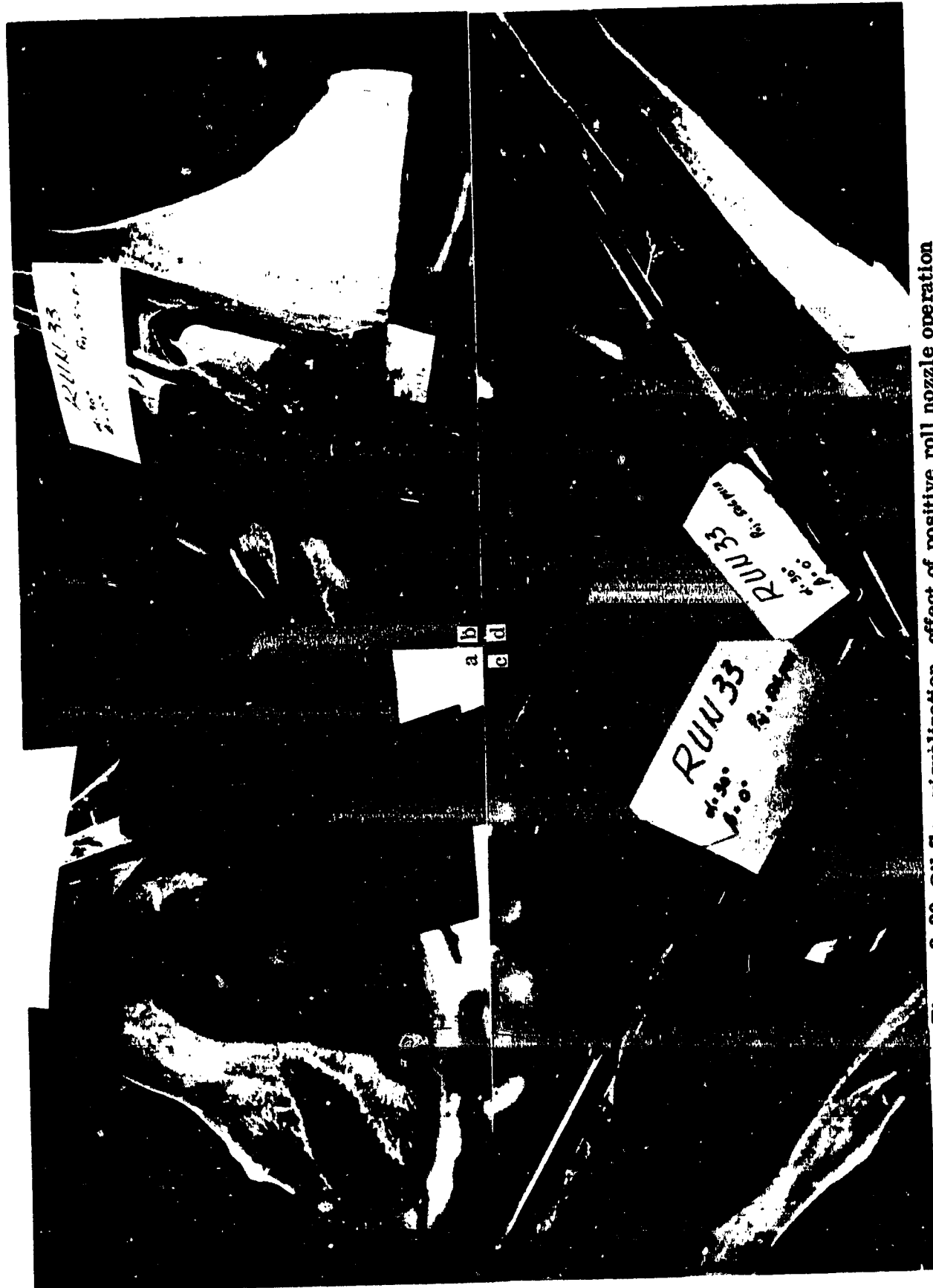
Figure 3-30. Oil flow visualization, effect of positive roll nozzle operation

($\sigma = 30°$, M = 7.4, P_{oj} = 506 psia)
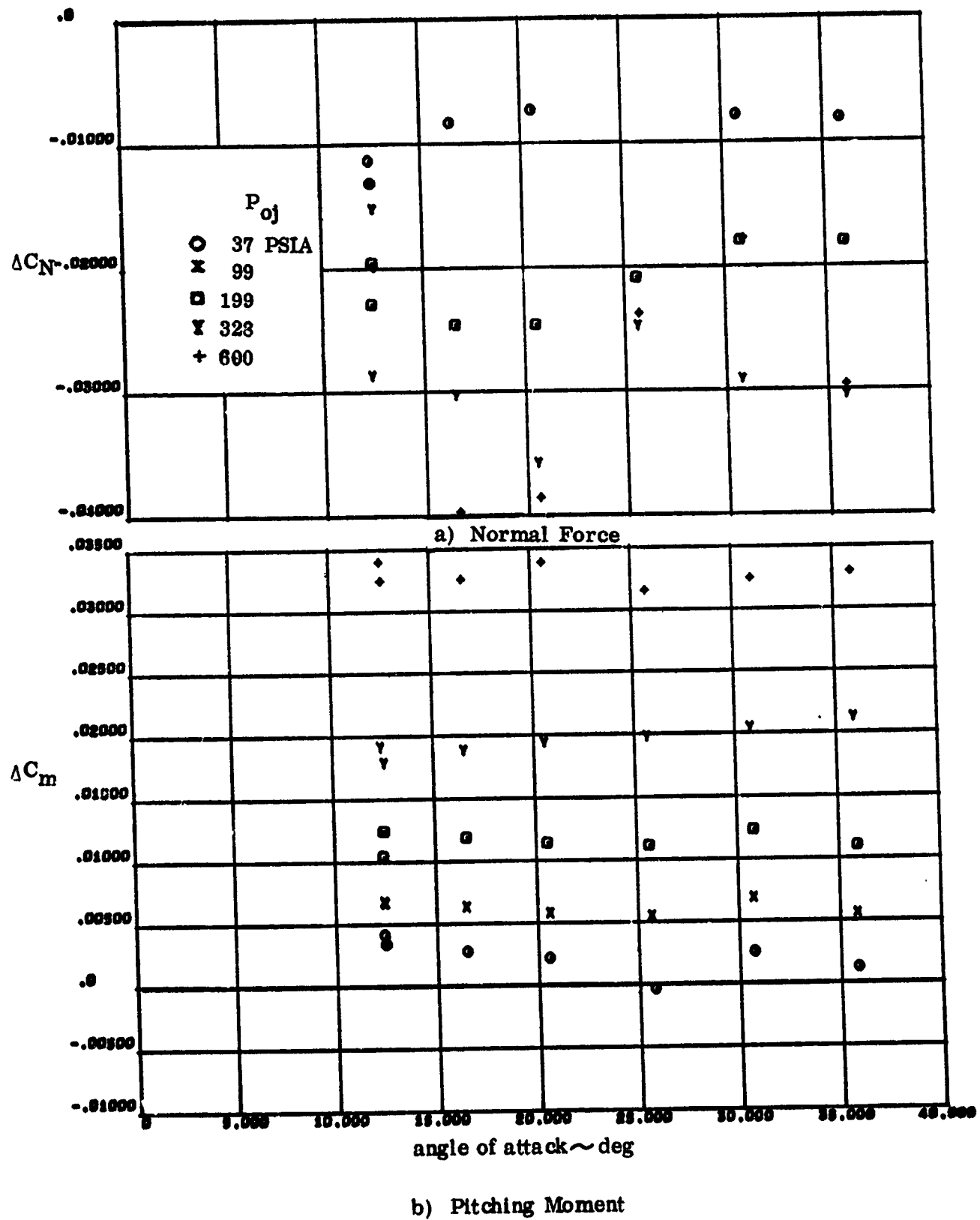
a) Normal Force

b) Pitching Moment

Figure 3-31. Roll Jet Induced Effects - Effect of Supply Pressure at
Mach 4.0, Re = 1×10^6/ft

c) Side Force

d) Yawing Moment
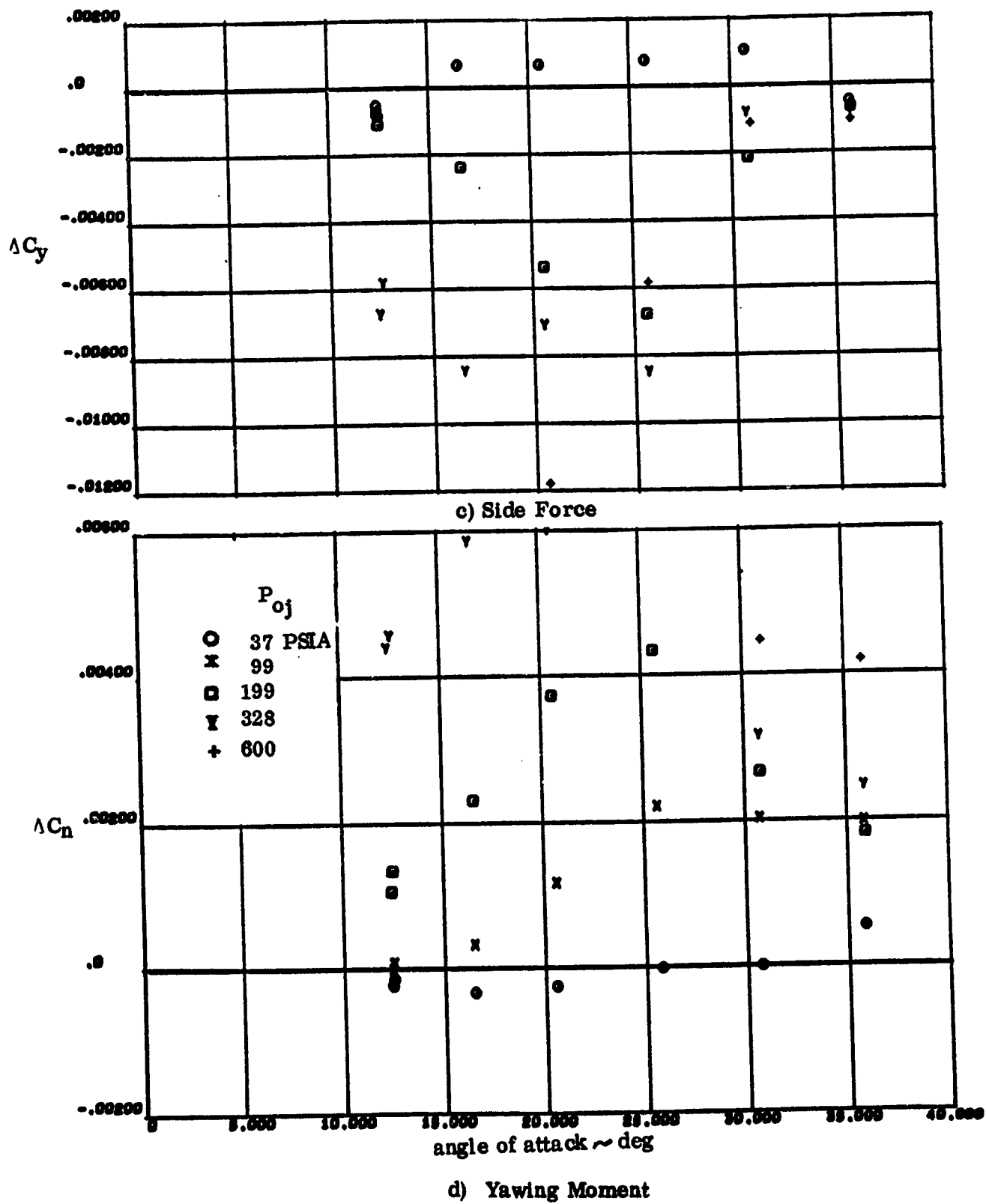
Figure 3-31. Roll Jet Induced Effects - Effect of Supply Pressure
at Mach 4.0, Re = 1×10^6/ft
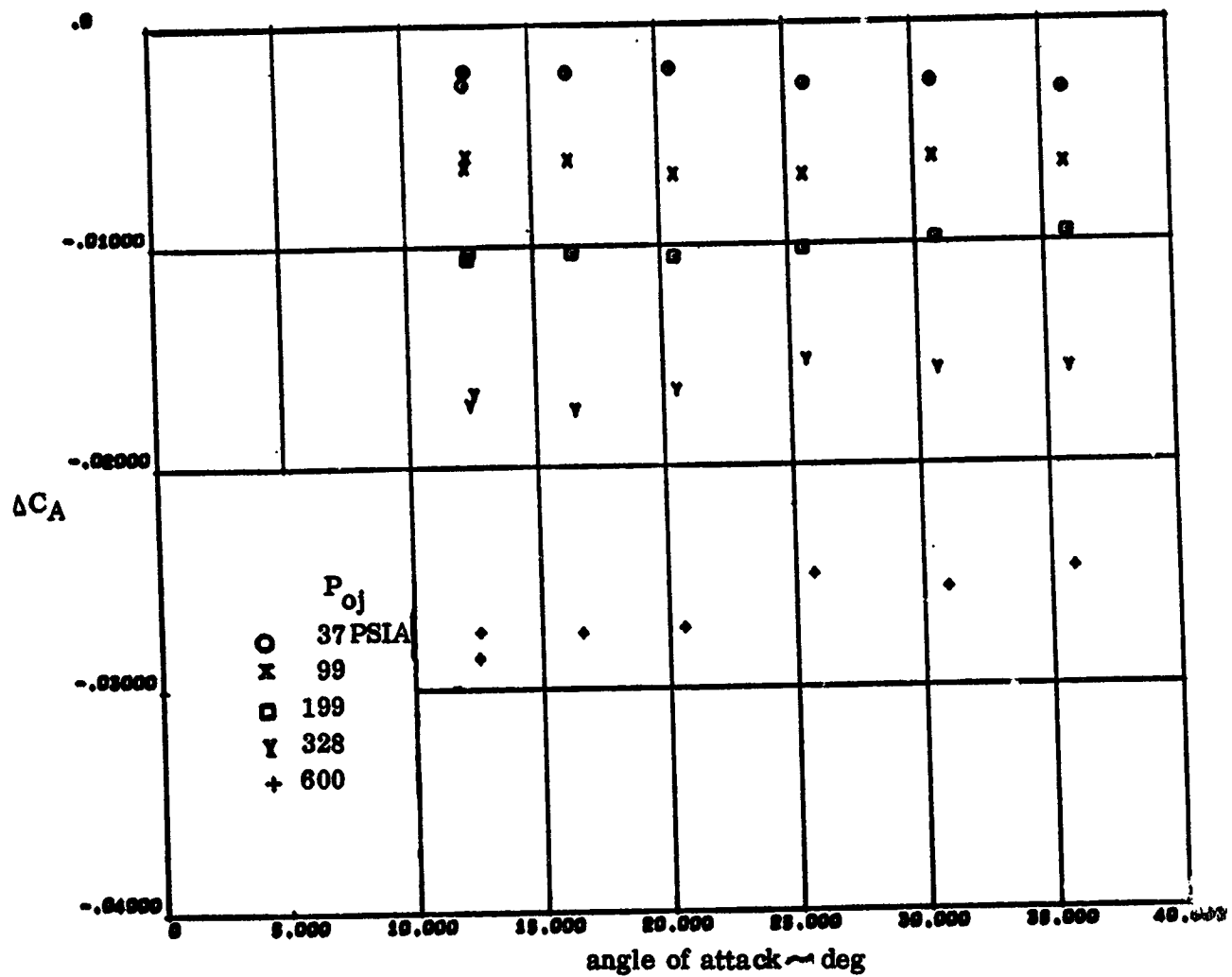
e) Axial Force

Figure 3-31. Roll Jet Induced Effects - Effect of Supply Pressure
at Mach 4.0, Re = 1×10^6/ft

a) Normal Force

Figure 3-32. Effect of Pressure With Left Pitch/Roll Jet Exhausting
Down at Mach 4.0

Angle of Attack ~ Deg
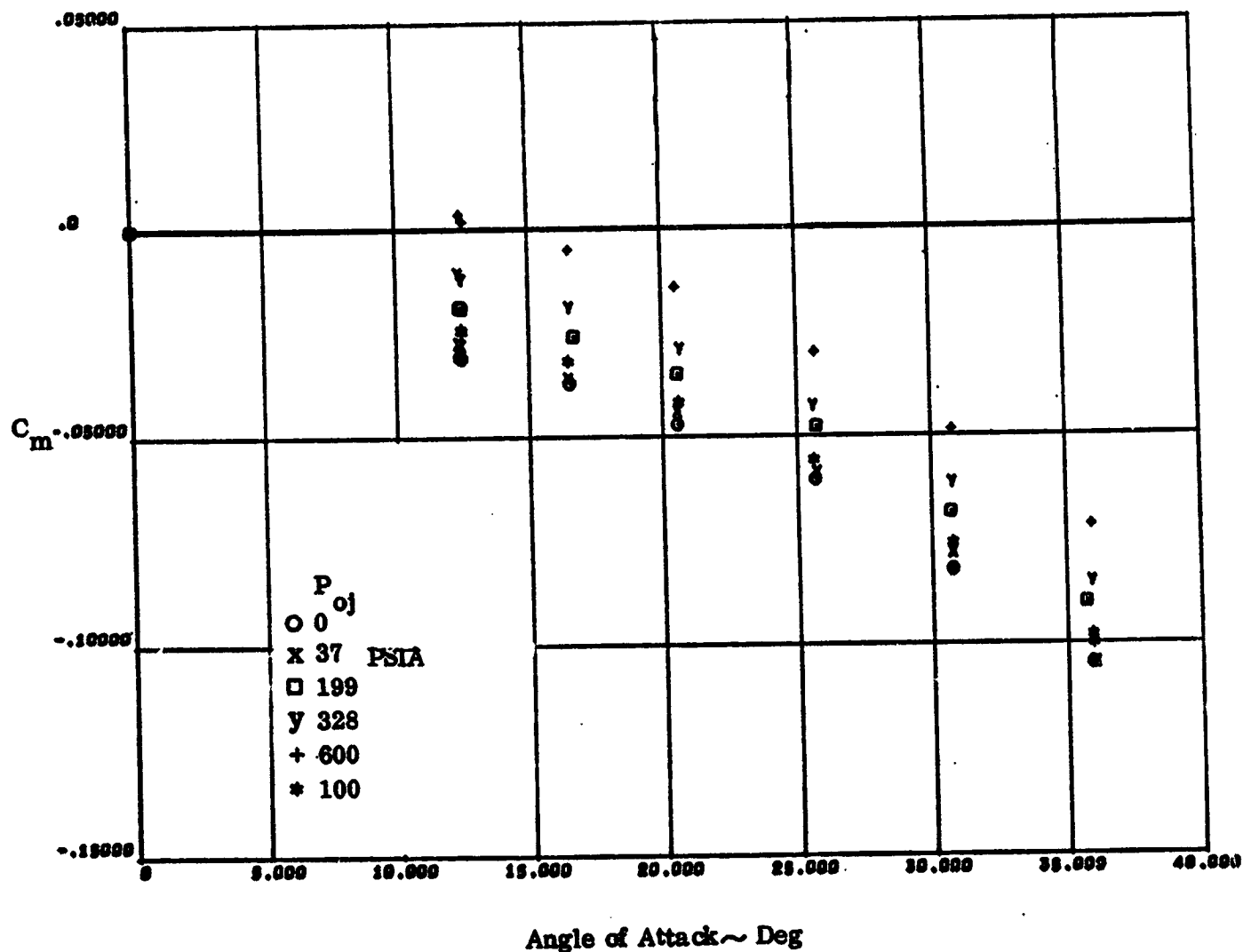
b) Pitching Moment

Figure 3-32. Effect of Pressure With Left Pitch/Roll Jet Exhausting
Down at Mach 4.0
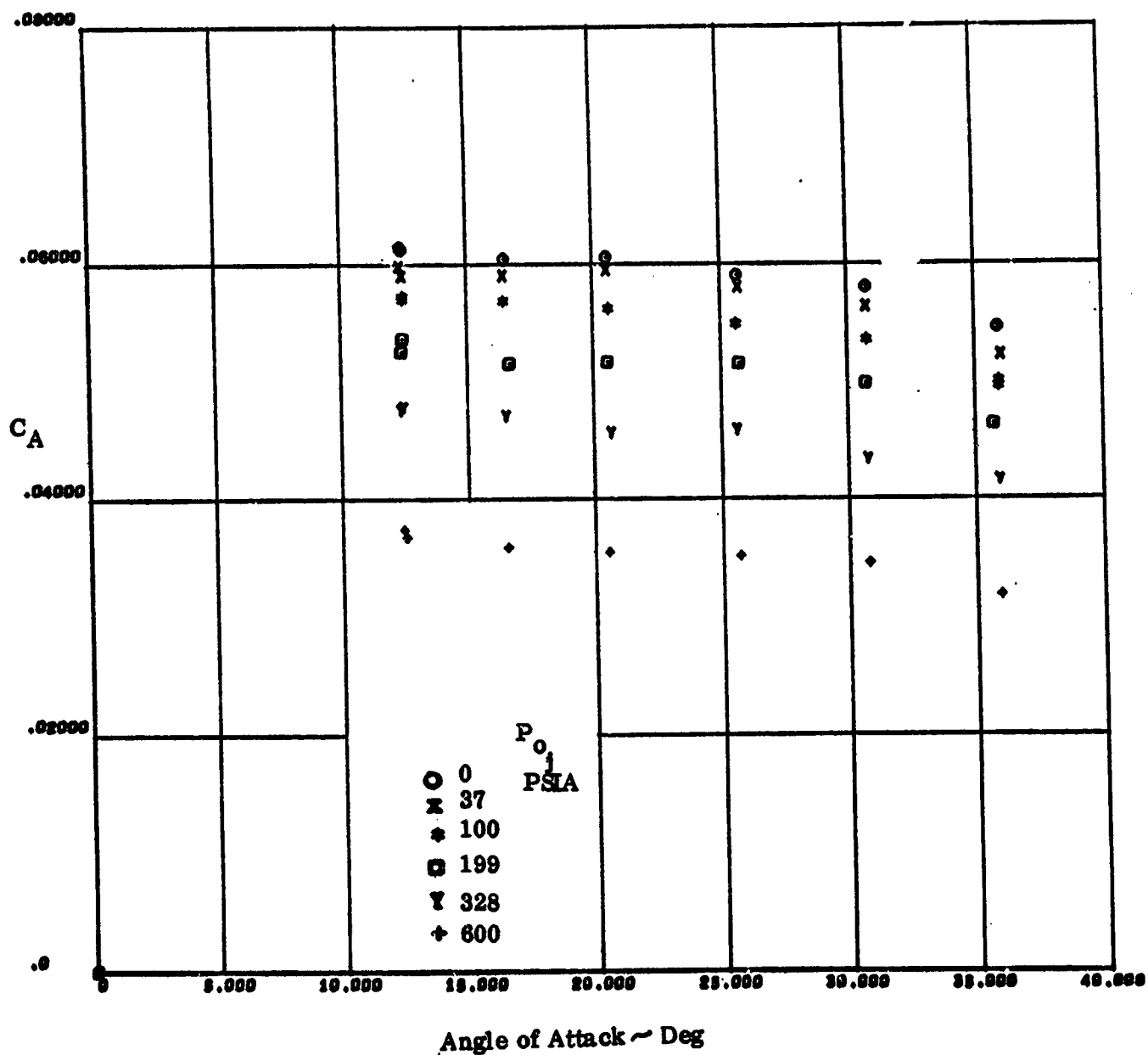
Angle of Attack ~ Deg

c) Axial Force

Figure 3-32. Effect of Pressure With Left Pitch/Roll Jet Exhausting
Down At Mach 4.0

Figure 3-33. Effect of Mach Number on RCS Nose-Down Pitching Moment
Amplification at Scaled Flight Conditions
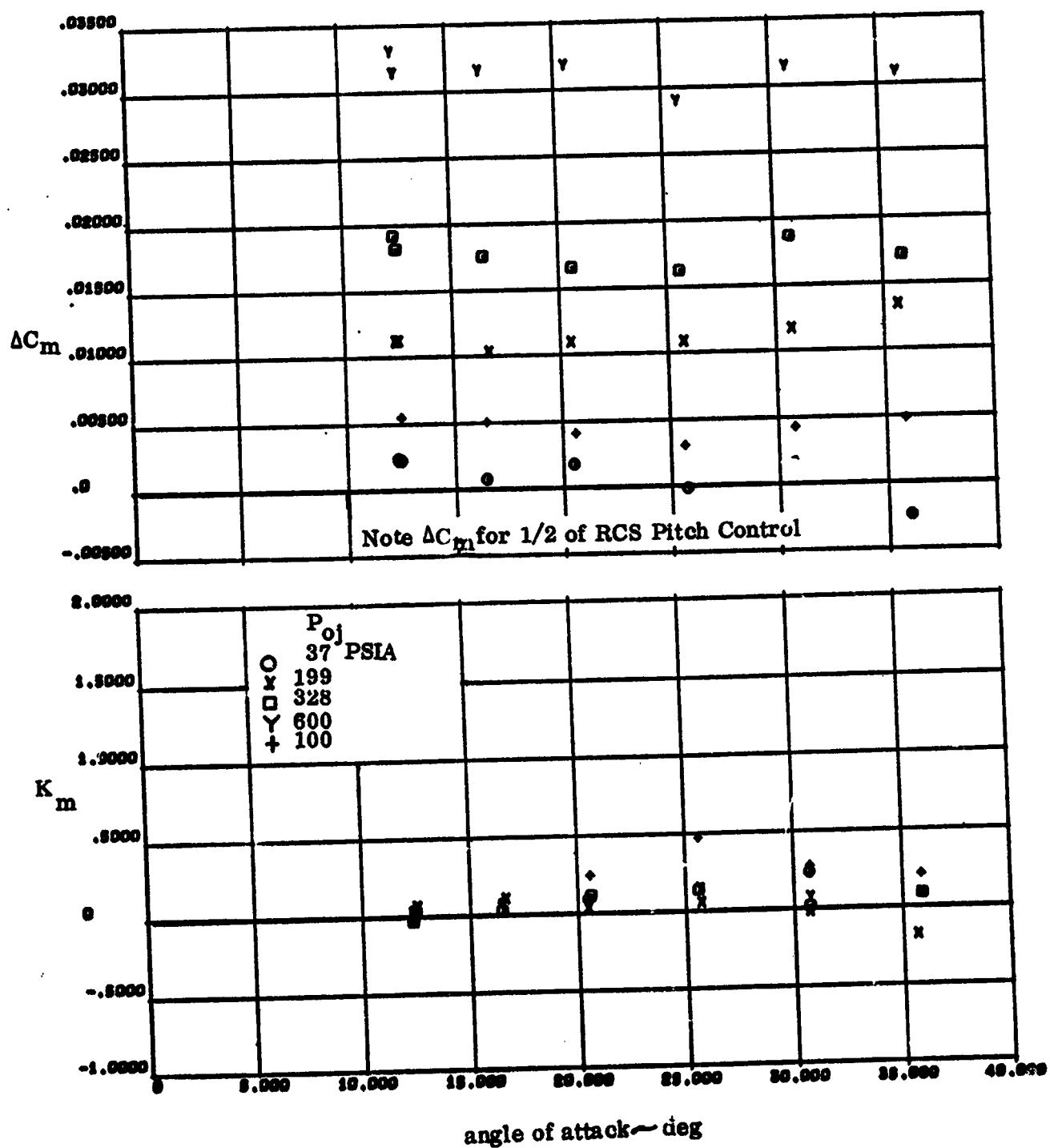
Figure 3-34. Effect of Supply Pressure on Nose Down Pitch Jet Normal Force Amplification at Mach 4.0, $R_e = 1 \times 10^6$/ft

3-73 .
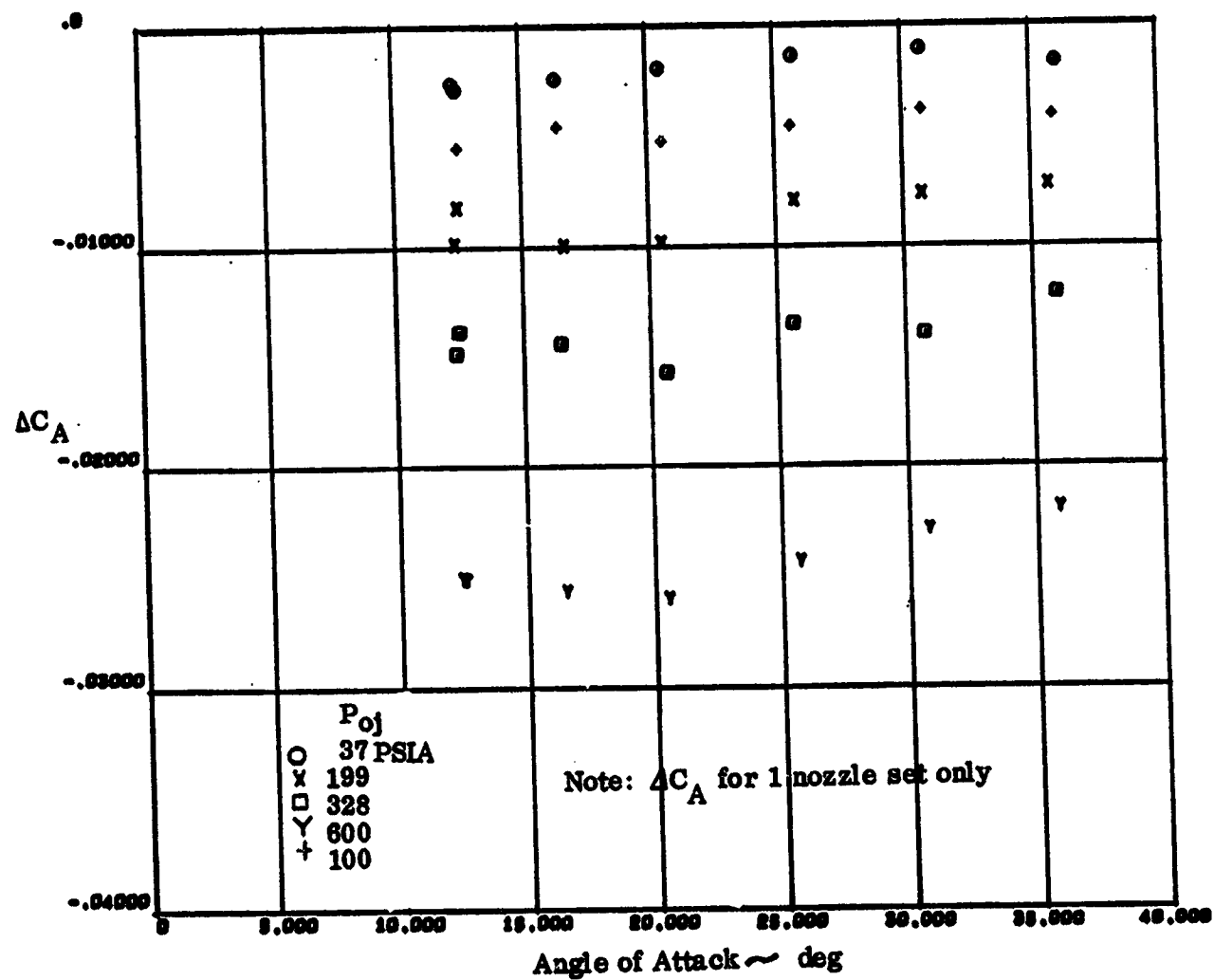
Figure 3-35. Axial Force Change due to Nose Down Jets at Mach 4.0, $R_e = 1\times10^6$/ft
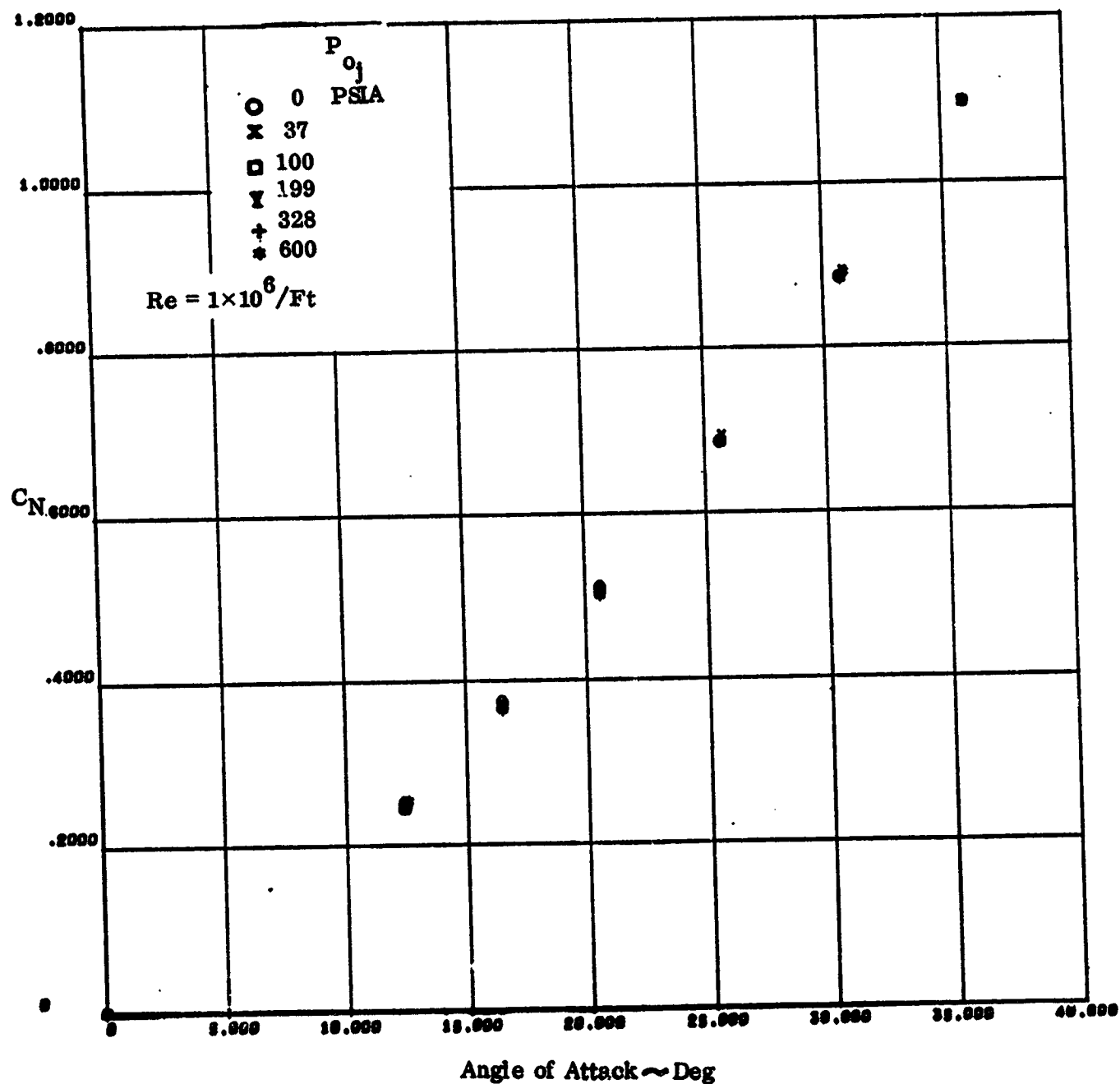
a) Normal Force

Figure 3-36. Effect of Pressure On Right Pitch/Roll Jet Exhausting
Upward at Mach 4.0
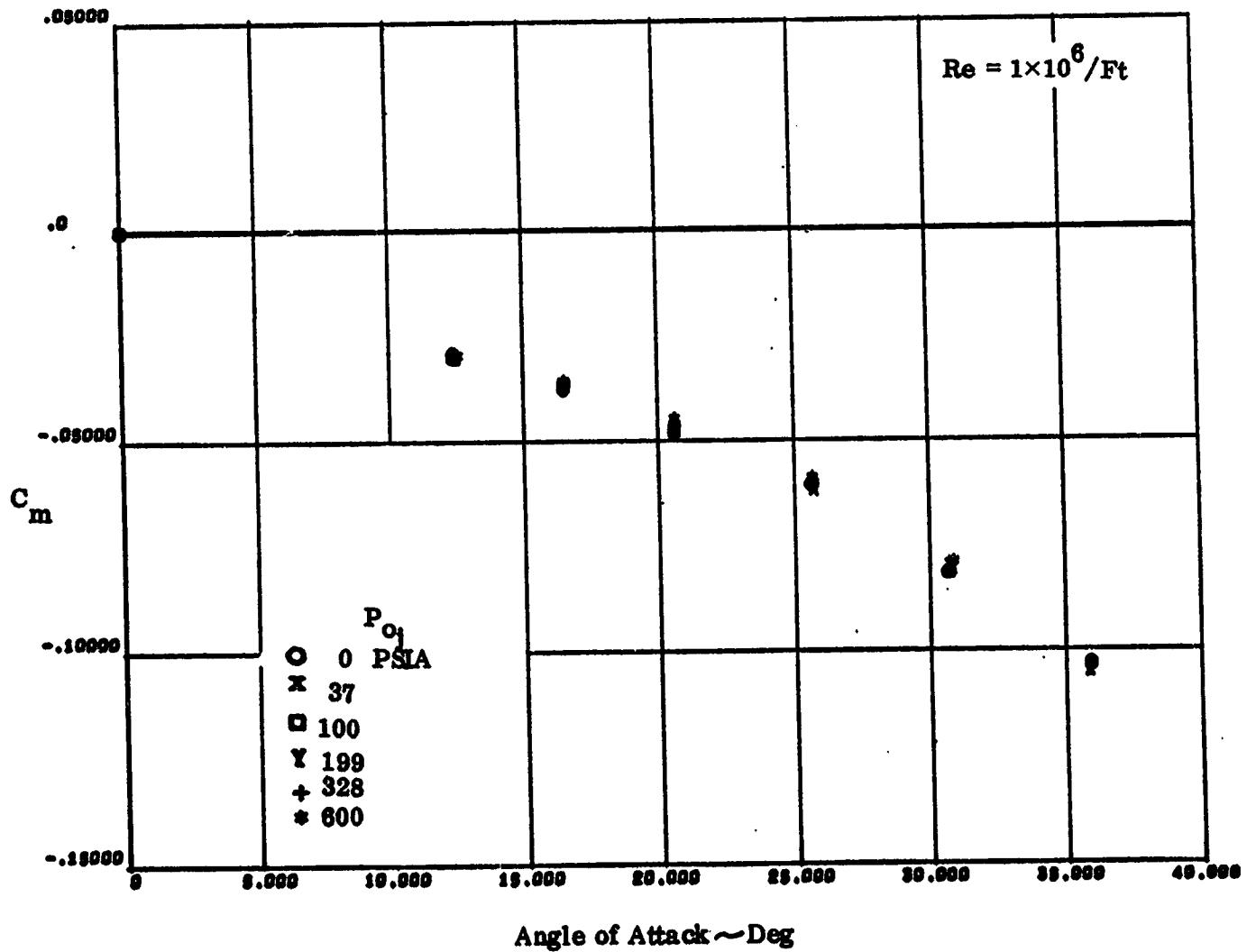
b) Pitching Moment

Figure 3-36. Effect of Pressure On Right Pitch/Roll Jet Exhausting Upward at Mach 4.0
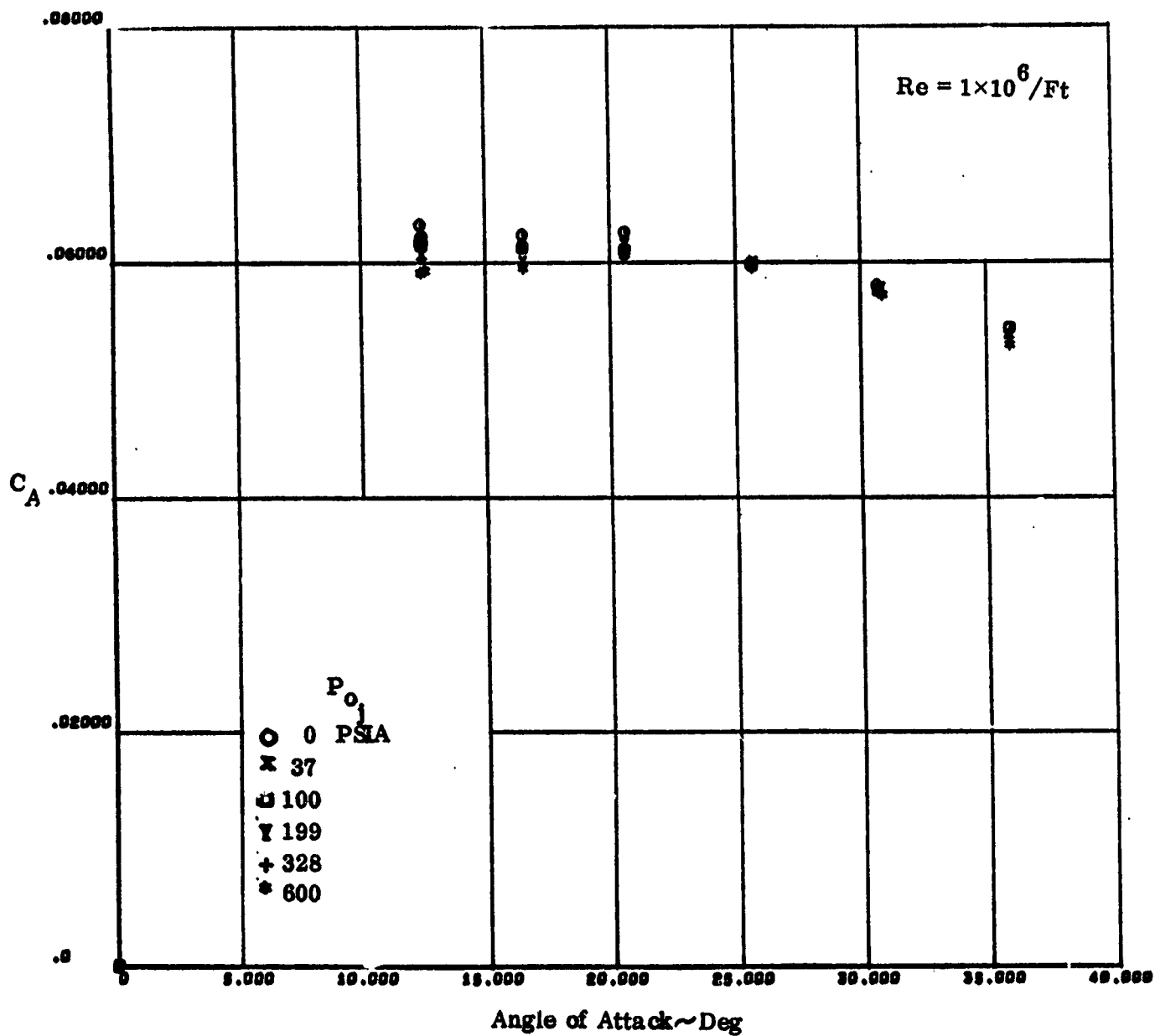
c) Axial Force

Figure 3-36. Effect of Pressure on Right Pitch/Roll Jet
Exhuasting Upward at Mach 4.0
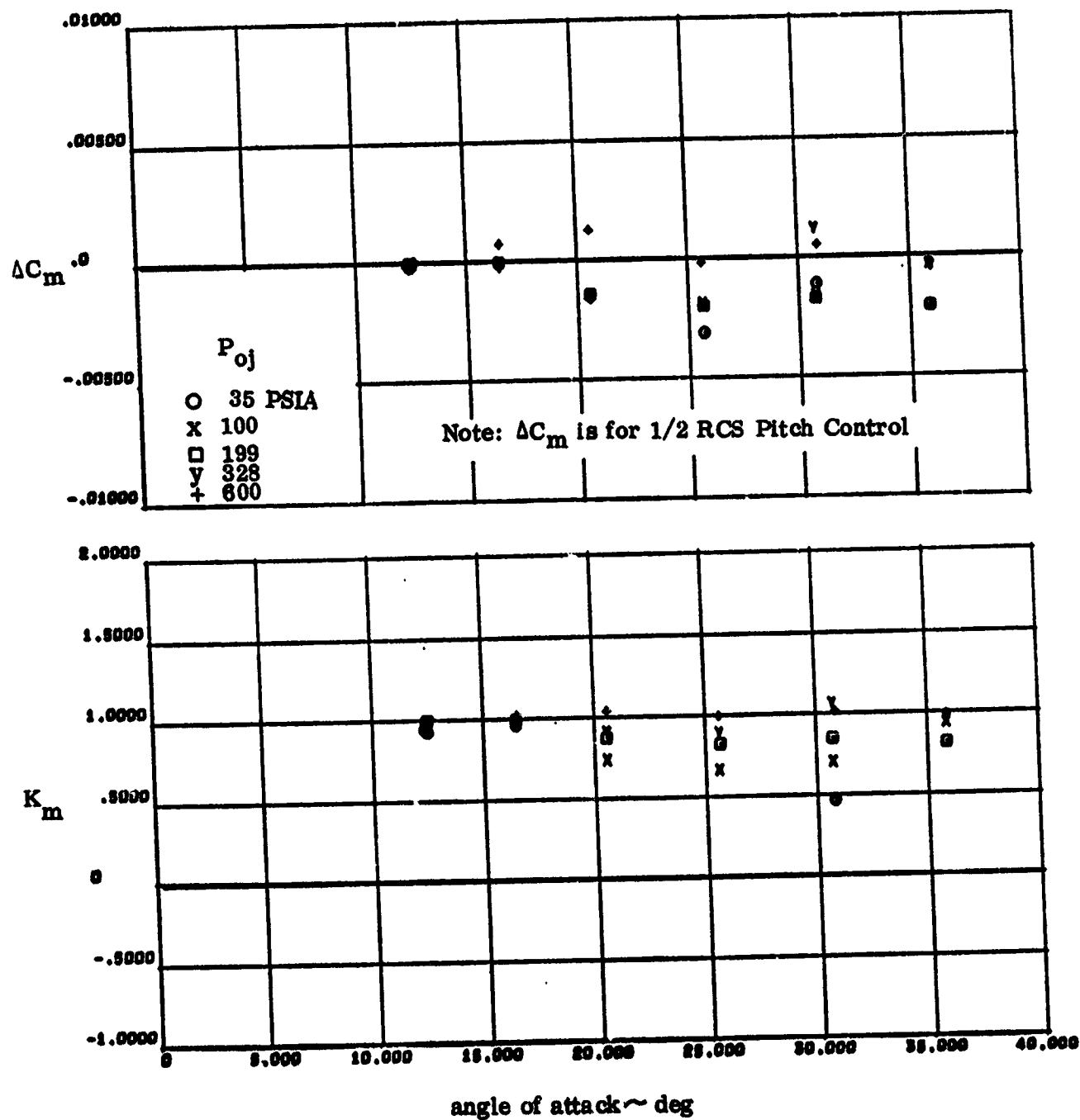
Figure 3-37. Effect of Supply Pressure on Nose Up Pitch Jet Pitching Moment Amplification at Mach 4.0, $Re = 1 \times 10^6/ft$

4.0 DATA ANALYSIS

In order to predict the effects of the reaction control system jets on the full scale vehicle, it is necessary to determine from the data, if possible, the major parameters which effect the plume/flow field interactions. Fortunately, the yaw amplification and the nose up pitch amplification appear very close to 1 so that no analysis of this data was required. The side force amplification and normal force amplification are of lesser importance and no analysis of this data was attempted because of the scatter and because the analysis of the moment data should be applicable to the force data. There then remain five interaction effects which must be analyzed if possible:

a)   rolling moment due to yaw control

b)   pitching moment due to yaw control

c)   rolling moment due to downward firing engines

d)   pitching moment due to downward firing engines

e)   rolling moment due to upward firing engine

f)   yawing moment due to upward firing engine

Not all of these interaction effects are of equal importance, the problems of nose downward pitch amplification and roll amplification are the most important by far. However, a limited amount of data analysis has been done on all of these interaction effects.

4.1 EFFECTS OF JET EXHAUSTING TOWARD WING

Section 2.1 presented a number of possible correlating parameters and Figures 4-1 to 4-11 present the incremental pitch and rolling moment coefficient data obtained from LRC runs 41 through 53 as well as the Mach 7.4 data from Ames run 38 correlated against a number of these parameters. These runs were used because the only jets being used are the pitch/roll jets exhausting toward the wing and body flap. Figure 4-1 shows a strong correlation at all Mach numbers (2.5-7.4) and Reynolds numbers $(1 \times 10^6/\text{ft}$ and $3 \times 10^6/\text{ft})$ for the incremental rolling moment with momentum ratio. The pitching moment data also shows strong nearly linear correlation except for the Mach 7.4 data. These same general results are shown in Figure 4-2 for thrust ratio, Figure 4-8 for exit pressure ratio, and Figure 4-9 for the ratio P_{oj}/q_∞. This was expected since all data at all Mach numbers was obtained from one nozzle and with one nozzle these parameters are constant factors times momentum ratio. In Figure 4-3 correlation of the data versus mass flow ratio show a very interesting trend. The incremental pitching moment at Mach 7.4 shows good correlation with the other Mach number data while incremental rolling moment is slightly poorer. The good correlation of the Mach 7.4 pitching moment data could be taken to mean that mass

flow ratio is the most important parameter not momentum ratio, but for a fixed nozzle based on nozzle exit area the mass flow ratio is equal to the square root of momentum

$$\frac{\dot{m}_j}{\dot{m}_\infty} = \left[\left(\frac{\Phi_j}{\Phi_\infty}\right) \quad \frac{A_j P_j}{A_\infty P_\infty} \quad \left(\frac{R_\infty T_\infty}{R_j T_j}\right)\right]^{1/2}$$ (4-1)

ratio times temperature ratio and this is interpreted as a possible temperature ratio effect in addition to the momentum ratio effect. Figure (4-4) shows the tunnel data was obtained at 4 kinetic energy ratios which consists of the product of temperature ratio and Mach number ratio. This figure shows that temperature effects must be a secondary effect compared to momentum ratio. Figure 4-5 shows a good correlation of the data at Mach 4 with the Mach disk height jet interaction parameter, given by 2-1 which also relates to momentum ratio at fixed Mach number. The lower Mach number data being off of the Mach 4 line leads to the interpretation that momentum ratio is the better parameter. Strike (reference 19) correlated jet interaction data to a parameter Φ based on an application of the blast wave analogy to the jet inter-action phenomenon and has the following form

$$\Phi = \left(\left(P_{oj}/P_\infty\right) M_\infty^2 \ (K\lambda_t)^{-3/4}\right) \sqrt{d_t/(c/\beta)}$$ (4-2)

where

c = wing chord length

$$\lambda_t = \rho_t u_t / \rho_\infty u_\infty$$

$$K = 1 + (1 + \frac{2}{\gamma_\infty - 1} M_\infty^2)\left(\frac{c_{p_j} T_{oj}}{c_{p_\infty} T_{o_\infty}}\right) + \frac{2}{\gamma_\infty - 1} \frac{1}{\gamma_\infty M_\infty^2}$$

$$\beta = \sqrt{M_\infty^2 - 1}$$

and

$$c_{p_j} = \frac{\gamma_j R_j}{\gamma_j - 1} \ , \ c_{p_\infty} = \frac{\gamma_\infty R_\infty}{\gamma_\infty - 1}$$

4-2

In this correlation parameter, all the jet properties are referenced to the conditions existing at the nozzle throat instead of the conditions existing at the nozzle exit. The data of Figure 4-6 shows good correlation at Mach 4.0 but the parameter does not work for the other Mach numbers. A correlation against plume initial turning angle is shown in Figure 4-7 where again some correlation is seen within the Mach 4 set but not at the other Mach numbers. The Mach 7.4 data on Figure 4-8 argue against exit pressure being a prime correlating parameter except as it occurs in the momentum ratio. Section 2.3 suggested that if a near vacuum plume impingement analogy were the primary cause of the induced loads then plume size and P_{oj}/P_∞ from equation 2-24 or Herron's parameter (reference 11) would be good correlating parameters. Figures 4-10 and 4-11 do indeed show that these parameters do correlate with the data at Mach 4.0 but again the other Mach number data must fall on different curves.

On an overall basis it appears that momentum ratio is the primary parameter causing the induced moments and that all other parameters are secondary.

4.1.1 PLUME IMPINGEMENT EFFECTS - If moment ratio is the primary parameter, is it because the plume impingement loads are the predominant effect? In order to answer this question and to be able to correct the data for the fact that the model pitch down nozzles were out of scaled position due to model stress requirements, the plume impingement moments were estimated using the 5 point method (equation 2-20) to define the plume radius at the wing and body flap based on an equivalent single nozzle (area equal to the sum of individual nozzle areas). Isentropic flow expansion was assumed from the nozzle to this area. Since the plume Mach number was high, a modified Newtonian approximation was used to define the stagnation pressure at the plume centerline. This stagnation pressure was assumed to apply across the entire plume radius since the buildup of body boundary layer from plume flow would keep pressures higher than the source flow assumptions of equation 2-25 and it should be a conservative assumption.

Figure 4-12 presents a sample of the prediction of pitching moment resulting from plume impingement at the Mach 4, $R_e = 1 \times 10^6$/ft test condition. Note that most of it comes from the body flap which is due in part to the pitch jets being inboard of their scale location, but is also an indication that the primary part of plume impingement effects is on the body flap and in the base region.

4.1.2 <u>PROPOSED EMPIRICAL MODEL</u> - Since Figure 4-12 showed that most of the plume impingement occurs in the body base region, the predicted plume impinge-ment rolling and pitching moments were removed from the incremental data of Figure 4-1.

$$\Delta C_{\ell_{int}} = \Delta C_{\ell} - C_{\ell_{imp}} \tag{4-3}$$

$$\Delta C_{m_{int}} = \Delta C_m - C_{m_{imp}} \tag{4-4}$$

The resultant interaction increments are shown in Figure 4-13 as a function of momentum ratio and from which the expressions

$$\Delta C_{\ell_{int}} = -0.00012805 \left(\frac{\Phi_j}{\Phi_\infty}\right)^{0.71236} \tag{4-5}$$

$$\Delta C_{m_{int}} = +0.0002637 \left(\frac{\Phi_j}{\Phi_\infty}\right)^{1.03824} \tag{4-6}$$

were derived.

Attempts were made to find ways of improving the correlation and to correlate based on the ratio of the interaction increment to jet moment as is done in amplifi-cation factor. Figure 4-14 shows that this results in much larger scatter at the low momentum ratios where thrust moments are near zero and no better correla-tions could be found at this time. Thus, the proposed empirical model of jet effects is:

a)   roll control

     I   rolling moment

$$C_{\ell_{induced}} = C_{\ell_D} + C_{\ell_u} \qquad (4\text{-}7)$$

       where C_{ℓ_u} will be defined in Section 4.3

       and $C_{\ell_D} = C_{\ell_{imp}} + \Delta C_{\ell_{int}}$ (4-8)

           $C_{\ell_{imp}}$ = predicted impingement rolling moment

           $\Delta C_{\ell_{int}}$ = equation 4-5

     II   pitching moment

$$C_{m_{induced}} = C_{m_{imp}} + \Delta C_{m_{int}} \qquad (4\text{-}9)$$

           $C_{m_{imp}}$ = predicted impingement pitching moment

           $\Delta C_{m_{int}}$ = equation 4-6

b)   pitch down control

$$C_{m_{induced}} = C_{m_{imp}} + 2(\Delta C_{m_{int}}) \qquad (4\text{-}10)$$

           $C_{m_{imp}}$ = predicted impingement moments

           $\Delta C_{m_{int}}$ = equation 4-6

4.2 EFFECTS OF JET EXHAUSTING PAST FIN - The data from Langley UPWT runs 54 to 66 was used in this correlation. No Mach 7.4 data was obtained for the single jet exhausting past the fin. The reaction jets mounted on the right side of the fin were used so that a positive rolling (right wing down) moment is obtained from the jet thrust. Figure 4-15 shows that a negative rolling moment is induced on the fin as well as nose right yawing moment by this half of the roll control. Figure 4-15 shows also that the induced effects are very sensitive to angle of attack and also to jet pressure. There appears to be an angle of attack near 40 degrees where all the induced effects disappear.

Figure 4-16 shows that there appear to be correlation of these induced effects with jet exit momentum ratio but that the angle of attack effects cause a large scatter. A number of correlations were attempted to remove this angle of attack effect without appreciable success. A correlation of the incremental data ratioed by the RCS thrust moments against momentum ratio showed that using such a parameter increases the scatter as the thrust moment approach zero.

Therefore a correlation was made of the peak induced effects against momentum ratio. Figure 4-17 shows that a rather consistant trend was found for the angle of attack at . which the peak incremental loads occur when plotted against jet momentum ratio. An extrapolation was also made of the data trends above 30 degrees and it appears that above 39 degrees all induced effects on the fin disappear. A correlation of the peak rolling and yawing moments was also made against momentum ratio and the following empirical relationships were obtained:

$$\Delta C_{\ell_p} = -.000087037 \left(\frac{\Phi_j}{\Phi_\infty}\right)^{.98545} \tag{4-11}$$

$$\Delta C_{n_p} = 0.00011216 \left(\frac{\Phi_j}{\Phi_\infty}\right)^{1.0676} \tag{4-12}$$

and these curves are shown in Figure 4-16.

Comparisons were made between the single jet exhausting upward data and the data for complete roll control with the jet down data removed. This data showed much less effectiveness for the jet exhausting upward caused by the down jet effects on the body   (see oil flow data in reference 1), and equation 4-11 was multiplied by 0.46 to account for this coupling effect.

4.2.1 EMPIRICAL MODEL - Equations 4-11 and 4-12 can be combined with Figure 4-17 to predict the peak yawing moment and rolling moments of the roll jet exhausting past the fin and the angle of attack at which they occur. The data on Figure 4-15 shows a sine curve shape for the data above and below the peak value angle of attack. Thus, the proposed empirical model for this part of the roll control becomes:

4-6

a) rolling moment

    I $\alpha > 39°$

$$C_{\ell_u} = 0 \tag{4-13}$$

    II $\alpha_{peak} < \alpha < 39°$

$$\alpha_{peak} = f\left(\frac{a_j}{\Phi_\infty}\right) \text{from Figure 4-17}$$

$$C_{\ell_u} = \Delta C'_{\ell_p} \sin\left(\frac{\pi}{2}\left(\frac{39 - \alpha}{39 - \alpha_{peak}}\right)\right) \tag{4-14}$$

$$\Delta C'_{\ell_p} = .46 \Delta C_{\ell_p} \quad \text{from equation 4-11}$$

    III $\alpha < \alpha_{peak}$

$$C_{\ell_u} = \Delta C_{\ell_p} \sin\left(\frac{\pi}{2} \frac{\alpha}{\alpha_{peak}}\right) \tag{4-15}$$

b) yawing moment

    I $\alpha > 39°$

$$C_{n_{induced}} = 0 \tag{4-16}$$

    II $\alpha_{peak} < \alpha < 39$

$$C_{n_{induced}} = \Delta C_{n_p} \sin\left(\frac{\pi}{2}\left(\frac{39 - \alpha}{39 - \alpha_{peak}}\right)\right) \tag{4-17}$$

$$\Delta C_{n_p} \text{ from equation 4-12}$$

    III $\alpha < \alpha_{peak}$

$$C_{n_{induced}} = \Delta C_{n_p} \sin\left(\frac{\pi}{2} \frac{\alpha}{\alpha_{peak}}\right) \tag{4-18}$$

No plume impingement corrections have been attempted with this data at this time but such corrections would be important for higher altitude simulations.

4.3 EFFECTS OF JETS EXHAUSTING OVER WING

Figure 3-15 showed that the yaw jets did induce a nose up pitching moment and a wing down rolling moment and the incremental induced data from Langley UPWT runs 1 through 20 as well as two Mach 7.4 runs were analyzed to see if correlations were possible for these induced effects. All yaw data was obtained with the yaw jets on the left side creating a negative (nose left) yawing moment. Figure 4-18 shows that these jets induced a left wing down (negative) roll and a nose up pitching moment which increased with increasing angle of attack up to the highest angle tested.

Figure 4-19 shows that there is a correlation with momentum ratio but that the scatter from other factors, principally angle of attack, is very large. All correlations of the incremental data showed this large scatter so correlations were made with the incremental data ratioed by the yaw thrust moment as shown in Figure 4-20. Note the change in signs caused by the negative yaw thrust moment.

Figure 2-21 showed that the angle of attack determined to a large degree the extent of the wake region at the exit plane of the yaw nozzles and Figure 4-21 shows two parameters which were generated based on this hypersonic approximation in an attempt to account for angle of attack effects. The first of these parameters is the distance along the centerline of the nozzles from the nozzle exits to the edge of the wake region (Y_{edge}) and the second parameter is a measure of distance from the plume maximum diameter (Y_{max}) to the edge of the wake region ($Y_{edge} - Y_{max}$). The plume distance to the maximum diameter was determined from the five point method. If ($Y_{edge} - Y_{max}$) is negative the plume tries to penetrate into the flow, if positive the plume fully expands inside the wake. Figures 4-22 and 4-23 show correlations of the incremental induced data with these parameters. The data shows a strong correlation but the momentum ratio or other thrust related effect still must be taken into account. Figure 4-24 shows the induced data ratioed by thrust moment again which removes most of the momentum ratio effect on rolling moment data although adding scatter at low thrust to the pitching moment data. The straight lines shown on this figure represent the data correlating equations:

$$\frac{\Delta C_{\ell}}{C_{n_T}} = 0.014036 \left(\frac{Y_{edge} - Y_{max}}{d_{equiv}} \right) + 0.1395 \qquad (4\text{-}19)$$

$$\frac{\Delta C_m}{C_{n_T}} = -0.031956 \left(\frac{Y_{edge} - Y_{max}}{d_{equiv}} \right) - 0.44956 \qquad (4\text{-}20)$$

4.4 EMPIRICAL MODEL SUMMARY

Based on the observed data of Section 3 and the data analysis of Section 4, the recommended empirical model for RCS thrust effects is:

4.4.1 NOSE UP PITCH RCS

$$C_{m_{control}} = C_{m_{thrust}} \qquad (4\text{-}21)$$

4.4.2 NOSE DOWN PITCH RCS

$$C_{m_{control}} = C_{m_{thrust}} + \Delta C_{m_{imp}} + \Delta C_{m_{ind}} \qquad (4\text{-}22)$$

$$\Delta C_{m_{ind}} = 0.0005274 \left(\frac{\Phi_1}{\Phi_\infty} \right)^{1.0328} \qquad (4\text{-}23)$$

$\Delta C_{m_{imp}}$ = predicted impingement (both sides)

4.4.3 ROLL RCS

$$\text{I} \qquad C_{\ell_{control}} = C_{\ell_{thrust}} + C_{\ell_{imp}} + C_{\ell_{ind}} \qquad (4\text{-}24)$$

$C_{\ell_{imp}}$ = predicted impingement (1 jet)

$$C_{\ell_{ind}} = C_{\ell_u} + C_{\ell_D} \qquad (4\text{-}25)$$

$$C_{\ell_D} = - \frac{C_{\ell_{thrust}}}{\left| C_{\ell_{thrust}} \right|} \, 0.00012805 \left(\frac{\Phi_1}{\Phi_\infty} \right)^{0.71236} \qquad (4\text{-}26)$$

a) $\alpha > 39°$

$$C_{\ell_u} = 0 \qquad (4\text{-}27)$$

b) $\alpha_{peak} < \alpha < 39°$

$$\alpha_{peak} = f\left(\frac{\Phi_1}{\Phi_\infty} \right) \qquad \text{Figure} \quad 4\text{-}17$$

$$C_{\ell_u} = \Delta C_{\ell_p} \sin\left(\frac{\pi}{2} \left(\frac{39 - \alpha}{39 - \alpha_{peak}} \right) \right) \qquad (4\text{-}28)$$

$$\Delta C_{\ell_p} = - \frac{C_{\ell_{thrust}}}{\left| C_{\ell_{thrust}} \right|} (.000040037) \left(\frac{\Phi_1}{\Phi_\infty} \right)^{.98545} \qquad (4\text{-}29)$$

c) $\alpha < \alpha_{peak}$

$$C_{\ell_u} = \Delta C_{\ell_p} \sin\left(\frac{\pi}{2} \frac{\alpha}{\alpha_{peak}}\right)$$

(4-30)

II   induced yaw

a) $\alpha > 39°$

$$C_{n_{ind}} = 0$$

(4-31)

b) $\alpha_{peak} < \alpha < 39°$

$$C_{n_{ind}} = \Delta C_{n_p} \sin\left(\frac{\pi}{2}\left(\frac{39-\alpha}{39-\alpha_{peak}}\right)\right)$$

(4-32)

$$\Delta C_{n_p} = \frac{C_{\ell_{thrust}}}{\left|C_{\ell_{thrust}}\right|} .0001216 \left(\frac{\Phi_1}{\Phi_\infty}\right)^{1.0676}$$

(4-33)

c) $\alpha < \alpha_{peak}$

$$C_{n_{ind}} = \Delta C_{n_p} \sin\left(\frac{\pi}{2} \frac{\alpha}{\alpha_{peak}}\right)$$

(4-34)

III   induced pitch

$$C_{m_{ind}} = C_{m_{imp}} + C_{m_{ind}}$$

(4-35)

$C_{m_{imp}}$ = 1 side jet impingement

$$C_{m_{ind}} = 0.0002637 \left(\frac{\Phi_1}{\Phi_\infty}\right)^{1.03824}$$

(4-36)

4.4.4 YAW RCS

I $C_{n_{control}} = C_{n_{thrust}}$

(4-37)

II   induced roll

$$C_{\ell_{ind}} = C_{n_{thrust}}\left(0.014206\left(\frac{Y_{edge} - Y_{max}}{de}\right) + .1395\right) \qquad (4\text{-}38)$$

III   induced pitch

$$C_{m_{ind}} = \left|C_{n_{thrust}}\right| \left(0.031956 \left(\frac{Y_{edge} - Y_{max}}{d_e}\right) + 0.44956\right) \quad (4\text{-}39)$$

$$Y_{edge} = f(x, \alpha, Z_{noz})$$

$$Y_{max} = Xmax \text{ from equation 2-20}$$

4.5 SCALING LAWS

The empirical model of the preceeding section broke the total induced load into a component caused by plume impingement and an induced component and scaling must account for these two parts of the total problem. It also appears that the scaling of one does not result in the scaling of the other.

4.5.1 <u>IMPINGEMENT</u> - The empirical impingement model of section 2.3 related both the plume impingement pressure and area to the plume diameter through the Newtonian pressure approximation, and isentropic expansion assumption. The plume diameter was then specified through a parameter which is approximately:

$$R_{max} = R_j (.69485) \left(\frac{A_t}{A_j}\right)^{.7398} \left(\frac{P_{o1}}{P_\infty}\right)^{.512} \frac{1}{(1 + \gamma_\infty M_\infty^2)^{.2418}}$$

$$x \frac{1}{(1 - \sin \theta_N)^{.3976}} \tag{4-40}$$

Thus to obtain a good approximation of the plume impingement loads it would appear that a scaled nozzle diameter, expansion ratio, exit angle, and chamber pressure to ambient pressure ratio are required. These requirements do not appear to be consistant to the scaling required for the interaction part of the problem and it would appear that impingement data should be obtained with scaled nozzles in a vacuum chamber where $\frac{P_{o1}}{P_\infty}$ would be corrected for $(1 + \gamma M_\infty^2)^{.2418}$. It also appears that the impingement part of all wind tunnel test data should be estimated and corrected out of the final interaction data.

4.5.2. <u>INTERACTION</u> - The empirical model of the preceeding section shows that jet exit momentum ratio is the primary parameter to be matched to scale pitch data to full scale and the thrust coefficient is the basic parameter for yaw data scaling.

The Mach 7.4 pitch data of Figure 4-3 also indicated a possible effect of temperature ratio as does the jet interaction data of equation 2-24 although Thayers criteria indicates that such effects should be small for these monopropellant thrusters.

Sufficient data does not exit from this test to isolate other parameters and at this time, the recommended procedure would be to match momentum ratio, thrust ratio, and temperature ratio in any other test to obtain a scaled nozzle and to correct the resulting induced data for the predicted scale nozzle impingement to obtain the interaction increments.
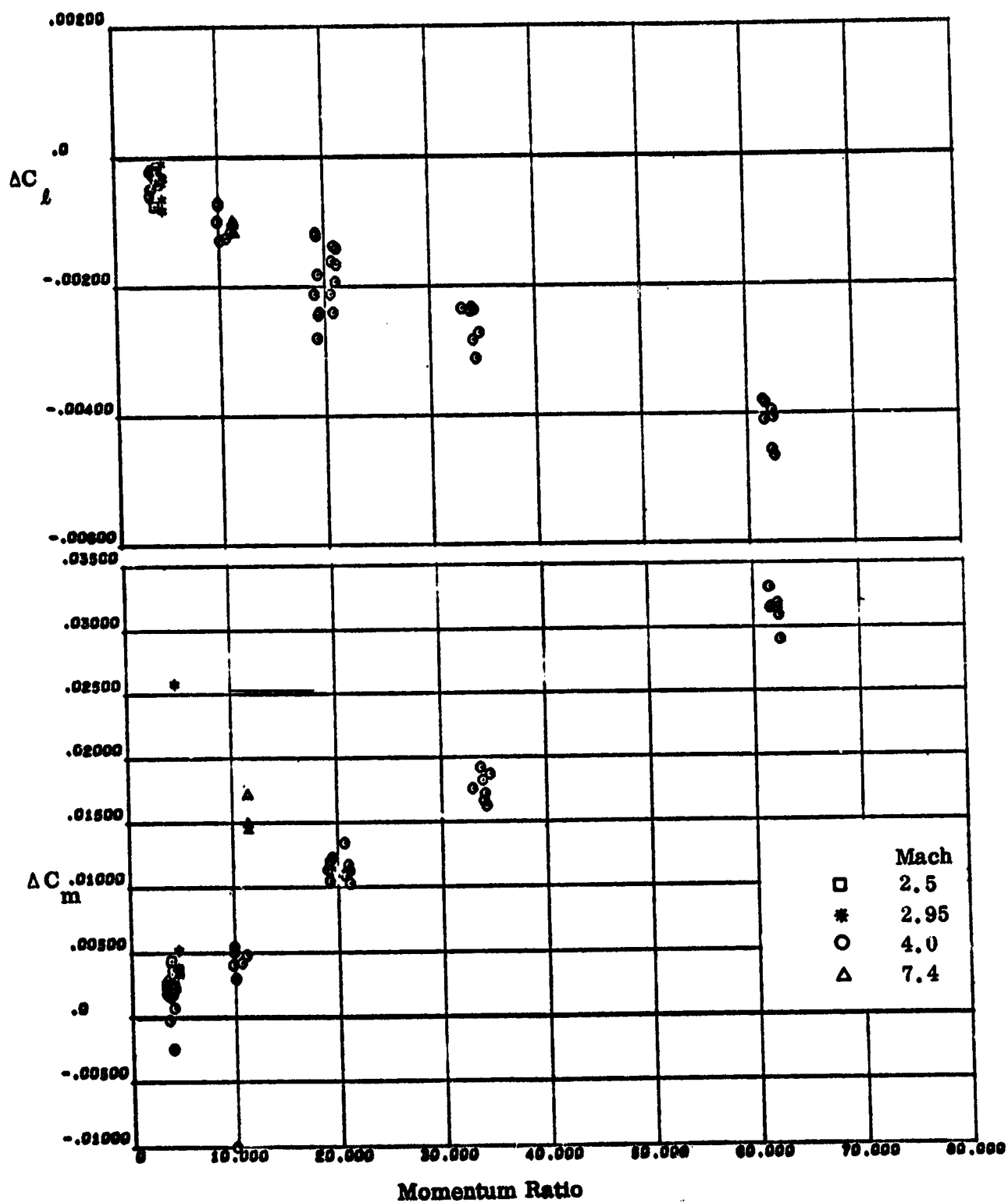
Figure 4-1. Incremental Pitch Down Jet Data Correlated to
Momentum Ratio
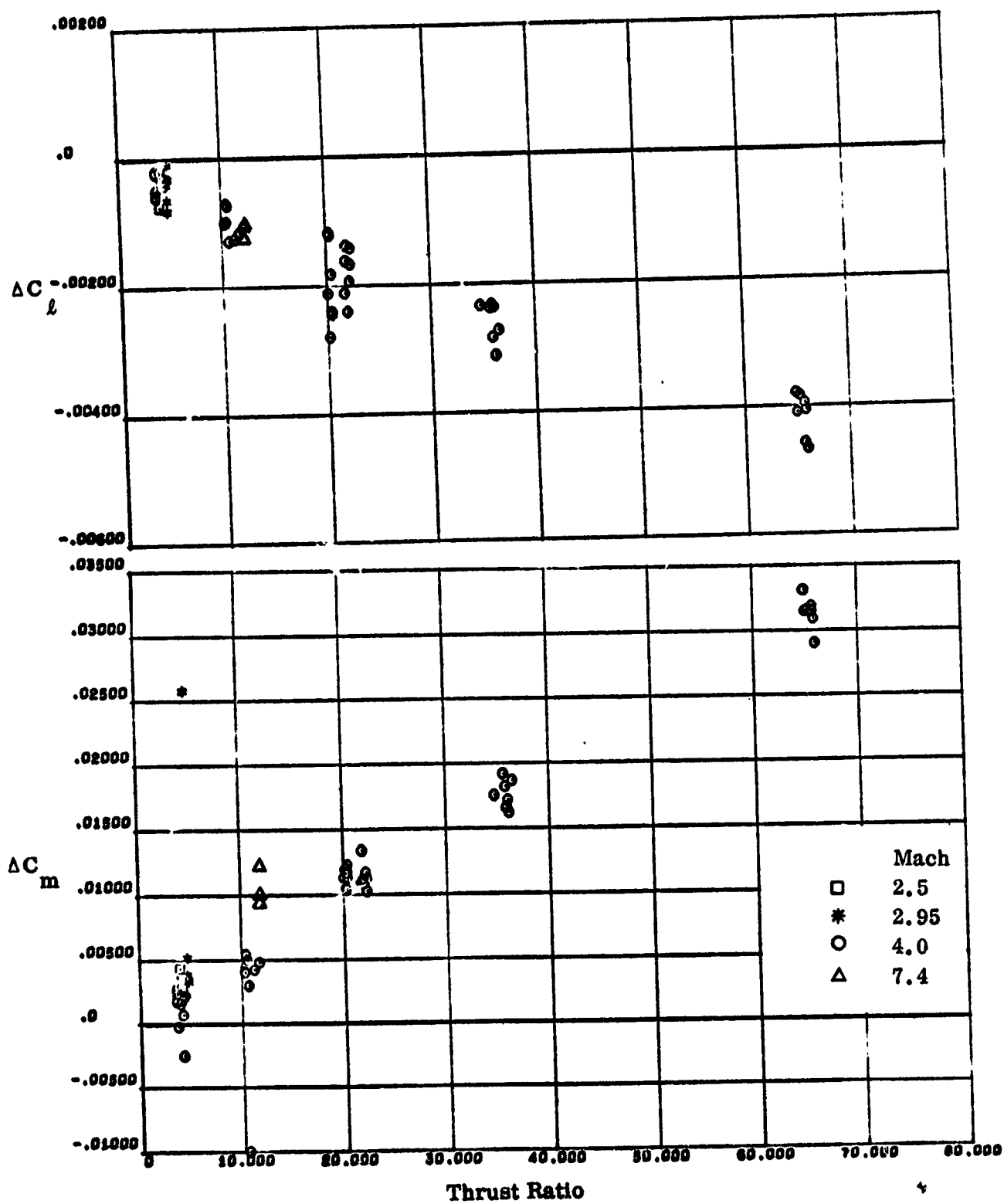
Figure 4-2. Incremental Pitch Down Jet Data Correlated to
Thrust Ratio

4-14
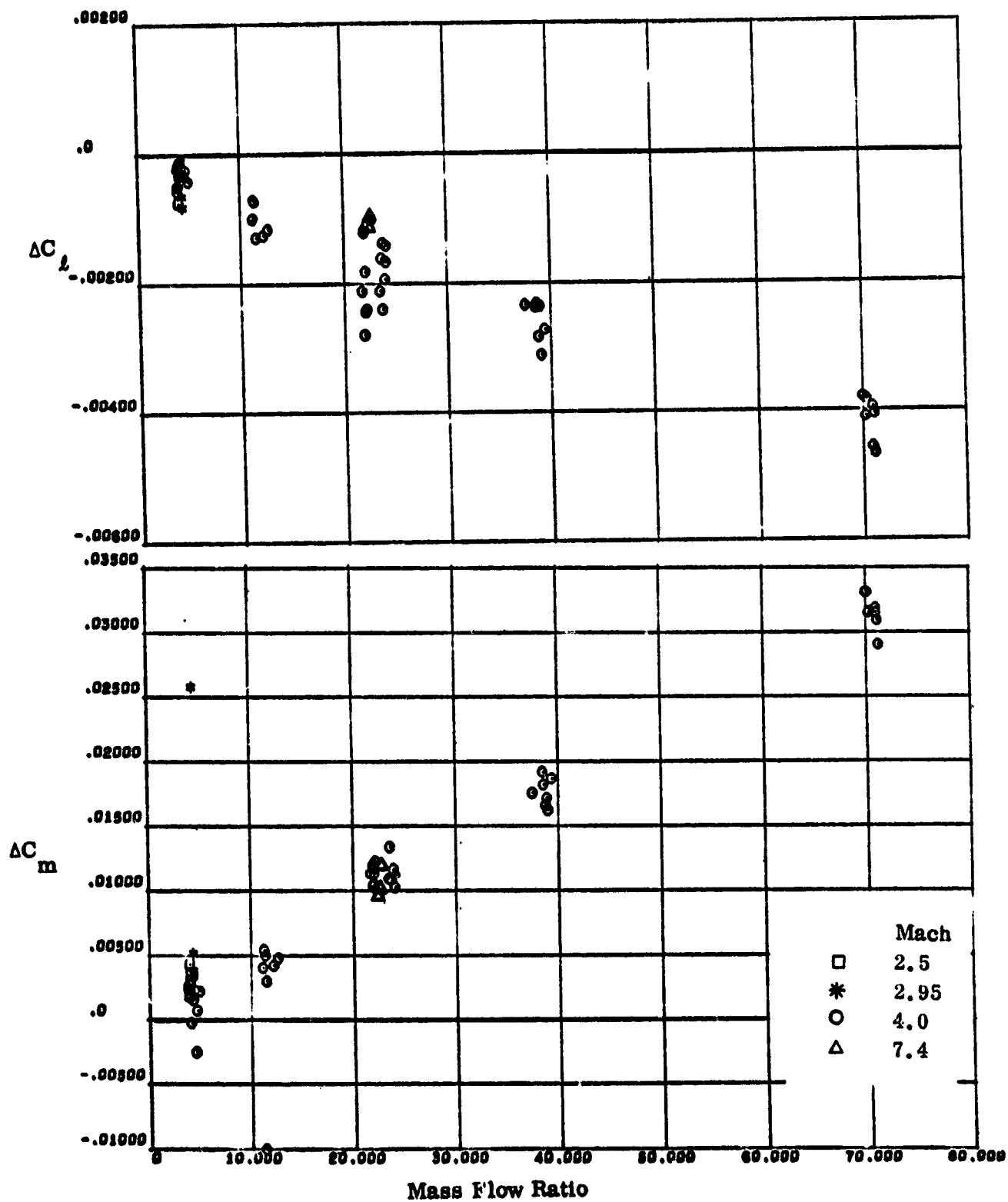
Figure 4-3. Incremental Pitch Down Jet Data Correlated to
Mass Flow Ratio
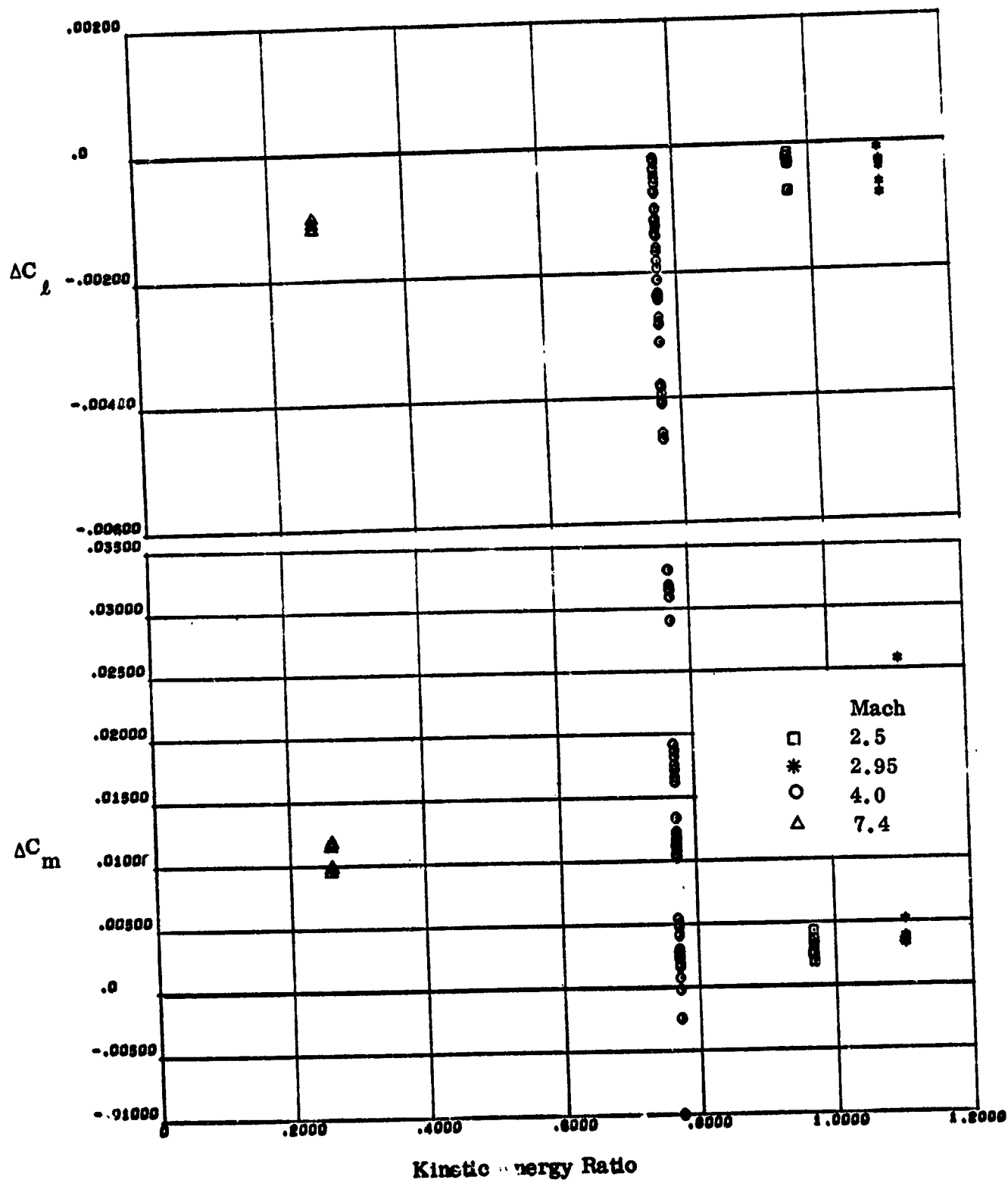
Figure 4-4. Incremental Pitch Down Jet Data Correlated to Kinetic Energy
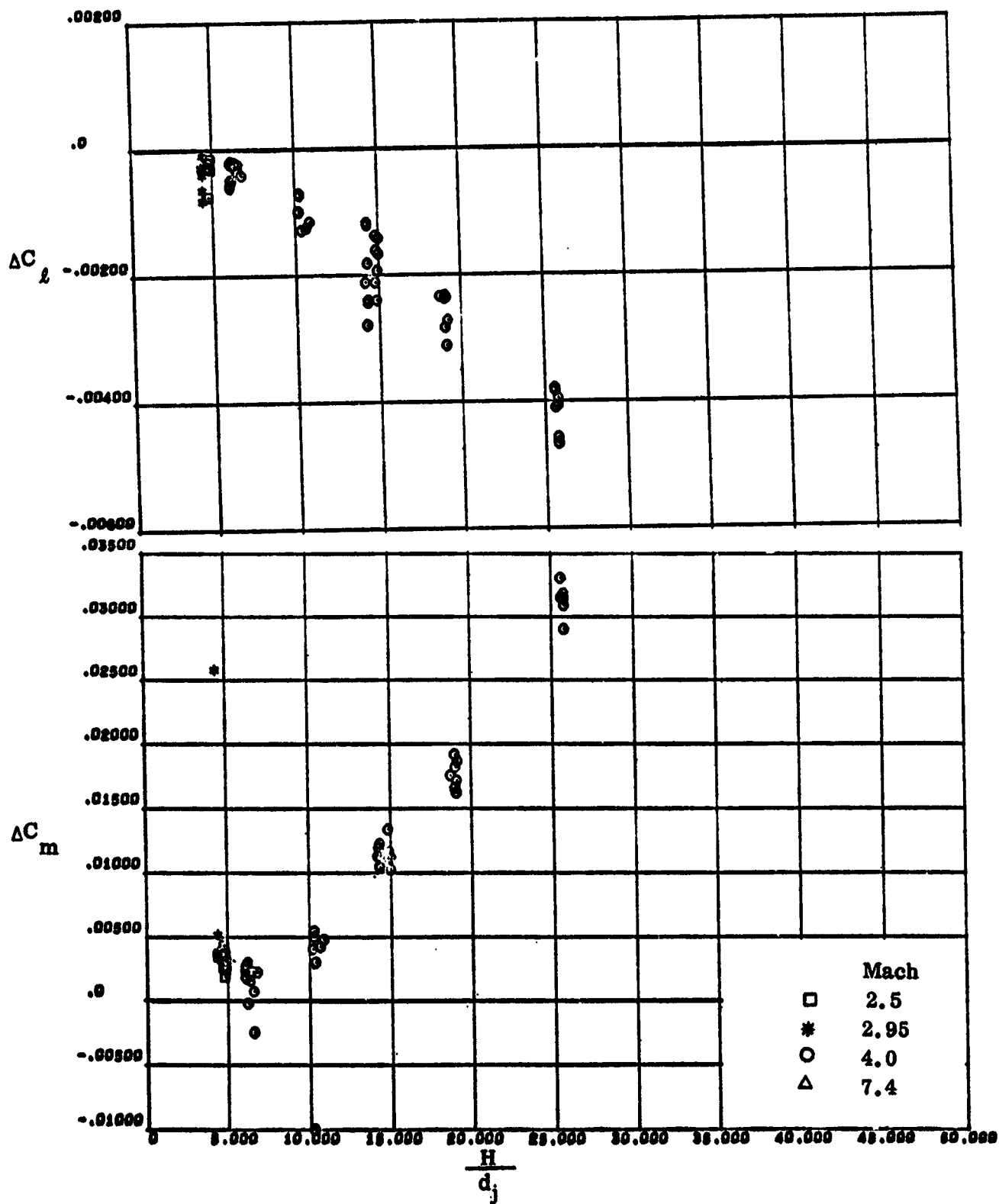
Figure 4-5. Incremental Pitch Down Jet Data Correlated to Mach Disk Height
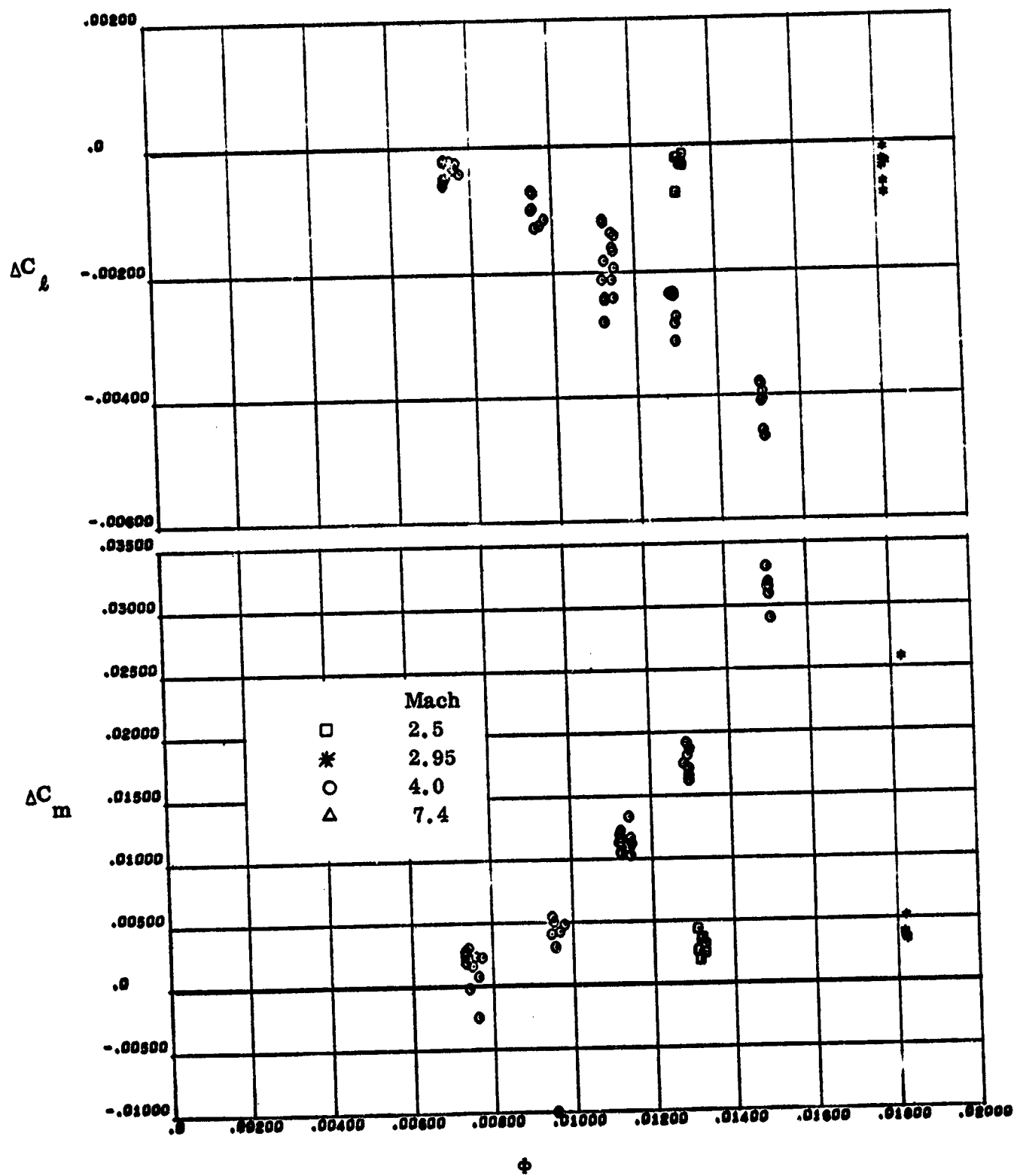
Figure 4-6. Incremental Pitch Down Jet Data Correlated to Strike's Jet Interaction Parameter
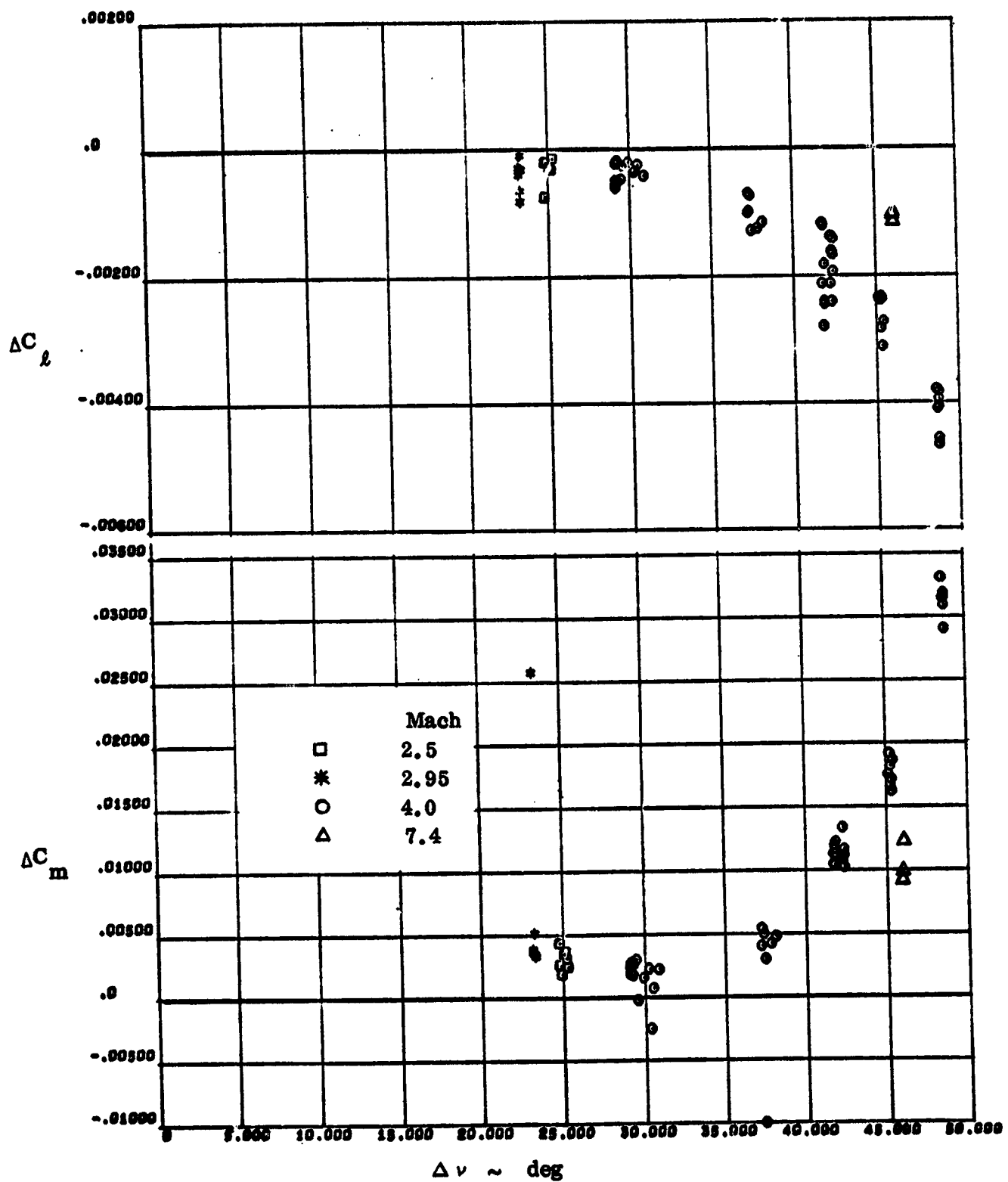
Figure 4-7. Incremental Pitch Down Jet Data Correlated to
Plume Initial Turning Angle

4-19
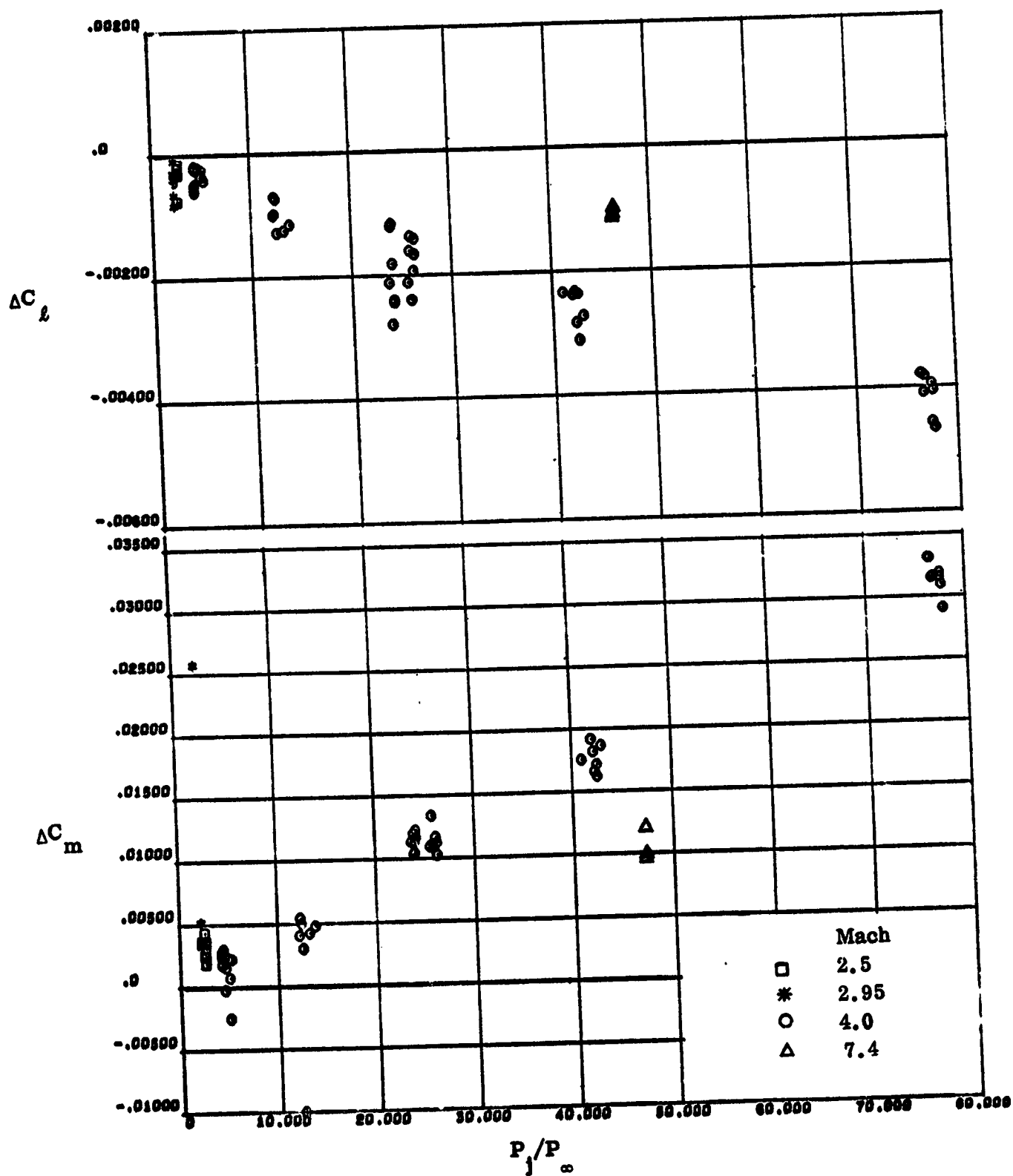
Figure 4-8. Incremental Pitch Down Jet Data Correlated with
Jet Exit Pressure Ratio
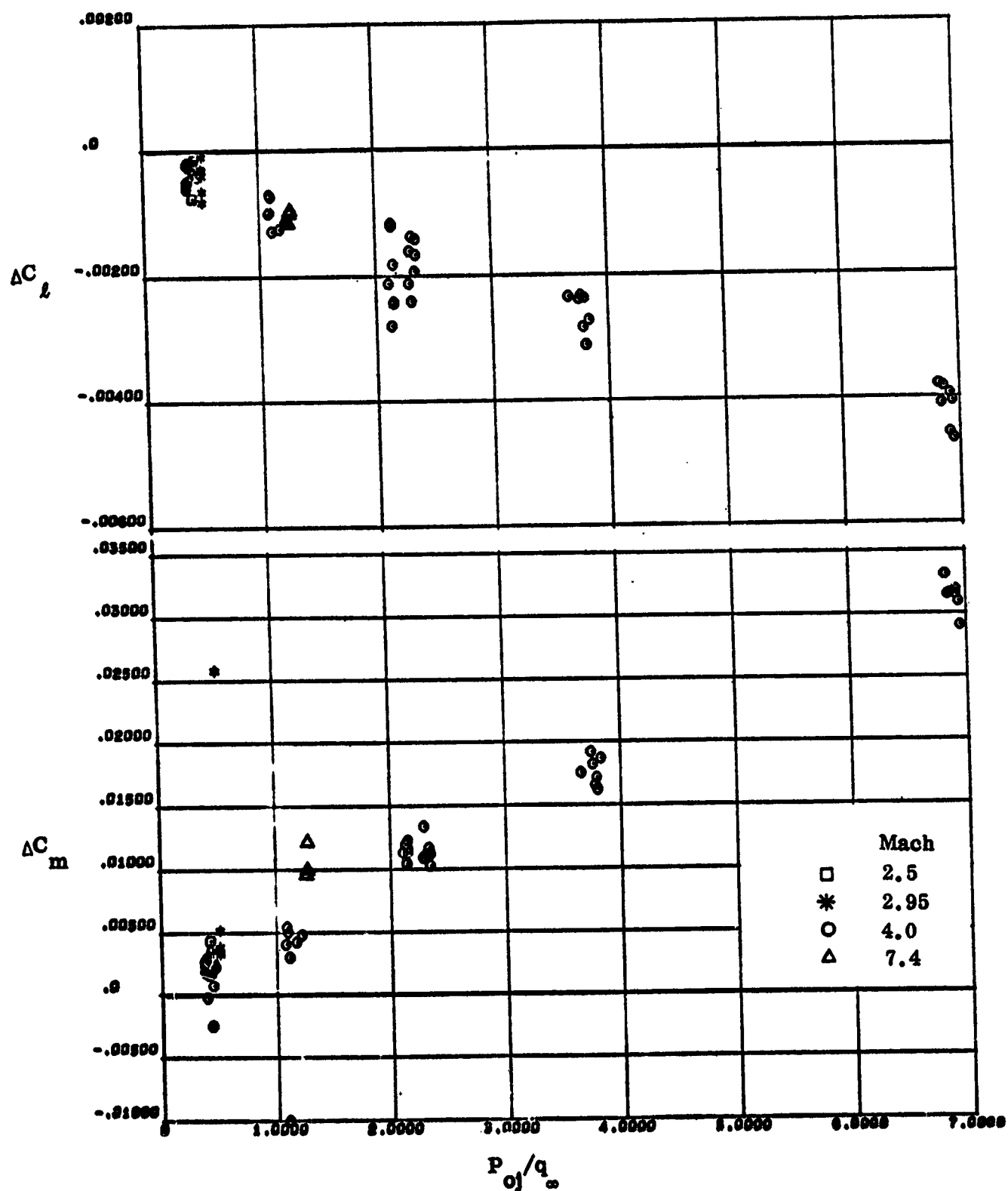
Figure 4-9. Incremental Pitch Down Jet Data Correlated with Supply Pressure Ratioed to Free Stream Dynamic Pressure

4-21
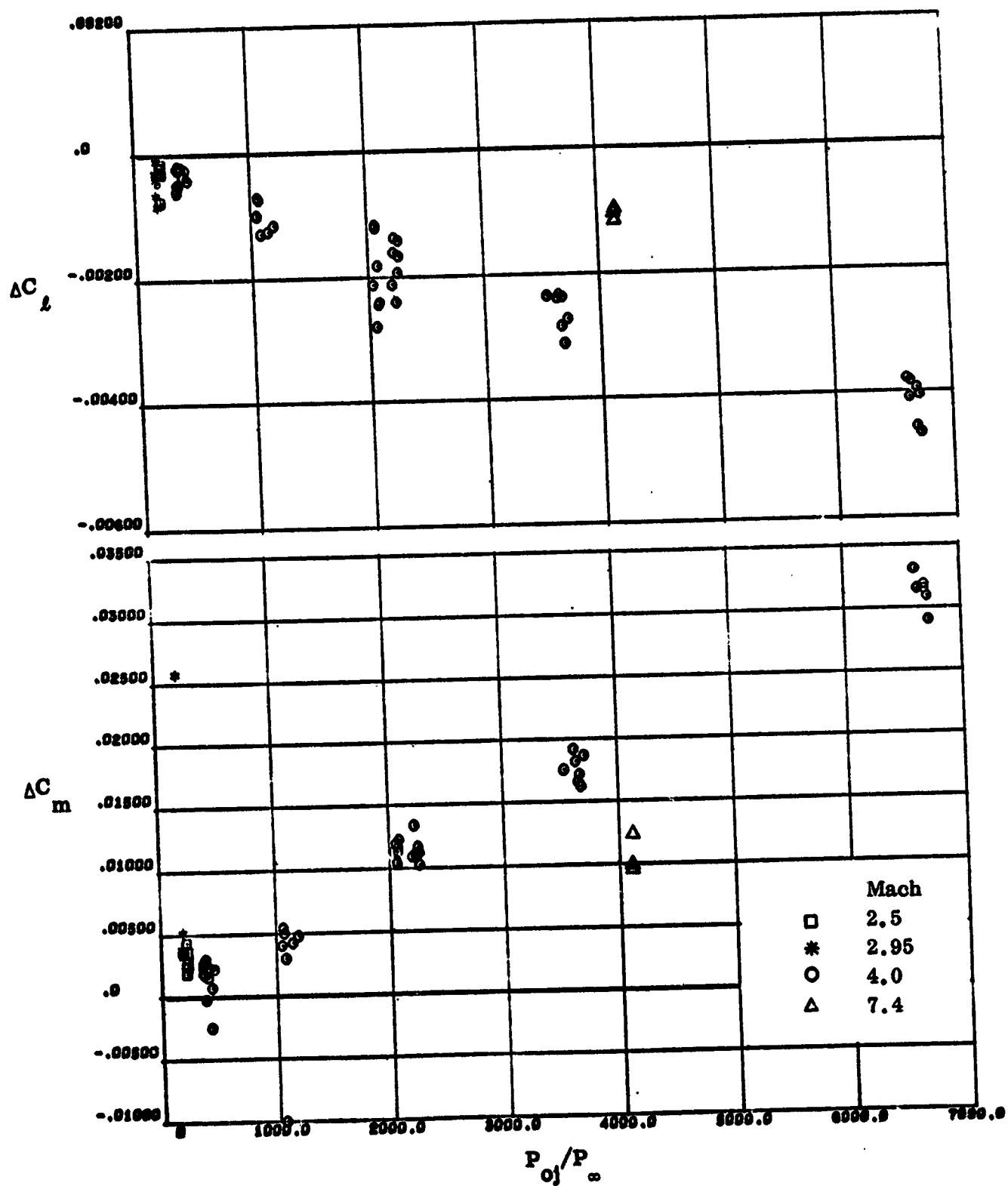
Figure 4-10. Incremental Pitch Down Jet Data Correlated to
Jet Supply Pressure Ratio
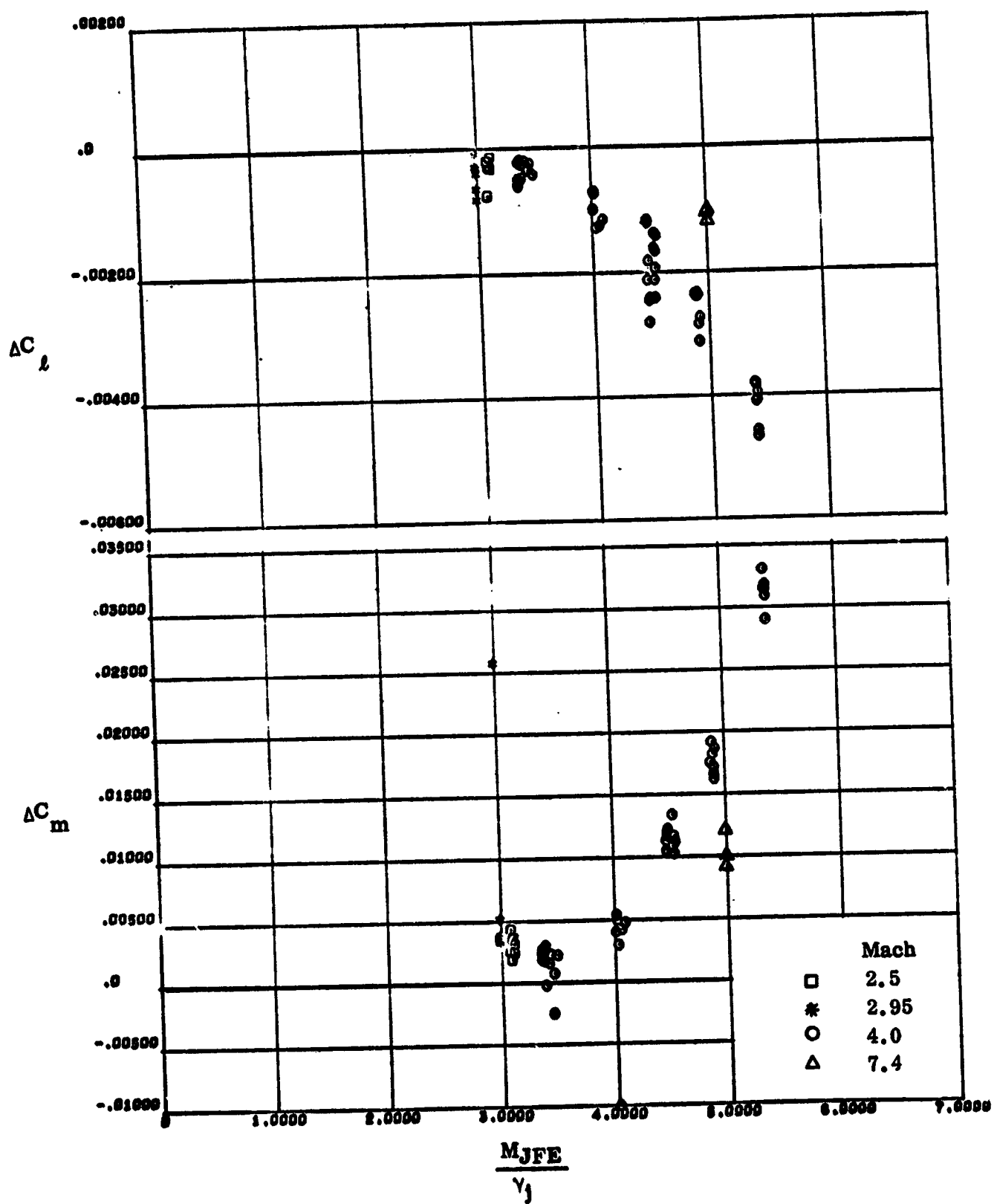
Figure 4-11. Incremental Pitch Down Jet Data Correlated
with Herrons Parameter

4-23
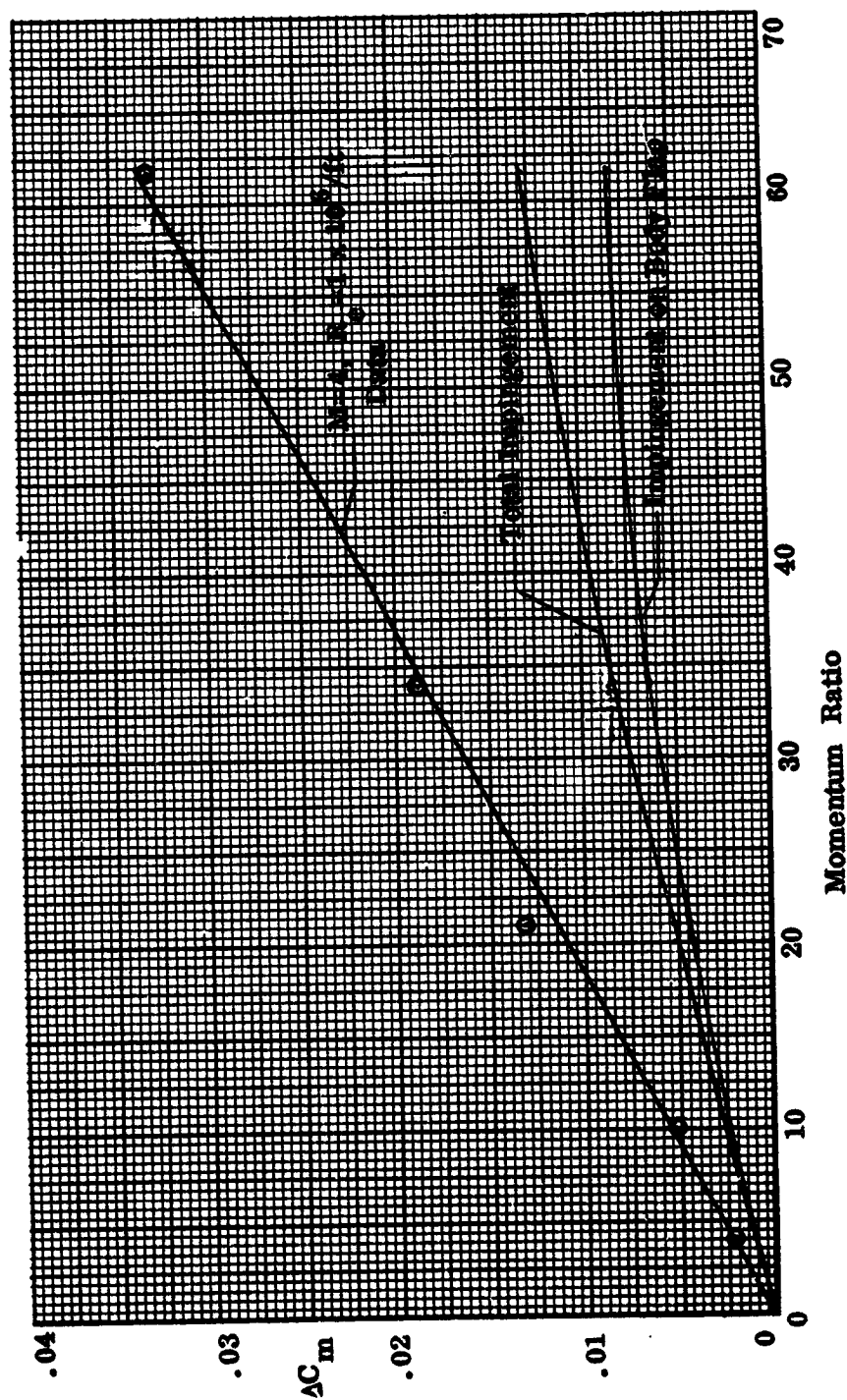
Figure 4-12. Estimated Impingement Moment at Mach 4 Test Condition
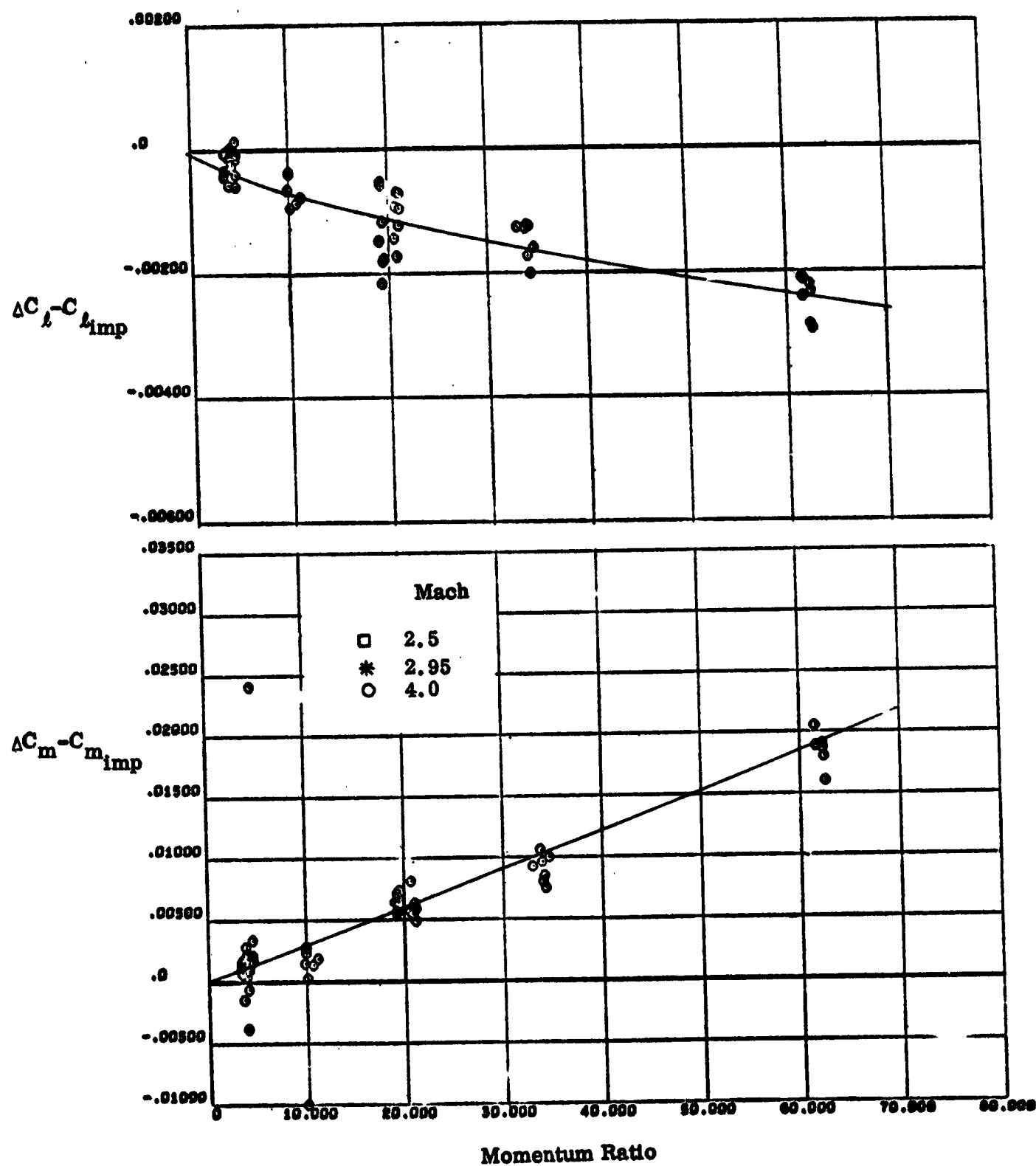
Figure 4-13. Incremental Data Corrected for
Impingement Correlated with
Momentum Ratio
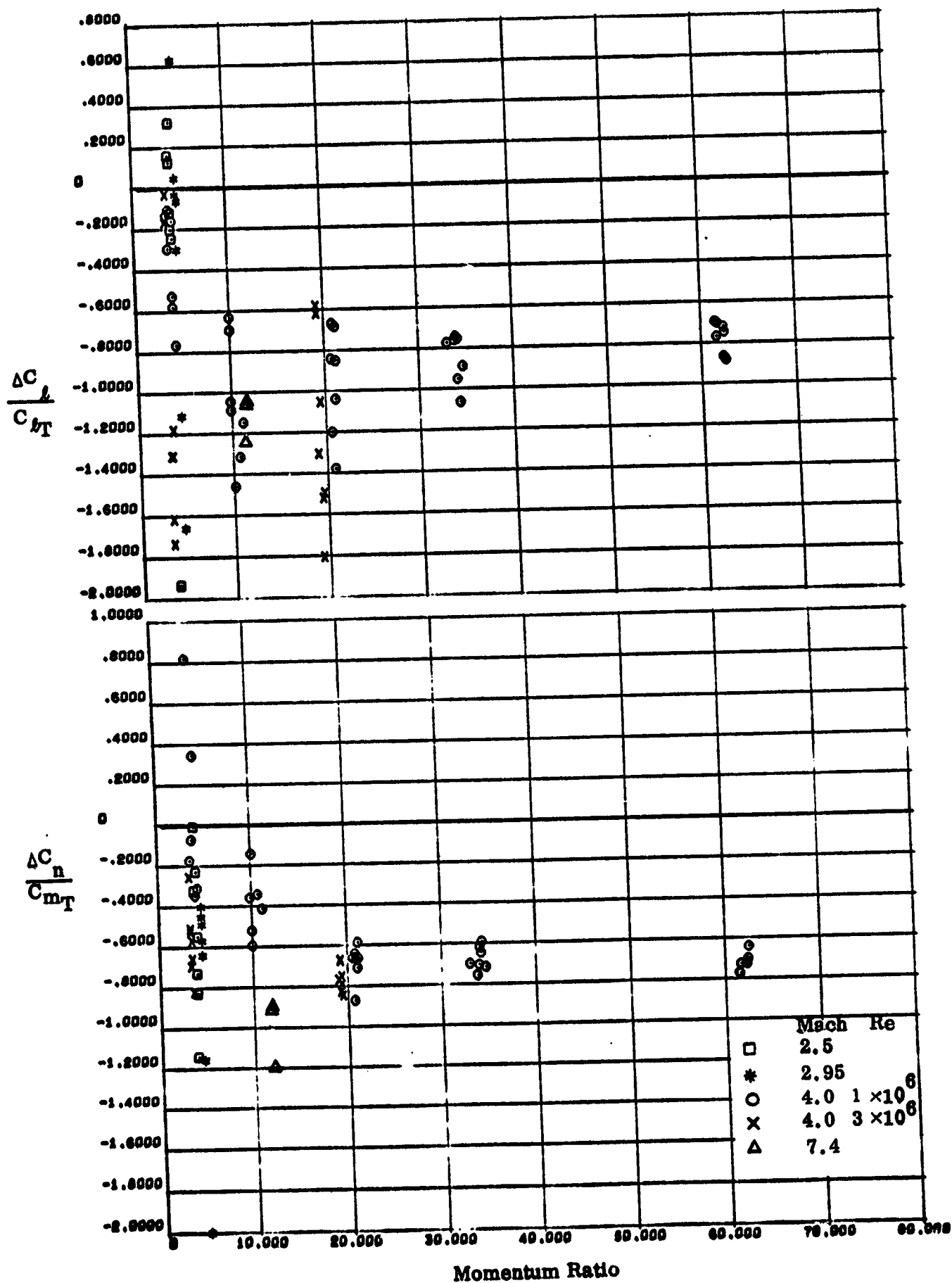
Figure 4-14. Incremental Data Ratios Correlated to Momentum Ratio
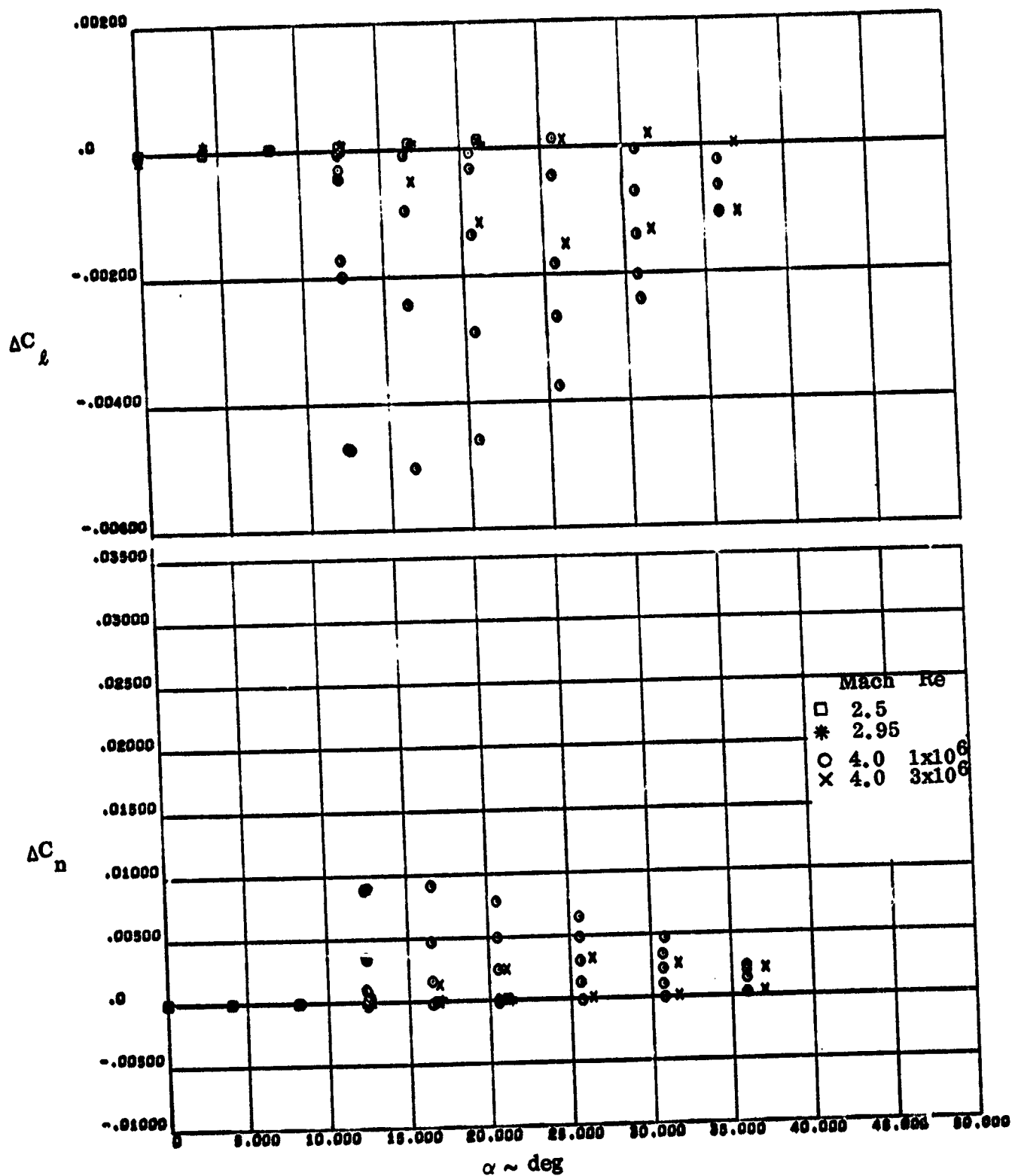
Figure 4-15. Incremental Pitch Up Jet Data

4-27
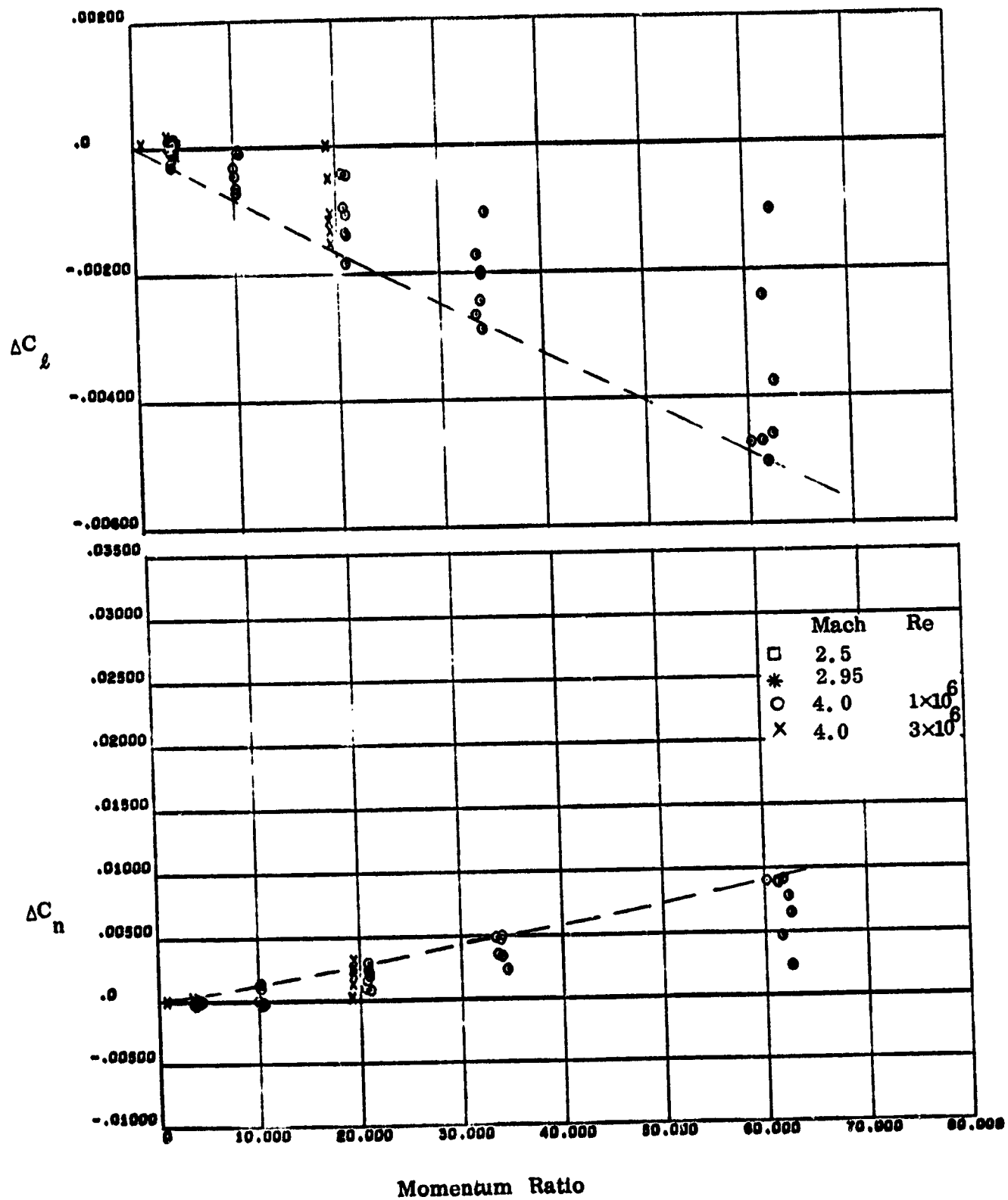
Figure 4-16. Incremental Nose up Pitch Jet Data Correlated with Momentum Ratio.
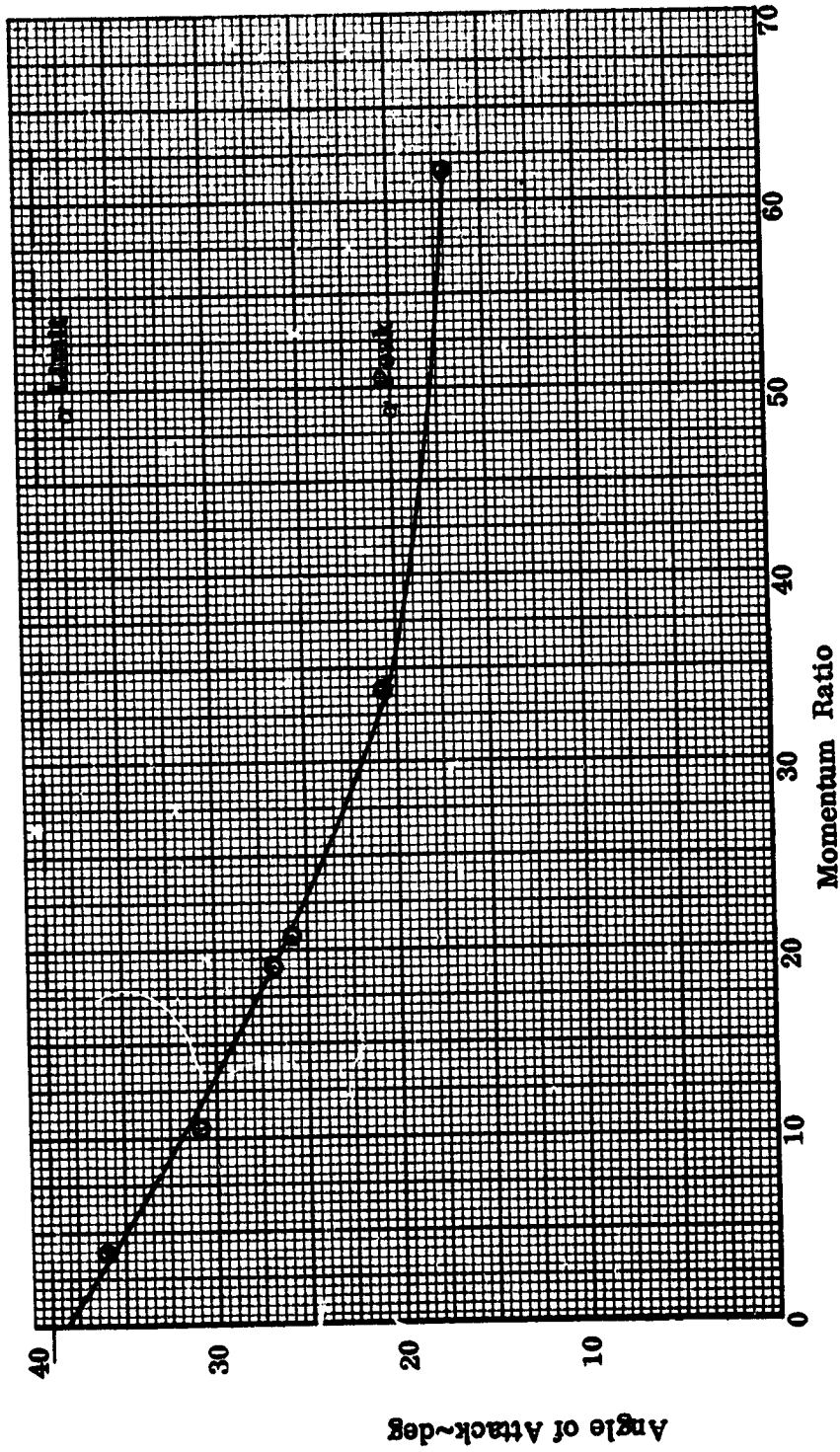
Figure 4-17. Peak Incremental Load Correlation
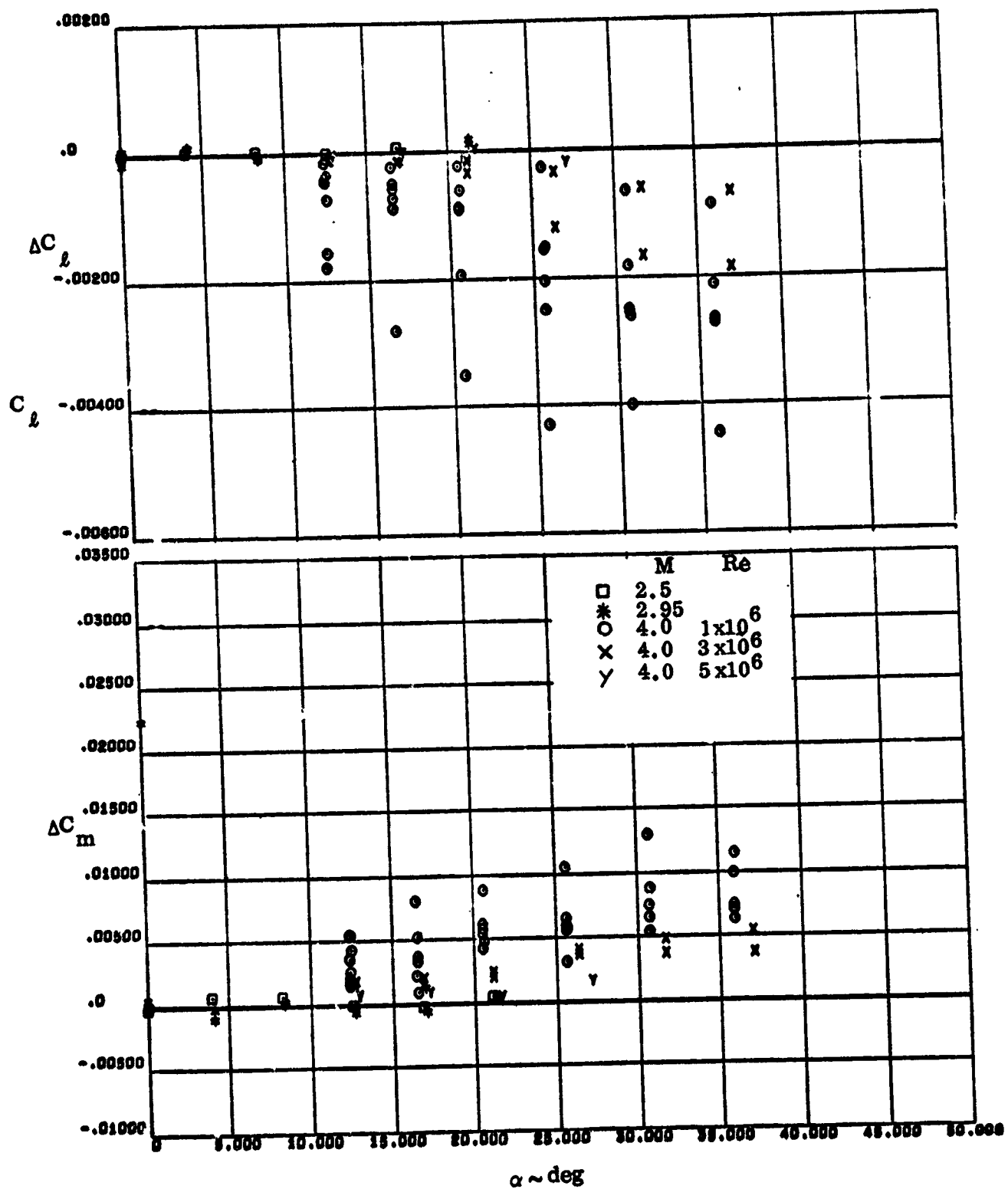
Figure 4-18. Yaw Jet Induced Effects

4-30
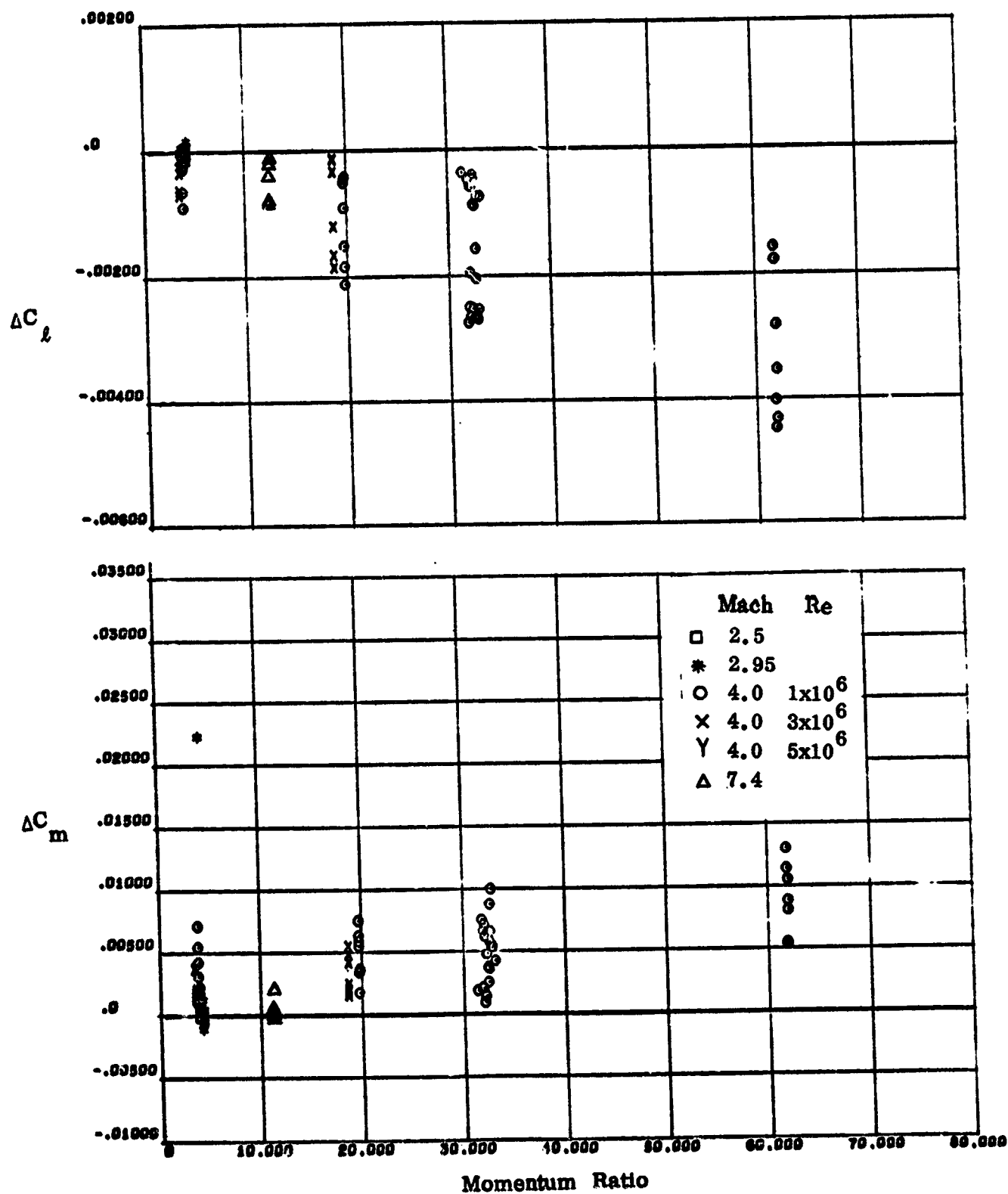
Figure 4-19.   Yaw Jet Induced data Correlated with
Momentum Ratio

4-31
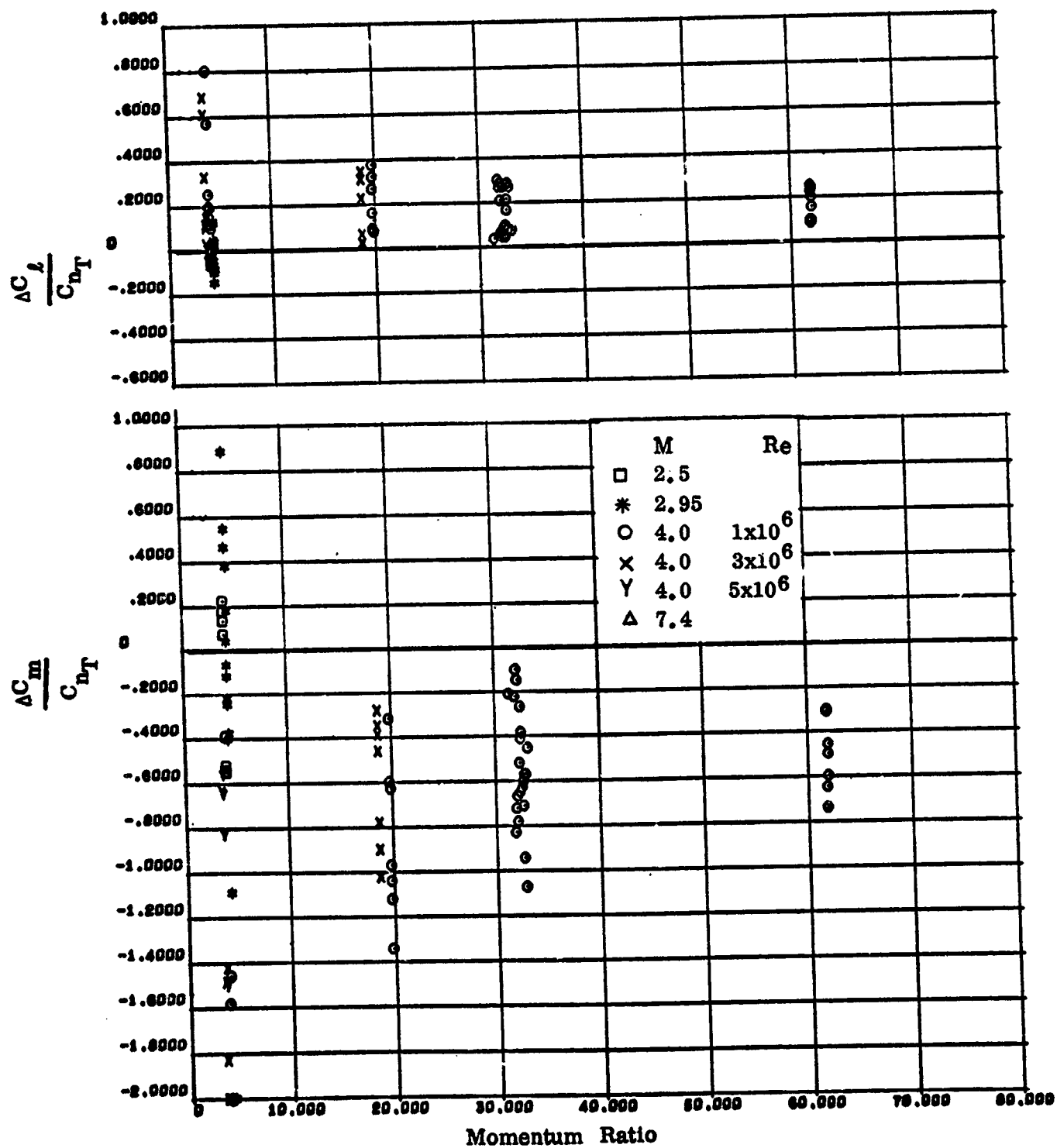
Figure 4-20.   Yaw Jet Induced Data Ratioed by
Yawing Moment
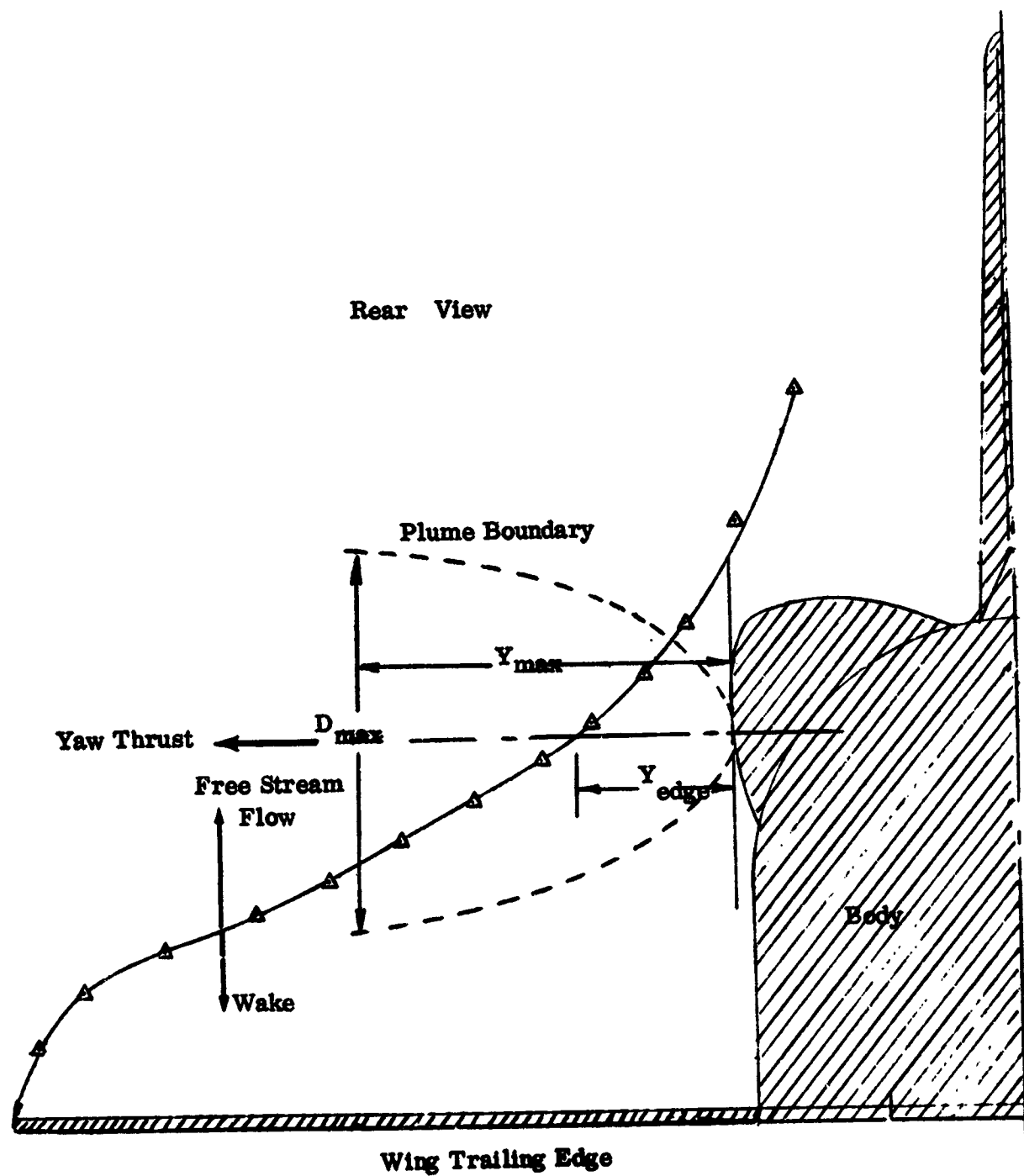
Figure 4-21. Plume Penetration Parameters
for Yaw Thrust
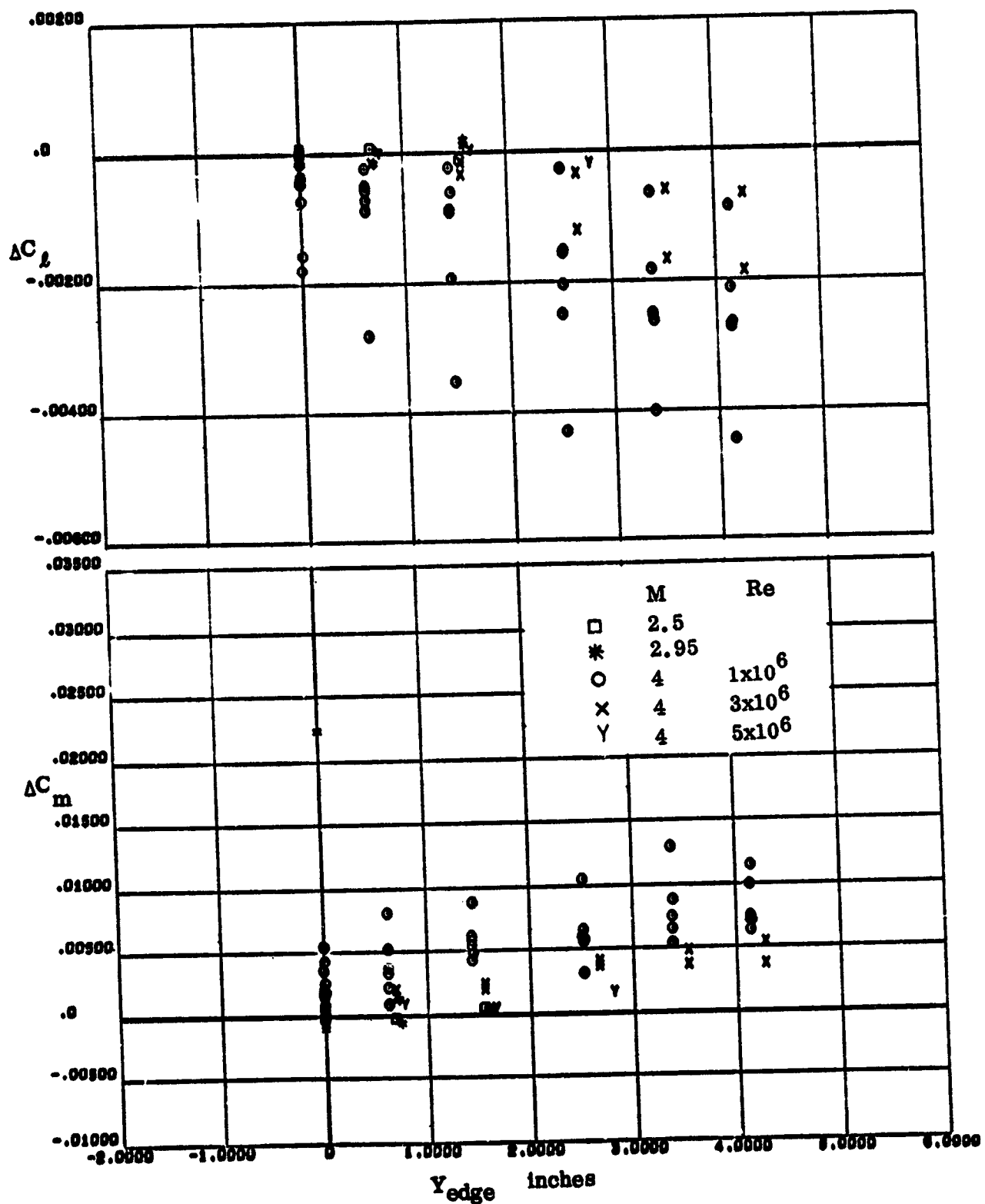
Figure 4-22. Induced Data Correlated with Distance to Edge
of Wake
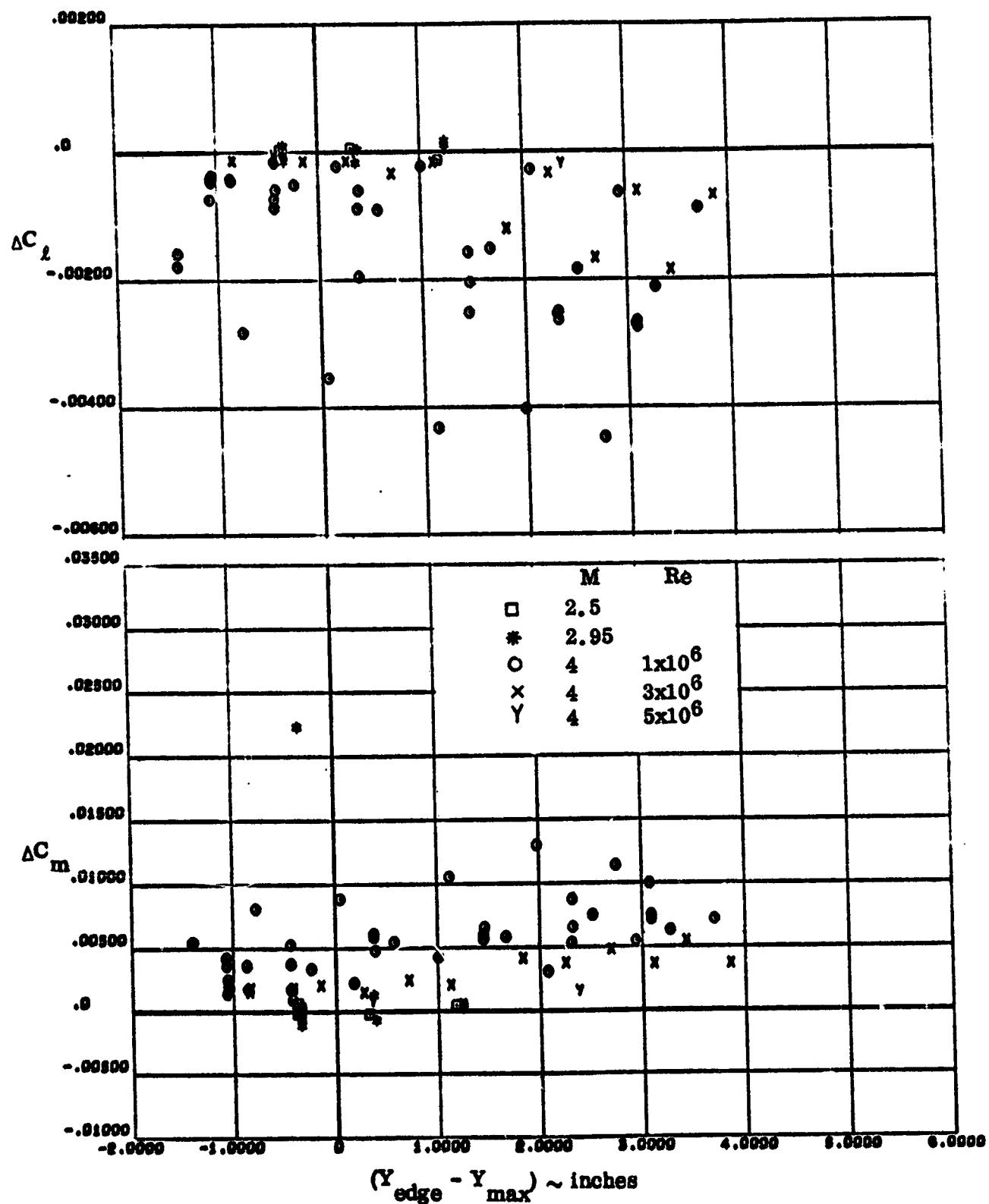
Figure 4-23. Induced Data Correlated with Penetration Parameter
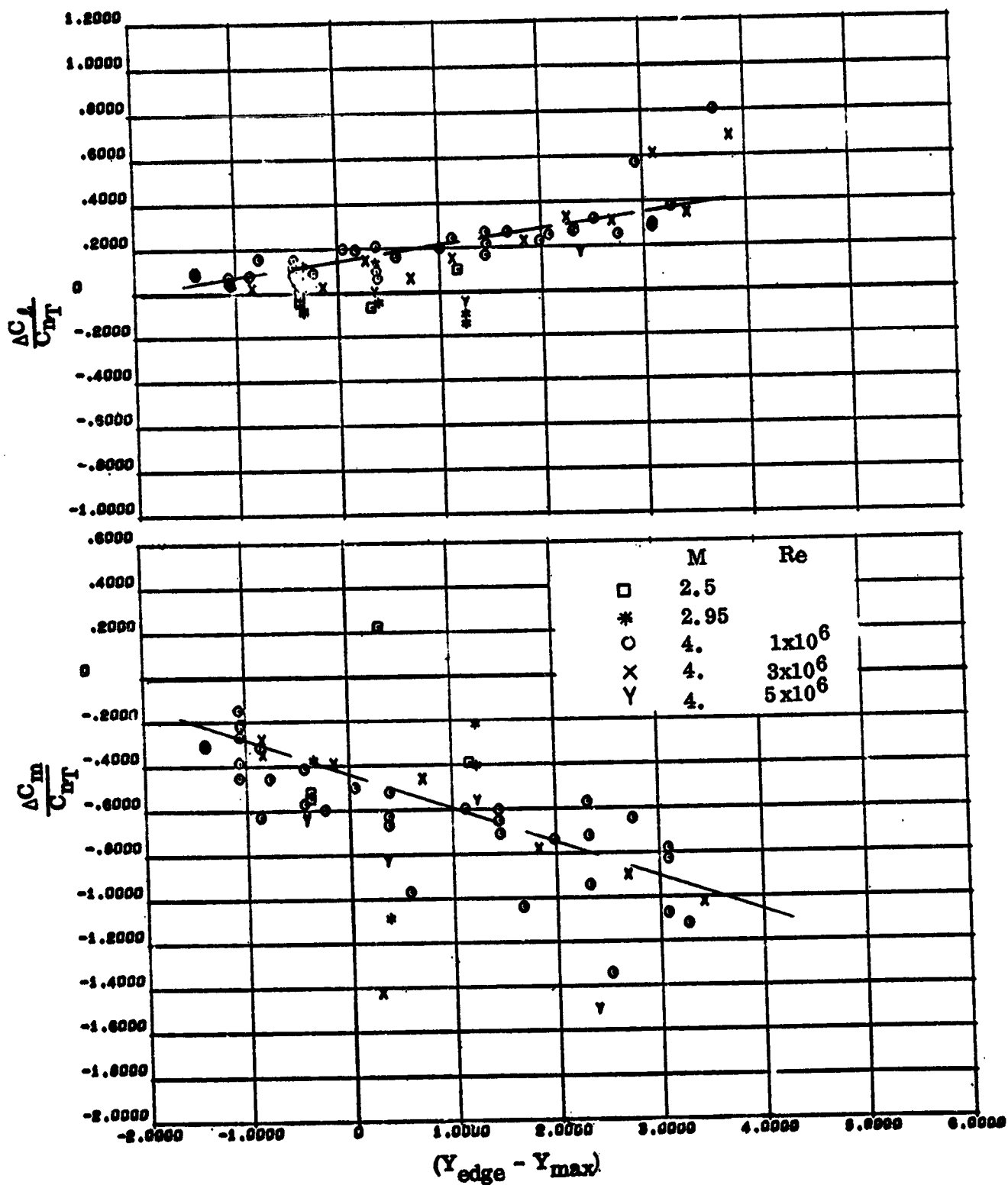
Figure 4-24. Yaw Induced Effects Ratioed by Yaw Thrust Moment
Correlated to a Penetration Parameter

5.0 AEROTHERMODYNAMIC PERFORMANCE

The severity of the aerodynamic heating during entry is presented in Figure 5-1 which is the reference heating rate to a one foot radius sphere. The heating rate history was computed from the Convair P5613 computer program, reference 20. It is noted that during the high aerodynamic heating portion of entry, the pitch and roll control thrusters are essentially non-operative, while the yaw thrusters will operate through the total heat pulse of the induced environment. Therefore, only the effect of yaw thrusters jet-stream interaction need to be considered in this analysis.

The RCS thrusters located on the aft fuselage pod is shown in Figure 5-2 with details of the left rear module, a cross section through the pod and the TPS arrangements and average dimensions as obtained from reference 21. As noted the pod will also include the orbital maneuvering system (OMS) oxidizer and fuel. Each module will contain 2 monopropellant helium pressurized tanks (hydrazine N_2H_4) to supplied 12 RCS thrusters using catalyst beds for propellant decomposition to provide orbiter pitch, roll and yaw control. The TPS of the pod consists of a ceramic reusable surface insulation (CRSI) which is a 12 pcf mullite material coated for water-proofing and handling protection. The CRSI is bonded with 88 pcf RTV to a 28 pcf foamed elastomeric strain isolator (SI) pad which is, in turn bonded to the aluminum structure with RTV. The maximum allowable surface temperature for the CRSI is 2500° F. Also, a minimum thickness of 0.5 inch for CRSI is established by handling and fabrication consideration. Sizing of the TPS over the pod was done by Rockwell International from theoretical aerodynamic heating simulation using a maximum temperature limit to the SI pad of 650°F or a 350°F maximum temperature on the aluminum structure during entry. The TPS dimensions shown in Figure 5-2 are representative for the pod. A coating over the CRSI external surface will have an $\alpha_s/\epsilon = 0.5$ with $\epsilon = 0.8$. In addition, the TPS will include TG 15000 insulation behind the aluminum structure to protect the RCS components such as the hydrazine propellant and lines to the maximum temperature limit of 150° F. Furthermore, heaters are required to maintain the propellant above the cold limit of 40° F during the orbital operation.

In order to perform the RCS module and OMS pod TPS analysis the heat flux experienced during the entry trajectory from the peak yaw thrusters jet-flow field interaction is required. The yaw thrusters which are used two at a time were assumed to be operative through the majority of the entry trajectory. The wind tunnel data correlations presented in Section 2 for the peak pressure, the corresponding peak heating and the peak distance from the jets were utilized. Correction for the jet gas temperature, jet gas molecular weight and jet clustering were also obtained from the experimental data. The heat transfer results obtained at NASA Ames 3.5 Ft HWT were then used for the extrapolation to flight.

The flight jet to free stream momentum parameter ratio, Φ_j/Φ_∞, along with the corresponding total temperature ratio, $T_{oj}/T_{0\infty}$, utilized with the experimental data are shown in Figure 5-3. Also shown is the flight Mach number, M_∞, and the momentum ratio which was simulated at NASA Ames 3.5 Ft HWT, using the 1.5% scaled RCS thrusters. The jet interaction peak heat transfer coefficient ratioed to the heating at the stagnation point of a one foot sphere nose radius is shown in Figure 5-4, based on data at an angle of attack $\alpha = 30°$, which will be experienced during most of the entry trajectory. An average jet interaction heat transfer coefficient which is about 15% of the sphere value is shown to be experienced over the pod. Exception is in the early phase of the trajectory, where the low free stream value of pressure will cause a higher peak. However, as noted in Figure 5-4, due to the much lower heating at the higher altitude, this peak heating level will be small. Also shown on the figure is the peak heating over the pod without jet interaction as caused by the wing vortex reattachment stagnation line, neglecting the effects of Mach number and Reynolds number. As noted in the heat transfer data presented in Section 3, a yaw angle β of 5° will double the heating environment. Therefore, if during entry long transient maneuver induces large yaw angles, this effect should be considered. The location of the peak over the pod as a function of entry time is presented in Figure 5-5. The results indicate clearly that the peak of the interaction will be limited mostly to the aft portion of the pod and that at the high altitudes the peak will move well upstream over the pod.

5.1 POD STRUCTURAL HEATING

The objective of the TPS thermal analysis was to verify a nominal sizing of the CRSI assuming an average thickness of 1/2 inch over the pod under the entry heating loads. In addition, resizing the CRSI was performed, its thickness being dictated by the 650° F maximum temperature limit at the foam pad bondline. The thermal environment used for the verification was those with and without jet interaction as shown in Figure 5-4. The transient temperature through the TPS was obtained with the aid of the Convair P4560 computer program, reference 22. A thermal model of the TPS was broken down into numerous nodes and the simulation used the materials thermal properties data defined in reference 21. A simplified one-dimensional thermal analysis was used since the low thermal conductivity of the CRSI and foam pad will not have much effect in reducing the peak local temperature from lateral conduction.

The results for the transient external surface temperature of the CRSI are presented in Figure 5-6 with and without jet interaction and show values which are within the capability of the material, which is a 2500° F temperature limit. However, the foam pad bondline allowable maximum temperature of 650° F will be exceeded in both cases, as induced from the stagnation line of the wing vortex reattachment (800° F) and the

jet-stream interaction (1200° F), assuming a constant CRSI coverage of 1/2 inch over the pod. Resizing of the CRSI was then accomplished and the thickness required to take the peak heat loads from jet-stream interaction is found to be 1-1/4 inches, from Figure 5-7. It should be noted that this CRSI thickness requirement will be applicable only to the aft portion of the pod and over the RCS engine module as indicated by the peak distance location in Figure 5-5.
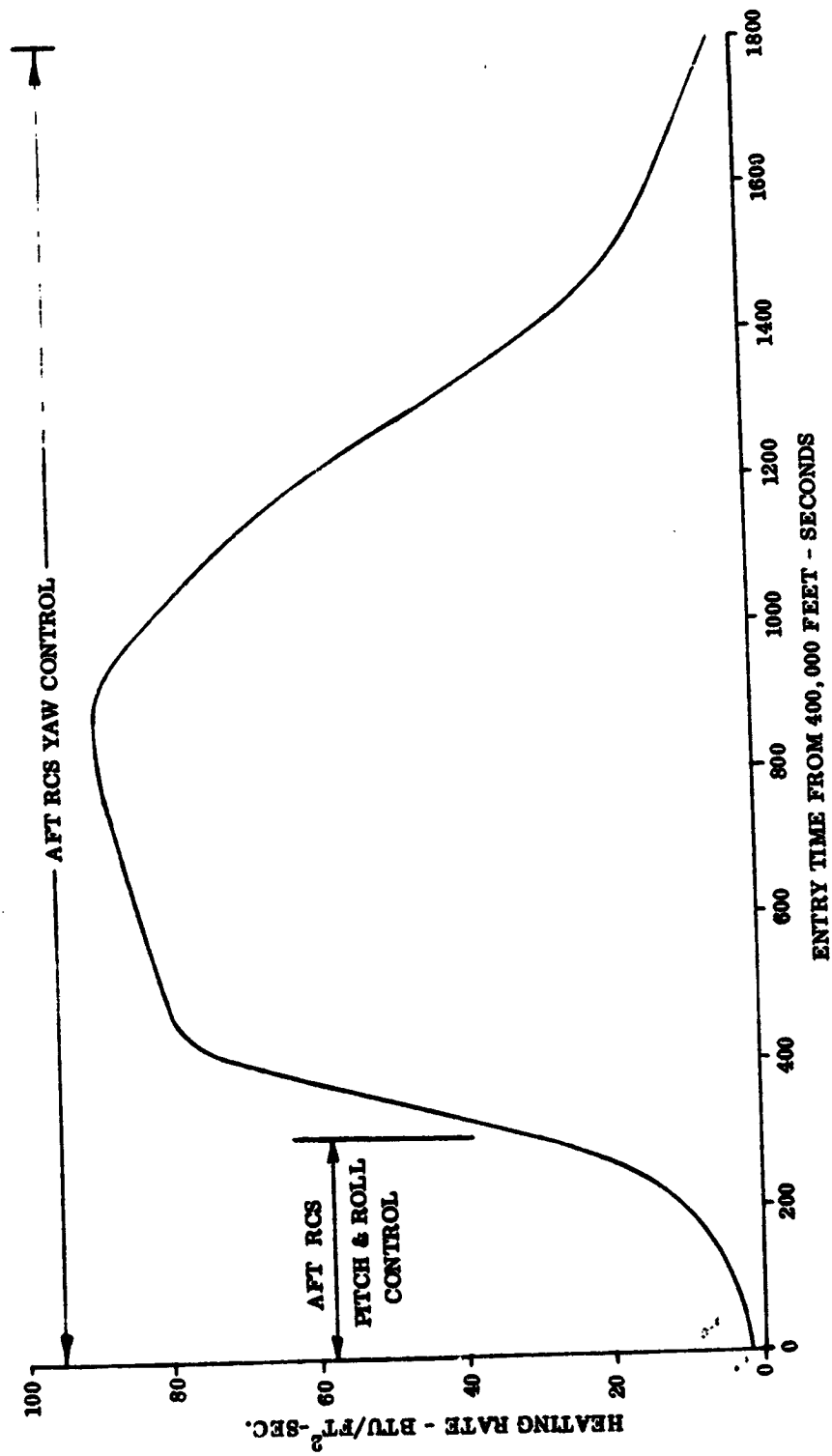
Figure 5-1. Reference Entry Heating Rate, One Foot Nose Radius, Cold Wall
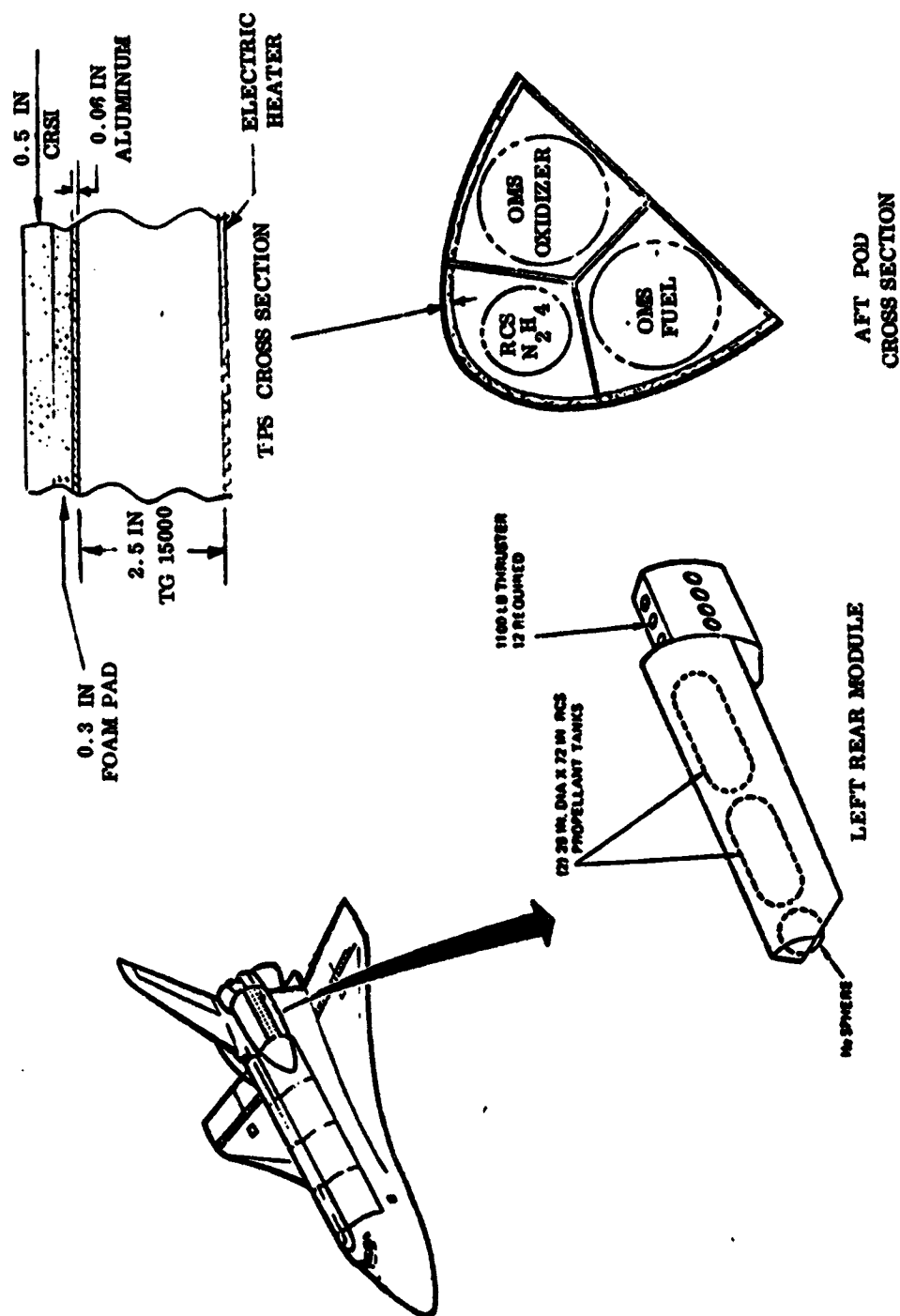
Figure 5-2. Orbiter OMS Pod, RCS Module and Pod TPS
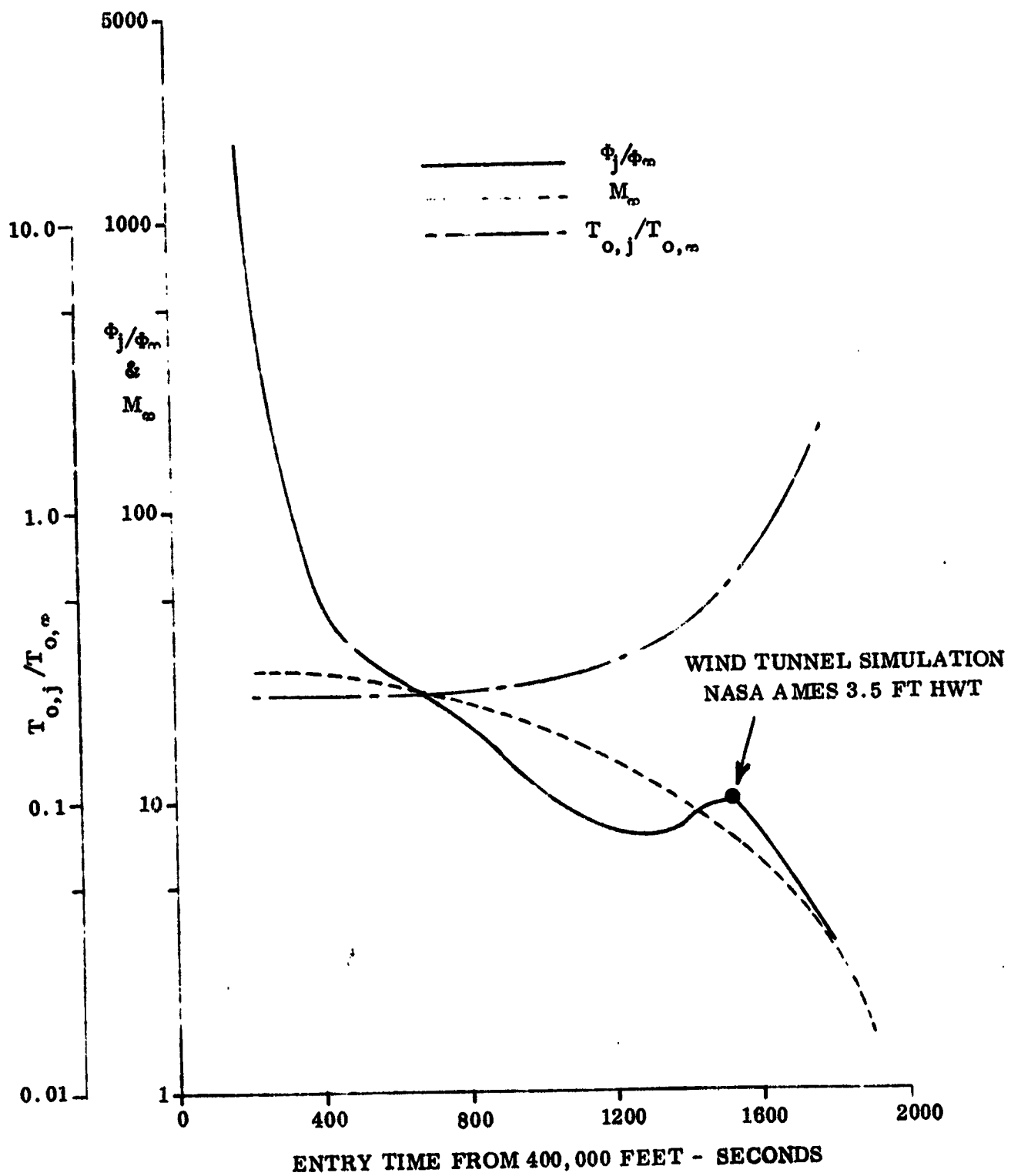
Figure 5-3. Mach Number, Jet to Free Stream Total Temperature and Momentum Ratios During Entry
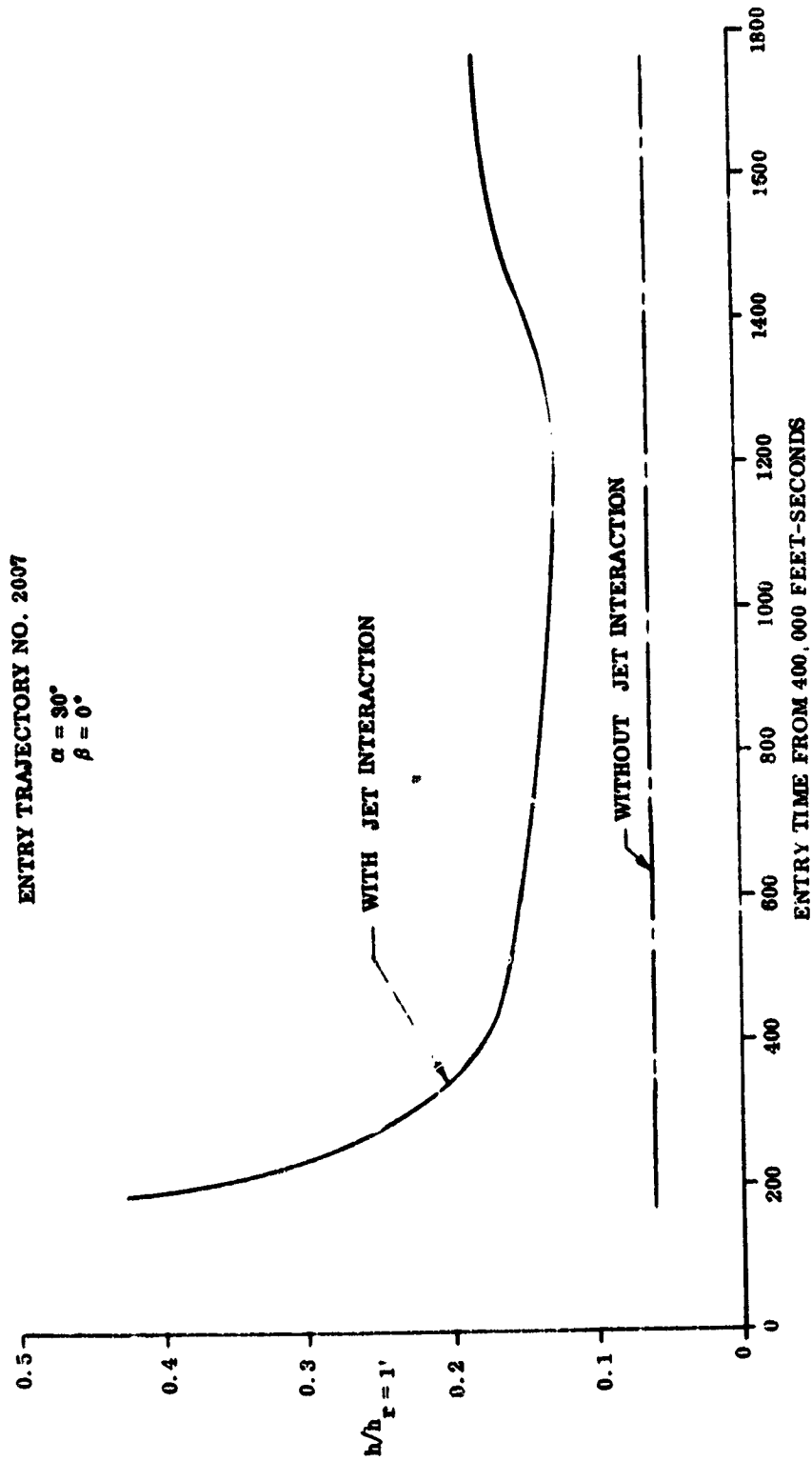
Figure 5-4. Peak Heating Environment Over RCS Module and OMS POD Surface During Entry
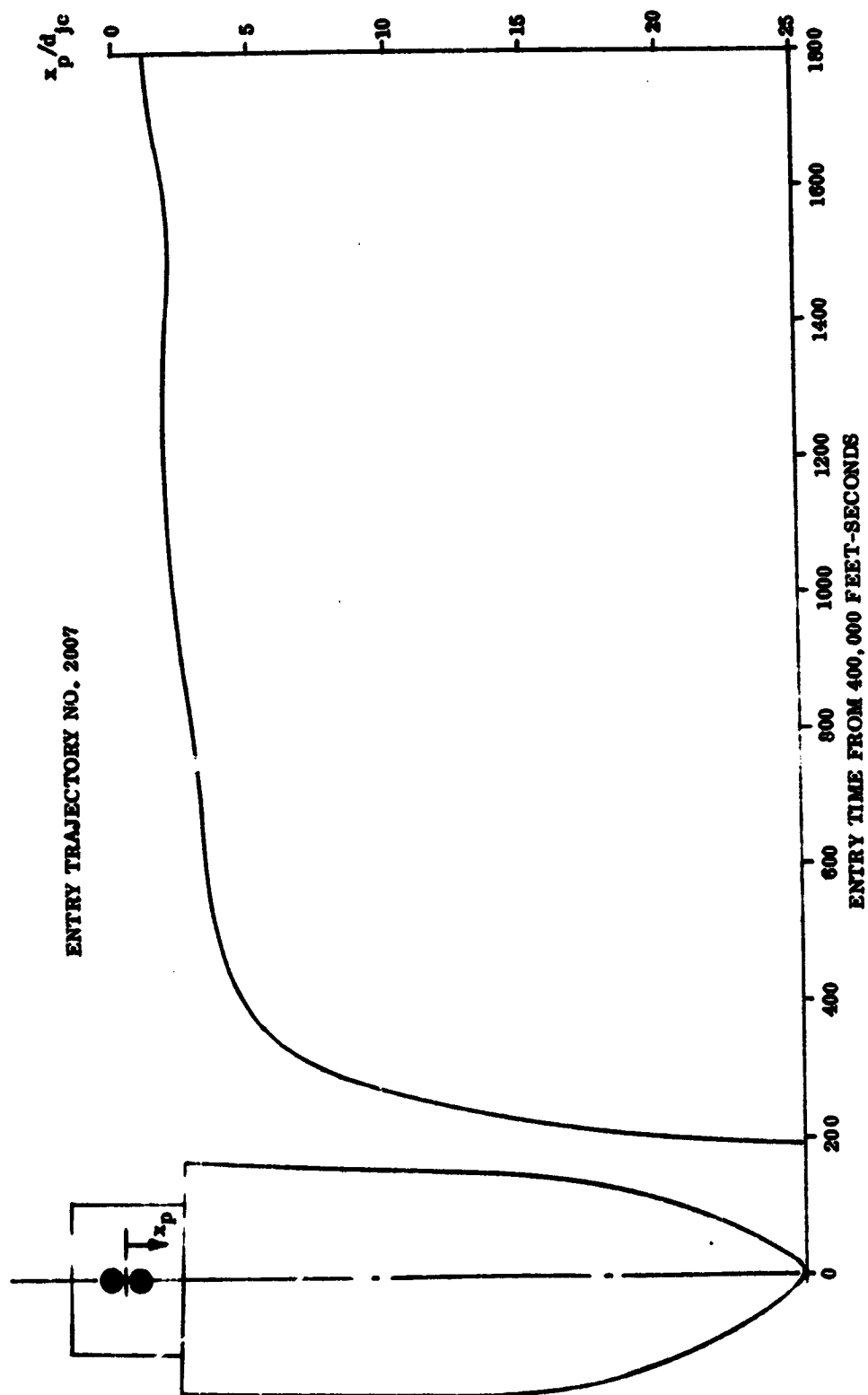
Figure 5-5. Peak Pressure and Heating Locations over OMS Pod Surface
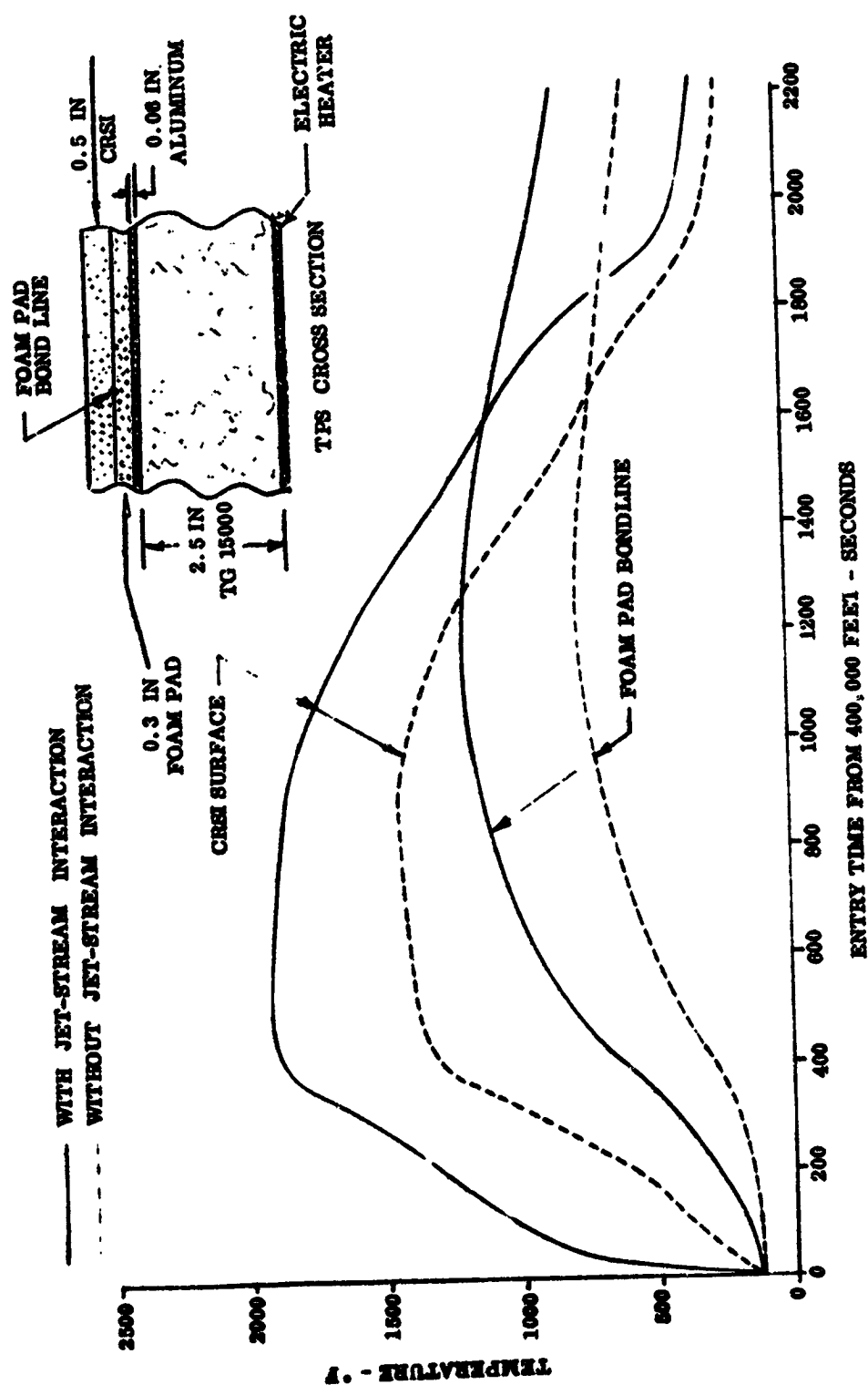
Figure 5-6. CRSI Surface and Foam Pad Bondline Temperature During Entry
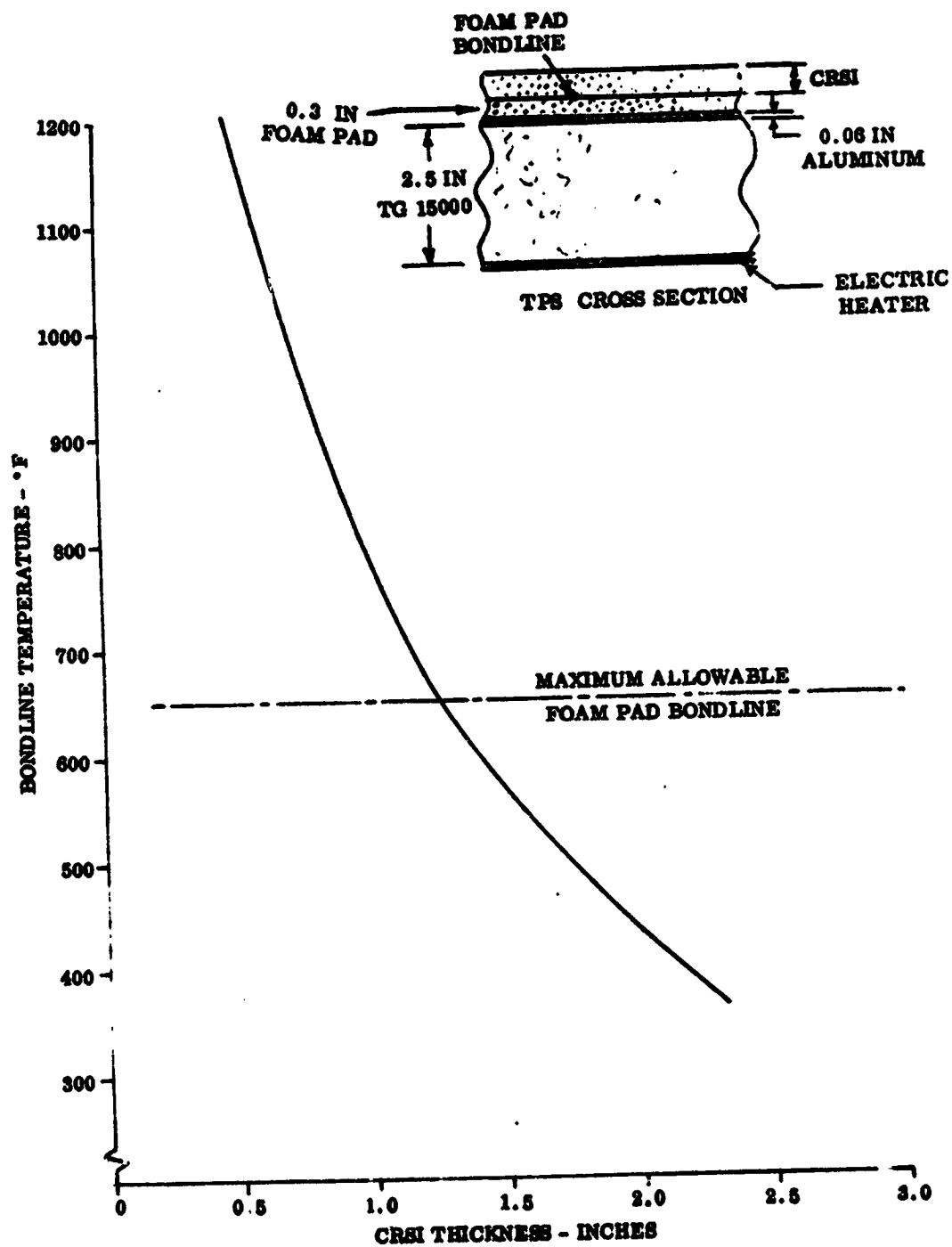
Figure 5-7. CRSI Sizing for Maximum SI Bondline Allowable Temperature
During Entry

6.0 FULL SCALE RCS CONTROL EFFECTS

In order to predict the full scale control effectiveness and induced effects of the monopropellant hydrazine reaction control engines during the PRR configuration entry it was necessary to combine the empirical model presented in section 4 with the vehicle geometry data and engine data of Section 2, the plume impingement model of Section 2.3, and the trajectory data of Figure 2-25. The data was generated using the mean annual Kennedy reference atmosphere as the model atmosphere for computing the flight conditions along the entry trajectory.

The momentum ratio which represents one of the most important scaling parameters is shown in Figure 6-1 as a function of Mach number, and is based on nozzle reference area. This figure shows that the momentum ratio remains fairly low and within the region of the test results up to a Mach number of 28 which occurs at an altitude of over 250,000 feet on the entry trajectory used in this study. Thus the results up to this Mach number lie within the range of the empirical model of Section 4 for the parameters based on momentum ratio and extrapolations are only made above this Mach during the very early portion of the entry where the free stream dynamic pressure is very low. Figure 6-2 presents the thrust coefficient for a single reaction control jet based on wing area as a function of entry Mach number to illustrate the increasing magnitude of thrust forces to aerodynamic forces at the very high altitude – Mach conditions.

In the longitudinal and lateral-directional control effects presented below, the moments are referenced to a wing area of 3225 ft^2 and are taken about a center of gravity location at 60% of body length. A wing mean aerodynamic chord of 43.8 ft is used for pitching moment reference length and a wing span of 84 feet was used as yaw moment and rolling moment reference length. Two nozzles were operated for control.

6.1 PITCH CONTROL

The empirical model shows that the nose up pitch control jets create no interaction and induce no other aerodynamic loads, thus, the nose up pitch amplification is always 1.0 and the magnitude of the pitching moment is equal to the thrust moment given in Figure 6-3 as a function of entry Mach number.

The nose down pitch control moment is given in the empirical model as the sum of the thrust component, the impingement component, and the interaction component. Figure 6-3 shows the total pitching moment of the nose down pitch RCS jets as well as the impingement component and the magnitude of the thrust component. The sign of the thrust component would be negative (-) if it were shown on the plot. The total moment of the nose down pitch control is nearly zero at all Mach numbers which is caused by the nose up impingement and interaction moments counteracting the nose down thrust moment. Figure 6-4 shows that the nose down pitch control has some

effectiveness at the lower Mach numbers but control reversal is exhibited at the highest Mach numbers. Figure 1-1 showed that the primary use of pitch control is at the highest Mach numbers where the controls become ineffective. Figure 6-3 also shows the large magnitude of plume impingement effects at these high Mach numbers and demonstrates the importance of obtaining scaled plume impingement data as suggested in Section 4 in order to make better estimates of control effectiveness at these high Mach numbers.

6.2 ROLL CONTROL

The roll control data presented in this section was generated at the nominal angles of attack during entry given in Figure 2-25. The roll control effectiveness and induced yaw effect are very sensitive to angle of attack through equations 4-28 to 4-32. Figure 6-5 presents the magnitude of the thrust rolling moment, the total rolling moment, and the magnitude of the impingement moment. The impingement moment always acts to oppose the thrust moment while the total moment has the same sign. Figure 6-6 shows that the rolling moment has its lowest effectiveness in the intermediate Mach range and increases at the higher Mach numbers. This is in large part due to the increasing nominal angle of attack (to $34°$) at the highest Mach numbers. Roll control effectiveness would be sharply reduced if the angle of attack is less than nominal at these Mach numbers.

The induced pitch and yaw caused by the roll control are shown in Figures 6-7 and 6-8. The pitch is always nose up (+) and is caused by the roll jets exhausting downward interacting with the wing flow. The yaw moment is low because of the high angle of attack on the nominal trajectory but will always have the same sign as the thrust rolling moment.

6.3 YAW CONTROL

The data of Section 3 showed that the yaw amplification was very close to 1 and the empirical model assumes that it is 1.0 which means no induced yaw moment, thus yawing moment is equal in magnitude to the yaw thrust shown in Figure 6-9.

The yaw control does induce a nose up pitching moment and a wing down rolling moment as shown in Figures 6-10 and 6-11. The pitching moment is always nose up (+) because the yaw jets interact with the flow on the trailing edge of the wing while the sign of the induced roll is always the same as that of the yaw thrust moment. Both of these curves peak in the intermediate Mach range where the correlation parameter ($(Y_{edge} - Y_{max})/de$) becomes more negative as the plume grows larger and Y_{max} increases at the higher altitudes. Eventually the size of the plume take the correlation well beyond the range achieved in these tests. Thus the high Mach data becomes very doubtful until more test results can extend the data range.
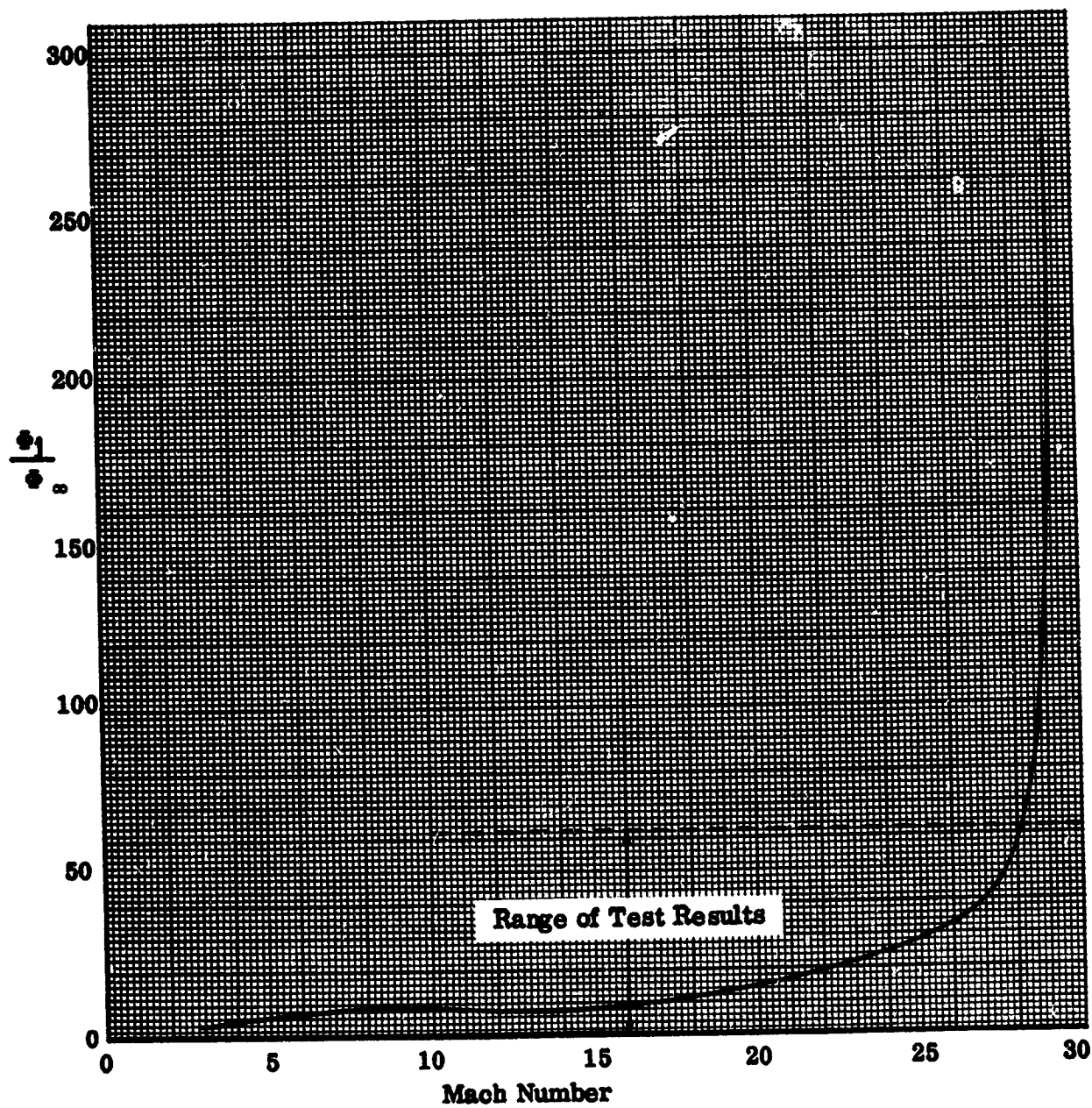
Figure 6-1. Momentum Ratio During PRR Entry
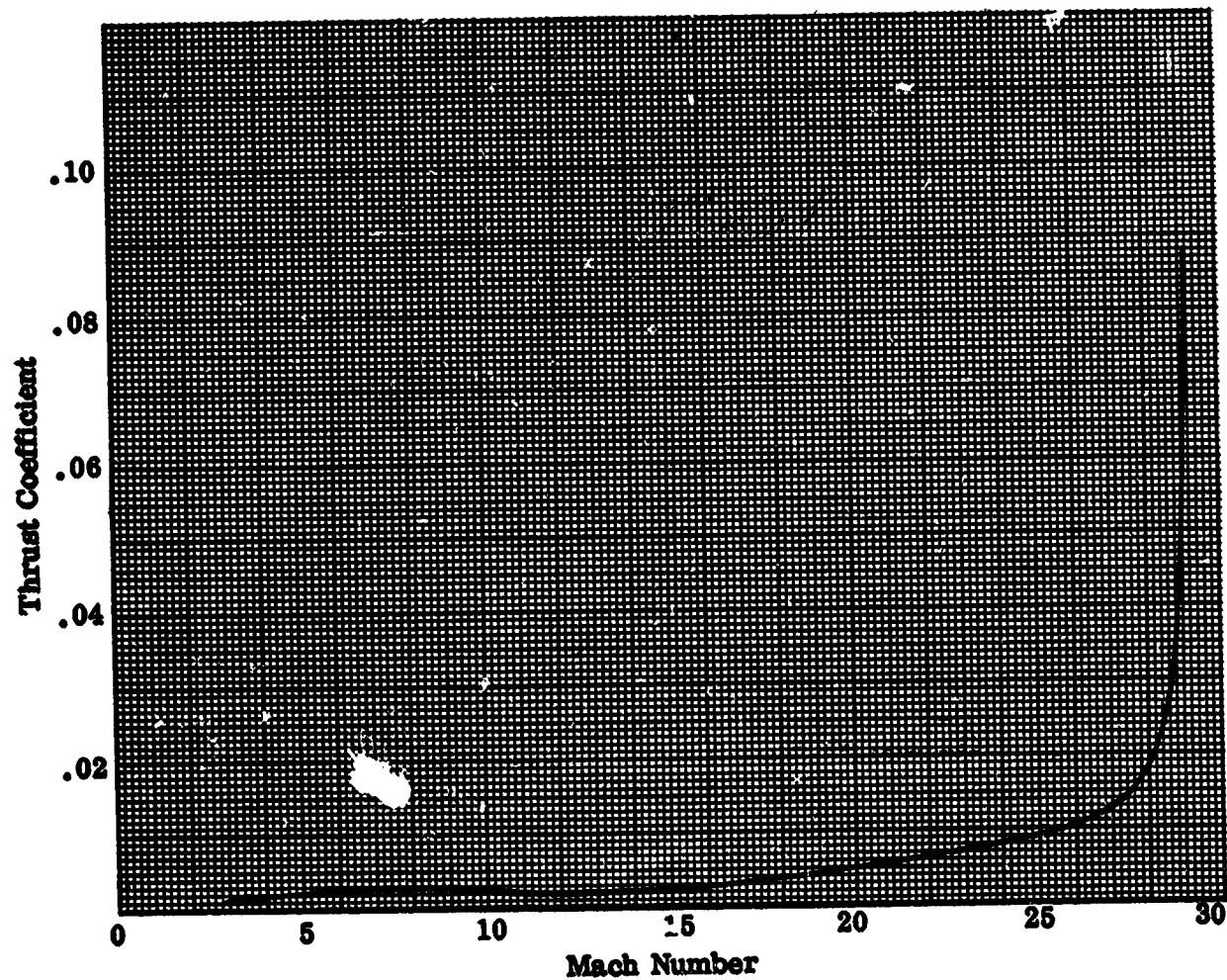
Figure 6-2. Thrust Coefficient During PRR Entry
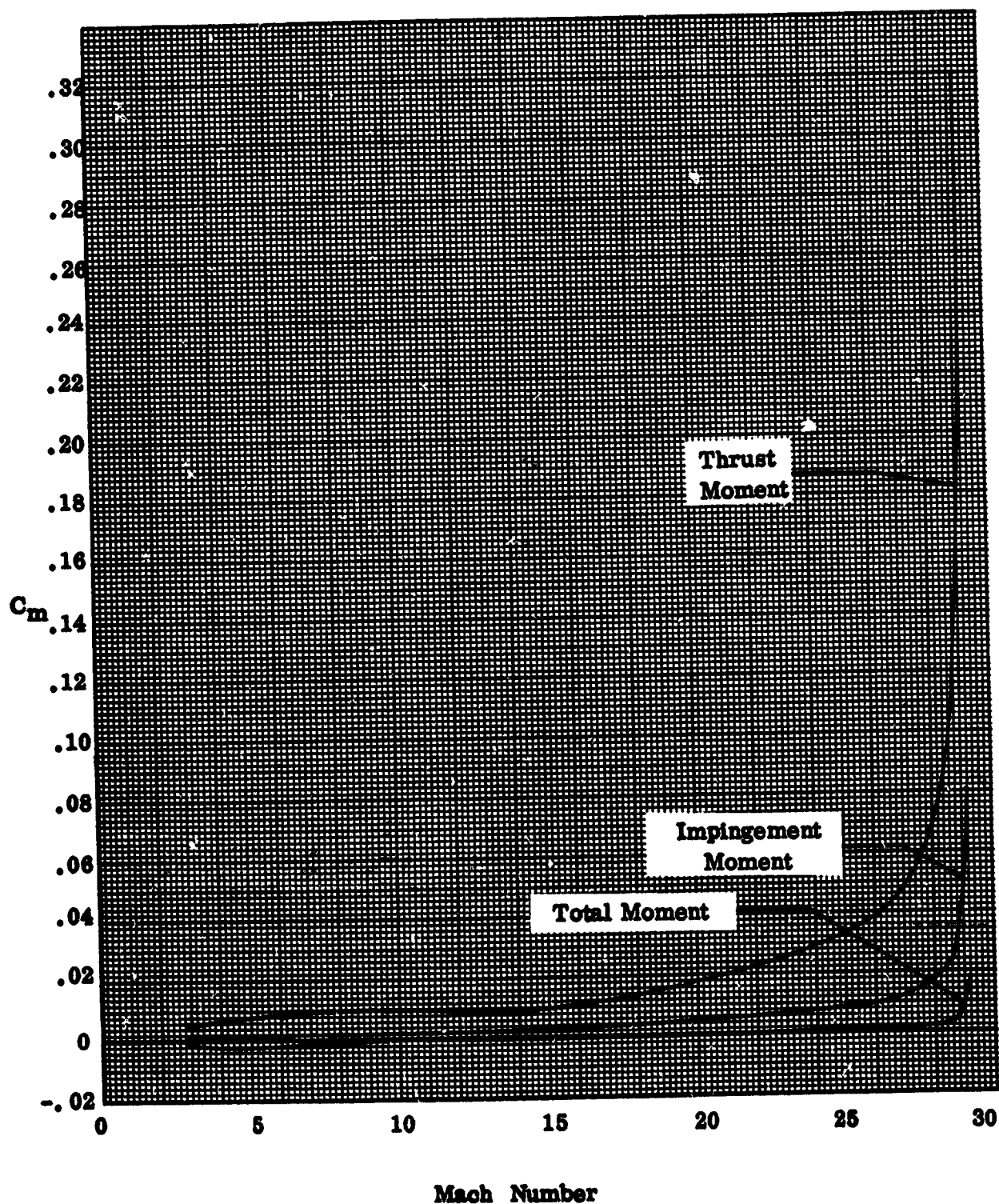
Figure 6-3. Pitching Moment During PRR Entry
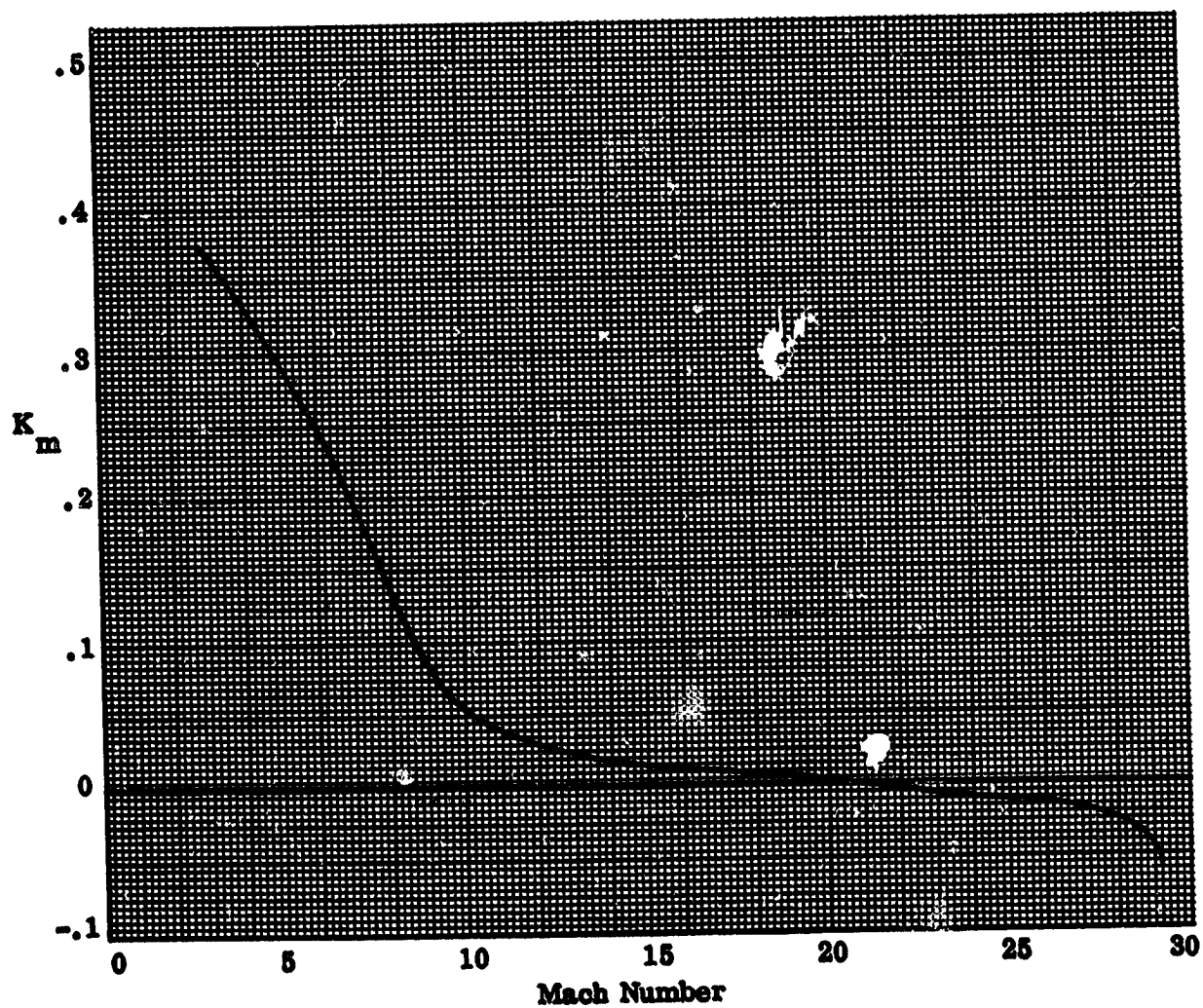
Figure 6-4.   Pitch Down Control Effectiveness During PRR Entry
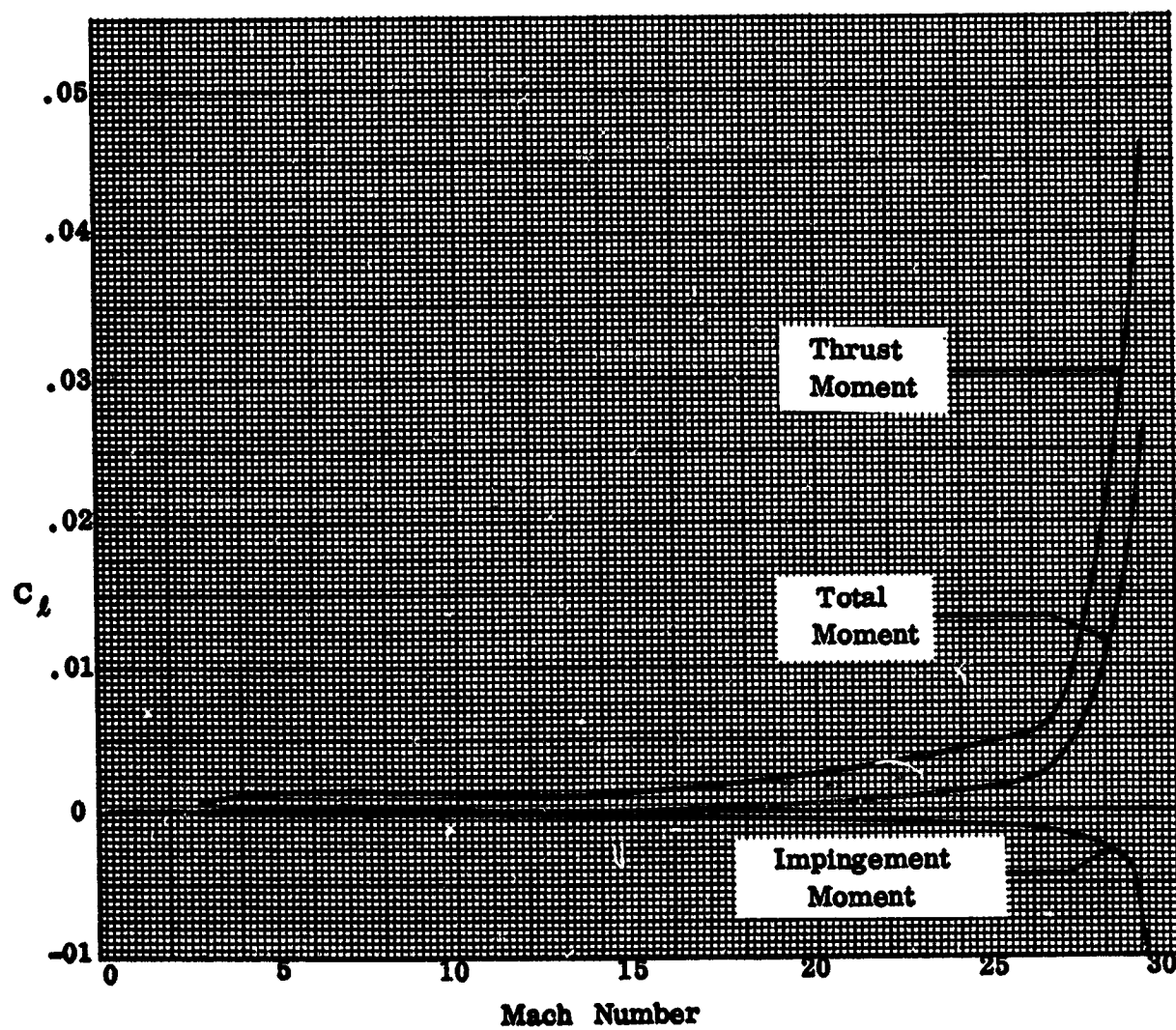
Figure 6-5.   Rolling Moment During PRR Entry
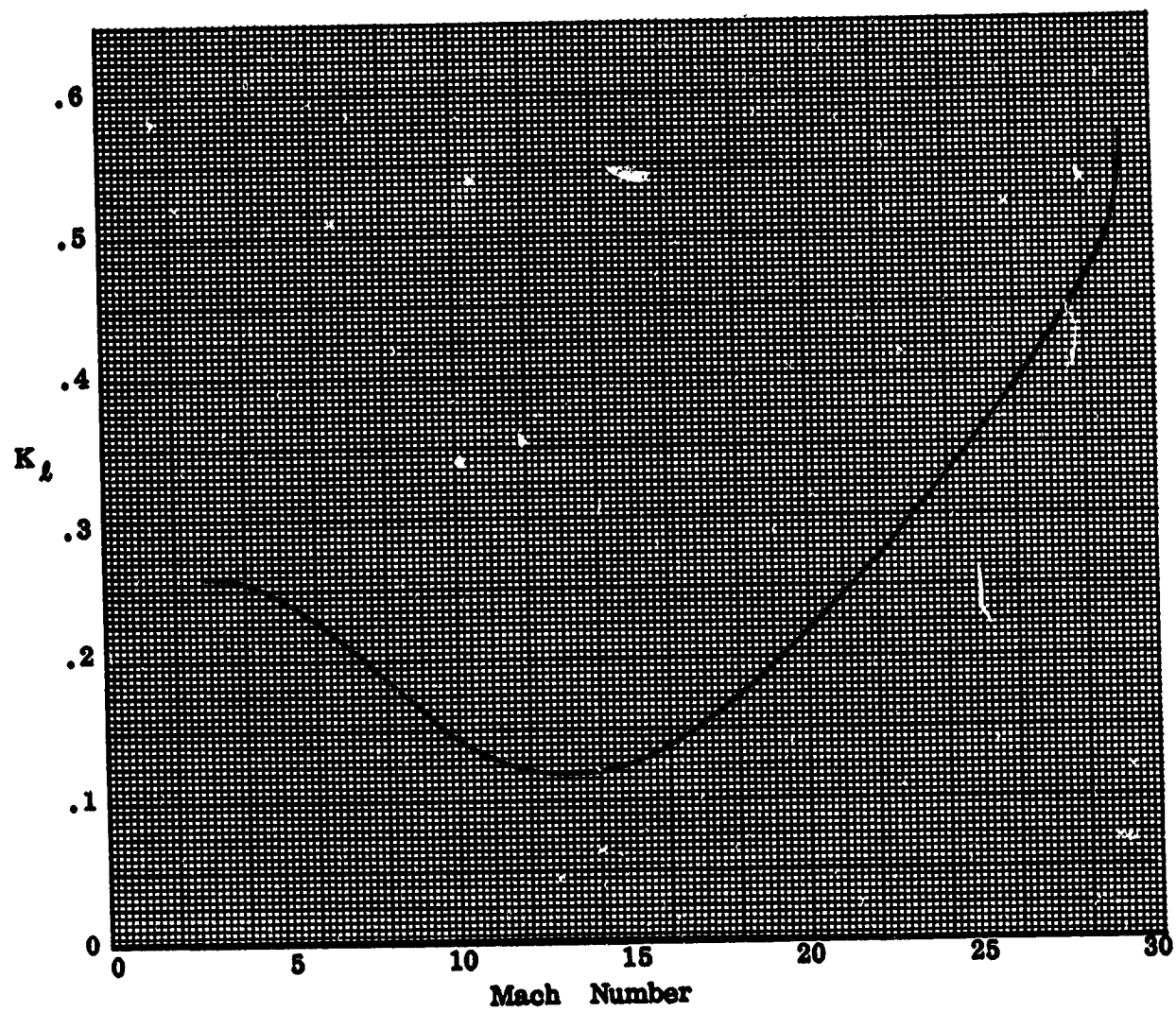
Figure 6-6. Roll Control Effectiveness During PRR Entry
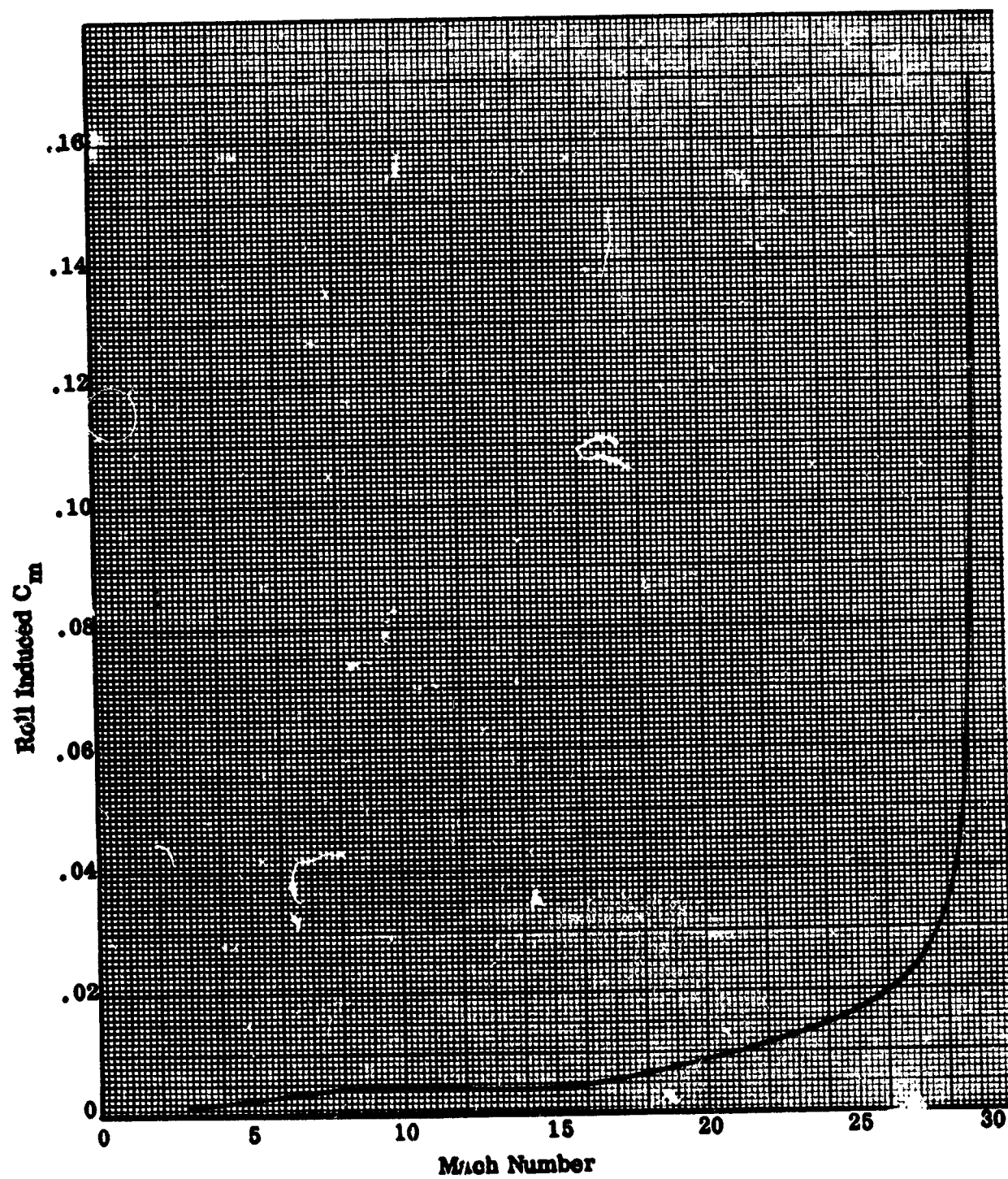
Figure 6-7. Pitching Moment Induced by Roll Control
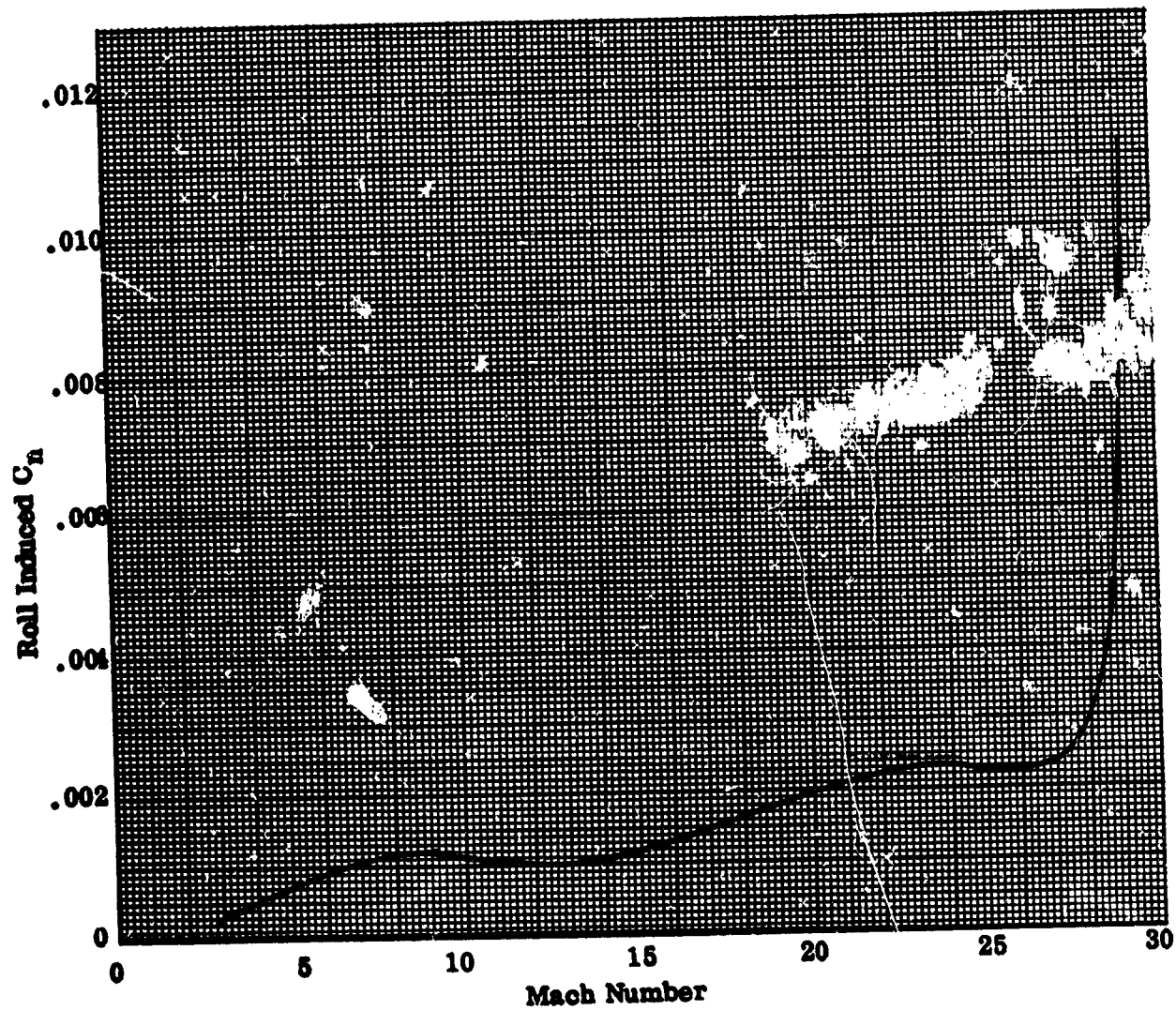
Figure 6-8. Yawing Moment Induced by Roll Control
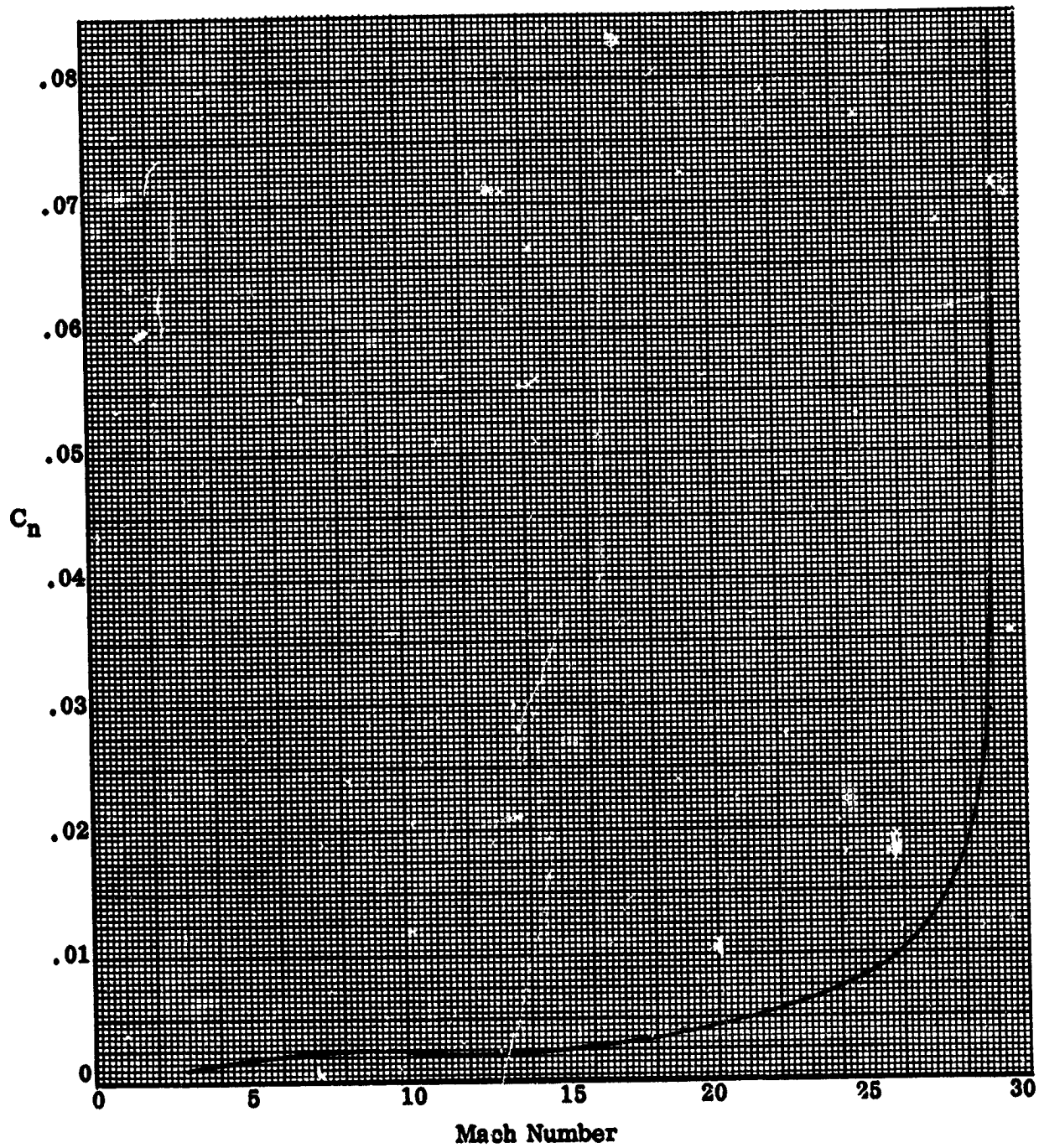
Figure 6-9. Yaw Control Moment During Entry
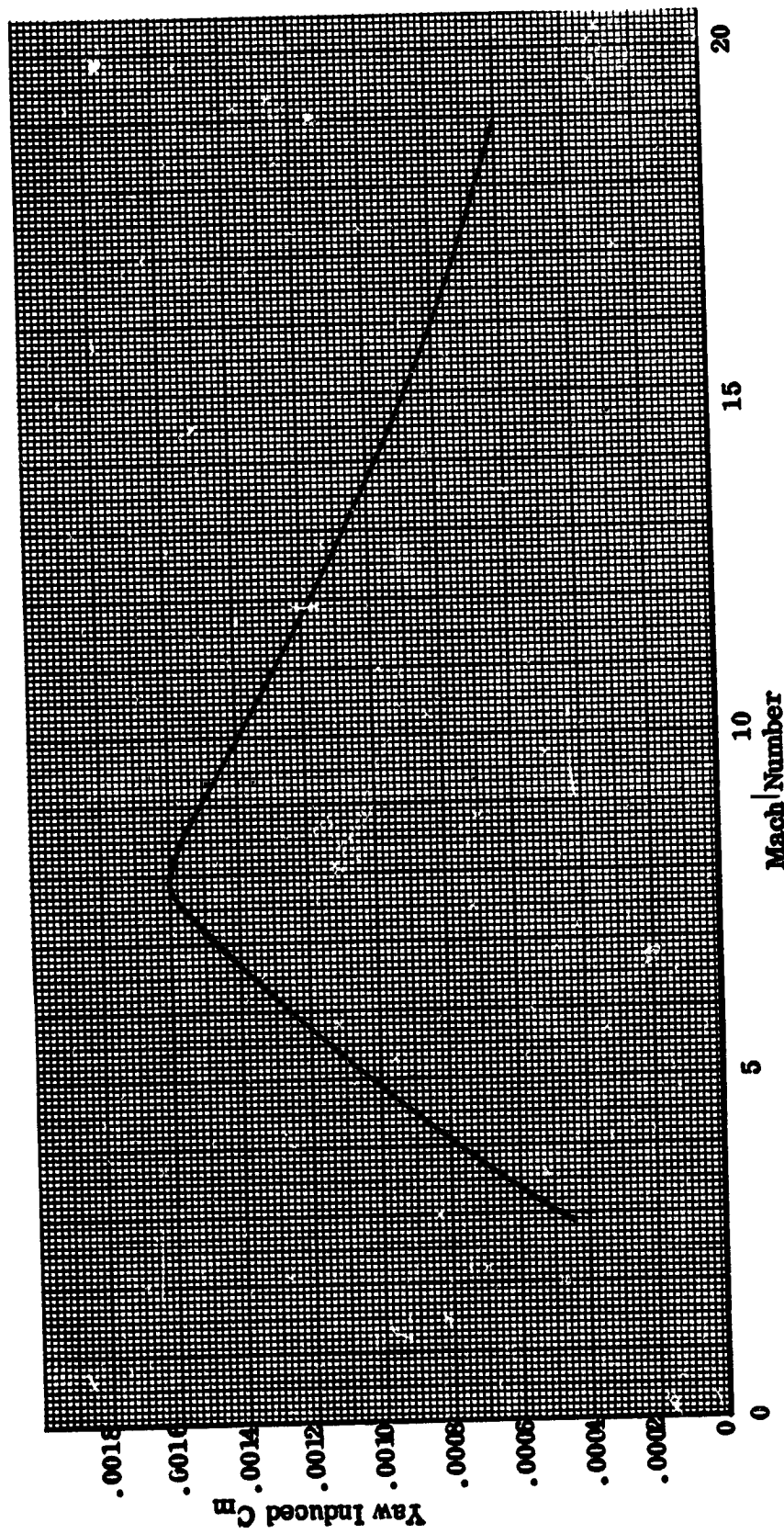
Figure 6-10. Pitching Moment Induced By Yaw Control
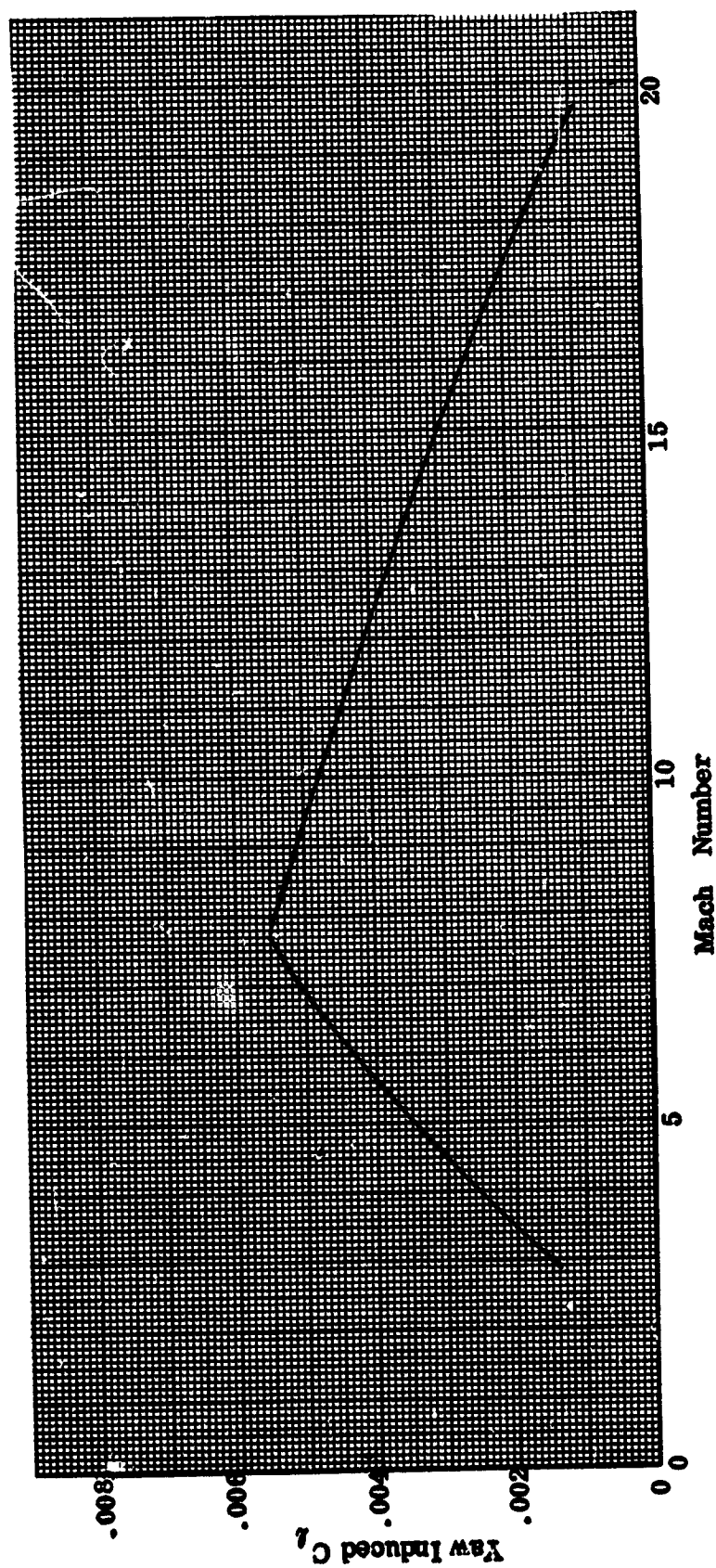
Figure 6-11. Rolling Moment Induced by Yaw Control

7.0 POSSIBLE SOLUTIONS TO ADVERSE JET INTERACTION

Sections 4 and 6 demonstrated that there are two major problems with the reaction control system at its present location; the adverse pitch up which occurs when the pitch down jets are fired and the adverse roll (and pitch up) induced when the roll jets are fired. Both effects have been shown to be connected largely to the jet exhausting downward onto the wing and body flap and it is the resolution of these problems for which the following possible solutions are proposed.

7.1 ALTERNATE LOCATIONS

Three alternate locations are suggested for the RCS as potential solutions to the jet interaction problems. They are discussed in the following sections.

7.1.1 WINDWARD SURFACE MOUNTING. A full resolution of these problems could be achieved if the nozzles firing downward would be moved from the OMS pod onto the bottom windward surface of the body or body flap. In addition to eliminating the adverse effects, the lower jets would act as classical jet interaction controls and should have amplification factors greater than 1. The net result would be that less fuel would be required or possibly even fewer engines so that a significant weight savings may be ac' 'ved. Location of the RCS thrusters on the lower surface of the orbiter, h<   ver, would result in turbulent separated flow due either to the nozzle cavities or to jet interaction and high heating would result. Reference 3 shows however that this increased heating can be and was satisfactorily handled in actual tests.

7.1.2 FORWARD FUSELAGE UPPER SURFACE. Another possible solution would be to move the pitch down jets onto the upper surface of the vehicle ahead of the center of gravity. Roll could be achieved by firing both fore and aft pitch thrusters on the same side.

7.1.3 LOWER SIDE MOUNT. Assuming that moving the pitch down jets is acceptable but the two previous locations are not, another possible location would be to mount these thrusters in separate pods much lower on the vehicle such as sketched in Figure 7-1. The pods would be located at sufficient height for elevon and body flap clearance and could be connected to the RCS tankage in the OMS pod. In this position most of the plume should be exposed to windward side flows and a strong possibility of positive interaction and amplifications greater than 1 exists.

7.2 GEOMETRIC CONSIDERATIONS

If the nozzles cannot be moved to another location, there are still some possible things which can be done to minimize the adverse effects.

7.2.1. <u>HIGHER EXPANSION RATIO NOZZLES.</u> The first solution of this kind would be to increase nozzle expansion ratio. The empirical model generated in Section 4 showed data correlations with momentum ratio and, for a fixed chamber pressure; increasing expansion ratio increases exit Mach number which results in decreasing exit momentum ratio as shown below:

$$\frac{\Phi_1}{\Phi_\infty} = \frac{P_1 \, \gamma_1 \, M_1^2 \, A_1}{P_\infty \, \gamma_\infty \, M_\infty^2 \, A_\infty} \tag{7-1}$$

$$\frac{\Phi_j}{\Phi_\infty} = K \quad P_j M_j^2$$

where $\quad K = \text{constant} = \dfrac{A_1 \, \gamma_1}{P_\infty \, \gamma_\infty \, M_\infty^2 \, A_\infty}$

$$P_j = P_{oj}(1 + \frac{\gamma_1 - 1}{2} M_j^2)^{-\frac{\gamma}{\gamma-1}} \tag{7-2}$$

for constant P_{oj} ; $K_1 = K P_{oj}$

$$\frac{\Phi_1}{\Phi_\infty} = K_1 \frac{M_1^2}{(1 + \frac{\gamma_j - 1}{2} M_j^2)^{\frac{\gamma}{\gamma-1}}} \tag{7-3}$$

For example

$$\text{At} \quad \gamma_j = 1.3 \text{ and } M_j = 3, \quad \frac{\Phi_1}{\Phi_\infty} = 0.221'16 \, K_1 \tag{7-4}$$

$$\text{If} \quad M_j = 4 \quad , \quad \frac{\Phi_1}{\Phi_\infty} = 0.07962 \, K_1$$

Also, increasing pitch/roll control expansion ratio is a feasible solution since it is intended to operate at high altitude only where the plumes are highly underexpanded and not at low altitude like the yaw thrusters where exit pressure ratios approach 1.

7.2.2 <u>SLOT BLOWING.</u> Another method of increasing the effective nozzle expansion ratio of the pitch/roll engines is to add two side walls (Figure 7-2) to the sides of the thruster module to restrain the plume expansion in the thrust direction by allowing the plumes to expand in the axial direction.

The slot should cause the plume to spread in an axial direction and less in the span-wise direction decreasing the plume width at the wing or flap and thus have less interaction.

7.2.3 BASE SIDE PLATES. Plume impingement in the base region is the largest impingement moment as was shown in Figure 4-12. Thus enclosing the base with side plates as illustrated in Figure 7-3 should eliminate this part of the problem and a net gain in control effectiveness should be the result. These side plates should not interfere with body flap or nozzle motion and probably do not need to be as large as shown in this figure.

7.2.4 BODY OR WING FLAPS. Retractable flaps mounted on the side of the body (Figure 7-4) or on the wing or elevon (Figure 7-5) could possibly work to shield the wing from plume flow and thus reduce the interaction between the plume and the wing flow. The wing flap height would be determined by the shock height from equation 2-21. Figure 7-5 shows two different wing or elevon flap combinations and the chordwise portion of the "b" set could be part of a fixed (or retractable) wing fence while the spanwise portion would be retractable like a spoiler. Flap "a" would be retractable. The body flap shown in Figure 7-4 would be hinged at the front edge and would be closed except during early in re-entry when the pitch/roll engines are used. The bottom of the flap will have to clear the elevons at their full deflection.

7.2.5 WING FENCES. The oil flow pictures of figure 3-23 and 3-30 showed that most of the interaction appears to occur near the wing tip, thus, wing fences such as shown in Figure 7-6 may prove effective in keeping the plume flow from reaching the tip and/or limiting the region of interaction.

Auxiliary Pod
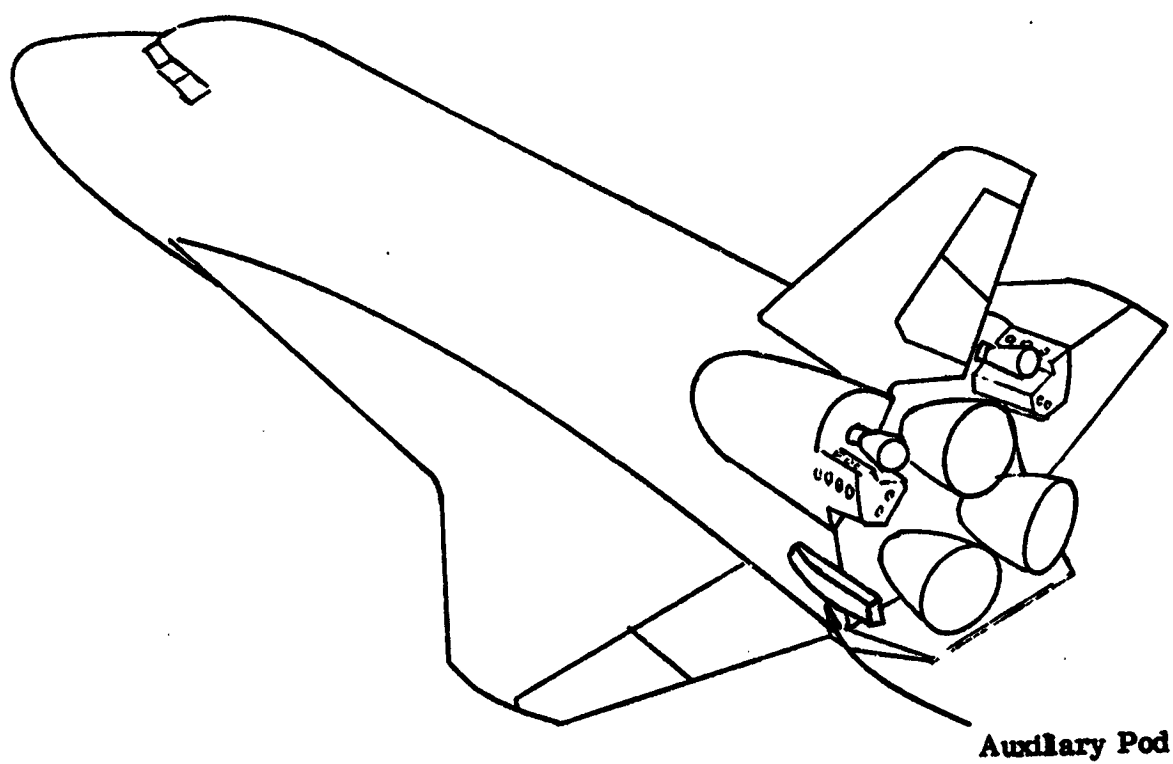
Not to Scale

Figure 7-1.. Separate Pitch Down Thruster Pod

Not to Scale

OMS
Pod

RCS
Engine
Nozzle

Slot Walls

Open at rear
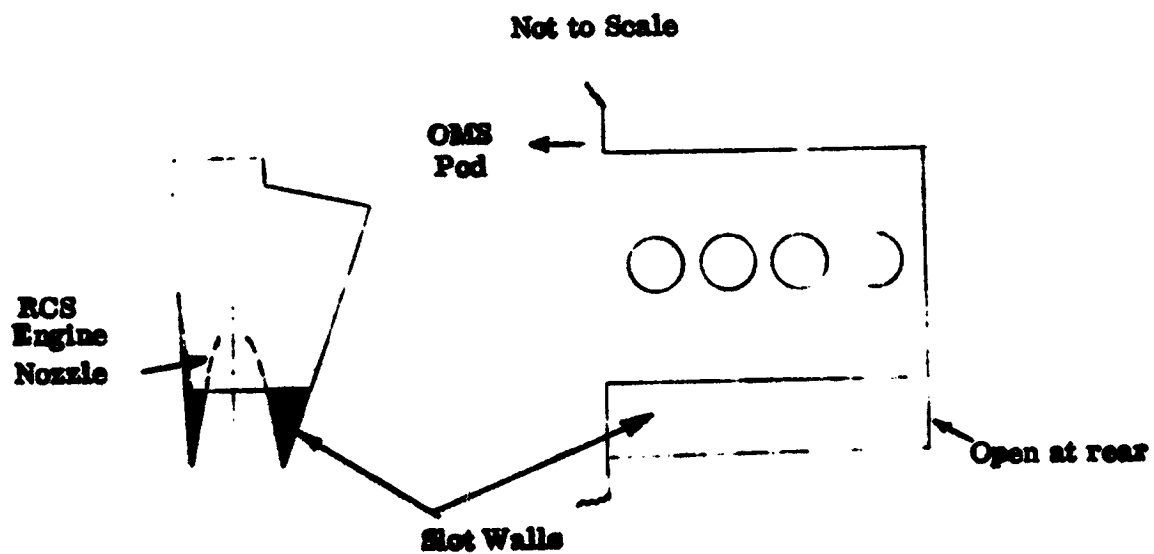
Figure 7-2. Slot Jet Modification

Not to Scale
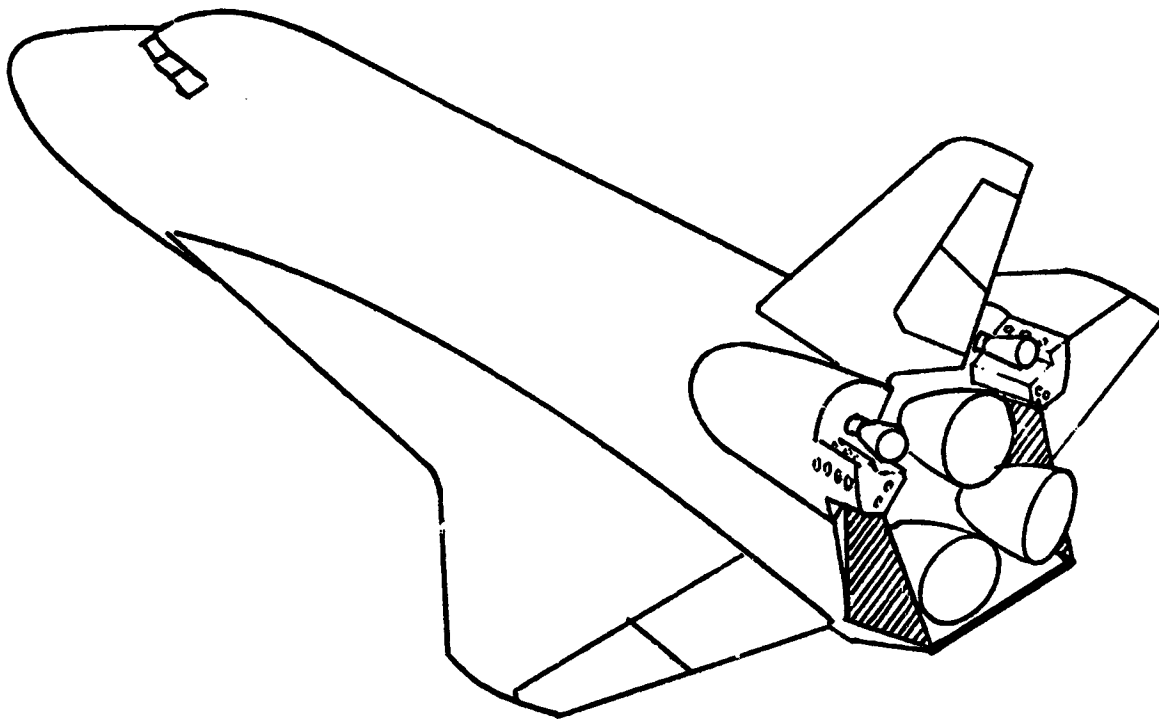
Figure 7-3. Base Side Plates

Not to Scale
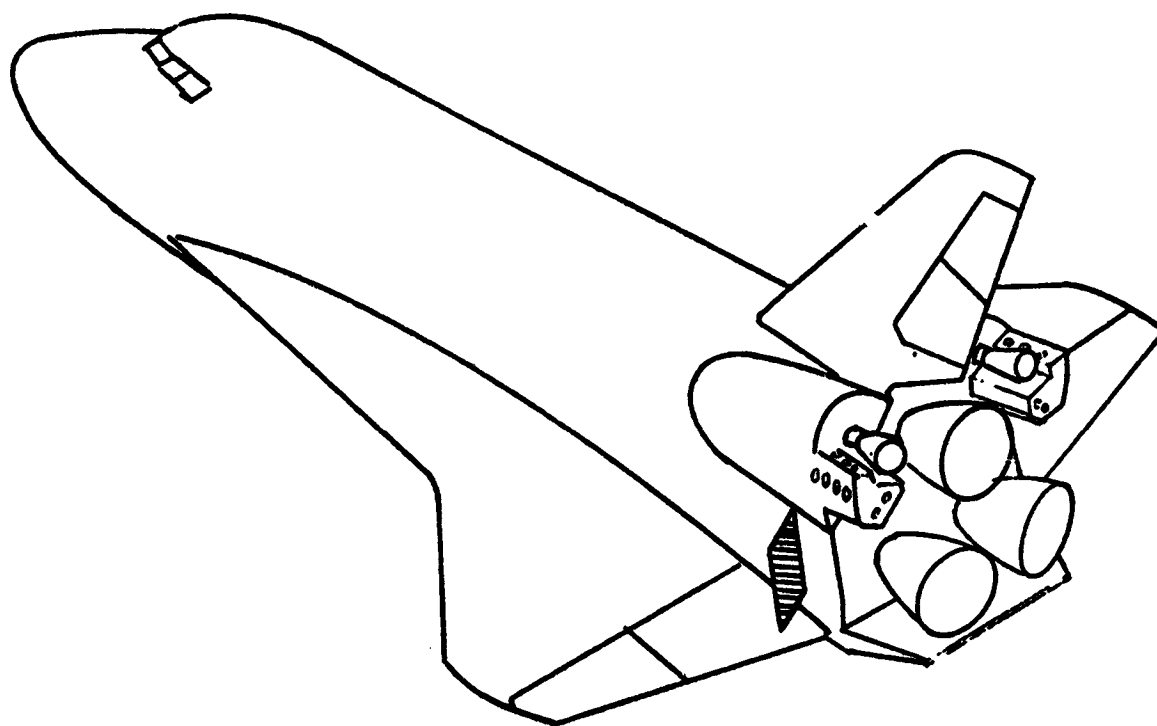
Figure 7-4. Body Flap

Not to Scale

Flap a

Flaps b
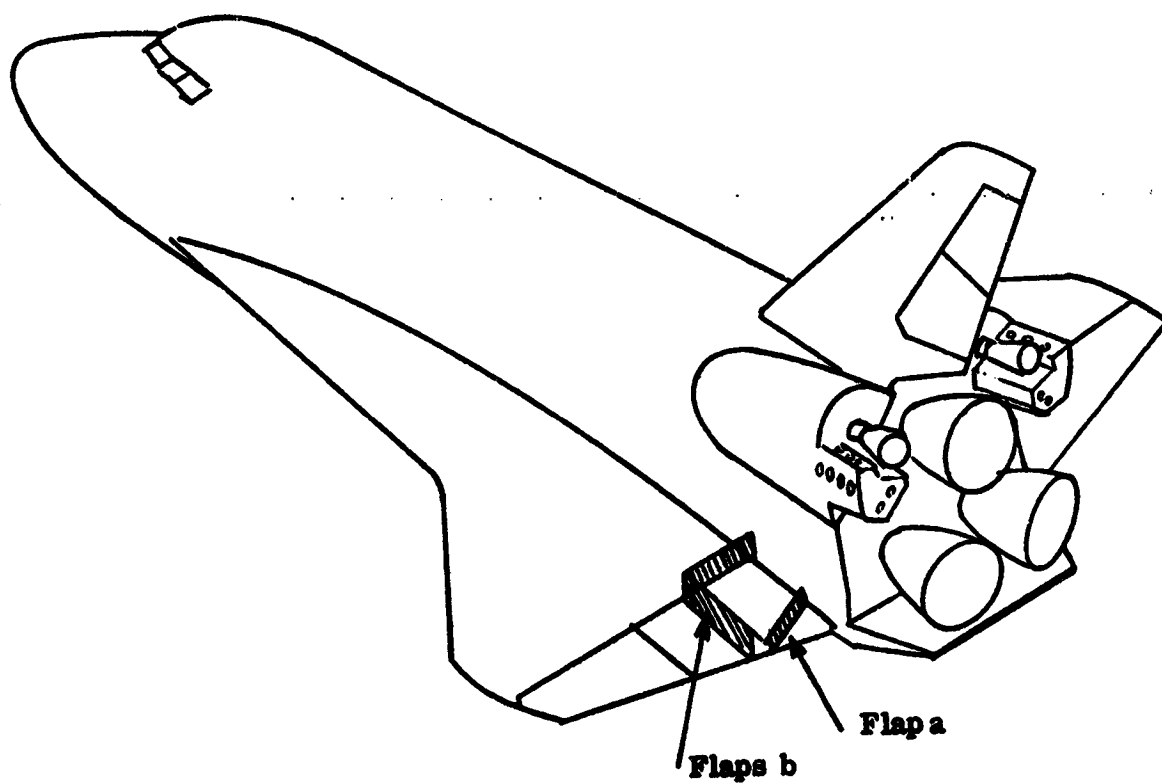
Figure 7-5. Wing Flap
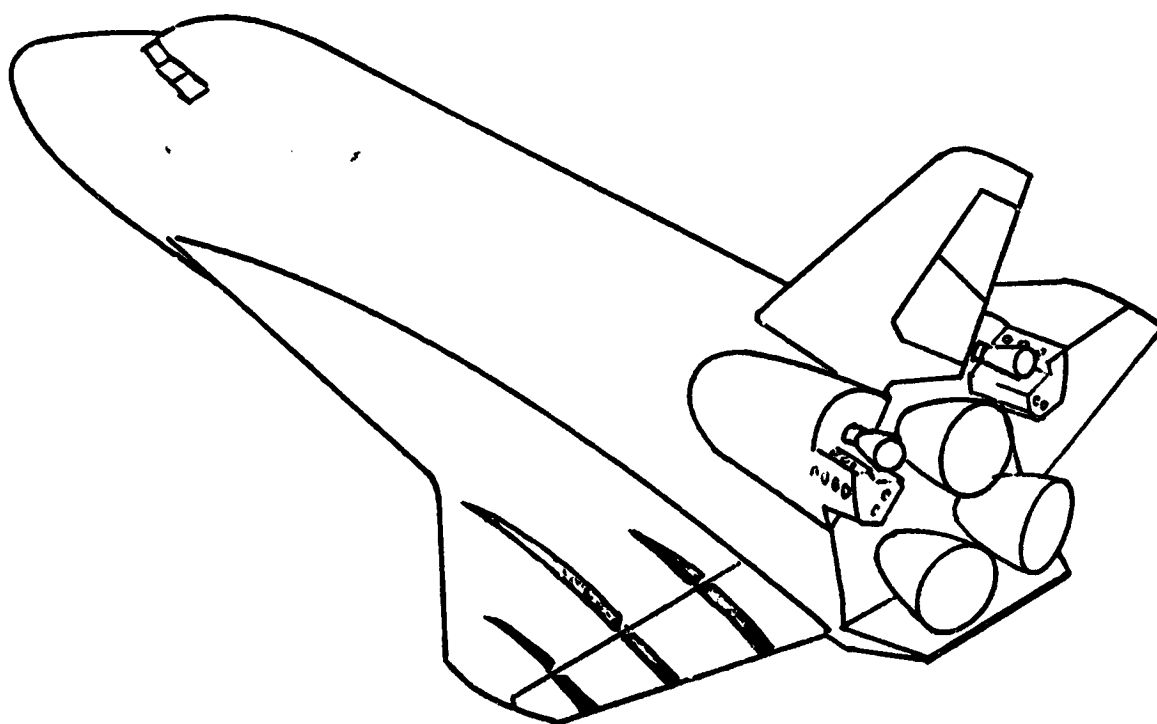
Figure 7-6. Wing Fences

8.0 CONCLUSIONS

The interaction between reaction control system plumes and flow over the leeward surfaces of the Shuttle Orbiter vehicle at high angle of attack in supersonic and hypersonic flow is a very complex interaction. The aerodynamic force and moments generated by this interaction have been shown to be large relative to the reaction control system forces and generally counteract the control input, especially when the plumes impinge on a vehicle surface and the control forces are reduced or in some instances reversed.

8.1 STUDY CONCLUSIONS

1. Cold flow simulation adequately matched temperature ratio of the full scale hydrazine rockets for force data based on Thayer's criteria.

2. Data accuracy of moment amplification data was found to be very good with a predicted scatter of less than 0.1 for most test data.

3. Yaw control interaction is small however yaw controls do induce unfavorable pitch up.

4. Roll control interactions are large causing roll reversal at angles of attack where the fin flow becomes important, very low effectiveness at all angles of attack, and a nose up pitching moment.

5. Roll control plume effects on wing are not angle of attack dependent but correlate best with plume momentum ratio; all other ratios appear to have lower importance.

6. Nose up pitch control interactions are small with little unfavorable effects.

7. Nose down pitch interactions are large causing pitch reversal and appear to be due primarily to plume impingement interactions on wing and on body flap.

8. The heat transfer data obtained indicate that the thermal protection system would have to be resized at least over the aft portion of the pod due to the increase in heating from the interaction.

9. The problem must be examined as two parts:
   a) plume impingement
   b) plume/flow interaction

   because the scaling parameters for these parts are not the same.

8.2 STUDY RECOMMENDATIONS

1. Further testing to define the pressure and heat transfer distributions on the upper surface of the wing, fuselage side, pod and tail surfaces is

required. Mach number and Reynolds number effects should be simulated. Integration of the surface pressure will determine the surface loading produced by the jet-stream interaction. The heat transfer distributions will be important to re-evaluate the thermal protection system on the wing upper surface tail and aft fuselage side.

2. A pressure test is required because it is more diagnostic than a force test and will allow better definition of the parameters which affect the plume interaction region and the induced pressure resulting from interaction allowing the results to be used to develop an empirical model of interaction.

3. A plume impingement test program should be undertaken in a vaccum facility such as the NASA-MSFC IBFF using exact scale nozzles to isolate the RCS plume impingement induced loads.

4. RCS yaw controls have a good location although sweeping the thrust vector 10° aft is recommended to reduce the induced pitch up.

5. RCS nose up pitch control have a good location although a small (10°) roll-out of the thrust axis to move the plume away from the fin would approve the rolling moment capability.

6. The RCS nose down pitch roll controls do not have a good location because plume interactions with the upper wing surface causes adverse pitch/roll interactions and an alternate location should be sought.

7. The most desirable alternate location (strictly from control standpoint) would be to mount the pitch down/roll nozzles on the aft fuselage body flap so that the nozzles extend through it onto the windward side of the vehicle. All interaction that would occur would then be positive $(K_m > 1., K_\ell > 1)$ and no canting would be necessary except if required for heating. Aero heating in this location is amenable to solution as indicated in reference 3.

8. The most desirable location would be on the side of the body just above the upper elevon limit canted to avoid impinging on the upper side of the body flap. Positive interaction should result.

9. Other solutions to the pitch down/roll problem might include:

   a) Increasing pitch thruster expansion ratio
   b) Creating a slot nozzle
   c) Forward fuselage upper surface mounting with roll by both fore and aft controls firing simultaneously
   d) Canting the nozzles to maximize total effectiveness

e) Upper wing surface fixed or retractable chord wise fences to keep the plume impingement flow from moving forward and spanwise on wing

Application of "jet interaction" theory to this problem is limited by the fact that the plume is not issuing from the surface experiencing the primary interaction but is rather impinging on it, and that the surface is a leeward surface which to a large degree is already experiencing separated flow. Thus, it appears that what is required is a hypersonic test program in which surface pressure is measured in sufficient detail to ascertain the extent of the interaction region, the pressures induced by interaction and to isolate the important free stream and nozzle parameters which control the interaction. Flow visualization runs are also needed to show the flow patterns which accompany the pressure data so that the contours of flow between pressure taps can be assessed. Heat transfer data is also very important to assess the flow impingement interaction effects particularly for the alternate configuration locations.

9.0 REFERENCES

1. Rausch, J.R., "Reaction Control System Aerodynamic Interference Test Report" General Dynamics Convair Aerospace Division Report CASD-NAS-73-012, August 1973.

2. Brevig, O., "Separated Hypersonic Flow Effects Induced by Reaction Control System (RCS) Thrusters," General Dynamics/Convair Aerospace Division Report No. GDCA-ERR-1718, December 1972.

3. Brevig, O., "Space Shuttle Attitude Control System (ACS) Thruster Penetration Heating," General Dynamics Convair Aerospace Division Report No. GDCA-DDB73-002, March 1973.

4. Vaughan, J. C., "A Two-Dimensional Study of the Jet Interaction and Downstream External Burning Resulting From a Gaseous Side Jet Expanding Into a Supersonic Airstream," Jet Propulsion Center, Purdue University, Report TM-70-5, June 1970.

5. Adams, T. C. Jr., and Nicolls J. A., "On The Structure of Jets From Highly Underexpanded Nozzles Into Still Air" Journal of Aeronautical Sciences, Volume 26 No. 1, January 1959.

6. Karydas A. L., and Kato H. T., "An Approximate Method for Calculating the Flow Field of A Rocket Exhausting Into a Vacuum," Philco Ford Aeronautic Report U-2630, June 1964.

7. Sibulkin M., and Gallaher W.H., "Some Aspects of the Interaction of A Jet With A Dust Covered Surface In A Vacuum Environment" General Dynamics Convair Aerospace Division Report ERR-AN-244, February 1963.

8. Fong, M. C. and Ehilich C. F. Jr., "Propulsion Effects On Aerodynamic Characteristics of Lifting Reentry Vehicles" Airforce Flight Dynamics Lab Report AFFDL-TR-70-12, March 1970.

9. Thayer, Wm. J., III, "The Two-Dimensional Separated Flow Region Upstream of Inert and Chemically Reactive Transverse Jets," Boeing Scientific Research Lab. Document D1-82-1066, March 1971.

10. Pinzola M. "Jet Simulation in Ground Test Facilities," NATO Advisory Group for Aeronautical Research and Development, AGARDograph 79, November 1963.

11. Herron R.D., "Investigation of Jet Boundary Simulation Parameters for Underexpanded Jets in a Quiescent Atmosphere," AEDC Report AEDC-TR-68-108, September 1968.

12. Rocket Research Corporation, "Monopropellant Hydraxine Design Data".

13. Ames Experimental Fluid Dynamics Branch Staff, "Test Planning Information for NASA-Ames 3.5 foot Hypersonic Wind Tunnel", Dec. 1972.

14. Anon, "Manual for Users of the Unitary Plan Wind Tunnel Facilities of the National Advisory Committee for Aeronautics," N43632, 1956.

15. Rockwell International Drawings, Numbered VL 70-000030, VL 70-000032, VL 70-000033, VL70-000034, VL-70000037, VL-70000040.

16. Rausch, J.R., "A Program for Computation of Nozzle Parameters", Convair Aeroballistics Technical Note TN-72-AE-10, Dec. 1972.

17. Jones, R.A., and Hunt, J. L., "Use of Fusible Temperature Indicators for Obtaining Quantitative Aerodynamic Heat Transfer Data," NASA TR-R-230, 1966.

18. Fay, J. A., and Riddell, F. R., "Stagnation Point Heat Transfer in Dissociated Air," Journal of Aero. Sci., Vol. 25, No. 2, pp 73-85, 1958.

19. Strike, Jr., W. T. and Best, Jr., J. T., "NASA-Convair ACS Space Shuttle Study at Mach Numbers 8.0," AEDC-TR-73-40, May 1973.

20. Shih, K. T., "Aerodynamic/Structural Heating Computer Program P5613," General Dynamics Convair Aerospace Division, Report No. GDCA-ERR-1707, June 1972.

21. Harthun, M. H., and Statham, C. L., "Space Shuttle Program Thermodynamic Design Data Book, " North American Rockwell Space Division Report No. SD72-SH-62-1, December 1972.

22. O'Neill, R. F. and Neuharth, E. R., "Convair Thermal Analyzer Computer Program No. P4560", General Dynamics/Convair Aerospace Division Report No. GDC-BTD69-005A 29 May 1969.

APPENDIX A

JET AND CAVITY INTERACTION WITH EXTERNAL FLOW BIBLIOGRAPHY

A-1   Chapman, D. R., "A Theoretical Analysis of Separated Flow", NACA TN-3792, October 1956.

A-2   Larson, H. K., "Heat Transfer in Separated Flow", Journal of Aerospace Sciences, Vol. 26, No. 11, November 1959, pp. 731-8.

A-3   Charwat, A. F., et al, "An Investigation of Separated Flows - Part I: The Pressure Field", J. of Aerospace Sciences, Vol. 28, No. 6, June 1961.

A-4   Charwat, A. F., et al, "An Investigation of Separated Flows - Part II: Flow in the Cavity and Heat Transfer", J. of Aerospace Sciences, Vol. 28, No. 47, July 1961.

A-5   Chung, P. M., and Viegas, J. R., "Heat Transfer at the Reattachment Zone of Separated Laminar Boundary Layers", NASA TN D-1072, September 1961.

A-6   Burggraf, O. R., "A Model of Steady Separated Flow in Rectangular Cavities at High Reynolds Numbers", Proceedings of the 1965 Heat Transfer and Fluid Mechanics Institute, Stanford University Press, Stanford, Ca., 1965.

A-7   Burgraf, O. R., "Analytical and Numerical Studies of the Structure of Steady Separated Flow", Journal of Fluid Mechanics, Vol. 24, 11. 113-151, 1966.

A-8   Rhudy, J. P., and Magnan, J. D., Jr., "Investigation on Heat-Transfer Distribution in Several Cavity and Step Configurations at Mach 10", AEDC-TDR-64-220, 1964.

A-9   Nestler, D. E., and Saydah, A. R., "Heat Transfer to Steps and Cavities in Hypersonic Turbulent Flow", AIAA Paper 68-673, presented at the AIAA Fluid and Plasma Dynamics Conference, Los Angeles, Ca., June 1968.

A-10   Wieting, A. R., "Experimental Investigation of Heat Transfer Distribution in Deep Cavities in Hypersonic Separated Flow", NASA TN D-5908, Sept. 1970.

A-11   Hodgson, J. W., "Heat Transfer in Separated Laminar Hypersonic Flow", AIAA Journal, December 1970, pp 2291-2293.

A-12   Coats, J. D., Rhudy, R. W., and Edmunds, E. W., "Effects of Surface Gaps and Steps on Laminar Heat-Transfer Rates at Local Mach Numbers from 3 to 10", AEDC TR-70-17, February 1970.

A-13   Emery, A. F., "Recompression Step Heat Transfer Coefficients for Super-sonic Open Cavity Flow", Transaction of the ASME, Vol. 91, No. 1, February 1969.

A-14   Hahn, Mansop, "Separated Flow Over a Cavity at Hypersonic Speed", AIAA Journal, Vol. 7, No. 6, June 1969.

A-15   Bogdonoff, S. M., and Vas, I.E., "Some Experiments on Hypersonic Separated Flows", ARS Journal, Vol. 3, No. 11, November 1962.

A-16.   Nicoll, K. M., "An Experimental Investigation of Laminar Hypersonic Cavity Flows", Parts I and II, Aerospace Research Laboratories Report ARL-63-73, January 1964.

A-17   Nestler, D. E., "Laminar Heat Transfer to Cavities in Hypersonic Low Density Flow", Proceedings of the Third International Heat Transfer Conference, American Society of Mechanical Engineers, Vol. II, 1966, pp. 251-261.

A-18   Haughen, R. L., and Dahnak, A. M., "Heat Transfer in Turbulent Boundary-Layer Separation over a Surface Cavity", J. of Heat Transfer (Transactions of ASME), Vol. 89, Series C, No. 4, November 1967.

A-19   Engel, C. D., "The Propulsive Attitude Control System – An Open Cavity Heating Problem", REMTECH Inc., Report RTR 008-1, Huntsville, Ala., April 1972.

A-20   Nestler, D. E., "An Engineering Analysis of Reattaching Shear Layer Heat Transfer", AIAA Paper 72-717, Presented at the AIAA 5th Fluid and Plasma Dynamics Conference, Boston, Mass., June 1972.

A-21   Brevig, O., "Separated Hypersonic Flow as Induced by Attitude Control System Thrusters", General Dynamics/Convair Aerospace Division Report No. GDCA-ERR-1678, December 1971.

A-22   Brevig, O., "Separated Hypersonic Flow Effects Induced by Reaction Control System (RCS) Thrusters", General Dynamics/Convair Aerospace Division Report No. GDCA-ERR-1718, December 1972.

A-23   Brevig, O., "Space Shuttle Attitude Control System (ACS) Thruster Penetration Heating", General Dynamics Convair Aerospace Division Report No. GDCA-DDB73-002, March 1973.

A-24   Strike, Jr., W. T. and Best, Jr., J. T., "NASA-Convair ACS Space Shuttle Study at Mach Number 8.0," AEDC-TR-73-40, May 1973.

A-25 Callaghan, Edmund E. and Ruggeri, Robert S., "Investigation of the Penetration of an Air Jet Directed Perpendicularly to an Air Stream", NACA TN 1615, June 1948.

A-26 Ruggeri, Robert S., Callaghan, Edmund E., and Bowden, Dean, T., "Penetration of Air Jets Issuing from Circular, Square, and Elliptical Orifices Directed Perpendicularly to an Air Stream", NACA TN 2019, February 1950.

A-27 Callaghan, Edmund E., and Ruggeri, Robert S., "A General Correlation of Temperature Profiles Downstream of a Heated-Air Jet Directed Perpendicularly to an Air Stream", NACA TN 2466, September 1951.

A-28 Hausmann, G. F., "Thrust Axis Control of Supersonic Nozzles by Airjet Shock Interference", United Aircraft Corp. Dept. Rep. R-83143-24, May 2, 1952.

A-29 Morkovin, M. V., Pierce, C. A., Jr., and Craven, C. E., "Interaction of a Side Jet with a Supersonic Main Stream', University of Michigan, Engineering Research Bulletin No. 35, 1952.

A-30 Ruggeri, Robert S., "General Correlation of Temperature Profiles Downstream of a Heated Air Jet Directed at Various Angles to Air Stream", NACA TN 2855, December 1952.

A-31 Ehrich, Fredric F., "Penetration and Deflection of Jets Oblique to a General Stream", J. Aero. Sci., V. 20, pp. 99-104, February 1953.

A-32 Fraser, J. P., "Three-Dimensional Study of a Jet Penetrating a Stream at High Angles", J. Aero-Sci., Vol. 21, pp. 59-60, January 1954.

A-33 Amick, J. L., Bond, C. E., and Liepman, H. P., "An Experimental Investigation of the Forces and Flow Fields Produced by a Jet Laterally from a Cone-Cylinder in a Mach 2.84 Stream", University of Michigan, Ann Arbor, Michigan, Department of Aero. Engg. WTM-255, November 1955.

A-34 Love, E. S. and Grigsby, C. E., "Some Studies of Axisymmetric Free Jets Exhausting from Sonic and Supersonic Nozzles into Still Air into Supersonic Streams", NACA RM L54L31, 1955.

A-35 Watts, G. A., "An Experimental Investigation of a Sonic Jet Directed Upstream Against a Uniform Supersonic Flow", University of Toronto, Toronto, Canada, Institute of Aerophysics, UTIA Tech. Note No. 7, January 1956.

A-36 Henning, A. B., Wineman, A. R., and Rainey, R. W., "Some Data on Body and Jet Reaction Controls", NACA RM L56L17, March 1957.

A-37   Lingen, A., "Jet-Induced Thrust Vector Ratios", United Aircraft Corp.
        Report R-0973-33, March 1957.

A-38   Callaghan & Ruggeri, "A General Correlation of Temperature Profiles
        Downstream of a Heated-Air Jet Directed Perpendicularly to an Air Stream",
        NACA TN 2466, 1957.

A-39   Jordinson, R., "Flow in a Jet Directed Normal to the Wind", Aero. Res.
        Council (Great Britain), R & M No. 3074, 1958.

A-40   Osofsky, Irving B., "The Use of Hot Gas Jets for Missile Control in the
        Atmosphere", Cornell Aeronautical Laboratory, Inc., Buffalo, New York,
        CAL Report No. BE-745-TO145, March 1959.

A-41   Ferrari, Carlo, "Interference Between a Jet Issuing Laterally from a
        Body and the Enveloping Supersonic Stream", Johns Hopkins University,
        Applied Physics Laboratory, Bumblebee Series Report No. 286, April 1959.

A-42   Vinson, P. W., etc., "Interaction Effects Produced by Jet Exhausting
        Laterally Near Base of Ogive-Cylinder Model in Supersonic Main Stream",
        NASA Memo 12-5-58W, 1959.

A-43   Amick, J. L. and Hays, P. B., "Interaction Effects of Side Jets Issuing
        From Flat Plates and Cylinders Aligned with a Supersonic Stream", WADC
        TR60-329, June 1960.

A-44   Carvalho, Gerad B. and Hays, Paul B., "Jet Interference Experiments
        Employing Body-Alone and Body-Fin Configurations at Supersonic Speeds",
        University of Michigan, Ann Arbor, Michigan, College of Engineering,
        Report No. CM-979, December 1960.

A-45   Cubbison, Robert W., Anderson, Bernhard H., and Ward, James J.,
        "Surface Pressure Distributions with a Sonic Jet Normal to Adjacent Flat
        Surfaces at Mach 2.92 to 6.4", NASA TN D-580, February 1961.

A-46   Janos, Joseph J., "Loads Induced on a Flat-Plate Wing by an Air Jet
        Exhausting Perpendicularly Through the Wing and Normal to a Free-Stream
        Flow of Mach Number 2.0", NASA TN D-649, March 1961.

A-47   Romeo, David J. and Sterrett, James R., "Aerodynamic Interaction Effects
        Ahead of a Sonic Jet Exhausting Perpendicularly from a Flat Plate into a
        Mach Number 6 Free Stream", NASA TN D-743, April 1961.

A-48   Falanga, Ralph A. and Janos, Joseph J., "Pressure Loads Produced on a
        Flat-Plate Wing by Rocket Jets Exhausting in a Spanwise Direction Below
        the Wing and Perpendicular to a Free-Stream Flow of Mach Number 2.0",
        NASA TN D-893, May 1961.

A-49   Wu, Jain-Ming, Chapkis, Robert L., and Mager, Artur, "Approximate
       Analysis of Thrust Vector Control by Fluid Injection", ARS J., V. 31, No.
       12, pp. 1677-1685, December 1961.

A-50   Kaufman, Louis G., III, "Classification of Interactions Due to High-Speed
       Flows Past Transverse Jets", Grumman Aircraft Engineering Corp.,
       Research Report RE-154, February 1962.

A-51   Hayman, Lovick, O., Jr., and McDearmon, Russell W., "Jet Effects on
       Cylindrical Afterbodies Housing Sonic and Supersonic Nozzles which Exhaust
       Against a Supersonic Stream at Angles of Attack from 90° to 180° ", NASA
       TN D-1016, March 1962.

A-52   Newton, J. F., Jr., and Spaid, F. W., "Interaction of Secondary Injectants
       and Rocket Exhaust for Thrust Vector Control", ARS J., V. 32, No. 8,
       pp. 1203-1211, August 1962.

A-53   Walker, R. E., Stone, A. R., and Shandor, M., "Interaction between
       Sonic Sidejets and Supersonic Duct Flow", The Johns Hopkins University,
       Applied Physics Laboratory, Bumblebee Series, Report No. 316,
       December 1962.

A-54   Hayman, L. O. and McDearmon, R. W., "Jet Effects on Cylindrical
       Afterbodies Housing Sonic and Supersonic Nozzles which Exhaust Against
       a Supersonic Stream at Angles of Attack from 90 to 180", NASA TN D-1016,
       1962.

A-55   Walker, R. E., Stone, A. R., and Shandor, M., "Secondary Gas Injection
       in a Conical Rocket Nozzle", AIAA J., V. 1, No. 2, pp. 334-338, February
       1963.

A-56   Amick, J. L., Stubblebine, W. and Chen, Paul C. Y., "Experimental
       Interaction Effects of Forward Located Side Jets on a Body of Revolution",
       University of Michigan, Ann Arbor, Michigan, Report No. WTM-276,
       March 1963.

A-57   Brindle, C. Carl and Moxley, David W., Jr., "Interaction Effects Produced
       by a Sonic Jet Exhausting from a Curved Two-dimensional Plate in a Super-
       sonic Stream", David Taylor Model Basin, AERO Report 1053, April 1963.

A-58   Volger, R. D., "Surface Pressure Distributions Induced on a Flat Plate by
       a Cold Air Jet Issuing Perpendicularly from the Plate and a Normal to Low-
       Speed Free-Stream Flow", NASA TN D-1629, March 1963.

A-59   Strike, W. T., Schueler, C. J., and Deitering, J. S., "Interactions Produced by Sonic Lateral Jets Located on Surfaces in a Supersonic Stream", Arnold Air Force Station, Tennessee, ARO Inc., AEDC-TDR-63-22, April 1963.

A-60   Watman, H. and Meyer, R. C., "A Review of Lateral Jet-Supersonic Stream Interactions with Reference to Reaction Control Applications", Grumman Aircraft Engineering Corp., Report No. ADR-01-07-63.2, April 1963.

A-61   Broadwell James E., "Analysis of the Fluid Mechanics of Secondary Injection for Thrust Vector Control", AIAA J., V. 1. No. 5 pp. 1067-1075 May 1963.

A-62   Romeo, J., "Aerodynamic Interaction Effects Ahead of Rectangular Sonic Jets Exhausting Perpendicularly from a Flat Plate into a Mach Number 6 Free Stream", NASA TN D-1800, May 1963.

A-63   Letko, William, "Loads Induced on a Flat Plate at a Mach Number of 4.5 with a Sonic or Supersonic Jet Exhausting Normal to the Surface", NASA TN D-1935, July 1963.

A-64   Dowdy, Mach W., and Newton, John F., Jr., "Investigation of Liquid and Gaseous Secondary Injection Phenomena on a Flat Plate", Jet Propulsion Laboratory, Tech. Report No. 32-542, December 23, 1963.

A-65   Mitchell, John W., "An Analytical Study of a Two-Dimensional Flow Field Associated with Sonic Secondary Injection into a Supersonic Stream", Palo Alto, California , VIDYA Tech. Note 9166-TN-2, March 1964.

A-66   Mitchell, J. W., "An Analytical Study of a 2-Dim. Flow Field Associated with Sonic Secondary Injection into a Supersonic Stream, AD450742, 1964.

A-67   Amick, James L. and Hawk, Norman E., "Jet Interaction Studies on a Body of Revolution at Angle of Attack", University of Michigan, Ann Arbor, Michigan, College of Engineering, Report No. WTM 273, April 1964.

A-68   Dahm, Thomas J., "The Development of an Analogy to Blast-Wave Theory for the Prediction of Interaction Forced Associated with Gaseous Secondary Injection into a Supersonic Stream", Palo Alto, California, VIDYA Tech. Note 9166-TN-3, May 1964.

A-69   Spaid, F. W., "A Study of Secondary Injection of Gases into a Supersoni Flow", Ph D Thesis, California Institute of Technology, June 1964.

A-70   Walker, R. E. and Shandor, M., "Influence of Injectant Properties for Fluid-Injection Thrust Vector Control", Journal of Spacecraft, Vol. 1, No. 4, pp. 409-413, July-August 1964.

A-71   Bradbury, L. J. S. and Wood, M. N., "The Static Pressure Distribution Around a Circular Jet Exhausting Normally from a Plane Wall into an Airstream", Ministry of Aviation, London, Technical Note No. AERO 2978 August 1964.

A-72   Zukoski, Edward E., and Spaid, Frank W., "Secondary Injection of Gases into a Supersonic Flow", AIAA J., V. 2, No. 10, pp. 1689-1696, October 1964.

A-73   Charwat, A. F., and Allegre, J., "Interaction of a Supersonic Stream and a Transverse Supersonic Jet', AIAA Journal, Vol. 2, No. 11, pp. 1965-1972, November 1964.

A-74   Bradbury, L.J.S. and Wood, M. N., "The Static Press. Dist. Around a Circular Jet Exhausting Normally from a Plane Wall into an Air Stream", Tech. Note AERO 2978, 1964.

A-75   Dahm, T. J., "The Development of an Analogy to Blastwave Theory for the Prediction of Interaction Forces Associated with Gaseous Secondary Injection into a Supersonic Stream", AD450743, 1964.

A-76   Hsia, H. T., Siefert, H. S., and Karamcheti, K., "Shocks Induced by Secondary Fluid Injection", Journal of Spacecraft and Rockets, Vol. 2 No. 1, pp. 67-72, January-February 1965.

A-77   Kaufman, Louis G., II, "Shock Tunnel Experiments on Flows Past Transverse Jets", Grumman Aircraft Engineering Corp., Report No. RE-209, April 1965.

A-78   Guhse, R. D., "An Experimental Investigation of Thrust Vector Control by Secondary Injection, MSME Thesis", Purdue University, June 1965.

A-79   Dershin, Harvey, "Forces Due to Gaseous Slot Jet Boundary Layer Interaction", Journal of Spacecraft V. 2, No. 4, pp. 597-599, July - August 1965.

A-80   Guhse, Richard E., "An Experimental Investigation of Thrust Vector Control by Secondary Injection", Purdue University, NASA CR-297, September 1965.

A-81   Crist, S., Sherman, P. M. and Glass, D. R., "Study of the Highly Underexpanded Sonic Jet", AIAA Journal, Vol. 4, No. 1. pp. 68-71, Jan. 1966.

A-82   Shetz, J. A., Billig, F. S., and others, "Hydrogen Jet Penetration Studies", in Research and Development Programs Quarterly Report, The Johns Hopkins University, Applied Physics Laboratory, January-March 1966, Silver Spring, Maryland, 1966.

A-83   Suttles, John T., and James, Robert L., Jr., "Effect of Nose-Mounted Control-System Jets in Roll-Control Positions on the Aerodynamics of a Space Vehicle", NASA TN D-3282, February 1966.

A-84   Strike, W. T. Jr., "Lateral Jet Interaction Effects on a 9-Deg Cone at Mach 10", Arnold Air Force Station, Tennessee, ARO, Inc., AEDC-TR-66-14, March 1966.

A-85   Zakkay, V., et al, "An Experimental Investigation of the Interaction between a Transverse Sonic Jet and a Hypersonic Stream", AIAA Journal, Vol. 9, No. 4, April 1966.

A-86   Strike, William, Jr., "A Study at Mach 10 of the Aerodynamic Disturbances Generated Over a Flat Containing Lateral Jets (U)", ARO, Inc., AEDC-TR-66-48 (Confidential), April 1966.

A-87   Maurer, F., "Three-Dimensional Effects in Shock-Separated Flow Regions Ahead of Lateral Control-Jets Issuing from Slot Nozzles of Finite Length", AGARD Conference Proceedings, No. 4, Part 2, pp. 597-634 May 1966.

A-88   Sterrett, J. R. and Barber, J. B., "A Theoretical and Experimental Investigation of Secondary Jets in a Mach 6 Free Stream with Emphasis on the Structure of the Jet and Separation Ahead of the Jet", NASA TMX 57137, presented at the Separated Flows Specialists Meeting Fluid Dynamics Panel - AGARD, May 1966.

A-89   Kaufman, L. G., III, Remarks on Hypersonic Flow Past Transverse Jets", Proceedings of the 7th U. S. Navy Symposium on Aeroballistics, Pt. Mugu, California, pp. 715-725, June 1966.

A-90   Reichenau, David E. A., "Interference Effects of Cold and Hot Rocket Exhausts Issuing Normal to the Air-Stream from a Flat Plate at Free-stream Mach Numbers from 0.6 to 1.4", AEDC-TR-66-127, June 1966.

A-91   Volz, W. C. and Werle, M. J., "Jet Interaction Studies", Proceedings of the 7th U. S. Navy Symposium on Aeroballistics, Pt. Mugu, California, pp. 689-713, June 1966.

A-92   Kaufman, L. G., III, "Hypersonic Flows Past Transverse Jets", Grumman Aircraft Eng. Corporation, Report No. RE-263, Bethpage, New York, August 1966.

A-93   Spaid, F. W., Zukoski, E. F., and Rosen, R., "A Study of Secondary Injection of Gases into a Supersonic Flow", Jet Propulsion Laboratory, Tech. Report No. 32-834, August 1966.

A-94   Barber, J. B., and Staylor, W. F., "Investigation of Secondary Jets on a Cone at a Mach number of 6", J. Spacecraft, V. 3, No. 10, pp. 1554-1555, October 1966.

A-95   Schetz, J. A. and Billig, F. S., "Penetration of Gaseous Jets Injected into a Supersonic Stream", J. of Spacecrafts and Rockets, Vol. 3, No. 11, pp. 1658-1665, November 1966.

A-96   Spaid, F. W. and Zukoski, E., "Further Experiments Concerning Secondary Injection of Gases into a Supersonic Flow", AIAA Journal, Vol. 4, No. 12 pp. 2216-2218, December 1966.

A-97   Suttles, J. T. and Jemes, R. L., "Effect of Nose-Mounted Control-System Jets in Roll Control Positions on the Aerodynamics of a Space Vehicle", NASA TN D-3282, 1966.

A-98   Kaufman, Louis G., III, "Hypersonic Flows Past Transverse Jets", J. Spacecraft, V. 4, No. 9, pp. 1230-1235, Sept. 1967, also AIAA Paper 67-190, January 1967.

A-99   Lee, Edwin, E., Jr., and Willis, Conrad M., "Interaction Effects of a Control Jet Exhausting Radially from the Nose of an Ogive-Cylinder Body at Transonic Speeds", NASA TN D-3752, January 1967.

A-100   Wooler, P. T., "On the Flow Past a Circular Jet Exhausting at Right Angles froma Flat Plate or Wing", RAS J. V. 71, pp. 216-218, March 1967.

A-101   Hawk, N. E. and Amick, J. L., "Two-Dimensional Secondary Jet Inter-action with a Supersonic Stream", AIAA J., Vol. 5, No. 4 pp. 655-660, April 1967.

A-102   Hayes, Clyde, "Effect of a Forward-Location Reaction Control on the Aerodynamic Characteristics of a Fin-Stabilized Missile at Mach 1.50 to 2.16", NASA TM X-1385, May 1967

A-103   Schetz, J. A., Hawkins, P. F., and Lehman, H., "Structure of Highly Underexpanded Transverse Jets in a Supersonic Stream", AIAA Journal, Vol. 15, No. 5, pp. 882-884, May 1967.

A-104   Dahm, Thomas J., "A Comprehensive Analytical Procedure for the Performance Prediction of Rocket Thrust Vector Control with Gaseous Secondary Injection", Aerotherm Corp. Final Report No. 67-11, AFRDL-TR-78-169, AD817962, June 1, 1967.

A-105 Barnes, J. W., Davis, J. G., Tang, H. H., "Control Effectiveness of Transverse Jets Interacting with a High Speed Freestream", Air Force Flight Dynamics Laboratory, Research and Technology Division, AFSC, Wright-Patterson Air Force Base, Ohio, AFFDL-TR-67-90.

A-106 Orth, Richard C., and Funk, John A., "An Experimental and Comparative Study of Jet Penetration in Supersonic Flow", J. Spacecraft, V. 4. No. 9, pp. 1236-1242.

A-107 Reichenau, E. A., "Interference Effects Produced by a Cold Jet Issuing Normal to the Airstream from a Flat Plate at Transonic Mach Numbers", AEDC-TR-67-220, October 1967.

A-108 Strike, W. T., "Analysis of the Aerodynamic Disturbances Generated on a Flat Plate Containing Lateral Jet Nozzles Located in a Hypersonic Stream (U)", AEDC, Arnold Air Force Station, Tenn., ARO, Inc. AEDC-TR-67-158 (Confidential), October 1967.

A-109 Wooler, P. T., Burghart, G. H., and Gallaher, J. T., "Pressure Distribution on a Rectangular Wing with a Jet Exhausting Normally into an Airstream", J. of Spacecraft and Rockets, Vol. 4, No. 6, pp. 537-543, November-December 1967.

A-110 Dahm, T. J., "A Comprehensive Analytical Procedure for the Performance Prediction of Rocket Thrust Vector Control with Gaseous Secondary Injection", AFRPL-TR-67-169, Final Report No. 67-1 .

A-111 Sterret, J. R., Barber, J. B., Alston, D. W., and Romeo, D. J., "Experimental Investigation of Secondary Jets from 2-Dim. Nozzles with Various Exit Mach No. for Hypersonic Control Application", NASA TN D-3795, 1967.

A-112 Strike, W. T., Jr., "Analysis of the Aerodynamic Disturbances Generated on a Flat Plate Containing Lateral Jet Nozzles Located in a Hypersonice Stream", AEDC-TR-67-158, January 1968.

A-113 Mahaffey, R. E. and Weinraub, R. A., "An Experimental Study of Supersonic Jet Penetration in a Supersonic Flow", AIAA Student Journal, Vol. 6, No. 1, February 1968.

A-114 Spaid, F. W. and Zukoski, E. E., "A Study of the Interaction of Gaseous Jets from Transverse Slots with Supersonic External Flows", AIAA Journal, Vol. 6, No. 2, pp. 205-212.

A-115 Schetz, J. A., Weinraub, R. A. and Mahaffey, Jr., R. E., "Supersonic Transverse Injection into a Supersonic Stream", AIAA Journal, Vol. 6, No. 5, pp. 933-934, May 1968.

A-116   Spring, D. J., "An Experimental Investigation of the Interference Effects Due to a Lateral Jet Issuing from a Body of Revolution over the Mach Number Range of 0.8 to 4.5", Report No. RD-TR-68-10, August 1968.

A-117   Phinney, R. E., Werle, M. J., Knott, J., and Zolz, W. C., "Slot Jet Interaction Studies of an Ogive Cylinder at M $_\infty$= 4 and 5", NOL TR 68-143, September 1968.

A-118   Kaufman, L. G., and Koch, F., "High Speed Flows Past Transverse Jets", Grumman Research Dept. Report RE-348, October 1968.

A-119   Spring, D. J., "An Experimental Investigation of the Interference Effects due to a Lateral Jet Issuing from a Body of Revolution over the Mach number Range of 0.8 to 4.5", RD-TR-68-10.

A-120   Wu, J. and Aoyama, K., "Analysis on Transverse Secondary Injection Penetration into Confined Supersonic Flow", AIAA Paper No. 69-2, January 1969.

A-121   Reis, R. J., Aucoin, P. J. and Stechman, R. C., "Prediction of Rocket Exhaust Flowfields," Journal of Spacecraft and Rockets, Vol. 7, No. 2, pp. 155-159, February 1969.

A-122   Orth, R. C., Schetz, J. A. and Billig, F. S., "The Interaction and Penetration of Gaseous Jets in Supersonic Flow", NASA CR-1386, July 1969.

A-123   Gilman, B. C., "Control Jet Interaction Investigation", Martin-Marietta Corporation, OR9975, July 1969.

A-124   Cassel, L. A., Durando, N. A., Bullard, C. W., and Kelso, J. M., "Jet Interaction Control Effectiveness for Subsonic and Supersonic Flight", Report No. RD-TR-69-21, September 1969.

A-125   Goldstein, M. E. and Braum, W., "Injection of an Attached Inviscid Jet at an Oblique Angle to a Moving Stream", NASA-TN D-5460 and 5501, 1969.

A-126   Strike, W. T. and Ruchanan, T. D., "Circular Sonic Lateral Jet Interaction Effects on a Flat Plate at Mach Number 18.5 Using a Small Solid Monopropellant Rocket Motor", AEDC-TR-69-205.

A-127   Charns, L. J. and Collins, D. J., "Stagnation Temperature and Molecualr Weight Effects in Jet Interaction", AIAA Journal, Vol. 8, No. 2, Feb. 1970.

A-128   Chrans, L. J. and Collins, D. J., "Stagnation Temperature and Molecular Weight Effects in Jet Pnetration", AIAA Journal, Vol. 8, No. 2, pp. 287-293, February 1970.

A-129   Nunn, R. N., "Jet Interaction Wrap-Around on Bodies of Revolution",
         Journal of Spacecraft and Rockets, Vol. 7, No. 3, March 1970.

A-130   Werle, M. J., Driftmyer, R. T. and Shaffer, D. G., "Jet Interaction-
         Induced Separation of Supersonic Turbulent Boundary Layers - The Two-
         Dimensional Problem", AIAA Paper No. 70-765, Los Angeles, 1970.

A-131   Werle, M. J., Driftmyer, R. T. and Shafter, D. G., "Two-Dimensional
         Jet Interaction with a Mach 4 Mainstream", NOLTR 70-50, May 1970.

A-132   Wilson, W. G., "Analysis of the Flow-Disturbance and Side Forces Due to
         Gaseous Secondary Injection into a Rocket Nozzle", Journal of Spacecraft
         and Rockets, Vol. 7, No. 5, May 1970.

A-133   Werle, M. J., Shaffer, D. G., and Driftmyer, R. T., "Downstream
         Pressure Distributions for Two-Dimensional Jet Interactions", AIAA
         Journal, 8, pp. 1165-1 67, June 1970.

A-134   Vaughan, J. C., "A Two-Dimensional Study of the Jet Interaction and
         Downstream External Burning Resulting from a Gaseous Side Jet Expanding
         into a Supersonic Airstream", Jet Propulsion Center, Purdue University
         Report TM-70-5, June 1970.

A-135   Povinelli, F. P., Povinelli, L. A. and Hersch, M., "Supersonic Jet
         Penetration (up to Mach 4) into a Mach 2 Airstream", Journal of Spacecraft
         and Rockets, Vol. 8, No. 8, pp. 988-992, August 1970.

A-136   Werle, M. J., Driftmyer, R. T., and Shaffer, D. G., "Supersonic Two-
         Dimensional Jet-Interaction Studies", NOLTR-70-242, December 1970.

A-137   Hersch, M., Povinelli, L. A., etc., "Optical Study of Sonic and Supersonic
         Jet Penetration from a Flat Plase into a Mach 2 Airstream", NASA TN D-
         5717, 1970.

A-138   Street, T. A., "Experimental Investigation if a Transverse Jet Ejecting
         from a Flat Plate into a Subsonic Free Stream", RD-TM-70-5.

A-139   Street, T. A., "An Oil Flow Study of a Sonic Reaction Jet Ejecting from a
         Body of Revolution into a Free Stream of Mach Number Range 1.75 to 4.5
         Versus Army Missile Command", RD-TM-70-7.

A-140   Lee, C. C. and Barfield, B. F., "Interaction of Sonic Transverse Jets with
         Supersonic External Flows", AIAA Journal Vol. 9, No. 2, pp. 304-308,
         February 1971.

A-141 Thayer, Wm. J., III, "The Two-Dimensional Separated Flow Region
Upstream of Inert and Chemically Reactive Transverse Jets", Boeing
Scientific Research Lab. Document D1-82-1066, March 1971

A-142 Cohen, L. S., Coulter, L. J. and Egan Jr., W. J., "Penetration and
Mixing of Multiple Gas Jets Subjected to a Cross Flow", AIAA Journal,
Vol. 9, No. 4, pp. 718-724, April 1971.

A-143 Billig, F. W., Orth, R. C., and Lasky, M., "A Unified Analysis of
Gaseous Jet Penetration", AIAA Journal, Vol. 9, No. 6, pp. 1048-1058,
June 1971.

A-144 Street, T. A., "Correlation of Transverse Jet Control Effectiveness on a
Body of Revolution with Angle of Attack at Mach Number 1.75", U. S. Army
Missile Command Report No. RD-TR-71-21, September 1971.

APPENDIX B

PLUME IMPINGEMENT BIBLIOGRAPHY

B-1   J. R. Rausch, "Plume Induced Pressures On A Parallel Staged
       Vehicle," GDCA-ERR-1667, February 1972.

B-2   C. Donaldson, R. S. Snedeker, "A Study Of Free And Impinging Jets."
       J. Fluid Mechanics (1971) Vol. 45, Part 2, pp. 281-319.

B-3   Hrycak, P.; Lee, D.T. ; Gaunter, J. \.   "Experimental Flow
       Characteristics Of A Single Turbulent Jet Impinging On A Flat Plate,"
       NASA TN-D-5690, February 1970.

B-4   Gauntner, J. W.; Livingood, J. N. B.; Hrycak, P. "Survey Of
       Literature Of Flow Characteristics Of A Single Turbulent Jet
       Impinging On A Plat Plate." NASA TN-D-5652, February 1970.

B-5   A. R. Maddox, "Impingement of Underexpanded Plumes On Adjacent
       Surfaces, " J. Spacecraft 5, 718-24 (1968).

B-6   K. C. Hendershot & R. Sergeant, "An Experimental Investigation Of
       Solid Propellant Rocket Plume Impingement Effects On Bodies At High
       Altitude." CAL Report AA-2302-Y-1, Jan. 1967.

B-7   F. P. Boynton & R. S. Janda, "Computer Program For Plume Impinge-
       ment Forces & Moments With Body Motion" GDC-DBE67-019, Aug.
       1967.

B-8   R. F. Yurczyk & L. E. Armfield, "A Program To Compute Forces
       On Bodies In A Hypersonic Flow Field." GDC-BTD67-067 15 Aug.
       1967.

B-9   E. T. Piesek, R. R. Koppang, and D. J. Simkin, "Rocket Exhaust
       Impingement On A Flat Plate At High Vacuum" J. Spacecraft 3,
       1950-57 (1966).

APPENDIX B

PLUME IMPINGEMENT BIBLIOGRAPY

B-10   I. Tani & Y. Komatsu, "Impingement Of A Round Jet On A Flat
       Surface." Proceedings Of The Eleventh International Congress Of
       Applied Mechanics. Henry Gortler, ed., Springer-Verlag, 1966.

B-11   A. J. Gopin & E. L. Margolin, "A Cold Gas, Short Duration Technique
       For High Altitude, Underexpanded Jet Exhaust Impingement Studies"
       NASA TN-D-2943, Nov. 1965.

B-12   W. H. Gallaher, M. Sibulkin, "Some Aspects Of The Interaction
       Of A Jet With A Dust Covered Surface In A Vacuum Environment."
       Generaly Dynamics/Astronautics Report ERR-AN-244, 10 February
       1963.

B-13   M. Poreh, J. E. Cermak, "Flow Characteristics Of A Circular
       Submerged Jet Impinging Normally On A Smooth Boundary." Sixth
       Midwestern Conference On Fluid Mechanics. University of Texas,
       1959, pp. 198-212.

B-14   "Determination Of Exhaust Plume, Impingement Pressures, And
       Heat Rates For Space Shuttle Engines." 11 p 1534 N72-20867.

B-15   "Computer Codes For Determining Effect Of Rocket Exhaust Plume
       Impingement On Sensitivie Space Vehicle Surfaces." AD-735722
       12 p. 1683 N72-21962.

B-16   "Wind Tunnel Investigation Of Jet Exhausting Into Cross Flow
       [AD-718-22] 13 p 2064 N71-24492.

B-17   "Space Shuttle Vehicle Rocket Plume Impingement Study For Separation
       Analyses" [NASA-CR-114875] 08 p. 1304 N71-18796.

B-18   "Scaling Parameters For Simulating Highly Expanded Rocket Exhaust
       Plumes & Resultant Impingement Forces On Imersed Bodies"
       [NASA-CR-102853] 24 p. 4622 N70-42180

APPENDIX B

PLUME IMPINGEMENT BIBLIOGRAPHY

B-19   "Impingement Forces & Moments & Centers Of Pressure Due To
        Air Jets In Vacuum Sphere" [NASA-TN-D-5147] 11 p 1869
        N69-23085.

B-20   "Computer Programs & Engineering Methods For Calculating
        Heating Rates & Forces In Jet Plume Impingement Problems"
        [NASA-CR-98329] 07 p 1242 N69-18037.

B-21   "Rocket Exhaust Jet Interaction With Lunar Surface Dust Layer"
        17 p 2970 N68-29011.

B-22   "Impingement of Condensed Rocket Exhaust Gases Upon Proximate
        Space Vehicles" 17 p 2873 N68-29012.

B-23   "Pressures And Heat Transfer Rates Predictions For Rocket
        Exhaust Impingement On Flat Plates & Curved Panels."
        [NASA-CR-61234] 17 p 2988 N68-29457.